Development of a two-phase flow up-scaling method in a macroporous medium

Tanguy Herry

To cite this version:

Tanguy Herry. Development of a two-phase flow up-scaling method in a macroporous medium. Fluid mechanics [physics.class-ph]. Université Gustave Eiffel, 2024. English. ⟨NNT : 2024UEFL2044⟩. ⟨tel-04969233⟩

HAL Id: tel-04969233
https://theses.hal.science/tel-04969233v1

Submitted on 27 Feb 2025

Développement d'une méthode de remontée d'échelle en thermohydraulique diphasique

Development of a two-phase flow up-scaling method

Thèse de doctorat de l'Université Gustave Eiffel

École doctorale n°531, Sciences, Ingénierie et Environnement (SIE)
Spécialité de doctorat: Mécanique des fluides
Unité de recherche : Laboratoire Modélisation et Simulation Multi-Echelle (MSME, UMR 8208 CNRS)

Thèse présentée et soutenue à l'Université Gustave Eiffel,
le 14/10/2024, par :

Tanguy HERRY

Composition du Jury

Catherine COLIN Professeure des universités, INP Toulouse	Présidente du jury
Bérengère PODVIN Directrice de recherche, EM2C	Examinatrice
Pierre RUYER Ingénieur de recherche, IRSN	Examinateur
Olivier SIMONIN Professeur des universités, INP Toulouse	Rapporteur
Christophe JOSSERAND Directeur de recherche, LadHyx	Rapporteur

Encadrement de la thèse

Bruno RAVERDY Ingénieur de recherche, CEA Saclay	Co-Encadrant de thèse
Stéphane MIMOUNI Ingénieur de recherche, EDF R&D Chatou	Directeur de thèse
Stéphane VINCENT Professeur des universités, MSME	Co-Directeur de thèse

Acknowledgment

Les trois années de travail qui ont donné cette thèse furent parfois passionnantes, parfois ont semblé me dépasser, mais ont toujours éveillé une grande curiosité en moi. Cette thèse n'a été rendue possible que grâce aux actions d'un certain nombre de personnes, et c'est pourquoi j'écris aujourd'hui ces quelques lignes afin de les remercier.

Tout d'abord, je tiens sincèrement à remercier Olivier Simonin et Christophe Josserand pour avoir accepté de rapporter cette thèse, que j'ai tenté de rendre de façon la plus claire possible malgré les nombreuses équations. En particulier, les questions et remarques pointilleuses d'Olivier Simonin m'ont permis d'améliorer le manuscrit, en corrigeant quelques erreurs. Ensuite, je remercie Catherine Colin pour avoir accepté de présider le jury, et Pierre Ruyer et Bérengère Podvin pour avoir accepté le rôle d'examinateurs et examinatrices de ma thèse. Votre présence au sein de mon jury de thèse est un honneur et j'espère avoir l'occasion de travailler avec vous dans le futur.

Ce travail n'aurait bien entendu jamais été possible sans le soutien inconditionnel de mes encadrants et directeurs de thèse : Stéphane Vincent, Stéphane Mimouni et Bruno Raverdy.

Je voudrais tout d'abord remercier Stéphane Vincent pour m'avoir apporté ton expertise sur certains sujets tels que les études a priori, ce qui m'a permis de prendre la bonne orientation dans la suite de cette thèse.

Ensuite, Stéphane Mimouni, je tiens à te remercier chaleureusement pour l'encadrement continu que tu m'as donné avec cette curiosité et ce positivisme qui te caractérisent et surtout pour ce nombre d'idées concernant la thèse que je ne compte plus. En effet, je suis ressorti de chacune de nos nombreuses réunions avec de nouvelles idées toujours très enthousiasmantes, qui donnent aujourd'hui la thèse telle qu'elle est. De plus, j'ai aimé pouvoir me baser sur ton expertise sur le code Neptune_CFD, et surtout sur la thermohydraulique diphasique en général.

Bruno, je dois dire que j'ai eu beaucoup de chance de t'avoir en tant qu'encadrant de thèse, tant du côté scientifique qu'humain. Je pense que tu m'as vu sous toutes mes couleurs, passionné parfois, perdu à d'autres moments, et tu as toujours su me montrer le positif dans mon travail et dans la recherche d'un point de vue général. Tu as réussi à canaliser mes idées afin de toujours garder cette cohérence globale dans cette thèse, le fil rouge comme tu dis, et de ne pas m'éparpiller. J'étais très heureux de voir cette complémentarité entre Stéphane M. et toi, cet équilibre trouvé entre les nombreuses idées proposées par Stéphane et ton objectif de ne jamais perdre le fil rouge. Enfin, du côté scientifique, je suis très heureux d'avoir autant appris à tes côtés. Merci !

Ensuite, je remercie tout l'équipe du LATF pour les discussions enrichissantes et les moments de convivialité que nous avons eu au cours de ces trois années. C'était un bel environnement de travail pour réaliser cette thèse. Je remercie particulièrement les chefs du laboratoire Laurent Salmon puis Aurélien Davailles qui m'ont accompagné durant ces années. Je remercie particulièrement Alberto, Benjamin et Antoine pour les différentes discussions techniques autour de ma thèse, Clotaire pour avoir entretenu le code Neptune_CFD sur les différents serveurs de calcul CEA. Enfin, je remercie les courageux qui se sont déplacés à Chatou pour assister à ma soutenance.

Je remercie aussi l'équipe support du code Neptune_CFD chez EDF, et notamment

Chaï Koren et Nicolas Mérigoux pour leur aide précieuse.

Un grand merci aussi à tous les actuels et anciens doctorants du STMF, notamment Corentin, Mathis, Elie, Clément, Andrew, Etienne, Angela, Songzhi et tous les autres pour les bons moments passés ensemble ! Merci particulièrement à Alexis, mon co-bureau, et maintenant c'est à toi de finir cette thèse !

Je remercie aussi les personnes rencontrées en conférences avec qui j'espère continuer à échanger à l'avenir pour les intéressantes discussions que nous avons pu avoir, notamment Luc, Sébastien, Stéphane P. et Edouard.

Un grand merci aux différents professeurs de l'école SeaTech qui m'ont donné goût à la simulation numérique, Frédéric Golay, Cédric Galusinski, Mehmet Ersoy, Gloria Faccanoni.

Je voudrais ensuite remercier mes amis présents à Paris durant cette thèse, je pense à Thomas, Etienne, Paul, Maxence, Hendrix, Nico, et Mélissa et Clémence pendant un temps. Je pense ensuite à mes amis d'école qui ont été présents durant ces années, Hugo B., Hugo M., Julien, Anaïs, Pierre, Alexis et les autres.

Et enfin, évidemment, j'aimerais remercier ma famille pour tout. Je vous remercie de toujours m'avoir laissé choisir ma voie en me soutenant au maximum, peu importe mes choix. Je me dois de vous remercier pour beaucoup de choses. D'abord pour l'éducation que vous m'avez donnée et que j'essaie de conserver depuis. Ensuite pour tous les bons moments que nous avons passés ensemble, que ce soit pendant les jeux de cartes, les journées plages ou camping, et bien d'autres. Et aussi pour toutes les fois où vous avez dû m'écouter vous expliquer ma thèse de façon absolument pas claire, jusqu'à la veille de la soutenance. Toutes ces tentatives d'explications m'ont aussi permis de m'améliorer pour la soutenance finale. Je ne serais pas là où j'en suis sans vous, et je me rends compte de la chance de vous avoir comme famille. Merci Maman, merci Papa, merci Lisa. Je souhaite aussi remercier le reste de ma famille, mamie et grand-mère, tontons, tatas, et cousins dont certains ont réussi à suivre ma soutenance à distance.

Enfin, merci Céline pour tout ce que tu m'as apporté ces cinq dernières années, et en particulier durant cette thèse. Je t'en suis tellement reconnaissant, et ces quelques mots ne suffiront évidemment pas à tout résumer. Merci de m'avoir écouté te parler de cette thèse pendant 3 ans, de mes problèmes, mes doutes, tu as toujours su trouver les bons mots. Je te remercie pour tes nombreux efforts qui m'ont permis de trouver un environnement sain pour m'épanouir et me concentrer pleinement sur cette thèse. Merci aussi pour ton aide sur les posters, schémas, et relectures. Merci ! J'ai hâte que l'on vive nos prochaines aventures ensemble.

"La vérité recule, mais le savant avance."
Henri Poincaré

Abstract

The safety of Pressurized Water Reactors (PWR) is ensured by both experimental and numerical studies in nominal and accidental conditions. The numerical studies are achieved using macroscopic codes, such as CATHARE, which predict the fluid mean behavior in a reactor. However, due to the extreme conditions encountered in PWR, the experimental measurements are limited. Consequently, it is challenging to develop models for macroscopic codes based on these limited data. Nevertheless, local numerical tools are able to simulate the phenomena happening in a PWR at a local scale, but only on reduced-scale geometries due to the high computational cost of these simulations. Therefore, once validated based on experiments, these numerical tools provide complementary information on the fluid behavior.

The thesis aims at developing an up-scaling method to identify and model the main physical phenomenon at the macroscopic scale, based on local simulations. The particularity of this study comes from the fact to consider two-phase flows that can be encountered in accidental conditions in PWR, especially sub-cooled boiling flows at high pressure, temperature, and flow rate.

The first step of this method is to develop a macroscopic formulation based on the application of a spatial average operator on the local Neptune_CFD equations. Next, this formulation is compared to the existing macroscopic code equations. Based on this comparison, it is then possible to estimate a priori the terms of the macroscopic codes based on a spatial average of the local variables simulated. This is why a local database of 86 sub-cooled boiling test cases conducted in industrial conditions is built on KIT and PSBT experiments, and validated on the mean void fraction. All the terms of the macroscopic formulation are calculated from an average of the simulated variables. Two principal pieces of information emerge from this evaluation: first, the turbulence and dispersion subgrid terms are not negligible compared to the convection, and second, the boiling and condensation terms are predominant.

However, the local simulations are validated only on the mean void fraction, which is insufficient for this database to be taken as the basis for the macroscopic model development. To this aim, separate effect tests are used where only the predominant phenomenon plays a key role. The TOPFLOW experiment consists of steam bubble condensation in sub-cooled water, with radial profile measurements of void fraction, gas velocity, bubble diameter, and liquid temperature.

Afterward, a new local modeling is developed based on the standard method of moments using a bubble size polydispersion assumption. Indeed, a quadratic bubble size distribution function is used, with the Chen-Mayinger correlation to predict the Nusselt number, and a model for the bubble collapse due to condensation. This modeling provides better results than using the monodisperse assumption and similar predictions to those obtained using a multiple-size group approach, which involves a higher computation cost. Therefore, a validated database is developed in this thesis on the TOPFLOW experiment using this new modeling.

Finally, using this database, the existing macroscopic models are evaluated, and some new models are proposed. The existing models considered in this thesis underestimate the condensation by approximately a factor of two, while a new model developed using a statistical approach has reduced the error to 5.5%. Nevertheless, in order to confirm its benefits for macroscopic codes, this new model needs to be evaluated by an a priori method on new condensation test cases and, next, by an a posteriori method.

Keywords: two-phase flows, CFD modeling, condensation, up-scaling method, macroscopic model

Résumé

La sûreté des Réacteurs à Eau Pressurisé (REP) est assurée par des études conjointes expérimentales et numériques dans des conditions industrielles nominales et accidentelles. Les études numériques sont réalisées l'aide de codes dits macroscopiques tels que CATHARE, qui prédisent le comportement moyen du fluide dans le réacteur. Cependant, dû aux conditions extrêmes rencontrées dans un REP, les mesures expérimentales sont limitées, ce qui complexifie le développement de modèles pour ces codes basés sur ces expériences. Toutefois, des codes dits locaux permettent de simuler de façon locale les phénomènes se produisant dans les REP, mais sur des géométries à taille réduites dû au coût de calcul plus important de ces simulations. Ainsi, après avoir été validés sur certaines expériences, ces codes permettent d'obtenir des informations complémentaires sur le comportement du fluide.

Cette thèse vise à développer une méthode de remontée d'échelle afin d'identifier et de modéliser le phénomène prépondérant à l'échelle macroscopique, en se basant sur des simulations locales. La particularité de cette étude vient du fait de considérer des écoulements diphasiques qui peuvent être rencontrés en situation accidentelles dans le cœur d'un REP, notamment d'ébullition sous-saturée à haute pression.

Pour cela, une formulation macroscopique est développée grâce à une moyenne spatiale des équations locales du code Neptune_CFD. Par comparaison avec les formulations des codes macroscopiques existants, il devient possible d'estimer de façon a priori les termes de ces codes par une moyenne spatiale des variables locales simulées. C'est pourquoi une base de données locale de 86 cas tests d'ébullition sous-saturée en conditions industrielles a été construite sur les expériences KIT et PSBT, validée sur la fraction volumique de vapeur moyenne. Tous les termes de la formulation macroscopique sont calculés par une moyenne des variables simulées. Deux informations principales ressortent de cette évaluation, premièrement, les termes de sous-mailles de turbulence et dispersion ne sont pas négligeables par rapport à la convection, et deuxièmement, les termes d'ébullitions et de condensations sont prédominants.

Toutefois, les calculs fins ne sont validés que sur une variables moyenne, ce qui est insuffisant pour servir de base au développement d'un modèle macroscopique. Pour cela, une expérience à effet séparée est utilisée sur un des phénomènes prédominants. L'expérience TOPFLOW met en jeu la condensation de bulles de vapeur dans de l'eau sous-saturée, avec des mesures de profils radiaux de fraction volumique et de vitesse vapeur, de diamètre de bulles, et de température liquide.

Ensuite, une nouvelle modélisation locale est développée basée sur la méthode des moments avec une hypothèse de polydispersion en taille de bulles. En effet, une distribution en taille de bulles quadratique est utilisée, avec la corrélation de Chen-Mayinger pour la prédiction du nombre de Nusselt, et avec l'introduction d'un modèle de collapse de bulle dû à la condensation. Cette modélisation donne de meilleures prédictions des variables mesurées qu'avec l'hypothèse de monodispersion en taille de bulles, et des prédictions équivalentes à celles obtenues avec la méthode de population de taille de bulles qui implique un temps de calculs plus important. Ainsi, une base de données validée est développée sur les essais TOPFLOW en utilisant cette nouvelle modélisation.

Enfin, en se basant sur cette base de données, les modèles macroscopiques existants de condensation sont évalués et de nouveaux modèles sont proposés. Alors que les modèles existants sous-estiment la condensation d'un facteur deux environ, un modèle développé par une approche statistique a permis de réduire l'erreur à 5.5%. Toutefois, ce nouveau modèle devra être évalué de façon a priori sur de nouvelles expériences en condensation, puis de façon a posteriori, afin de valider son intérêt pour les codes macroscopiques.

Mots-clés: écoulement diphasique, modélisation CFD, condensation, méthode de remontée d'échelle, modèle macroscopique

Contents

List of Figures

List of Tables

Nomenclature

Acronyms

Symbol	Description
ATHLET	Analysis of Thermal Hydraulics of LEaks and Transients
BETHSY	Boucle d'Etude ThermoHydraulique SYstème
BWR	Boiling Water Reactor
CATHARE	Code Avancé de ThermoHydraulique pour les Accidents de Réacteurs à Eau
CEA	Commissariat à l'Énergie Atomique et aux Énergies Alternatives
CFD	Computational Fluid Dynamics
CPU	Central Processing Unit
DNB	Departure from Nucleate Boiling
DNS	Direct Numerical Simulation
EDF	Électricité De France
GTD	Generalized Turbulent Dispersion
IATE	Interfacial Area Transport Equation
IJC	Interfacial Jump Conditions
iMUSIG	inhomogeneous MUlti-SIze Group
IRSN	Institut de Radioprotection et de Sûreté Nucléaire
LES	Large Eddy Simulation
LOCA	Loss of Coolant Accident
MARS-KS	Multi-dimensional Analysis of Reactor Safety - Korean institute of nuclear Safety
NEA	Nuclear Energy Agency
ONB	Onset of Nucleate Boiling
OSV	Onset of Significant Void
PDF	Probability Density Function (m^{-1})
PSBT	PWR Sub-channel and Bundle Tests
PWR	Pressurized Water Reactor

RANS	Reynolds Averaged Navier-Stokes
RELAP	Reactor Excursion and Leak Analysis Program
RIA	Reactivity Insertion Accident
SMM	Standard Method of Moments
SPACE	Safety and Performance Analysis CodE
TOPFLOW	Transient TwO Phase FLOW Test Facility
TRACE	**T**RAC/**R**ELAP **A**dvanced **C**omputational **E**ngine

Statistical Operators

Symbol	**Description**
MAE	Mean Absolute Error: $\mathrm{MAE} = \frac{1}{N} \cdot \sum_{I=1}^{N} \left\lvert \xi_{eval}^{I} - \xi_{ref}^{I} \right\rvert$
MAPE	Mean Absolute Percentage Error: $\mathrm{MAPE} = 100 \cdot \frac{1}{N} \cdot \sum_{I=1}^{N} \left(\frac{\left\lvert \xi_{eval}^{I} - \xi_{ref}^{I} \right\rvert}{\left\lvert \xi_{ref}^{I} \right\rvert} \right)$
ME	Mean Error: $\mathrm{ME} = \frac{1}{N} \cdot \sum_{I=1}^{N} \left(\xi_{eval}^{I} - \xi_{ref}^{I} \right)$
RPSB	Relative Percentage Statistical Bias: $\mathrm{RPSB} = 100 \cdot \frac{1}{N} \cdot \sum_{I=1}^{N} \left(\frac{\xi_{eval}^{I} - \xi_{ref}^{I}}{\xi_{ref}^{I}} \right)$
RPSD	Relative Percentage Standard Deviations: $\mathrm{RPSD} = 100 \cdot \sqrt{\frac{1}{N} \sum_{I=1}^{N} \left(\frac{\xi_{eval}^{I} - \xi_{ref}^{I}}{\xi_{ref}^{I}} - \mathrm{RSB} \right)^{2}}$
RSB	Relative Statistical Bias: $\mathrm{RSB} = \frac{1}{N} \cdot \sum_{I=1}^{N} \left(\frac{\xi_{eval}^{I} - \xi_{ref}^{I}}{\xi_{ref}^{I}} \right)$

Dimensionless Numbers

Symbol	**Description**
$\mathrm{Eo} = \frac{(\rho_l - \rho_g) g d^2}{\sigma}$	Eötvös number (-)
$\mathrm{Nu}_b = \frac{h_l d_b}{\lambda_l}$	Bubble Nusselt number (-)
$\mathrm{Pr} = \frac{\mu_l C_{p_l}}{\lambda_l}$	Prandtl number (-)
$\mathrm{Re}_b = \frac{\rho_l \lvert\lvert v_r \rvert\rvert d_b}{\mu_l}$	Bubble Reynolds number (-)
$\mathrm{Re}_l = \frac{\alpha_l \rho_l \lvert\lvert v_l \rvert\rvert D_h}{\mu_l}$	Liquid bulk Reynolds number (-)
$\mathrm{y+} = \frac{y U_\tau}{\nu_l}$	Non-dimensional wall distance (-)

Greek letters

Symbol	Description
α_k	Volumetric fraction (or void fraction for vapor) (-)
β	Non-dimensional bubble diameter (-)
β_b	Non-dimensional bubble diameter which characterizes the boundary between the heat transfer-controlled and the inertia-controlled regions (-)
χ	Indicator function (-)
χ_c	Heating perimeter (m)
$\Delta\xi$	Experimental uncertianty of a variable ξ (-)
$\Delta T = \|T_{sat} - T_l\|$	Temperature difference to saturation (super-heat or sub-cooling) (K)
Δt	Residence time (s)
δ	Dirac function (-)
ϵ	Turbulent dissipation $(m^2.s^{-3})$
Γ	Interfacial mass transfer rate $(kg.m^{-3}.s^{-1})$
γ	Order of the statistical moment μ (-)
Γ^c	Part of Γ induced by bulk transfer $(kg.m^{-3}.s^{-1})$
Γ^{nuc}	Part of Γ induced by nucleate boiling $(kg.m^{-3}.s^{-1})$
λ	Thermal conductivity $(W.m^{-1}.K^{-1})$
$\lambda_c = \sqrt{\frac{\tilde{\sigma}}{g(\tilde{\rho}_l - \tilde{\rho}_g)}}$	Capillary length (m)
μ	Statistical moment (-)
μ_k	Dynamic viscosity of phase k $(Pa.s)$
$\nu = \frac{\mu}{\rho}$	Kinematic viscosity $(m^2.s^{-1})$
ω	Interfacial velocity $(m.s^{-1})$
Φ	Porosity (-)
ϕ	Source term of the IATE $(m^{-1}.s^{-1})$, or parameter of the heat flux partitioning model $(W.m^{-3})$
Φ_w	Wall heat input (W)
Π'	Part of Π independant of the mass transfer $(W.m^{-3})$
Π	Bulk interfacial heat transfer rate $(W.m^{-3})$
ψ	Factor depending on the shape of the bubbles (-)
ρ	Density $(kg.m^{-3})$
σ	Surface tension $(N.m^{-1})$
τ	Stress tensor $(kg.m^{-1}.s^{-2})$

τ^*	Normalized mean of subgrid terms (-)
τ_i	Interfacial friction (CATHARE closure term) ($N.m^{-3}$)
ξ	Generic variable (-)
$\zeta = \alpha_l \rho_l C_{p_l} T_l$	$\Delta\zeta$ is a variable related to the change of enthalpy per cubic meter due to a temperature or volume fraction difference ($J.m^{-3}$)

Latin letters

Symbol	**Description**
$\mathbb{I}$	Unit tensor (-)
$\mathbb{P}$	Probability density function (m^{-1})
A	Area, cross-section (m^2)
a_i	Interfacial area concentration (m^{-1})
C_0, C_1, C_2, C_3	Coefficients of the bubble Nusselt number (-)
C_0	Volumetric flux distribution parameter of the drift flux model (-)
C_D, C_L	Drag and lift interfacial force coefficients (Neptune_CFD closure term) (-)
C_k	Friction coefficient of phase k (CATHARE closure term) (-)
C_v	Distribution parameter (-)
C_p	Specific heat ($J.kg^{-1}.K^{-1}$)
C_{slip}	Macroscopic relative velocity coefficient (CATHARE closure term) (-)
d	Bubble diameter (m)
D_h	Hydraulic diameter (m)
d_{10}	Arithmetic mean diameter (m)
d_{32}	Sauter mean diameter (m)
D_{ph}	Critical bubble diameter (m)
E	Energy (J)
e	Apparent internal energy ($J.kg^{-1}$)
F	Force (N)
f	Bubble size distribution function (m^{-4}), or volumetric force in TRACE formulation ($N.m^{-3}$)
G	Mass flow rate ($kg.m^{-2}.s^{-1}$)
g	Gravitational acceleration ($m.s^{-2}$)
H	Total enthalpy per unit of mass ($J.kg^{-1}$)
h	Interfacial heat transfer coefficient ($W.m^{-2}.K^{-1}$)
H_{lg}	Latent heat of vaporization ($J.kg^{-1}$)

I	Interfacial momentum transfer rate ($kg.m^{-2}.s^{-2}$)
j	Mixture volumetric flux ($m.s^{-1}$)
K	Singular friction coefficient (-)
L	Length (m)
L_ξ	Length scale of the macroscopic quantities variations (m)
l_ξ	Length scale of the local quantities variations (m)
M	Interfacial momentum transfer rate, without mass transfer contribution ($kg.m^{-2}.s^{-2}$)
n	Bubble number density (m^{-3})
N_D, N_L	Coefficients from the drag and lift forces (-)
P	Pressure (Pa)
$q''_{k,i}$	Interfacial heat flux density ($W.m^{-2}$)
q	Volumetric heat source ($W.m^{-3}$)
R	Pipe radius (m)
r_0	Length scale of the averaging volume (m)
R_i	Wall friction (One-phase formulation) ($m.s^{-2}$)
R_j	Changing rate of a_i due to bubble break-up or coalescence ($m^{-3}.s^{-1}$)
R_{ij}	Reynolds stress tensor components ($m^2.s^{-2}$)
R_{ph}	Changing rate of a_i due to a phase change ($m^{-3}.s^{-1}$)
S	Source term in the standard method of moments ($m^{-4}.s^{-1}$), or surface area (m^2)
T	Macroscopic subgrid term tensor in momentum ($N.m^{-2}$) and energy ($W.m^{-2}$) equations
T	Temperature (K)
t_c	Characteristic time (s)
U_τ	Wall friction velocity ($m.s^{-1}$)
V	Averaging volume (m^3)
v	Velocity ($m.s^{-1}$)
v_r	Relative velocity ($m.s^{-1}$)
X	Mass fraction (-)
x_{eq}	Thermodynamic quality (-)
$y+$	Non-dimensional wall distance (-)
Z	Altitude (m)
$\underline{n}$	Normal vector (-)

Mathematical Conventions

Symbol	**Description**
$\tilde{\xi}$	Indicate that ξ is a macroscopic variable, i.e., is statistically and spatiallly averaged
$\underline{\underline{\xi}}$	Indicate that ξ is a tensor
$\underline{\xi}$	Indicate that ξ is a vector
$\delta_i\xi$	Spatial devation of ξ with respect to the intrinsic average
$\delta_k\xi$	Spatial devation of ξ with respect to the phasic average
$\delta_{k\rho}\xi = \delta\xi$	Spatial devation of ξ with respect to the phasic mass-weighted average
$\frac{D\xi}{Dt}$	Lagrangian derivative of ξ
${<}\!\!\!\!\mid\xi\mid\!\!\!\!{>}$	Superficial average
$\langle\xi\rangle$	Intrinsic average of ξ
$\langle\xi\rangle_k$	Phasic spatial average of ξ
$\langle\xi\rangle_\Psi$	Average of ξ weighted by Ψ
$\langle\xi\rangle_{k\rho}$	Phasic mass-weighted average of ξ
$\overline{\overline{\xi}}$	Mass-weighted phasic average operator of ξ
$\overline{\xi}$	Statistical average operator of ξ
$\overline{\xi}^{I}$	Statistical average of ξ at interface
$\overline{\xi}^{k}$	Reynolds phasic average of ξ
$\overline{\xi}^{Ie}$	Statistical average of ξ at interface, suited for the enthalpy
$\overline{\xi}^{Im}$	Statistical average of ξ at interface weighted by the mass transfer rate
$\overline{\xi}^{k\rho}$	Mass-weighted phasic average of ξ
ξ''	Fluctuation of ξ with respect to Mass-weighted phasic average
ξ'	Fluctuation of ξ with respect to statistical average

Superscripts

Symbol	**Description**
AM	Added-Mass
D	Drag
I	Value of a variable at the center of the cell I
L	Lift
T	Turbulent dispersion

Subscripts

Symbol	Description
b	Bubble
BB, bk	Bubble break-up
$BC, coal$	Bubble coalescence
CFD	Calculated from an average of the CFD database. An average of a product of local variables can be used.
$CO, coll$	Bubble collapse by condensation
cor	Calculated from a macroscopic correlation. Only averaged variables are used, but these variables can be calculated from the CFD database.
DB	Dispersed bubble
exp	Experimental
f	Fluid phase
g	Gas phase
h	Hydraulic
i	Interfacial
in	Inlet
k	k phase
l	Liquid phase
m	Molecular
nuc	Nucleation
PC	Phase change
PV	Pressure change
r	Radial direction
sat	Saturation
T	Turbulent
$term$	Terminal
w	Wall
z	Axial direction

Publications

Journals

1. **Herry, T.**; Raverdy, B.; Mimouni, S.; Vincent, S. “Volume Average of Two-Fluid RANS Equations and a Priori Estimation of Subgrid Terms on Subcooled Boiling Experiments”. International Journal of Heat and Mass Transfer, 2024, 223, 125232. https://doi.org/10.1016/j.ijheatmasstransfer.2024.125232.

2. **Herry, T.**; Raverdy, B.; Mimouni, S.; Vincent, S. ”Modeling and Simulation of Bubble Condensation Using Polydisperse Approach with Bubble Collapse Model”. International Journal of Multiphase Flow 2024, 104846. https://doi.org/10.1016/j.ijmultiphaseflow.2024.104846.

International Conferences

1. **Herry, T.**; Raverdy, B.; Nguyen, E.; Mimouni, S. ”Two-Phase Flow Upscaling Method in a Macroporous Medium”. In Proceedings of Advances in Thermal Hydraulics (ATH 2022); Anaheim, USA, 2022; pp 575–588. https://doi.org/10.13182/t126-38104.

2. **Herry, T.**; Raverdy, B.; Mimouni, S. ”Evaluation of Condensation Models on TOPFLOW Experiment”. In ICMF 2022-11th International Conference on Multiphase Flow; Kobe, Japan, 2023; p 662.

3. **Herry, T.**; Raverdy, B.; Mimouni, S.; Vincent, S.” Improvement of Interfacial Area Prediction on Condensing Steam-Water Flow Using Bubble Collapse Model”. In Proceedings of the 9th World Congress on Momentum, Heat and Mass Transfer (MHMT 2024); London, UK, 2024. https://doi.org/10.11159/icmfht24.108.

Poster presentation

1. **Herry, T.**; Raverdy, B.; Nguyen, E.; Mimouni, S. ”Two-phase flow upscaling method in a porous medium”. 34th seminar on Computational fluid dynamics at the Institut Henri Poincaré in Paris, 2022.

Introduction

Nuclear energy

The world's electricity generation is currently provided by several different fuels, as shown in Figure 1. Coal remains the dominant fuel used to produce electricity, and electricity production by renewable energies has increased during the last 20 years. However, considering global warming and the several measures to mitigate it, electricity generation by fossil fuels such as coal, oil, and natural gas should decrease in the following decades in order to achieve carbon neutrality in 2050. Nuclear energy currently represents around 10% of the total electricity generation, but it is worth noting that the mix is contrasting between countries. Indeed, as shown in Figure 2, most countries do not have any nuclear power in their energy mix, while few countries concentrate most of the nuclear reactors. It can be seen that the United States, France, China, and Russia are the leading countries producing electricity from nuclear sources, with respectively 92, 56, 54, and 37 nuclear reactors at the end of 2022 (IAEA, 2023).

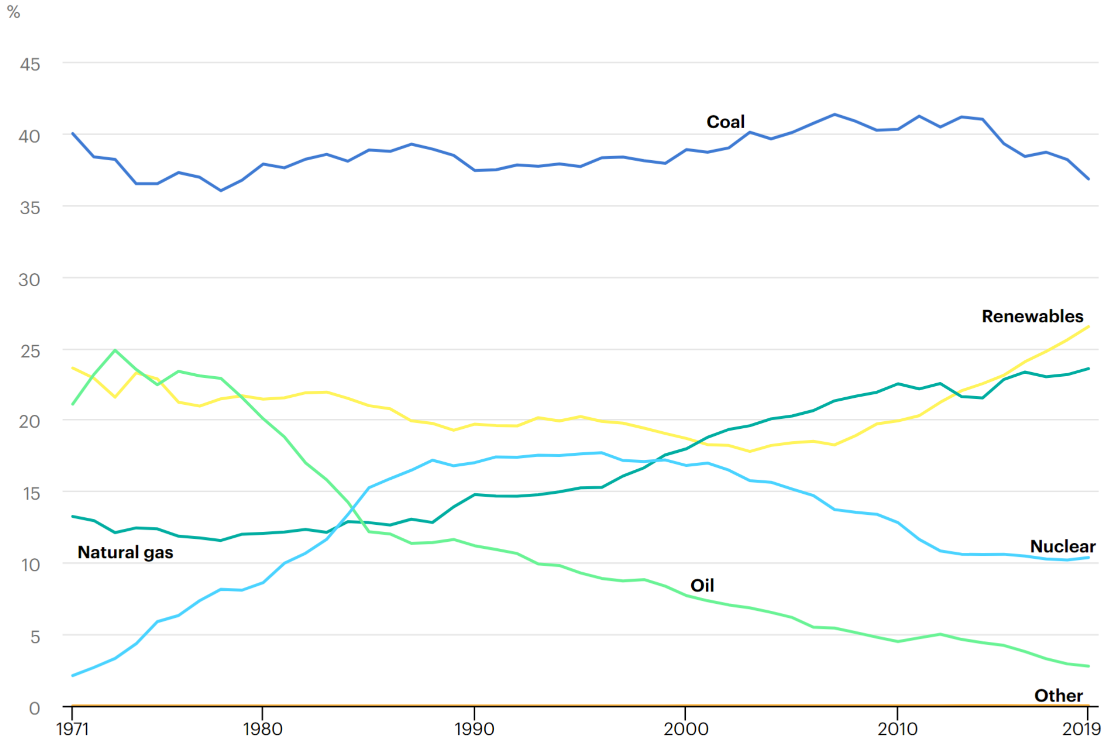

Figure 1: World electricity generation mix by fuel (IEA, 2021).

In 2020, France had a total of 136.2 GW of installed electrical power plants with an annual total production of 500.1 TWh, 67.1% of which came from nuclear reactors. The French government plans to build at least six nuclear reactors before 2050.

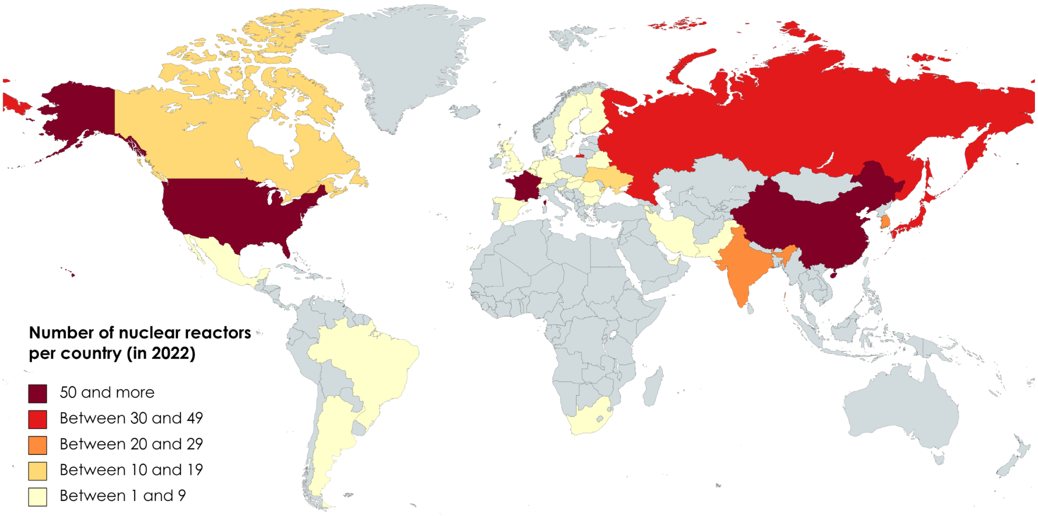

Figure 2: Number of nuclear reactors in operation in the world in 2022 (IAEA, 2023).

Thermal-hydraulic and safety of PWRs

Thermal-hydraulic in PWRs

Pressurized Water Reactors (PWRs) are the world's most widely used type of nuclear reactor. Known for their robust safety features and reliable performance, PWRs are a crucial technology in the global nuclear power industry. This section provides an overview of PWRs, including their design, operational principles, global distribution, and significance in the world and France's energy landscape.

PWRs dominate the nuclear power sector, accounting for approximately 70% of all nuclear reactors worldwide. As of 2023, there are over 300 PWRs in operation across the globe, contributing significantly to the world's electricity supply. They are also the only type of nuclear power plant operated in France for electricity production. A simplified sketch of a PWR is presented in Figure 3.

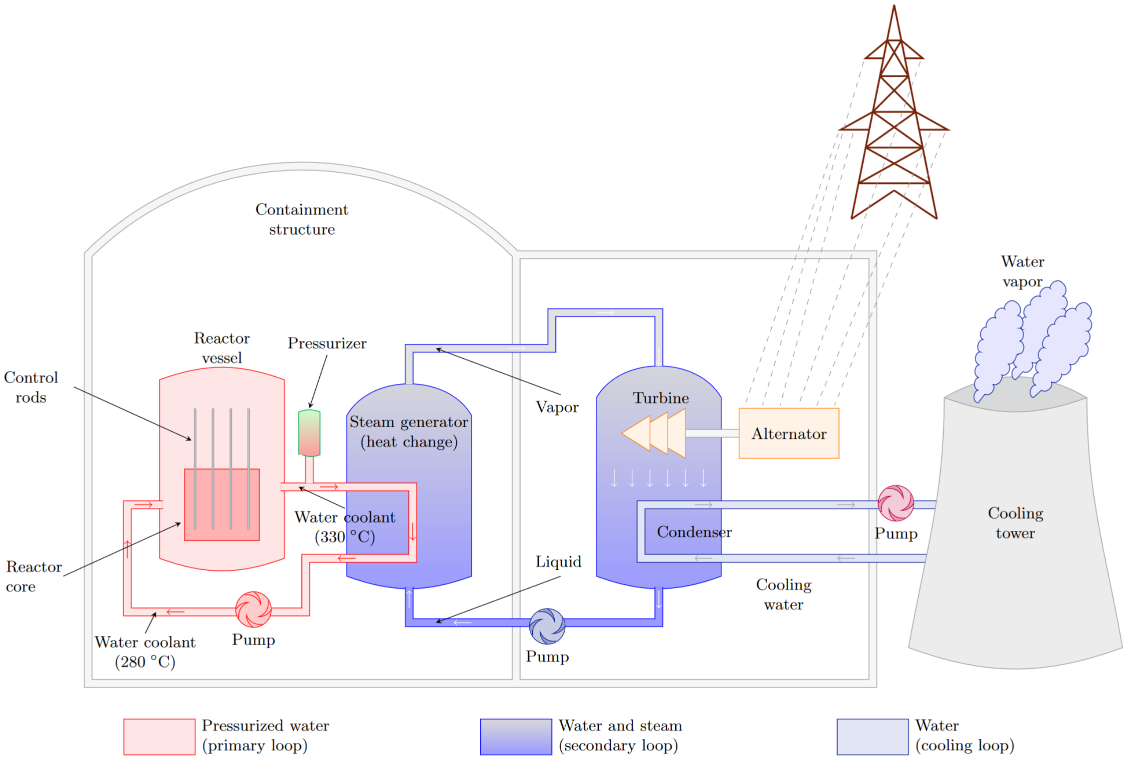

Figure 3: Sketch of a Pressurized Water Reactor (Favre, 2023).

The PWRs can be divided into three loops: the primary, the secondary, and the cooling loops.

The primary loop is designed to collect the thermal energy produced by fission reactions within the nuclear fuel rods. Water circulating through the core absorbs this energy and transfers it to the steam generator while also serving as a moderator to sustain the nuclear chain reaction in the fuel. This loop is completely sealed, operating at a pressure of approximately 155 bar, a temperature of 300°C, and mass flow rates between 3000 and 5000 kg/m^2s (about 20 tons per second) at the core inlet. Several pumps supply water to the reactor vessel, each connected to its own cooling circuit and steam generator. One of these cooling circuits is linked to the pressurizer, which regulates the pressure throughout the primary loop. In France, 900 MW reactors have three primary pumps, while 1300 MW and 1450 MW reactors have four.

The secondary loop intends to absorb thermal energy transferred from the primary loop to vaporize its water. This vapor is utilized to generate electricity by converting its mechanical energy via turbines that are connected to alternators. The vapor expands and condenses upon exiting the turbines before returning to the steam generators. Thus, the secondary loop operates as a closed circuit for water and steam. Typically, the steam generator operates under conditions of 60 bar pressure, heating water from 220°C to 275°C, the temperature at which the water is evaporated.

The purpose of the cooling loop is to reduce the temperature and to condense the steam discharged from the turbines. Depending on the location of the nuclear power plant, the heat sink can either be natural (such as a lake or sea) or manufactured (like a cooling tower). This cooling loop operates as a fully open circuit.

This thesis aims to work on thermal-hydraulic phenomena that happen in the fluid part among the fuel rods inside the core. Then, the structure of a PWR core is expressed in the following.

Reactor Pressure Vessel The reactor core is contained within a stainless steel vessel called the reactor pressure vessel. Along with the primary loop, the reactor pressure vessel forms the second ”containment barrier,” a critical system designed to prevent the release of radioactive materials. As such, the vessel is a crucial safety component of the reactor, for which the mechanical integrity and performance must be guaranteed under all operational conditions.

Fuel assembly and core structure A fuel assembly consists of 17 × 17 rods and guide thimbles, including 264 nuclear fuel rods. Among these, 25 are guide thimbles designed to hold absorbing rods, which are used to stop the chain reaction by neutron absorption during incidental or accidental situations. Moreover, one thimble is dedicated to instrumentation. The assembly’s top nozzle maintains stability with a hold-down spring. The structure is 4 meters high (Figure 4) in French PWRs. The number of fuel assemblies in a reactor core varies based on the reactor’s electrical output: 157 assemblies for 900 MW units, 193 for 1300 MW units, and 205 for 1450 MW units.

Fuel rods and grids Fuel rods are the fundamental components of the reactor’s core, containing nuclear fuel pellets made of enriched uranium. These pellets are encased in a neutron-transparent tubular cladding made of Zircaloy, allowing neutrons to pass through and induce fission reactions in adjacent rods. This cladding acts as the first containment barrier.

The arrangement of the rods in bundles allows water to flow between them, moderating neutrons produced from recent fission events. This configuration also provides a large surface area for heat exchange, improving fuel cooling. Each fuel rod typically measures 4 meters in height, 9.5 mm in diameter, and weighs 2 kg.

Within the fuel assembly, the rods are supported by eight grids spaced evenly at 50 cm, as can be seen in Figure 4. These grids help the structure support the significant hydrodynamic forces exerted by the high flow rate of water. There are two types of grids used in fuel assemblies. First, the spacer grids ensure the mechanical stability of the assembly and prevent rod deformation due

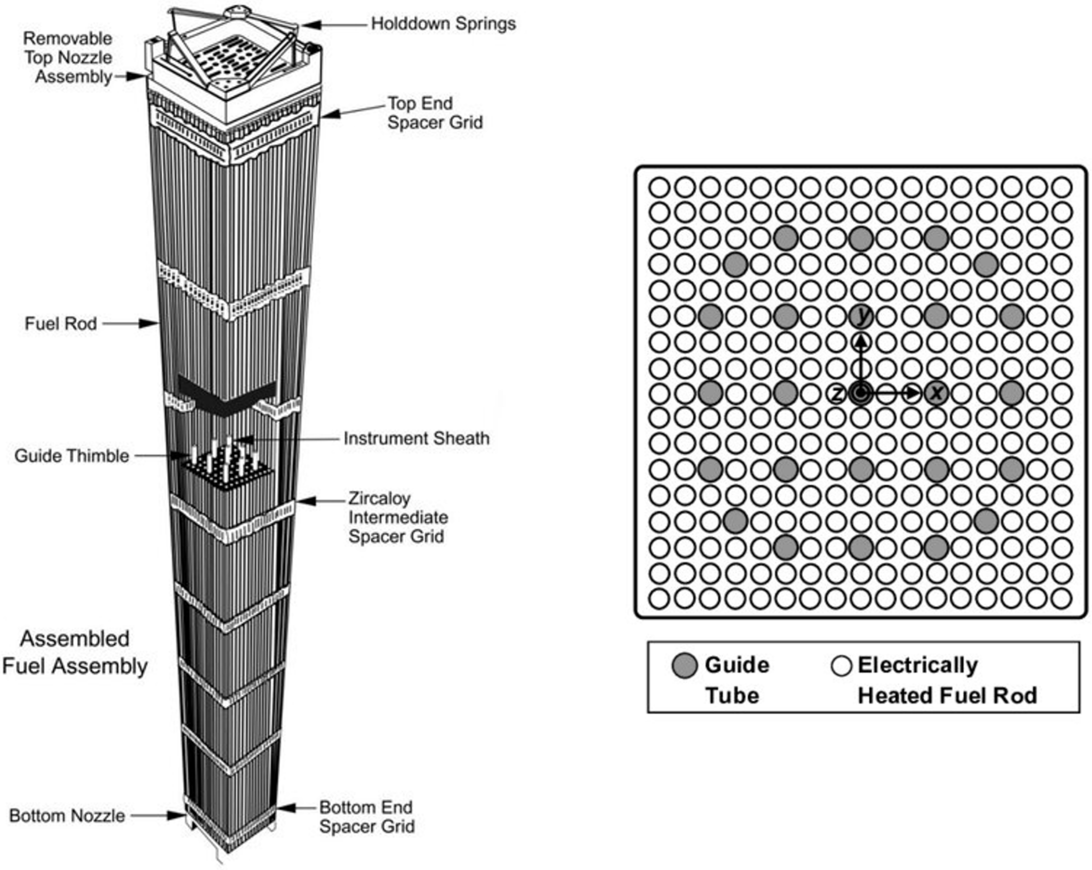

Figure 4: Sketch of a nuclear fuel assembly. Adapted from Kenich (2019).

to heating. Second, the mixing grids have vanes that provide rotational motion to the axially flowing fluid, enhancing turbulence and mixing to homogenize its temperature.

Safety of PWRs

Regarding radioactivity, the safety of PWRs is ensured by three containment barriers:

- The fuel rod cladding
- The Reactor Pressure Vessel and primary loop
- The containment building

The thermal-hydraulic design of a PWR must account for any situation that could potentially threaten these containment barriers. Precisely, the water used as a coolant in the core must effectively remove heat from the fuel rods under nominal, transient, and incidental conditions. The components of the primary loop involved in the cooling process must withstand potential dynamic changes during reactor operation and avoid damaging other parts of the circuit, particularly those related to containment barriers (such as fuel rods and the reactor pressure vessel).

In incidental conditions, the water surrounding the fuel rods may experience a significant increase in thermal power per unit volume, causing it to heat above its saturation temperature and start boiling. This can lead to two-phase boiling flow regimes in the core, potentially resulting in a critical situation known as the boiling crisis that can severely damage the nuclear fuel rod claddings. This is why the study of two-phase flows in PWRs is of significant importance, and these flows are described in detail in the following section.

Two-phase boiling flows encountered in PWRs core

In nuclear reactors, water enters the fuel assemblies from the bottom and flows upward, getting heated as it ascends along the 4-meter height of the fuel rods. Initially, the water is highly sub-cooled, meaning its temperature $T_{l,\text{in}}$ is significantly below the saturation temperature T_{sat} (usually a difference of $\Delta T_l = T_{\text{sat}} - T_{l,\text{in}} \approx 50°\text{C}$, with $T_{\text{sat}} \approx 345°\text{C}$ at 155 bar). When it exits the fuel assembly, this temperature difference reduces to $\Delta T_l = 15°\text{C}$. Therefore, the process involves the physics of vertical sub-cooled boiling flows. In accident conditions, such as the Loss Of Coolant Accident (LOCA) or the Reactivity Insertion Accident (RIA), multiple two-phase boiling flow regimes occur in the core. These regimes are described in Figure 5. It can be noted that the flow regimes encountered in Boiling Water Reactor (BWR) or PWR are different.

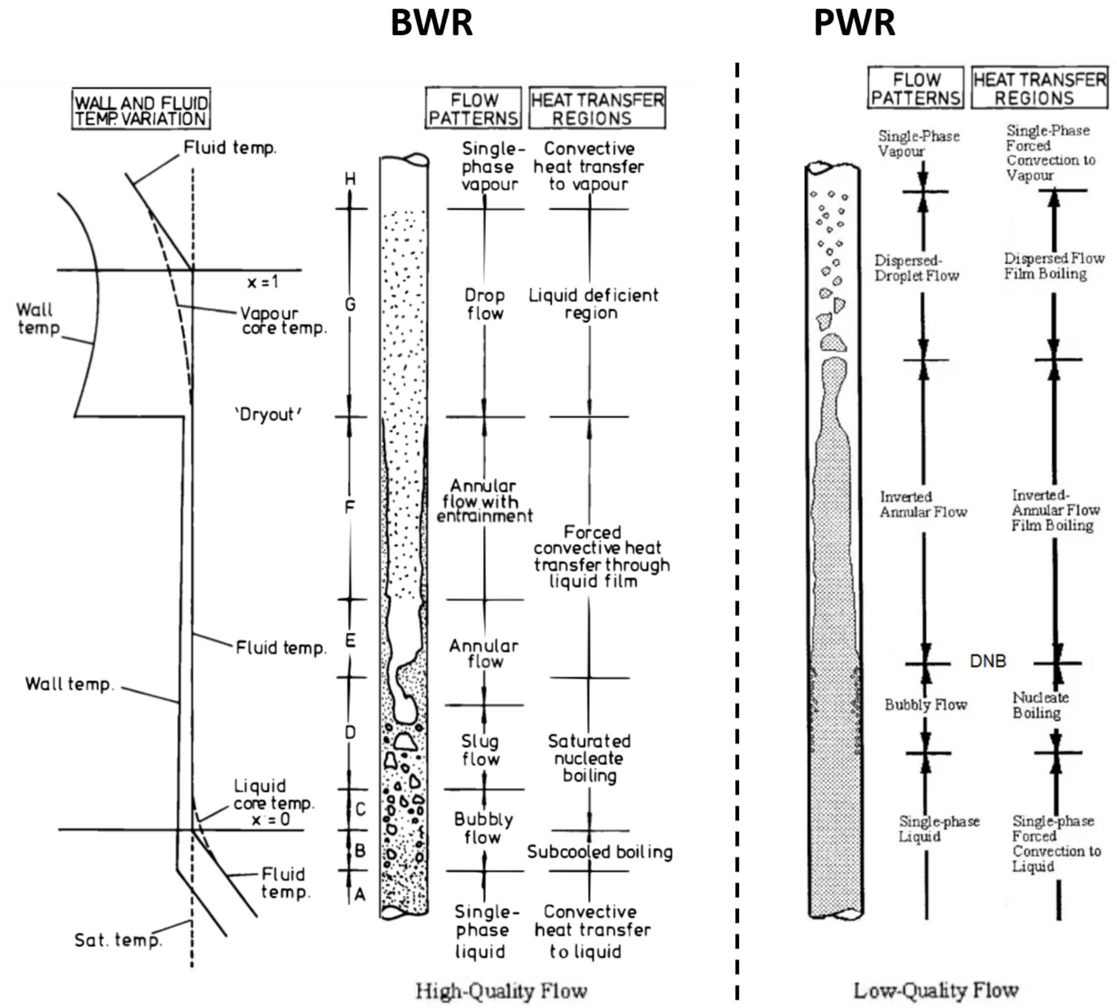

Figure 5: Sketch of the different vertical flow boiling regimes in a vertical tube at high and low heat flux from Delhaye et al. (2008). Here, x denotes the local thermodynamic quality noted x_{eq} in the text.

Different heat exchange regimes can occur alongside various two-phase flow regimes during phase change as the liquid heats up while flowing upwards. These regimes are typically defined by the liquid's thermodynamic quality x_{eq}, which is calculated as:

$$x_{\text{eq}} = \frac{H_m - H_{l,\text{sat}}}{H_{g,\text{sat}} - H_{l,\text{sat}}}, \tag{1}$$

where $x_{\text{eq}} < 0$ indicates sub-cooled flow, and $0 \leq x_{\text{eq}} \leq 1$ indicates that the mixture is at saturation. Moreover, H_m is the mixture enthalpy, $H_{g,\text{sat}}$ and $H_{l,\text{sat}}$ are respectively the gas and liquid enthalpy at saturation. The regimes also depend on the spatial and temporal distribution of the liquid and gas phases. In a simple vertical tube, Figure 5 illustrates the various flow and heat transfer regimes during vertical flow boiling in a tube with a negative inlet liquid quality. Two configurations are possible, namely high- and low-quality flows. Regarding the so-called high-quality flow, at the left in Figure 5, a low but constant heat flux is applied along the tube, sufficient to result in pure vapor flow ($x_{\text{eq}} \geq 1$) by the end. The boiling crisis happens at high-quality flow due to a dry-out phenomenon and is mainly studied in the case of BWR. The second configuration, called low-quality flow, can be seen in the right part of Figure 5 when a high heat flux is applied, and the boiling crisis is obtained at low-quality flow by a Departure from Nucleate Boiling (DNB). The DNB is mainly studied for PWR. The different steps happening in the first configuration, the high-quality flow, are described in the following.

Initially, the liquid enters the tube in a sub-cooled state, i.e., below the saturation temperature, leading to pure liquid convective heat transfer (zone A). This single-phase region is also found for low-quality flow, as shown in the right of Figure 5.

As the wall temperature rises above the saturation point, the Onset of Nucleate Boiling (ONB) occurs, allowing vapor bubbles to form at nucleation sites on the wall. The density of these sites increases with heat flux or wall temperature. This boiling happens first in regions where the average temperature of the fluid is still below saturation, known as sub-cooled boiling (zone B). As the liquid moves upwards, boiling intensifies and bubbles detach from the wall, marking the Onset of Significant Void (OSV). These bubbles migrate into the bulk flow and condense in the sub-cooled liquid. This region corresponds to bubbly flow, where the vapor phase is dispersed in the continuous liquid phase.

> **Note:** The sub-cooled boiling region happens below the boiling crisis for low- and high-quality flows. For this reason, this flow regime will be studied in detail in this thesis.

When the average liquid temperature reaches saturation ($x_{\text{eq}} = 0$), saturated boiling begins. Initially, the vapor phase consists of small dispersed bubbles (zone C). As the liquid remains at saturation temperature, vapor bubbles stop condensing and more coalescence happens, forming larger inclusions that lead to slug flow (zone D).

Further along, the vapor volume at a given height exceeds the liquid volume, resulting in high local void fractions (the ratio of vapor volume to total volume). Then, the flow regime shifts to annular flow, where vapor occupies the core flow and liquid is pushed to the wall, creating a liquid film that enhances effective thermal conductivity and limits wall nucleation (zones E & F).

Finally, when the liquid film completely evaporates, the wall comes into direct contact with the vapor phase (zones G & H). This condition, known as dry-out, causes a sharp increase in wall temperature due to the reduced heat transfer coefficient associated with the low thermal conductivity of vapor.

Therefore, multiple flow regimes can be encountered in a reactor core in accident conditions. Experiments can be carried out to ensure reactor safety, but the complexity of the implementation, the cost, the time required, and the limited number of tests and measurements make them difficult to use. Numerical simulation can be used as a complement in order to achieve more operating conditions and to have access to variables that are inaccessible experimentally. The numerical tools used to ensure reactor safety are introduced in the next section.

Numerical simulations to ensure reactor safety

As mentioned above, complex two-phase flows can be encountered in nuclear reactor cores, with physical phenomena at different spatial scales ranging from the meter, such as asymmetric flow between fuel assemblies, to the micrometer, such as turbulence generation or bubble interactions. As part of the safety analysis, it is necessary to demonstrate that all elements are well-designed for both operational and accident situations. Indeed, for a wide range of thermal-hydraulic conditions, the occurrence of two-phase flows can lead to the destruction of one or more systems. Complementary numerical and experimental works are being carried out to qualify systems and assess the thermal-hydraulic effects of two-phase flows.

Regarding the numerical work, different strategies are employed to simulate some of these phenomena at different scales. At the finest scale, Direct Numerical Simulations (DNS) are used to study very local effects such as bubble generation, or to solve all scales of turbulence. At an intermediate scale, Reynolds-Averaged Navier-Stokes (RANS) equations can be used. Solving these RANS equations, combined with turbulence models, provides a detailed prediction of the flow field in the fuel assembly but remains too computationally intensive to simulate the entire core of a nuclear reactor, i.e., over a hundred fuel assemblies. Finally, macroscopic modeling can be used to simulate average flow quantities on a large scale. Flow through the core is then considered as flow through a porous medium, which reduces the computational cost and makes it possible to simulate the entire nuclear reactor core. These three different scales are presented in the Figure 6. The system and component scales are gathered in the category of macroscopic scale in this work. These various scales are described in the following, starting with the finest scale.

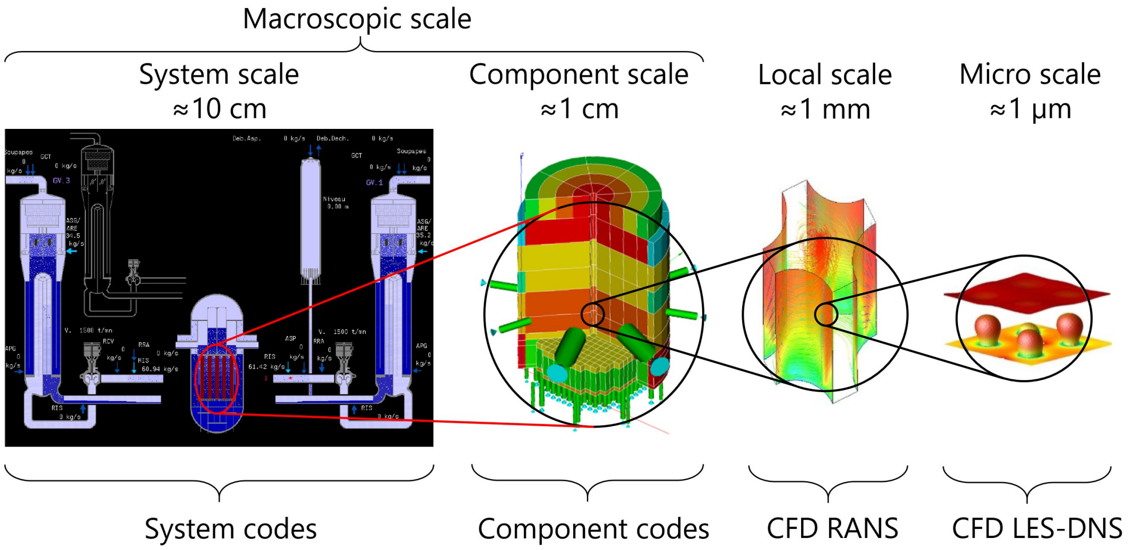

Figure 6: Code scales categories in nuclear thermal-hydraulic (Ciechocki, 2023).

Micro scale (DNS)

At the finest scale, DNS solves local instantaneous conservation equations on the entire length scale range of the turbulence eddies and the smallest bubbles. Indeed, this scale aims to simulate all flow phenomena, such as the smallest drops and bubbles, and also the smallest turbulence eddies. Despite the high accuracy of the results that can be obtained at this scale, current computing resources make it impossible to use this method to simulate a complete fuel assembly with all its complex structures. There are many DNS numerical tools available, and for example, TrioCFD and TrioIJK are used at CEA in France.

Moreover, the Large Eddy Simulation (LES) approach, such as Mimouni et al. (2017a), can also be categorized at the micro scale. This approach applies space filtering on the local instantaneous equations in order to resolve the largest turbulent eddies and to model the effects of the smallest. The computation cost of this approach depends on the size of the space filter but lies between the cost of the DNS approach, where all turbulent eddies are solved, and the cost of the RANS approach, where the effects of all the eddies are modeled.

Local scale - Statistically averaged scale (RANS)

In contrast to DNS, simulations at a local scale using RANS equations offer significant computational efficiency and cost-effectiveness, making them feasible for practical engineering problems in the nuclear industry. However, RANS simulations are less accurate in predicting detailed turbulent structures and are heavily dependent on the chosen turbulence model, which can introduce variability in results. By averaging out turbulent fluctuations, RANS provides steady-state solutions that are sufficient for many applications, reducing the need for detailed transient analysis. This broad applicability is particularly advantageous for the study of various components, such as the flow between fuel rods and in heat exchangers such as steam generators. For example, it is possible to predict the radial movement of bubbles within a subchannel. The numerical tools Star-CCM+ (Siemens, 2017) and Neptune_CFD (Guelfi et al., 2007) solve RANS equations for two-phase flows.

However, the simulations done at this scale remain too computationally intensive to simulate the entire core of a nuclear reactor, i.e., over a hundred fuel assemblies. An entire core can only be simulated at a macroscopic scale, which is described in the next section.

Macroscopic scale - Statistical-volume averaged scale (Component and system scales)

As shown in Figure 6, the macroscopic scale can be divided into two categories, component scale and system scale.

Regarding the component scale, the solid structures are included in the discretization cells using the porosity principle. The global influence of solid structures is taken into account in different models. Flow through the core is then considered as flow through a porous medium, which reduces the computational cost. The minimum spatial resolution corresponds to the size of the sub-channels, which is of the order of centimeters. This scale is known as the sub-channel scale, and is able to model an entire core. The codes at this scale are intended for the study of multiple applications, for example, the main steam line break transient, rod ejection reactivity transient, or even the core re-flooding processes. The numerical tools THYC (Sylvie Aubry and Rascle, 1995) and FLICA (Toumi et al., 2000) are component codes.

The system scale is dedicated to the study and description of reactor circuits as a whole. Due to the size of a reactor and the large number of components and phenomena that occur within it, the studies of design basis accidents are typically achieved using system codes. The primary and secondary systems of a reactor are modeled by coupling several dozen 0-D, 1-D, and 3-D modules and sub-modules to represent the different components. The scale studied in 3-D modules of system codes corresponds to the component scale. The finest cell size in component code is equivalent to the sub-channel scale. The macroscopic scale considered in this thesis corresponds to this scale, i.e., the component scale or the scale studied in the 3-D modules of system codes.

System codes are expected to be highly robust and to use strictly measured uncertainties. The code must be validated and verified, and its scalability must be demonstrated. System codes are divided into two categories: the conservative and the best-estimate codes. The conservative codes aim to predict the lower and upper limits of a process. In comparison, the best-estimate codes aim to predict the process with the best accuracy throughout the transient (D'Auria, 2017). The first best-estimate codes developed in the late 1970s and 1980s are TRACE (USNRC, United States), RELAP5 (INL, United States), and CATHARE (CEA - EDF - Framatome - IRSN, France). The module 3-D of CATHARE is equivalent to component scale codes.

Towards an up-scaling method to improve system code predictions

The study of two-phase flows in nuclear reactor core conditions requires the prediction by a macroscopic code of the overall fluid behavior across the entire industrial system, such as the mean velocity, void fraction, temperature, and pressure. However, until now, most of the models used for mean variables are developed on the basis of limited local variables, which are potentially far from the industrial conditions. Therefore, some models may not be representative of industrial conditions, or worse, the lack of experimental data on some variables may make it impossible to model or even evaluate some terms in industrial conditions. Indeed, for example, the bubble condensation models in macroscopic scale codes are either modeled from a purely empirical model or by a more generic model but which is developed at the local scale and used as such at the macroscopic scale.

In order to develop generic models adapted to macroscopic scale based on local variables, Nakayama and Kuwahara (1999) and later Pedras and De Lemos (2001) have proposed a new strategy that we call 'up-scaling method' in this thesis. It consists of using a validated local database based on CFD calculations to develop a model at the macroscopic scale. This method can be divided in four main steps: first to average local equations as well as local closure laws to obtain the macroscopic ones, thus some new unknown terms appear, then to perform local simulations with an experimental validation on some variables to obtain a validated local database. The next step is to propose a model for an unknown term using macroscopic variables and optimization constants, and finally, to calibrate these constants using a local database and to assess the macroscopic model. They have applied this method to model the turbulence diffusion term. This has allowed the development of models at the macroscopic scale using data from CFD calculation, which are not available experimentally. However, this work has been done only in one-phase liquid flow on academic cases. Then, Pinson (2006) and later Drouin et al. (2013) have applied this methodology to model together the subgrid terms of the turbulence diffusion and the dispersion linked to spatial fluctuations. This has made it possible to model these terms despite the limited experimental data, and these models have been developed on the basis of averaged data. This work has been done on academic cases of one-phase flows. Bois (2021) has extended this methodology to a macroscopic mixture model for two-phase turbulent flows. This opens up opportunities to model the subgrid void distribution or relative velocity at the macroscopic scale from CFD simulations. Nevertheless, this method has not yet been applied and is adapted to a mixture model and not to two-fluid models.

To summarize, these studies have established macroscopic equations for one and two-phase flows from local equations. Some authors have modeled the subgrid terms of turbulence and dispersion by an up-scaling method. However, there are no models, or even evaluations, of these terms in representative conditions of a nuclear reactor core in accidental situations, i.e., for two-phase flows at high pressure, temperature, and flow rate. Moreover, to the best of our knowledge, there are no condensation models at the macroscopic scale developed by an up-scaling method similar to those developed for the turbulence and dispersion subgrid terms.

These reasons justify this thesis, which consists of developing an up-scaling method to identify and model the main physical phenomenon at the macroscopic scale, based on local simulations.

The particularity of this study comes from the fact to consider two-phase flows that can be encountered in accidental conditions in nuclear reactor cores, especially sub-cooled boiling flows at high pressure, temperature, and flow rate.

Content of this thesis

For this purpose, this thesis is divided into five chapters as follows:

- Chapter 1 is intended to develop the up-scaling strategy for industrial two-phase flows that will be used in this thesis. This strategy is based on a literature review. Moreover, the local and macroscopic codes that are used in this thesis are described in this chapter.
- Chapter 2 presents the establishment of a macroscopic two-fluid formulation based on Neptune_CFD local equations. This allows us to compare the terms from the local database that are averaged to the terms from macroscopic equations. For that, we apply average operators suitable for two-phase flows on Neptune_CFD local equations. Then, we are able to highlight some hypotheses done in existing macroscopic codes by comparing their equations to the new formulation.
- Chapter 3 presents the identification of predominant terms in macroscopic conservation equations for sub-cooled boiling flows representative of industrial conditions. An a priori method is used for this aim. It consists of two steps: first, to build a local CFD database,

with experimental validation by comparison of predicted and measured void fraction, and then to average the variables of the local database and compare the averaged variable values. The predominant term identified using this method is then selected to be modeled at the macroscopic scale, and it turns out that the bubble condensation term will be chosen. However, many phenomena intervene in this database, and therefore, it is better to create a new database on separate effect tests where only the bubble condensation plays a key role. This allows us to develop a macroscopic model based on a trusted database afterwards.

- Chapter 4 focuses on the creation of a local CFD database on separate effect tests on bubble condensation. A new modeling is developed in order to obtain a fully validated database, i.e., with predicted local profiles of temperature, void fraction, velocity and bubble size close to the experimental ones. This new modeling involves the method of moments using a polydisperse bubble size distribution function, and also a bubble collapse model. Its benefits are evaluated in comparison to the current modeling and to other models from the literature.
- Chapter 5 aims at evaluating the existing macroscopic bubble condensation models, and then developing new ones based on the CFD database established in chapter 3. Statistical tools are used in order to develop a new model, and the advantages of this new model are evaluated in comparison to existing models.

Next, a feedback on the up-scaling method developed in this thesis is given, with a scheme that represents this method in 17 steps. Finally, the conclusions and perspectives are provided.

Note: A summary of the up-scaling method developed and applied in this thesis is shown in Figure 7 on page 158.

Chapter 1

Towards an up-scaling strategy for industrial two-phase thermal-hydraulics based on the State of the Art

Contents

The up-scaling method consists of evaluating and developing models at a coarse scale based on simulations done at a finer scale. The coarse and fine scales can be diverse. However, two couples of scales are most commonly used, namely the DNS to RANS scales and the RANS to macroscopic scales. Some existing up-scaling methods of both couples of scales are discussed, and a generic plan of up-scaling method is established in the following section. Then, the reference French codes at the coarse and fine scales are described in sections 1.2 and 1.3. These codes will be used for the up-scaling method developed in this thesis. Finally, an up-scaling strategy adapted to industrial two-phase flows is expressed in section 1.4.

1.1 Addressing the up-scaling issue

1.1.1 Existing up-scaling methods from DNS to RANS

In the thesis of Du Cluzeau (2019), an up-scaling work has been achieved on two-phase flows to collect some statistical information from DNS simulations in order to improve the modeling at the RANS scale. This work has focused on the turbulence models and on the interfacial forces responsible for lateral bubble migrations.

Moreover, Fleau (2017) has used an *a priori* method in order to evaluate some terms here at the LES scale from DNS simulations. This work has been done to improve LES models and not RANS ones, but the method is also applicable from DNS to RANS, or from RANS to macroscopic scale. This method has been applied to evaluate some subgrid terms that need to be modeled at the LES scale, and that can be directly calculated at DNS scale. The DNS simulations are then used to assess the order of magnitude of these terms in order to identify those that will require a more significant modeling effort due to their importance.

> **Note:** This *a priori* method will be adapted in the chapter 3 of this thesis in order to evaluate some terms at macroscopic scale from RANS simulations.

1.1.2 Existing up-scaling methods from RANS to macroscopic scale

In the literature, some up-scaling methods have already been developed and applied to model phenomena at the macroscopic scale based on the RANS scale. Most of them consist of modeling at the macroscopic scale the subgrid terms of turbulence and dispersion, which are linked respectively to statistic and spatial fluctuations. The physical meanings of these terms are described in section 1.3.3. In this section, the overall methodology of all these studies is described, and the differences between them are highlighted. According to us, all these methods can be divided into nine parts as follows:

1. Choice of a flow type and geometry
2. Establishment of macroscopic formulation
3. Choice of a phenomenon to model
4. Creation of a local database
5. Homogenize local model
6. Analysis of unknown terms order of magnitude
7. Modeling unknown terms using known variables and optimization constants
8. Constants calibration using local database
9. Evaluation of the new macroscopic modeling on a new database

These different parts are described based on the previous up-scaling works of Nakayama and Kuwahara (1999); Pedras and De Lemos (2001); Flick et al. (2003); Chandesris (2006); Pinson (2006); Teruel and Rizwan-uddin (2009); Drouin et al. (2010).

1. To the extent of our knowledge, the up-scaling methods that have been applied in order to develop a model at a macroscopic scale are always applied on incompressible liquid flows. This is the case of all the works mentioned above. A method has been developed by Bois (2021) for two-phase flows but has not yet been applied. Moreover, all the studies have been done on academic test cases. However, a large variety of geometries has been studied. Flick et al. (2003) have studied flows in sphere bundle while Chandesris (2006) has investigated parallel flows in tube bundle. On the other hand, Nakayama and Kuwahara (1999); Pedras and De Lemos (2001); Teruel and Rizwan-uddin (2009) have studied transverse flow in rod bundles, and Pinson (2006); Drouin (2010) have considered flows in plane and circular channels.

2. Although all the authors have established a statistic-volume average formulation, some discrepancies can be found in the establishment, which have a direct impact on further modeling. There are three ways to develop a macroscopic formulation from local instantaneous Navier-Stokes equations. The first one is to apply a statistic average and then a spatial average, the second one is the reverse, i.e., a spatial average and then a statistic one. The last one consists of applying both averages simultaneously. Delhaye (1977) has proven that all the ways give the same macroscopic formulations. However, the strategy to apply first the statistical average is most used since the RANS equations are obtained

first, and next, the macroscopic equations are obtained using a spatial average. Therefore, RANS simulations can be performed, and the RANS modeling can also be used as a basis to develop the macroscopic modeling. This is why most authors have used this method (Nakayama and Kuwahara, 1999; Pedras and De Lemos, 2001; Fleau, 2017; Chandesris, 2006; Pinson, 2006; Drouin et al., 2013). The macroscopic momentum equation obtained by this method is written in equation (1.1.1). The fluid porosity Φ is expressed as $\Phi = V_f/V$, with V_f and V respectively the fluid and total volume in a macroscopic cell. The overbar represents the statistical average, and the operator $\langle . \rangle$ represents the spatial average. A spatial deviation δ appears due to the spatial average as: $\langle \xi\psi \rangle = \langle \xi \rangle \langle \psi \rangle + \langle \delta\xi\delta\psi \rangle$. This spatial deviation is analogous to the statistical fluctuation linked to the turbulence. These spatial operators are described in detail in section 2.1.

$$\begin{aligned} \Phi \frac{\partial \left\langle \underline{\overline{v}} \right\rangle_f}{\partial t} + \underline{\nabla}.\left(\Phi \left\langle \underline{\overline{v}} \right\rangle_f \left\langle \underline{\overline{v}} \right\rangle_f \right) &= -\frac{\Phi}{\rho} \underline{\nabla} \left\langle \overline{P} \right\rangle_f + \underline{\nabla}.\left(\nu_f \underline{\nabla} \Phi \left\langle \underline{\overline{v}} \right\rangle_f \right) + \Phi \left\langle g_i \right\rangle \\ &- \underbrace{\underline{\nabla}.\left(\Phi \left\langle \overline{\underline{v}'\underline{v}'} \right\rangle_f \right)}_{\text{Turbulence}} - \underbrace{\underline{\nabla}.\left(\Phi \left\langle \delta\underline{\overline{v}}\ \delta\underline{\overline{v}} \right\rangle_f \right)}_{\text{Dispersion}} + \underbrace{\Phi \left\langle \left(-\frac{\delta \overline{P}}{\rho} \delta_{ij} + \nu_f \underline{\nabla} \underline{\overline{v}} \right) n_j \delta_\omega \right\rangle_f}_{\text{Wall friction}} . \end{aligned} \tag{1.1.1}$$

To our knowledge, the only different method in the literature has been developed by Teruel and Rizwan-uddin (2009), where both average operators are applied simultaneously on local instantaneous conservation equations. Then, a double over-line operator $\overline{\overline{\cdot}}$ is introduced and corresponds to a statistic and volume averaged variable. The macroscopic momentum equation is then written:

$$\frac{\partial \overline{\overline{\underline{v}}}}{\partial t} + \underline{\nabla}.\left(\overline{\overline{\underline{v}}} \times \overline{\overline{\underline{v}}} \right) = -\frac{1}{\rho} \underline{\nabla} \overline{\overline{P}} + \underline{\nabla}.\left(\nu_f \underline{\nabla}\, \overline{\overline{\underline{v}}} \right) + \overline{g_i} - \underbrace{\underline{\nabla}.\left(\overline{\overline{\underline{v}'''\underline{v}'''}} \right)}_{\text{Dispersion + Turbulence}} + \underbrace{R_i}_{\text{Wall friction}} , \tag{1.1.2}$$

with:

$$\overline{\overline{\underline{v}'''\underline{v}'''}} = \left\langle \overline{\underline{v}'\underline{v}'} \right\rangle_f + \left\langle \delta\underline{\overline{v}}\ \delta\underline{\overline{v}} \right\rangle_f . \tag{1.1.3}$$

Both formulations are equivalent, but Teruel and Rizwan-uddin (2009) have gathered both the subgrid terms of turbulence and dispersion in a single term, and propose to model both terms together.

3. All these authors have chosen to model the subgrid terms. However, some authors as Nakayama and Kuwahara (1999); Pedras and De Lemos (2001); Flick et al. (2003); Chandesris (2006) have tried to model only the turbulence diffusion term. On the other side, due to the different methods used by Teruel and Rizwan-uddin (2009), the authors have chosen to study both turbulence and dispersion terms together. Finally, Pinson (2006); Drouin et al. (2013) have developed a new method in order to describe both turbulence and dispersion terms. This method is based on a two-scale analysis that allows them to describe the energy exchanges between scales.

4. Next, local databases are developed using numerical tools at the local scale. Some authors have chosen to perform DNS simulations, due to the academic test case, and some others have performed calculations at RANS scale. It is worth noting that the turbulence variables are already modeled at the RANS scale.

5. Excluding the work of Teruel and Rizwan-uddin (2009), all the other works are based on the turbulence transport equations already existing at the RANS scale. They have all applied the spatial average to the turbulent kinetic energy k transport equation, and some also applied it to the turbulent dissipation ϵ transport equation, while Drouin et al. (2013) have proposed an algebraic relation. In addition to that, Pinson (2006); Drouin et al. (2013) have also developed transport equations for the dispersion energy and wake dissipation, in order to model the dispersion subgrid term. Teruel and Rizwan-uddin (2009) are not able to use the same methodology since the RANS scale is not used. However,

they have built a transport equation for their subgrid terms using the same procedure as the one that has been done at the RANS scale. Then, they have developed transport equations for the variables k and ϵ, which here represent simultaneously the turbulence and dispersion terms. For all the new transport equation formulations, several unknown terms are generated by this average process.

6. Some authors as Pinson (2006) have studied the order of magnitude of the unknown terms that appear in the transport equations in order to focus on the predominant terms, and to neglect secondary terms. Some others develop models for all the unknown terms, with occasionally a single formulation used to model multiple terms.

7. All the models developed in these up-scaling works are varied but have some similarities. Indeed, they all consist of known variables and optimization constants. Some physical insights are used in order to develop these models, but they all need calibrations of the optimization constants in order to be ready for use.

8. The calibrations are done using the local database previously developed in step 4. For each work, the model error is calculated using multiple sets of constants on the entire local database, and the set that minimizes the overall error is kept.

9. Once the model has been developed, some authors have decided to evaluate their model on other databases.

A summary of the models developed by Chandesris (2006) and Drouin (2010) is given in Appendix V. Therefore, this section proves that some new models have been developed at the macroscopic scale using local databases. In order to use a similar method in this thesis to improve the accuracy of macroscopic codes, the first step is to choose the coarse and fine scales that are going to be used. In the same way as most authors cited above, the statistical average is first applied in this thesis in order to benefit from RANS codes, and the spatial average is applied later. Therefore, the fine code in this thesis solves two-phase RANS equations, while the coarse code solves statistical and spatially averaged equations.

Since the aim of this thesis is to predict better the flows in nuclear reactor core under industrial and accidental conditions, the French reference codes at macroscopic and RANS scales, namely the CATHARE and Neptune_CFD codes, are used.

First, the Neptune_CFD code, which solves statistical-averaged equations, is described in section 1.2. Then, the 3-D module of CATHARE code, which solves statistical and spatially averaged equations, is detailed in section 1.3. Finally, the strategy to improve the 3-D module of the CATHARE code using Neptune_CFD simulations is expressed in section 1.4.

1.2 French reference code for two-phase thermal-hydraulic at RANS scale: Neptune_CFD

Neptune_CFD code is developed in the NEPTUNE multiscale thermal-hydraulic platform, which is financially supported by EDF (Electricité de France), CEA (Commissariat à l'énergie atomique et aux énergies alternatives), IRSN (Institut de radioprotection et de sûreté nucléaire) and Framatome. Neptune_CFD is a 3D multifield CFD code using the Eulerian approach (Guelfi et al., 2007). The solver is based on a pressure correction method simulating multi-component multiphase flows by solving three statistically averaged balance equations for each phase. Moreover, it is based on a finite-volume discretization along with a collocated arrangement of the variables. Thanks to its face-based data structure, Neptune_CFD allows the use of all types of meshes (hexahedral, tetrahedral, pyramids, etc.), even non-conforming ones.

This numerical tool has been extensively validated for bubbly flows on adiabatic and subcooled boiling flows (Guelfi et al., 2007; Mimouni et al., 2017b; Laviéville et al., 2017; Favre, 2023). The simulations done during this thesis have been conducted using version 7.0 of Neptune_CFD.

The Neptune_CFD equations are obtained by applying a statistical average on the two-phase local instantaneous balance equations. In the following, the averaging operators used to obtain Neptune_CFD equations are described.

Statistical average operators

The statistical average operator $\overline{\xi}$ and its fluctuation ξ' are defined in equation (1.2.1).

$$\overline{\xi}(x,t) = \lim_{p\to\infty}\frac{1}{p}\sum_{n=1}^{p}\xi_n(x,t), \quad \xi'(x,t) = \xi(x,t) - \overline{\xi}(x,t). \tag{1.2.1}$$

$\xi_n(x,t)$ corresponds to the n^{th} realization of the ξ variable at point x at time t. This average operator is well suited for the study of random quantities. Therefore, it is relevant for the study of turbulent flows. This statistical average verifies the three Reynolds axioms: linearity, idempotency, and commutativity with derivation operators, which are useful properties to handle averaged differential equations.

A Reynolds phasic average $\overline{\xi}^k$, and a mass-weighted phasic average $\overline{\xi}^{k\rho}$, relevant to the study of two-phase flow, are introduced in equation (1.2.2), using the volume fraction α_k which is equal to the statistical average of the phasic indicator function χ_k. The phasic indicator function $\chi_k(x)$ is equal to 1 if phase k is present at x, 0 otherwise. In the following, subscripts $k = l$ or g denotes the liquid or gas phase, i and I correspond to the interfacial quantities, and w to the wall contribution.

$$\alpha_k = \overline{\chi_k}, \quad \overline{\xi}^k = \frac{\overline{\chi_k\xi}}{\overline{\chi_k}} = \frac{\overline{\chi_k\xi}}{\alpha_k}, \qquad \overline{\xi}^{k\rho} = \frac{\overline{\rho_k\xi}^k}{\overline{\rho_k}^k}. \tag{1.2.2}$$

Moreover, a spatial deviation related to the mass-weighted phasic average can be introduced as $\xi'' = \xi - \overline{\xi}^{k\rho}$. The Reynolds axioms are still verified, but the statistical mean of the mass-weighted phasic fluctuating part is no longer centered: $\overline{\xi''} \neq 0$. By introducing $\delta(f)$ equal to 1 at the phase interface and 0 otherwise, an average of a quantity ξ at the interface can also be defined as:

$$\overline{\xi}^I = \frac{\overline{\xi\delta(f)}}{\overline{\delta(f)}}. \tag{1.2.3}$$

Neptune_CFD equations are obtained by applying the statistical average operator $(\bar{\cdot})$ to local instantaneous equations and using the single pressure assumption with $P = p_l = p_v$. The obtained equations are given below. The terms represented in red correspond to unknown terms that need closure laws.

Mass balance equation

$$\frac{\partial}{\partial t}\left(\alpha_k\overline{\rho}_k^k\right) + \nabla\left(\alpha_k\overline{\rho}_k^k.\underline{\overline{v}}_k^{k\rho}\right) = \textcolor{red}{\Gamma_k}. \tag{1.2.4}$$

Where α_k, $\overline{\rho}_k^k$, $\underline{\overline{v}}_k^{k\rho}$ are the volume fraction, averaged density and velocity of phase k; $\textcolor{red}{\Gamma_k} = \Gamma_{k,i} + \Gamma_{k,w}$ the interfacial mass transfer term per unit of volume and time split between bulk and wall contribution. The wall contribution is also known as the mass transfer term due to nucleation.

Momentum balance equation

The momentum equations are solved in their non-conservative form, which allows a better treatment of the vanishing phase k in two-phase flow computation. This momentum equation in non-conservative form is written as:

$$\begin{aligned}\overline{\rho}_k^k\frac{\partial}{\partial t}\underline{\overline{v}}_k^{k\rho} + \underline{\overline{v}}_k^{k\rho}\frac{1}{\alpha_k}\nabla\left(\alpha_k\overline{\rho}_k^k\underline{\overline{v}}_k^{k\rho}\right) + \frac{1}{\alpha_k}\nabla\left(\alpha_k\overline{\rho}_k^k\underline{\overline{v}}_k^{k\rho}.\underline{\overline{v}}_k^{k\rho}\right) &= \frac{1}{\alpha_k}\nabla.\left(\alpha_k\underline{\underline{\overline{\tau_m}}}_k^k + \textcolor{red}{\underline{\underline{\overline{\tau_T}}}_k}\right) - \nabla\overline{P}^k \\ &+ \overline{\rho}_k^k\underline{g} + \frac{1}{\alpha_k}\left[\textcolor{red}{\underline{M}_{ik}} + \Gamma_k\left(\textcolor{red}{\underline{\overline{v}}_k^{Im}} - \underline{\overline{v}}_k^{k\rho}\right)\right].\end{aligned} \tag{1.2.5}$$

with:

- The acceleration due to gravity g.

- The pressure P, with the single-pressure hypothesis $P = p_l = p_v$.

- The viscous stress tensor $\underline{\underline{\tau_m}}_k$.

- $\underline{\underline{\tau_T}}_k = -\alpha_k \overline{\rho}_k^k \overline{\underline{v}_k'' \underline{v}_k''}^{k\rho}$ is the turbulent stress tensor. The fluctuation velocity terms are those defined in equation 1.2.2.

- $\overline{\underline{v}}_k^{Im}$ represents the mean velocity at the interface.

- $\underline{M}_{ik}$ is the total interfacial momentum transfer rate between the interface and phase k. This term can be divided into a drag force, an added-mass force, a lift force, and a turbulent dispersion force.

Energy balance equation

The energy balance equation is considered for the total enthalpy variable:

$$H_k = e_k + \frac{1}{2} v_k^2 + \frac{P}{\rho_k}, \quad \text{with } e_k \text{ the apparent internal energy: } \overline{e}_k^{k\rho} = \overline{u}_k^{k\rho} + \frac{\overline{(v_k')^2}^{k\rho}}{2}, \tag{1.2.6}$$

with u_k the internal energy. Using this notation and the same assumptions that have been made previously, the Neptune_CFD energy equation is written:

$$\begin{aligned} \frac{\partial}{\partial t}\left(\alpha_k \overline{\rho}_k^k \overline{H}_k^{k\rho}\right) + \nabla.\left(\alpha_k \overline{\rho}_k^k \overline{H}_k^{k\rho} \overline{\underline{v}}_k^{k\rho}\right) - \alpha_k \frac{\partial \overline{P}^k}{\partial t} = &- \nabla.\left[\alpha_k \left(\overline{\underline{q_m}}_k^k + \underline{\overline{q_T}}_k\right)\right] + q_{wk} \\ &+ \underline{\nabla.\left(\alpha_k \overline{\underline{\underline{\tau_m}}}_k^k . \overline{\underline{v}}_k^{k\rho}\right)} + \alpha_k \overline{\rho}_k^k \overline{v}_k^{k\rho} \underline{g} + \underbrace{\Gamma_k \overline{H}_k^{Ie} + \Pi_k'}_{\Pi_k} + \underline{\underline{M}_{ik} \overline{\underline{v}}_k^{Im}}, \end{aligned} \tag{1.2.7}$$

with:

- Π_k the interfacial heat transfer between each phase and Π_k' the component of Π_k independent of the mass transfer. The mean enthalpy at the interface is defined as:

$$\overline{H}_k^{Ie} = \overline{e}_k^{Im} + \frac{\overline{p}_k^I}{\overline{\rho}_k^{Im}} + \frac{1}{2}(\overline{u}_k^{Im}). \tag{1.2.8}$$

- $\overline{\underline{q_m}}_k^k$ is the conduction heat flux and $\underline{\overline{q_T}}_k = \alpha_k \overline{\rho}_k^k \overline{H_k \underline{v}_k''}^{k\rho} + \alpha_k \overline{\underline{\underline{\tau_m}} . \underline{v_k}''}^k$ is the turbulent heat flux. In Neptune_CFD, the conductive thermal flux $(\underline{q_m}_k + \underline{q_T}_k)$ is calculated by: $\underline{q_m}_k + \underline{q_T}_k = -\lambda_k \nabla T_k$. The thermal conductivity λ_k takes into account both conduction and turbulent parts.

- q_{wk} represents the heat exchanges between wall and phase k.

- The two underlying terms are currently neglected in the code.

Interfacial jump conditions

In addition to those six balance equations, three Interfacial Jump Conditions (IJC) can be defined, as well as one volumetric continuity condition. The interfacial source term for momentum M_m is neglected as it is much smaller than the drag force itself. Similarly, the interfacial source term for energy E_m is neglected in relation to the large energy exchanges involving latent heat during phase change.

Volumetric continuity: $$\sum_{k=l,g} \alpha_k = 1, \tag{1.2.9}$$

Mass interface jump condition: $$\sum_{k=l,g} \Gamma_k = 0, \tag{1.2.10}$$

$$\text{Momentum interface jump condition:} \quad \sum_{k=l,g} \Gamma_k \overline{\underline{v}}_k^{Im} + \underline{M}_{ik} = M_m = 0, \tag{1.2.11}$$

$$\text{Energy interface jump condition:} \quad \sum_{k=l,g} \Pi_k = \sum_{k=l,g} \Gamma_k \overline{H}_k^{Ie} + \Pi'_k = E_m = 0. \tag{1.2.12}$$

Determinism

Mathematically, the principle of determinism requires as many equations as there are unknowns. As shown in the table 1.2.1, there are 28 variables (DV + AP) and 10 equations. Therefore, 18 additional closure relations are required to close the system. The closure relations that are described here correspond to a modeling adapted to bubbly flows. This set of closure relations is going to be used in the chapter 3.

Equations	**DV (No)**	**AP (No)**			
Volumetric (1)	α_k (2)				
Mass (2)	$\overline{\underline{v}}_k^{k\rho}$ (2)	Γ_k (2)	$\overline{\rho}_k^k$ (2)		
Momentum (2)	$\overline{P}^k$ (1)	$\overline{\underline{\underline{\tau_m}}}_k^k$ (2) $\overline{\underline{v}}_k^{Im}$ (2)	$\overline{\underline{\underline{\tau_T}}}_k$ (2)	$\underline{g}$ (1)	$\underline{M}_{ik}$ (2)
Energy (2)	$\overline{e}_k^{k\rho}$ (2)	$\overline{\underline{q_m}}_k^k$ (2)	$\overline{\underline{q_T}}_k$ (2)	Π_k (2)	q_{wk} (2)
IJC (3)					

Table 1.2.1: Summary of the Dependant Variables (DV) and Auxiliary Parameters (AP) for the two-fluid model used in code Neptune_CFD.

First of all, the temperature, pressure, density and enthalpy are linked by equations of state. Moreover, in Newtonian fluids, heat conduction $\overline{\underline{q_m}}_k^k$ obeys Fourier's law, and the viscous stress tensor $\overline{\underline{\underline{\tau_m}}}_k^k$ is linear with respect to the strain rate. The models used for the other variables are briefly presented in the following paragraphs.

Turbulence model The turbulence stress tensor $\overline{\underline{\underline{\tau_T}}}_k$ is taken into account only in the liquid phase for bubbly flows. It can be obtained by different models, and here, this term is modeled using the $R_{ij} - \epsilon$ SSG model from Speziale et al. (1991) adapted to two-phase boiling flows by Mimouni et al. (2011). The turbulent heat flux $\overline{\underline{q_T}}_k$ is modeled in the same form as the conduction heat flux.

Wall boiling model The term related to the heat transfer at the wall q_{wk} is modeled following Kurul and Podowski (1990) work. The resolution of this term is based on a Heat Flux Partitioning model where the q_{wk} term is divided into three terms:

- A single phase convective heat flux ϕ_c heating the liquid through the fraction of the wall area unaffected by the vapor bubbles.
- A vaporization heat flux ϕ_e which accounts for the generation of vapor through heterogeneous nucleation.
- A quenching heat flux ϕ_q that represents the thermal impact of bubbles departing from the wall and being replaced by cooled liquid.

Interfacial heat and mass transfers Using the energy interface jump condition, both heat and mass transfer terms are linked in Neptune_CFD as follows:

$$\Gamma_l = \frac{\Pi'_l + \Pi'_g}{H_g - H_l} = a_i \frac{(q_{li} + q_{gi})}{H_{lg}}, \tag{1.2.13}$$

with $H_{lg} = H_g - H_l$ the interfacial enthalpy jump. The variables q_{li} and q_{gi} are, respectively, the liquid and gas interfacial heat flux densities. The interfacial heat transfer is usually expressed as follows:

$$\Pi'_k = a_i h_k \left(T_{sat}(P) - T_k\right), \quad \text{with: } a_i = \frac{6\alpha_g}{d_{32}}, \tag{1.2.14}$$

with a_i the interfacial area concentration, h_l the interfacial heat transfer coefficient, and d_{32} the Sauter diameter. In the case of subcooled liquid, studied in this thesis, the h_l term is modeled using the correlation developed by Ranz and Marshall (1952) recalled in equation (1.2.15).

$$h_l = \frac{\mathrm{Nu}_b \lambda_l}{d_{32}}, \quad \mathrm{Nu}_b = 2 + 0.6\mathrm{Re}_b^{1/2}\mathrm{Pr}^{1/3}, \text{ with } : \mathrm{Re}_b = \frac{\rho_l ||v_r|| d_{32}}{\mu_l} \text{ and } \mathrm{Pr} = \frac{\mu_l Cp_l}{\lambda_l}. \tag{1.2.15}$$

with Nu_b the bubble Nusselt number, Re_b the Reynolds bubble number, Pr the Prandtl number, v_r the relative velocity, μ_l the dynamic viscosity, and C_{p_l} the liquid specific heat.

Some other models exist for super-heated liquid, but these flow types are not used in this thesis. For the vapor phase, a simple law that ensures the gas temperature stays close to the saturation temperature is used.

Interfacial area transport equation (IATE) The interfacial area concentration a_i does not appear directly in the balance equations but is used in several closure laws, such as in the interfacial heat and mass transfer models presented in the previous section. This variable is modeled by the interfacial area transport equation of Ruyer and Seiler (2009), which is able to take into account the coalescence and fragmentation of bubbles. This equation is written in this form:

$$\frac{\partial a_i}{\partial t} + \underline{\nabla}.\left(a_i \underline{v}_g\right) = \phi_{PC} + \phi_{PV} + \phi_{BB} + \phi_{BC} + \phi_{BN}, \tag{1.2.16}$$

with ϕ_{PC} and ϕ_{PV} mean the source and sink terms of an expansion or shrinkage due to a phase change and a pressure change, respectively. ϕ_{BB} and ϕ_{BC} correspond to the source term due to a bubble break-up and the sink term due to a bubble coalescence. Finally, ϕ_{BN} is linked to the bubble nucleation. ϕ_{CO} corresponds to the sink term linked to the bubble collapse due to condensation, but this term is currently neglected in Neptune_CFD and most CFD codes.

For condensing flows without coalescence and break-up phenomena, which are the assumptions considered when the IATE is studied in chapter 4, the IATE is expressed as:

$$\frac{\partial a_i}{\partial t} + \underline{\nabla}.\left(a_i \underline{v}_g\right) = -\frac{2}{3}\frac{a_i}{\alpha_g \rho_g}\Gamma_{l,i} - \frac{2}{3}\frac{a_i}{\rho_g}\frac{d\rho_g}{dt}. \tag{1.2.17}$$

Interfacial forces The total interfacial momentum transfer rate between the interface and phase k, $\underline{M}_{ik}$, is modeled by a linear combination of several known interfacial forces:

$$\underline{M}_{ik} = \underline{M}_k^D + \underline{M}_k^{AM} + \underline{M}_k^L + \underline{M}_k^T, \tag{1.2.18}$$

with:

- $\underline{M}^D$ is the standard drag force representing the skin and form drag under steady-state conditions, which is modeled by Ishii and Zuber (1979) correlation.
- $\underline{M}^{AM}$ is the added mass force, which accounts for the force needed to accelerate the apparent mass of the surrounding phase when the relative velocity changes. It is modeled by Zuber (1964) correlation.
- $\underline{M}^L$ is the lift force, and this force is normal to the relative velocity due to rotation of fluid, the Tomiyama et al. (2002) model is used.
- $\underline{M}^T$ is the turbulent dispersion force due to concentration gradient. The Generalized Turbulent Dispersion (GTD) model developed by Haynes (2004) and presented by Laviéville et al. (2017) is used.

Wall functions Classical logarithmic wall functions are used to describe velocity and temperature profiles close to the wall, which allows the use of a larger $y+$.

Moreover, the mean velocity at interface $\overline{\underline{v}}_k^{Im}$ is closed to ensure stability as:

$$\overline{\underline{v}}_k^{Im} = \overline{\underline{v}}_g^{g\rho} \quad \text{if } \Gamma_l > 0 \text{ , } \overline{\underline{v}}_k^{Im} = \overline{\underline{v}}_l^{l\rho} \quad \text{else.} \tag{1.2.19}$$

Therefore, the mathematical description of the system is complete.

1.3 Macroscopic reference code in France: CATHARE

CATHARE (Code Avancé de ThermoHydraulique pour les Accidents de Réacteurs à Eau) is a system code that has been developed in 1979 by a collaboration between the CEA (French Alternative Energies and Atomic Energy Commission) and EDF (Electricity of France) in its first version, CATHARE 1. It was initially developed to perform safety analysis with best estimate computations of thermal-hydraulic transients in PWR. It has also been used as a nuclear power plant analyzer in simulator applications since 1983, providing real-time results for a full training scope. The first tests on the French integral test facility BETHSY in 1986 established the basis for the Verification, Validation, and Qualification Strategy process and resulted in the release of the first validated version of the CATHARE 1 code in 1987 (Bestion, 1990). In 2019, the first industrial version of CATHARE 3 for PWR applications has been released and is used in this manuscript (Préa et al., 2020). This code consists of 0-D, 1-D, and 3-D modules and sub-modules to represent the different components. The macroscopic scale studied in this thesis corresponds to the scale studied in the 3-D module of CATHARE. Therefore, the 3-D module of this code is described in detail in the following section.

1.3.1 Description of the module 3-D of CATHARE code (macroscopic scale)

The three-dimensional (3-D) module of CATHARE is based on the "porous" two-fluid six-equation model (Barré et al. (1995), Parent et al. (1991) and Brun et al. (1990)). Therefore, one set of mass, momentum, and energy balance equations is written for each phase.

The main application is to model the vessel of a PWR in a three-dimensional way. In this application, all the meshes of the three-dimensional vessel contain a large number of solid structures, such as the rod-bundles, the spacer grids, etc.

A scalar definition of the porosity is used, which gives the relative volumes occupied by the fluid and by the structures. This porosity is calculated according to the geometry and the mesh and is imposed by the user through the input deck.

$$\Phi = \frac{V_{fluid}}{V_{mesh}} = 1 - \frac{V_{structures}}{V_{mesh}}, \tag{1.3.1}$$

with V_{fluid}, $V_{structures}$ and V_{mesh} the fluid, structure and geometrical volumes of the mesh cell. The volumetric momentum and energy transfers between the solid structures and the fluid are also taken into account through algebraic terms in the equations.

In this section, the operator $(\tilde{.})$ is used to represent the fact that the variable is a time and volume averaged variable. Moreover, the main CATHARE variables for the three-dimensional module are:

- $\tilde{P}$: the pressure,
- $\tilde{i_l}$, $\tilde{i_g}$: the liquid/gas internal energies,
- $\tilde{\alpha_g}$: the gas volume fraction,
- $\tilde{\underline{v}_l}$ and $\tilde{\underline{v}_g}$: the liquid/gas velocity vectors.

The conservation equations of the CATHARE code are described below. The space discretization of the equations follows the finite volume approach for all the scalar mass and energy balance equations and the finite difference approach for the momentum balance equations. This difference is due to the use of the non-conservative form for the momentum balance equation. Two coordinate options are available: the user can use either Cartesian coordinates or cylindrical coordinates. The time discretization of the equations is based on the semi-implicit scheme.

In these balance equations, the black variables correspond to the main variables. These terms are directly calculated by macroscopic codes. The variables in blue represent constant terms that are known, such as porosity or gravity force. The green terms correspond to variables that are calculated from equations of state or constitutive equations. The red terms correspond to variables that need to be modeled by closure laws.

Mass balance equation

$$\frac{\partial(\Phi\tilde{\alpha}_k\tilde{\rho}_k)}{\partial t} + \nabla.\,(\Phi\tilde{\alpha}_k\tilde{\rho}_k\underline{\tilde{v}}_k) = (-1)^n\Phi\tilde{\Gamma}. \tag{1.3.2}$$

Φ is the porosity, and $n = 0$ for the liquid and $n = 1$ for the gas phase. $\tilde{\Gamma}$ is the mass transfer at the interface ($\tilde{\Gamma} = -\tilde{\Gamma}_l = \tilde{\Gamma}_g$).

Momentum balance equation

The momentum equation of the module 3-D of CATHARE is solved in a non-conservative way as follows:

$$\begin{array}{clll}
 & \Phi\tilde{\alpha}_k\tilde{\rho}_k\left[\frac{\partial(\underline{\tilde{v}}_k)}{\partial t} + \underline{\tilde{v}}_k\nabla.\,(\underline{\tilde{v}}_k)\right] + \Phi\tilde{\alpha}_k\nabla\tilde{P} + \Phi\tilde{P}_i\nabla\tilde{\alpha}_k = & & \\
+ & \Phi(-1)^n\underline{\tilde{\tau}}_i & \text{interfacial friction} & \\
- & \Phi\frac{2}{D_h}\tilde{\rho}_k C_k\underline{\tilde{v}}_k|\underline{\tilde{v}}_k| & \text{wall regular friction} & \\
- & \Phi\frac{K}{2\Delta\underline{X}}\tilde{\alpha}_k\tilde{\rho}_k\underline{\tilde{v}}_k|\underline{\tilde{v}}_k| & \text{singular friction} & (1.3.3) \\
+ & \Phi\tilde{\alpha}_k\tilde{\rho}_k\underline{\tilde{g}} & \text{gravity force} & \\
+ & \nabla.\left[\left(\tilde{\nu}_{tk}^{\Phi} + \tilde{\nu}_{dk}^{\Phi}\right)\left(\underline{\nabla}(\Phi\underline{\tilde{v}}_k) + \underline{\nabla}^T(\Phi\underline{\tilde{v}}_k) - \frac{2}{3}\underline{\nabla}.(\Phi\underline{\tilde{v}}_k)\underline{\underline{\mathbb{I}}}\right)\right]. & \text{Turbulence-dispersion term} &
\end{array}$$

The variable $\Delta\underline{X}$ in the singular friction term is equal to ΔX in x direction, ΔY in y direction, and ΔZ in z direction. The turbulence-dispersion term is not present in the standard version of the module 3-D of CATHARE but is added as an option for sub-channel studies. This term is discussed in section 1.3.3, and described in detail in the Appendix IV. Therefore, in the standard version, the porosity Φ disappear from this equation. This momentum equation can also be expressed in conservative form, as:

$$\begin{array}{clll}
 & \Phi\frac{\partial(\tilde{\alpha}_k\tilde{\rho}_k\underline{\tilde{v}}_k)}{\partial t} + \nabla.\,(\Phi\tilde{\alpha}_k\tilde{\rho}_k\underline{\tilde{v}}_k\underline{\tilde{v}}_k) + \Phi\tilde{\alpha}_k\nabla\tilde{P} + \Phi\tilde{P}_i\nabla\tilde{\alpha}_k = & & \\
+ & \Phi(-1)^n\underline{\tilde{\tau}}_i & \text{interfacial friction} & \\
- & \Phi\frac{2}{D_h}\tilde{\rho}_k C_k\underline{\tilde{v}}_k|\underline{\tilde{v}}_k| & \text{wall regular friction} & \\
- & \Phi\frac{K}{2\Delta\underline{X}}\tilde{\alpha}_k\tilde{\rho}_k\underline{\tilde{v}}_k|\underline{\tilde{v}}_k| & \text{singular friction} & (1.3.4) \\
+ & \Phi(-1)^n\tilde{\Gamma}\underline{\tilde{v}}_i & \text{interfacial mass transfer} & \\
+ & \Phi\tilde{\alpha}_k\tilde{\rho}_k\underline{\tilde{g}} & \text{gravity force} & \\
+ & \nabla.\left[\left(\tilde{\nu}_{tk}^{\Phi} + \tilde{\nu}_{dk}^{\Phi}\right)\left(\underline{\nabla}(\Phi\underline{\tilde{v}}_k) + \underline{\nabla}^T(\Phi\underline{\tilde{v}}_k) - \frac{2}{3}\underline{\nabla}.(\Phi\underline{\tilde{v}}_k)\underline{\underline{\mathbb{I}}}\right)\right]. & \text{Turbulence-dispersion term} &
\end{array}$$

Energy balance equation

The energy balance equation considered in the 3-D module of CATHARE is expressed in equation (1.3.5) for the internal energy: $\tilde{i_k} = \tilde{H}_k - \frac{\tilde{P}}{\rho_k}$.

$$\begin{array}{clll}
 & \frac{\partial(\Phi\tilde{\alpha_k}\tilde{\rho_k}\tilde{i_k})}{\partial t} + \nabla.\left(\Phi\tilde{\alpha_k}\tilde{\rho_k}\tilde{i_k}\underline{\tilde{v_k}}\right) = & & \\
- & \tilde{P}\left[\tilde{\alpha_k}\frac{\partial\Phi\tilde{\alpha}_k}{\partial t} + \nabla.\left(\Phi\tilde{\alpha}_k\underline{v}_k\right)\right] & \text{Pressure term} & \\
+ & \Phi\tilde{q_{ik}} + \chi_c\tilde{q_{wk}} & \text{Heat transfer} & (1.3.5) \\
+ & \Phi(-1)^n\tilde{\Gamma}\tilde{H}_k & \text{Impulsion transfer} & \\
+ & \nabla.\left(\tilde{\alpha_k}\underline{q}_k^T\right) & \text{Turbulent and dispersion heat flux,} &
\end{array}$$

with χ_c the heating perimeter. The turbulent and dispersion heat flux term is discussed in section 1.3.3, and described in detail in Appendix IV.

This equation can also be written in terms of the total enthalpy H_k, as:

$$\begin{array}{clll}
 & \frac{\partial(\Phi\tilde{\alpha_k}\tilde{\rho_k}\tilde{H_k})}{\partial t} + \nabla.\left(\Phi\tilde{\alpha_k}\tilde{\rho_k}\tilde{H_k}\underline{\tilde{v_k}}\right) = & \text{Advection terms} & \\
+ & \Phi\tilde{\alpha_k}\frac{\partial\tilde{P}}{\partial t} & \text{Pressure term} & \\
+ & \Phi\tilde{q_{ik}} + \chi_c\tilde{q_{wk}} & \text{Heat transfer} & (1.3.6) \\
+ & \Phi(-1)^n\tilde{\Gamma}\tilde{H}_k & \text{Impulsion transfer} & \\
+ & \nabla.\left(\tilde{\alpha_k}\underline{q}_k^T\right) & \text{Turbulent and dispersion heat flux.} &
\end{array}$$

1.3.2 The Verification and Validation of the 3-D module of CATHARE

To achieve confidence in the results of the 3-D module of the CATHARE code predictions, it is necessary to ensure that the physical laws and models are accurate. These closure laws involve many correlations deduced from the literature and validated on separate effect tests. An overview of these correlations is given by Bestion (1990).

The wall friction correlation of the 3-D module of CATHARE is briefly used in chapter 3, and therefore, its formulation can be found in Appendix III. Moreover, the models for the interfacial mass and heat transfer terms ($\tilde{\Gamma}$, $\tilde{q}_{ik}$) in the case of bubble condensation are evaluated in chapter 5, alongside the models from TRACE code (Bajorek, 2008). The formulations of these models are described in detail in section 5.2. Moreover, a focus is placed on the turbulence-dispersion terms in the following section to describe the physical meanings of these terms, and to highlight the requirement of quantification of these terms.

Research and Development work is undertaken to identify good relationships for all the closure laws describing all the phenomena and mechanisms at work in a nuclear reactor in an accidental situation. This code verification and validation work is carried out in particular by comparing the experimental results of the separate effect tests (SET) and the prediction results of the CATHARE code. Figure 1.3.1 illustrates some separate effect tests used for CATHARE verification and validation (for the 0-D, 1-D, and 3-D modules) within the many components of a reactor. This Figure is non-exhaustive, some other test cases are used and are not represented here. Moreover, some examples of SET and Integral Effect Tests (IET) used for the CATHARE 3-D module validation are given in Table 1.3.1. The acronyms LB-LOCA and IB-LOCA stand for Large Break Loss Of Coolant Accident, and Intermediate size Break Loss Of Coolant Accident.

As mentioned above, this thesis focuses especially on the evaluation of the subgrid terms of turbulence and dispersion, and then on the evaluation and development of macroscopic models for the interfacial transfer terms of condensation. Therefore, the two following sections focus on the physical meaning and the current macroscopic modeling of these terms. The models of the CATHARE 3-D module are also compared to other models from other codes.

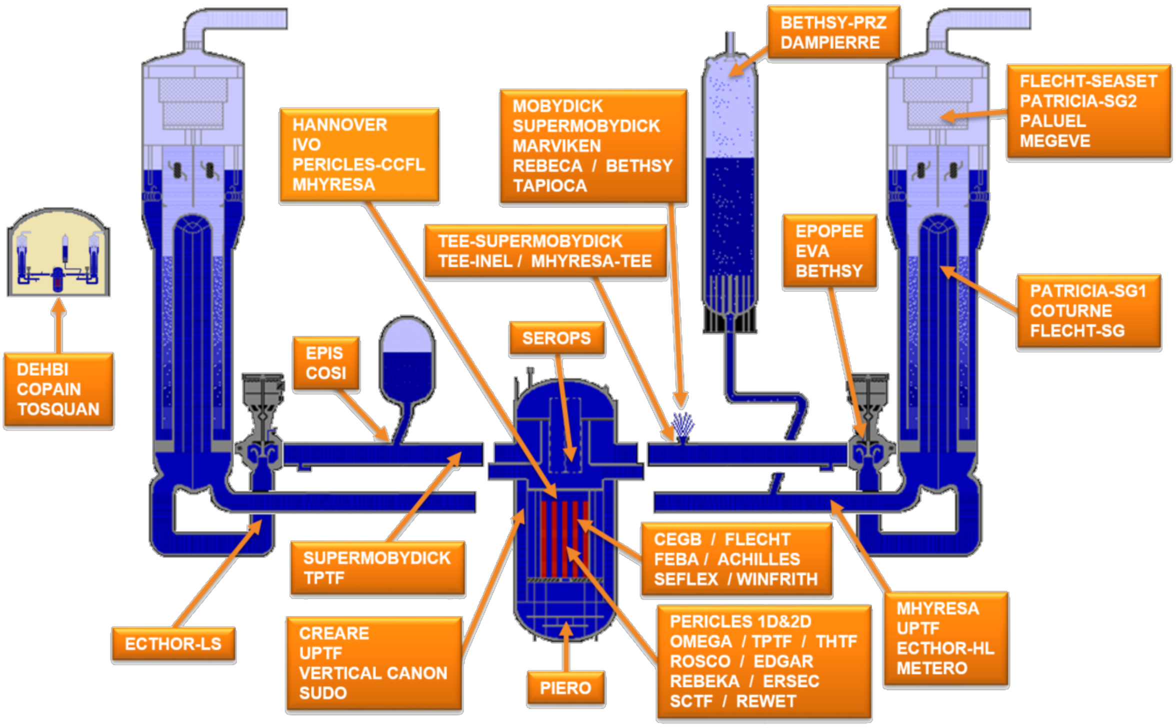

Figure 1.3.1: Separate effect tests used in the CATHARE code verification and validation Ciechocki (2023).

Application	Phase / component	Test	Type
LB-LOCA	Blowdown phase, lower plenum voiding	PIERO	SET
	Downcomer refilling phase	UPTF tests 6 and 7	SET
	Boiling phenomena in downcomer (late reflooding phase)	JAERI-SUBO	SET
	Reflooding phase: 3D effects in core	PERICLES 2D reflooding, SCTF	SET
	Transient	LOFT L2-5 and LP02-6	IET
IB-LOCA	Cold leg 13% break	ROSA 2/LSTF test 7	IET
LOCA	Countercurrent flow limit (CCFL) at the core upper plate	UPTF test 10c	SET
	Core uncovery	PERICLES 2D boil-up	SET
Fuel ballooning	Core	CEGB, ACHILLES, FLECHT, FEBA, SEFLEX	SET
Mixing effects in core	Core	BFBT, PSBT, OMEGA, GRAZIELLA, AGATE, PERICLES	SET

Table 1.3.1: Examples of SET and IET used for the CATHARE 3D module validation (NEA, 2024).

1.3.3 Focus on the subgrid turbulence and dispersion terms

Physical meaning of these terms

The turbulence and dispersion terms are representative of physical phenomena happening on a smaller scale than the mesh. Indeed, the turbulence is characterized by temporal or statistic fluctuations through the temporal or statistic filter. On the other hand, the dispersion term is characterized by spatial fluctuations within the spatial filter. The turbulence and dispersion terms are written respectively $\left\langle \overline{\underline{v}''.\underline{v}''} \right\rangle$ and $\langle \delta\overline{\underline{v}}\delta\overline{\underline{v}} \rangle$. It is recalled that the overline corresponds to the statistic average operator, while $\langle . \rangle$ is the spatial average operator. Moreover, $\delta\xi$ represents the spatial deviation of ξ, and ξ'' corresponds to the statistic fluctuation of ξ. Therefore, $\xi = \overline{\xi} + \xi''$, and $\xi = \langle \xi \rangle + \delta\xi$. As it can be seen in Figure 1.3.2, temporal fluctuations exist in turbulent flows. Then, the term $\overline{\underline{v}''.\underline{v}''}$ is non-null for turbulent test cases. This turbulence phenomenon has been extensively studied at the RANS scale.

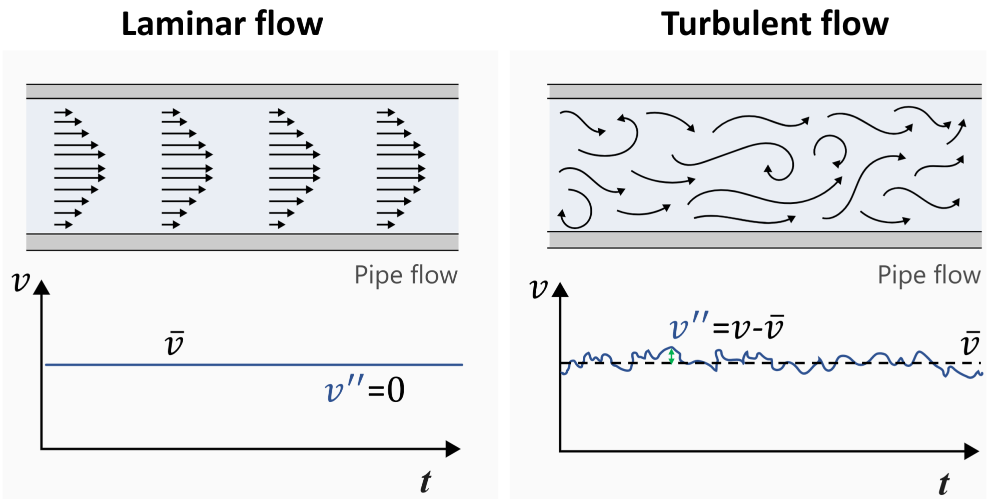

Figure 1.3.2: Description of turbulence phenomenon.

The dispersion phenomenon has been less studied since it happens at the macroscopic scale but not at the RANS scale. First, fictional radial liquid velocity profiles, which are already statistically averaged, are introduced in Figure 1.3.3.

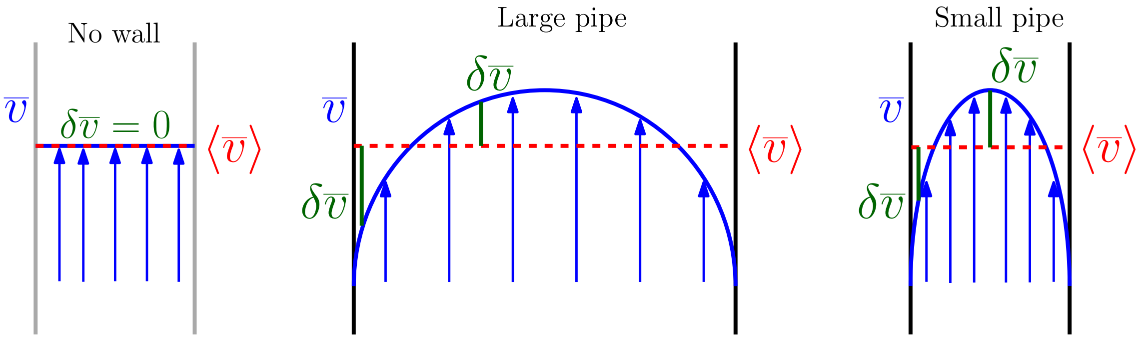

Figure 1.3.3: Description of liquid velocity dispersion phenomenon inside a pipe.

First, at left, a geometry without walls is considered and results in a flat profile, and so, the statistically averaged velocity $\overline{v}$ is equal everywhere to the spatial average $\langle\overline{v}\rangle$. Therefore, the spatial deviation $\delta\overline{v}$ is null everywhere. However, the velocity profiles are curved in the case of pipe with non-slip conditions, due to the wall shear, resulting in non-null spatial deviations. Moreover, it can be seen that in small pipes, the profile is curvier, and consequently, the spatial deviation is more significant on average. As a consequence, the geometry has an impact on the spatial deviation, and so, on the dispersion term $\langle \delta\overline{\underline{v}}\delta\overline{\underline{v}} \rangle$.

Moreover, in two-phase flows, the void fraction can impact the velocity profile and, therefore, the dispersion term. Finally, multiple variables can influence the averaged velocity, such as the averaged velocity, the wall heat flux, the pressure, etc. These turbulence and dispersion terms are treated differently by macroscopic codes, some of them neglect these terms, while others try to model them.

Models and assumptions in macroscopic codes

In the existing macroscopic codes for nuclear applications, these dispersion-turbulence terms are often neglected, even though some codes propose an option to take these terms into account. The codes SPACE (Ha et al., 2011) and TRACE (Bajorek, 2008) neglect these terms in all situations. The codes ATHLET (Lerchl et al., 2019) and MARS-KS (Jeong et al., 1999) optionally allow for the consideration of the turbulent term by algebraic models but do not consider the dispersion term.

In contrast, the CATHARE code (Valette, 2012) proposes an option to take into account both turbulence $\tilde{\nu}_{tk}$ and dispersion $\tilde{\nu}_{dk}$ terms simultaneously, based on the work of Teruel and Rizwan-uddin (2009) which has been done by an up-scaling method. A description of this model is given in Appendix IV. Regarding the enthalpy dispersion and turbulence terms, the SPACE, TRACE, and ATHLET codes neglect the turbulence-dispersion heat terms. The code MARS-KS proposes an algebraic model for the turbulent thermal mixing term and neglects the dispersion term. In the 3-D module of CATHARE, a model is proposed to consider both the turbulent and dispersion heat terms. This model is described in Appendix IV. Finally, in chapter 15 of the book written by Ishii and Hibiki (2011), a correlation is proposed for the momentum dispersion term, which will be evaluated in chapter 3, section 3.2.2. Therefore, few macroscopic codes propose options to model the turbulent terms, and only CATHARE proposes an option to model the dispersion term. However, no quantitative values are given for these terms in turbulent flows representative of nuclear reactor cores, either for transient or developed flows.

> **Note:** A recent report made by the Nuclear Energy Agency (NEA) on the status of simulation capability of 3D system-scale Codes (NEA, 2024) states on the turbulent-diffusion terms that 'it would be better to quantify such terms than qualitatively neglecting them'.

Discussions

Therefore, several studies have been carried out to model the subgrid terms at the macroscopic scale by an up-scaling method on academic test cases. Also, Ishii and Hibiki (2011) have suggested to neglect the energy dispersion term and have proposed a simple correlation to model the momentum dispersion term. However, to the extent of our knowledge, these subgrid terms have never been evaluated on industrial conditions that can be encountered in nuclear reactor cores under different circumstances. This lack of data for these subgrid terms has been highlighted in the report from NEA (2024).

For these reasons, we propose to evaluate the momentum dispersion and turbulence terms, as well as energy dispersion term, in chapter 3 on experiments with flows similar to those encountered in nuclear reactor cores with different geometries. In fact, a priori simulations can be carried out by Neptune_CFD code on sub-cooled boiling flows at high pressure, temperature, and flow rate, and the local variables obtained can be averaged in order to estimate those macroscopic subgrid terms and thus validate or not the hypothesis of neglecting these terms.

1.4 Assessment and Objectives

In this section, the existing up-scaling methods have been described, and it shows that the first step of an up-scaling method is to define the coarse and fine scales, which can be multiples.

The aim of this thesis is to apply an up-scaling method on two-phase flows representative of industrial conditions of nuclear reactor cores subjected to different situations. Since CATHARE is the code used in France to demonstrate the safety of a nuclear reactor under all conditions, this code is chosen at the macroscopic scale. The objective is then to develop a model for this code. Moreover, the Neptune_CFD code is currently the most commonly used code in France in the nuclear field at the RANS scale to simulate two-phase flows. Thus, the up-scaling method is applied in this thesis from the Neptune_CFD code to the CATHARE one. Once the coarse and fine codes are defined, the usual strategy done in literature follows the following steps:

1. Choice of a flow type and geometry
2. Establishment of macroscopic formulation
3. Choice of a phenomenon to model
4. Creation of a local database
5. Homogenize local model
6. Analysis of unknown terms order of magnitude
7. Modeling unknown terms using known variables and optimization constants
8. Constants calibration using local database
9. Evaluation of the new macroscopic modeling on a new database

This strategy is slightly adapted in this thesis since industrial conditions are considered. The adapted strategy used in this thesis is described below.

1. First, it has been said in the introduction that sub-cooled boiling situations are encountered below the boiling crisis for both low- and high-quality flows. This is why the sub-cooled boiling flows are studied in this thesis. Moreover, different geometries are considered to evaluate the influence of the geometry.

2. Chapter 2 aims at establishing a macroscopic formulation from the Neptune_CFD equations. Then, we want to compare the macroscopic formulation obtained to the CATHARE and TRACE formulations in order to identify some assumptions made by these codes.

3. The third step in the usual strategy is to choose a phenomenon to model. Since many different models play a key role in industrial conditions, it is difficult to know in advance which phenomenon to model. This is why, in this study, we will evaluate all the terms of the balance equations using a local database to identify the predominant terms, and then to choose wisely which phenomenon to model.

4. The local CFD database is developed in chapter 3, section 3.1, on sub-cooled boiling conditions with different geometries using the Neptune_CFD code. At this point, two new steps are introduced, which can be found in section 3.2.

∗ This database is first used to evaluate the assumptions done in many macroscopic codes to neglect the turbulence-dispersion terms. Moreover, this evaluation corresponds to a suggestion from the Nuclear Energy Agency (NEA, 2024) to quantify these turbulence-dispersion terms.

∗ Next, this CFD database is used to identify the predominant macroscopic terms in the balance equations in sub-cooled boiling conditions. At the end of the chapter 3, the phenomenon of bubble condensation is identified as predominant.

3 bis. Using the findings of the previous step, step 3, which consists of choosing a phenomenon to model, can now be completed. Indeed, the bubble condensation phenomenon is chosen to be modeled at the macroscopic scale, and a local database has already been developed. However, the database has been developed in sub-cooled boiling conditions, and thus includes many different phenomena that play a key role in the flow behavior. Therefore, the best solution is to create a new CFD database on separate effect experiments in which only bubble condensation plays a key role.

4 bis. Consequently, the chapter 4 is dedicated to the development of a bubble condensation database on a separate effect experiment. In order to get a validated database, a

new modeling with a polydisperse approach is defined. This approach is based on the method of moments with a quadratic bubble size distribution function, and a model to take into account the bubble collapse due to condensation.

5-8. The four next steps consist of developing a new model at the macroscopic scale. These steps can be found in the chapter 5 where we want both to evaluate the current correlations of macroscopic codes and to develop a new model for the bubble condensation. In the same way as the usual strategy described in steps 7 and 8, we want in section 5.3.2 to develop a new model that consists of only macroscopic variables and optimization constants, and then to calibrate these constants using the local database.

9. Finally, a strategy to evaluate the new modeling by an a posteriori method will be proposed in section 5.4.

Remark: This initial strategy is slightly adjusted during this thesis, and the final strategy is summarized in Figure 7 on page 158.

Chapter 2

Establishment of a macroscopic two-fluid model formulation from local Neptune_CFD equations

Contents

From local Neptune_CFD equations, we want to obtain a full macroscopic two-fluid model formulation similar to the existing system (macroscopic) code equations, but which would be more generic and not use any assumption. Indeed, some macroscopic formulations already exist (CATHARE code, TRACE code, Delhaye (1968), Ishii and Hibiki (2011)). Still, they are established using some assumptions, such as constant density in a macroscopic cell or the fact the average of a product is equal to the product of averages. Moreover, as a starting point, they use different local equations from those of Neptune_CFD, which makes the a priori evaluation of macroscopic terms from Neptune_CFD more difficult. The work of this chapter has been published in section 2 of the article Herry et al. (2024b).

Three main methods can be found in the literature to get a macroscopic representation of a porous media from local equations.

The **stochastic methods** are widely used to study natural porous mediums, where the porous medium is highly irregular and cannot be known in detail. These methods consider the studied variables as random functions in space (Renard and De Marsily, 1997). The local quantities are defined as random variables, and the transition to the macroscopic scale is done using a probability-weighted average. The spectral method, perturbation method, field theory, and Monte-Carlo method belong to the stochastic methods. Considering that the geometry of a nuclear reactor can be known in a deterministic way, this method is not so suitable for the present work.

The **homogenized method** (Bensoussan et al., 2011; Tartar, 2009) is by far the most mathematically rigorous, but it is quite challenging to analyze the physical phenomena by this method. This method differs from others in that the spatial average is used only at the end of the analysis. Two space variables are introduced, a fast one X^* and a slow one $\tilde{X}^* = X^*/\epsilon$, ϵ assumed to be small. Then, the variable is decomposed into an asymptotic expansion with respect to ϵ (Pinson, 2006). Subsequently, the various orders of magnitude of ϵ are separated to get different problems, which are generally linked.

The **volume averaging method** has been introduced in 1967 (Whitaker, 1967; Slattery, 1967; Anderson and Jackson, 1967). This method combines the incorporation of a spatial average and an indicator function that distinguishes the solid and fluid phases. The transport equations of different physical quantities are then averaged by this process, and some new unknown terms appear. These terms represent the effect of microscopic phenomena at the macroscopic scale and need to be modeled. This method retains a physical representation of each term and is, therefore, well-suited to the study of turbulent flows.

The main purpose of this work is to study turbulent two-phase flows, so the volume averaging method is the most suitable method to get a macroscopic representation of this flow pattern. In order to use it, some indicator functions and average operators need to be introduced.

2.1 Selection of average operators from the literature

We chose only to introduce space average operators since the Neptune_CFD equations are already statistically averaged. The local statistical-averaged two-fluid model formulation used by Neptune_CFD is extensively described in the section 1.2. Moreover, the operators chosen need to be applicable to two-phase equations.

2.1.1 Spatial average operators definition

The first step in the volume averaging method is to define an averaging volume V, which includes both solid and fluid phases. Using the notation of Ransom (1989), the superficial average over this volume is defined by:

$$\nless \xi \ngtr (x,t) = \frac{1}{V(x)} \int_{V(x)} \xi(y,t) dV(y). \tag{2.1.1}$$

Despite being generic, this average is not well suited to this work. Indeed, the Navier-Stokes equations apply only to the fluid phase, and it is, therefore, more interesting to calculate the average of the fluid phase only. Similarly to the phase indicator function, a fluid indicator function is introduced as follows:

$$\chi_f(x,t) = \begin{cases} 1, \text{ if the fluid is present at x and t} \\ 0, \text{ otherwise.} \end{cases} \tag{2.1.2}$$

The derivatives of the indicator function χ_f are described in the equation 2.1.3, where $\underline{\omega_i}$ is the velocity of the solid interface, $\underline{n}$ is the outgoing normal of the fluid phase, and δ_ω the Dirac function of dimension l^{-1}. The Dirac function is one at the fluid-solid interface and zero elsewhere. In the context of this work, solid structures are static, which means that the time derivative of this function is zero.

$$\frac{\partial \chi_f}{\partial t} = -\underline{\omega}_i.\nabla\chi_f = 0, \quad \nabla\chi_f = -\underline{n}_i\delta_\omega. \tag{2.1.3}$$

The porosity of the medium can be defined as:

$$\Phi = \lessdot \chi_f \gtrdot = V_f/V. \tag{2.1.4}$$

Using these definitions, the intrinsic average $\langle . \rangle$, which is an average over the fluid volume V_f included in V, is defined in equation 2.1.5. Its spatial deviation δ_i is also defined similarly to the fluctuation of the statistical average.

$$\langle \xi \rangle(x,t) = \frac{\lessdot \chi_f \xi \gtrdot}{\lessdot \chi_f \gtrdot} = \frac{1}{V_f(x)} \int_{V_f(x)} \xi dV, \qquad \delta_i \xi = \xi - \langle \xi \rangle. \tag{2.1.5}$$

Moreover, three characteristic length scales are introduced to represent the porous medium:

- The length scale of the averaging volume r_0,
- The length scale of the local quantities variations l_ξ:

$$O\left(\frac{1}{l_\xi}\right) = \frac{1}{\xi}\|\nabla\xi\|, \tag{2.1.6}$$

- The length scale of the macroscopic quantities variations L_ξ:

$$O\left(\frac{1}{L_\xi}\right) = \frac{1}{\langle\xi\rangle}\|\nabla\langle\xi\rangle\|. \tag{2.1.7}$$

A representation of the length scales for ordered and disordered porous medium is shown in Figure 2.1.1. The averaging volume V must satisfy some length scale constraints; it needs to include plenty of pores ($r_0 >> l_\xi$) for a disordered porous medium and can be an elementary pattern of the solid matrix for ordered porous media ($r_0 \approx l_\xi$). The spatially averaged equations are generally considered valid when the length-scale constraints mentioned are satisfied (Quintard and Whitaker, 1994; Sanchez-Palencia, 1980; Whitaker, 1969).

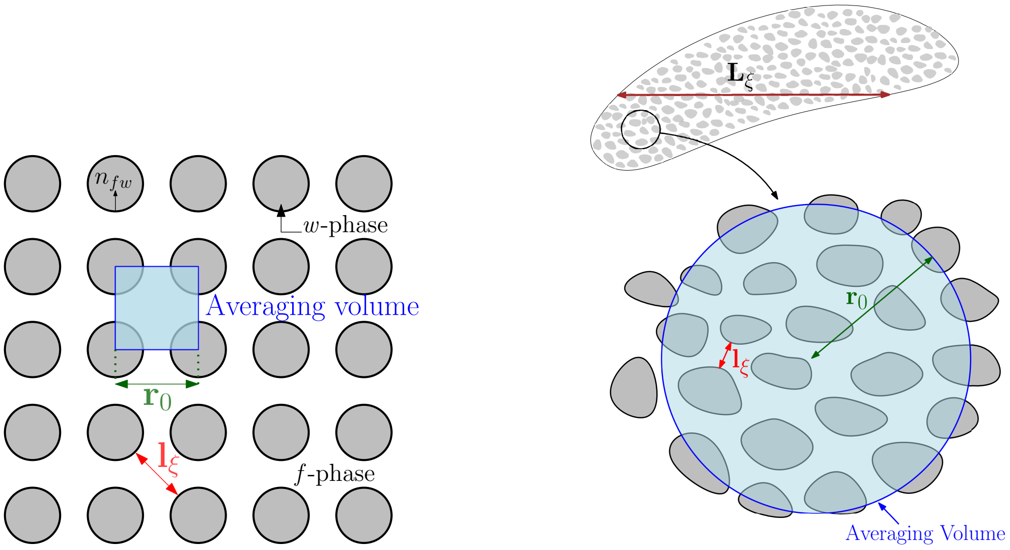

(a) Ordered porous media (b) Disordered porous media

Figure 2.1.1: Characteristic length scales of porous media.

However, it is necessary to study the properties of this intrinsic spatial average operator, especially to investigate if this operator has the three properties known as the Reynolds axioms.

2.1.2 Spatial average operators properties

The Reynolds axioms are the linearity, the idempotency, and the commutativity between the derivatives and the spatial average.

Linearity The linearity of the intrinsic average operator comes from the linearity of the continuous summation of a bounded interval.

Idempotency The spatial filter is not always idempotent. The double average is written as:

$$\Phi\langle\langle\xi\rangle\rangle(x) = \frac{1}{V}\int_{V(x)} \langle\xi\rangle(r)\chi_f(r)dV_r. \tag{2.1.8}$$

We define $r = x + y$. The Taylor development of the quantity $\langle\xi\rangle$ around r is:

$$\langle\xi\rangle(x+y) = \langle\xi\rangle(x) + y.\nabla\langle\xi\rangle(x) + \frac{1}{2}y \circledast y : \nabla\nabla\langle\xi\rangle(x) + O\left(\|y\|^2\right). \tag{2.1.9}$$

The filter operator is applied a second time:

$$\Phi\langle\langle\xi\rangle\rangle(x+y) = \langle\chi_f\rangle\langle\xi\rangle(x) + \langle y\chi_f\rangle.\nabla\langle\xi\rangle(x) + \frac{1}{2}\langle y \circledast y\chi_f\rangle : \nabla\nabla\langle\xi\rangle(x) + O\left(\|y\|^2\right). \tag{2.1.10}$$

By definition, y is bounded by the filter length r_0. Therefore, using the characteristic length scales (2.1.6), (2.1.7):

$$\langle y\chi_f\rangle.\nabla\langle\xi\rangle(x) = 0\left(\frac{r_0}{L_\xi}\Phi\right)\langle\xi\rangle(x), \tag{2.1.11}$$

$$\frac{1}{2}\langle y \circledast y\chi_f\rangle : \nabla\nabla\langle\xi\rangle(x) = 0\left(\frac{r_0^2}{L_\xi^2}\Phi\right)\langle\xi\rangle(x). \tag{2.1.12}$$

Then, the intrinsic average operator can be considered as idempotent when the two last terms are negligible, i.e. when:

$$r_0 << L_\xi. \tag{2.1.13}$$

Therefore, the intrinsic average operator is idempotent if the next conditions on the filter length are fulfilled:

For a ordered porous medium: $l_\xi \approx r_0 << L_\xi$,
For a disordered porous medium: $l_\xi << r_0 << L_\xi$.

Spatial average of derivatives The presence of walls results in the non-commutativity between intrinsic average and derivative operators. Using the divergence theorem, Howes and Whitaker (1985) have demonstrated these rules:

$$\int_{V_f} \nabla\xi dV = \nabla\left[\int_{V_f} \xi dV\right] + \int_{A_{fw}} \underline{n}_w \xi dA, \tag{2.1.14}$$

$$\iff V_f.\underbrace{\frac{1}{V_f}\int_{V_f}\nabla\xi dV}_{\langle\nabla\xi\rangle} = \nabla\left[\frac{V_f}{V}.V.\underbrace{\frac{1}{V_f}\int_{V_f}\xi dV}_{\langle\xi\rangle}\right] + V_f.\underbrace{\frac{1}{V_f}\int_{A_{fw}}\underline{n}_w\xi dA}_{\langle\underline{n}_w\xi\delta_w\rangle}, \tag{2.1.15}$$

$$\iff \Phi\langle\nabla\xi\rangle = \frac{1}{V}\nabla\left(V\Phi\langle\xi\rangle\right) + \Phi\langle\underline{n}_w\xi\delta_w\rangle. \tag{2.1.16}$$

Ransom (1989); Lahey and Drew (1988) have used an arbitrary control volume, and so, did not make any further simplifications. Anyway, some authors (Pinson, 2006; Drouin, 2010; Quintard and Whitaker, 1994) have used control volume which always has the same size; only the porosity may change. On the basis of their work, a constant control volume is taken in this work, and so with this assumption, the last equation becomes:

$$\Phi \langle \nabla \xi \rangle = \nabla \left(\Phi \langle \xi \rangle \right) + \Phi \langle \underline{n}_w \xi \delta_w \rangle. \tag{2.1.17}$$

Using the decomposition defined in equation (2.1.5) and using the idempotency property, one can obtain:

$$\Phi \langle \nabla \xi \rangle = \Phi \nabla \langle \xi \rangle + \Phi \langle \underline{n}_w \delta \xi \delta_w \rangle. \tag{2.1.18}$$

Similarly, the rule about the commutativity of intrinsic average with time derivative operators can be defined:

$$\Phi \left\langle \frac{\partial \xi}{\partial t} \right\rangle = \frac{\partial \Phi \langle \xi \rangle}{\partial t} + \Phi \langle \underline{n}_w \xi \omega_w \delta_w \rangle, \tag{2.1.19}$$

where ω_w is the moving velocity of the wall. In this work, the wall is assumed immobile, so the rule becomes:

$$\Phi \left\langle \frac{\partial \xi}{\partial t} \right\rangle = \frac{\partial \Phi \langle \xi \rangle}{\partial t} = \Phi \frac{\partial \langle \xi \rangle}{\partial t}. \tag{2.1.20}$$

To summarize, the rules about commutativity between intrinsic average and derivative operators are given by:

$$\Phi \langle \nabla \xi \rangle = \nabla \left(\Phi \langle \xi \rangle \right) + \Phi \langle \xi \underline{n}_w \delta_w \rangle = \nabla \left(\Phi \langle \xi \rangle \right) + \frac{1}{V} \int_{A_{fw}} \underline{n}_w \xi dA \tag{2.1.21a}$$

$$\Phi \langle \nabla \xi \rangle = \Phi \nabla \langle \xi \rangle + \Phi \langle \delta \xi \underline{n}_w \delta_w \rangle = \Phi \nabla \langle \xi \rangle + \frac{1}{V} \int_{A_{fw}} \underline{n}_w \delta \xi dA \tag{2.1.21b}$$

$$\Phi \left\langle \frac{\partial \xi}{\partial t} \right\rangle = \Phi \frac{\partial \langle \xi \rangle}{\partial t} \tag{2.1.21c}$$

Therefore, this intrinsic average operator is always linear and is idempotent under the assumption of scale separation between the microscopic and macroscopic variations. In the case of quasi-homogeneous macroscopic flow, this assumption allows us to consider a homogenization volume as small as the subchannel (Bestion, 2012). The derivation rules linked to the intrinsic average operator are summarized in the equations (2.1.21). In order to model two-phase flows, some new operators are introduced using this intrinsic average.

2.1.3 Extension of the spatial average to two-phase flows

Based on the definitions given previously, one can notice that the intrinsic average of the volume fraction α_k of phase k corresponds to the volume of phase k divided by the fluid volume:

$$\langle \alpha_k \rangle = \frac{V_k}{V_f}. \tag{2.1.22}$$

In order to consider the two-phase characteristics of the flow in a good way, some new spatial averages need to be introduced. First, a phasic spatial average is provided:

$$\langle \xi \rangle_k = \frac{\langle \alpha_k \xi \rangle}{\langle \alpha_k \rangle}, \quad \xi = \langle \xi \rangle_k + \delta_k \xi. \tag{2.1.23}$$

Moreover, a phasic mass-weighted average can also be defined similarly:

$$\langle \xi \rangle_{k\rho} = \frac{\langle \alpha_k \rho_k \xi \rangle}{\langle \alpha_k \rho_k \rangle} = \frac{\langle \alpha_k \rho_k \xi \rangle}{\langle \alpha_k \rangle \langle \rho_k \rangle_k} = \frac{\langle \rho_k \xi \rangle_k}{\langle \rho_k \rangle_k}, \quad \xi = \langle \xi \rangle_{k\rho} + \delta_{k\rho} \xi. \tag{2.1.24}$$

> **Remark:** The average operators $\langle . \rangle$, $\langle . \rangle_k$, $\langle . \rangle_{k\rho}$ are used in the following to establish the macroscopic formulation.

For clarity, the spatial deviation linked to the mass-weighted average is named δ in this work instead of $\delta_{k\rho}$.

These average operators are applied to the local Neptune_CFD equations in order to establish a macroscopic two-fluid model.

2.2 Formulation of two-phase macroscopic equations from local Neptune_CFD equations

The aim of this section is to apply the average operators defined in the previous section on the Neptune_CFD two-fluid model formulated in the section 1.2. First, the two-fluid model balance equations of Neptune_CFD are recalled in the equations (2.2.1). It is worth noting that the gravity term in the energy equation is not considered since it was not taken into account in previous versions of Neptune_CFD code and is negligible in the conditions treated in this thesis. For the sake of clarity, mathematical symbols of statistical averaging are dropped in the formulation of the following sections, except those that apply at the interface.

$$\frac{\partial}{\partial t}\left(\alpha_k \rho_k\right) + \nabla(\alpha_k \rho_k . \underline{v}_k) = \Gamma_k \tag{2.2.1a}$$

$$\begin{aligned}\frac{\partial}{\partial t}\left(\alpha_k \rho_k \underline{v}_k\right) + \nabla(\alpha_k \rho_k \underline{v}_k . \underline{v}_k) = {} & \nabla . \left(\alpha_k \underline{\underline{\tau_m}}_k + \underline{\underline{\tau_T}}_k\right) - \alpha_k \nabla p_k + \alpha_k \rho_k \underline{g} + \Gamma_k \underline{v}_k^{Im} + \underline{M}_{ik} \\ & + \left(p_k^I - p_k\right) \nabla \alpha_k - \underline{\underline{\tau_m}}_k^I \nabla \alpha_k ,\end{aligned} \tag{2.2.1b}$$

$$\frac{\partial}{\partial t}\left(\alpha_k \rho_k H_k\right) + \nabla . (\alpha_k \rho_k H_k \underline{v}_k) - \alpha_k \frac{\partial P}{\partial t} = -\nabla . \left[\alpha_k \left(\underline{q_m}_k + \underline{q_T}_k\right)\right] + \underbrace{\Gamma_k H_k^{Ie} + \Pi_k'}_{\Pi_k} + q_{wk} \tag{2.2.1c}$$

2.2.1 Volume average of mass balance equation

Following the work of Pinson (2006), the first step is to multiply the local two-fluid model equations by the indicator function χ_f relative to the fluid phase, defined in (2.1.2). Simultaneously, the superficial volume average operator is applied to the equations:

$$\nless \chi_f \frac{\partial}{\partial t}(\alpha_k \rho_k) \ngtr + \nless \chi_f \nabla(\alpha_k \rho_k . \underline{v}_k) \ngtr = \nless \chi_f \Gamma_k \ngtr . \tag{2.2.2}$$

Using the intrinsic average operator defined in (2.1.5), the assumption of static solid phase and the no-slip condition at solid-fluid interface, the following equation is obtained:

$$\Phi \frac{\partial}{\partial t}\left(\langle \alpha_k \rho_k \rangle\right) + \nabla(\Phi \langle \alpha_k \rho_k . \underline{v}_k \rangle) = \Phi \langle \Gamma_k \rangle \tag{2.2.3}$$

In this equation, there are averages of local variables products $\langle \alpha_k \rho_k \rangle$ and $\langle \alpha_k \rho_k . \underline{v}_k \rangle$, but at a macroscopic scale, only the product of averaged variables can be calculated. To this end, the average operators adapted to two-phase flows introduced in equations (2.1.23) and (2.1.24) are applied. Using them, the equation becomes:

$$\Phi \frac{\partial}{\partial t}\left(\langle \alpha_k \rangle \langle \rho_k \rangle_k\right) + \nabla . \left(\Phi \langle \alpha_k \rangle \langle \rho_k \rangle_k \langle \underline{v}_k \rangle_{k\rho}\right) = \Phi \langle \Gamma_k \rangle . \tag{2.2.4}$$

Thanks to the introduction of average operators relative to two-phase flows, no new terms appear. Some authors (Lee et al., 2009; Bois, 2021) have suggested considering the density of each phase constant on the averaging volume. This assumption is valid as soon as the transverse pressure gradient within a subchannel is relatively small. For the sake of generality, this hypothesis is not formulated in this work.

2.2.2 Volume average of momentum balance equation

By multiplying the local momentum balance equation by the indicator function χ_f and applying the superficial volume average operator, the following equation is obtained:

$$\begin{aligned}&\underbrace{\nless \chi_f \frac{\partial}{\partial t}\left(\alpha_k \rho_k \underline{v}_k\right) \ngtr}_{\mathbf{a}} + \underbrace{\nless \chi_f \nabla(\alpha_k \rho_k \underline{v}_k . \underline{v}_k) \ngtr}_{\mathbf{b}} = \underbrace{\nless \chi_f \nabla . \left(\alpha_k \underline{\underline{\tau_m}}_k + \underline{\underline{\tau_T}}_k\right) \ngtr}_{\mathbf{c}} - \underbrace{\nless \chi_f \alpha_k \nabla P_k \ngtr}_{\mathbf{d}} \\ & + \underbrace{\nless \chi_f \left(p_k^I - P_k\right) \nabla \alpha_k \ngtr}_{\mathbf{e}} + \underbrace{\nless \chi_f \underline{\underline{\tau_m}}_k^I \nabla \alpha_k \ngtr}_{\mathbf{f}} + \underbrace{\nless \chi_f \alpha_k \rho_k \underline{g} \ngtr}_{\mathbf{g}} + \underbrace{\nless \chi_f \left(\Gamma_k \underline{v}_k^{Im} + \underline{M}_{ik}\right) \ngtr}_{\mathbf{h}} .\end{aligned} \tag{2.2.5}$$

The volume average steps of each term will now be detailed. The volume average of the unsteady term comes naturally:

$$\mathbf{a} = \frac{\partial}{\partial t}\left(\Phi\langle\alpha_k\rho_k\underline{v}_k\rangle\right) = \frac{\partial}{\partial t}(\Phi\langle\alpha_k\rangle\langle\rho_k\rangle_k\langle\underline{v}_k\rangle_{k\rho}). \tag{2.2.6}$$

The volume average of the convective term is expressed as:

$$\begin{aligned}\mathbf{b} &= \Phi\left\langle\nabla.(\alpha_k\rho_k\underline{v}_k\underline{v}_k)\right\rangle, &(2.2.7)\\ &= \nabla.\left(\Phi\left\langle\alpha_k\rho_k\underline{v}_k\underline{v}_k\right\rangle\right), &(2.2.8)\\ &= \nabla.\left(\Phi\langle\alpha_k\rangle\langle\rho_k\rangle_k\langle\underline{v}_k\underline{v}_k\rangle_{k\rho}\right). &(2.2.9)\end{aligned}$$

From the volume average of this convective term, a volume average of a product of microscopic quantities is obtained.

> **Remark:** In order to transform an average of product $\langle a.b\rangle$ into a product of average $\langle a\rangle.\langle b\rangle$, the strategy is to split the local variables into a mean value and a spatial deviation: $\langle a.b\rangle = \Big\langle\Big(\langle a\rangle + \delta a\Big).\Big(\langle b\rangle + \delta b\Big)\Big\rangle = \langle a\rangle\langle b\rangle + \langle\delta a\delta b\rangle$.

Therefore, to transform the equation (2.2.9) into a product of macroscopic quantities, the velocity term is divided into a mean value related to the phasic mass-weighted average $\langle\rangle_{k\rho}$ and a spatial deviation, as $v_k = \langle v_k\rangle_{k\rho} + \delta v_k$. This decomposition is applied in equation (2.2.10).

$$\langle\underline{v}_k\underline{v}_k\rangle_{k\rho} = \langle\underline{v}_k\rangle_{k\rho}\langle\underline{v}_k\rangle_{k\rho} + \langle\delta\underline{v}_k\delta\underline{v}_k\rangle_{k\rho}. \tag{2.2.10}$$

Using this decomposition, the volume average of the convective term is expressed as:

$$\mathbf{b} = \nabla.\left[\Phi\langle\alpha_k\rangle\langle\rho_k\rangle_k\langle\underline{v}_k\rangle_{k\rho}\langle\underline{v}_k\rangle_{k\rho}\right] + \nabla.\left[\Phi\langle\alpha_k\rangle\langle\rho_k\rangle_k\langle\delta\underline{v}_k\delta\underline{v}_k\rangle_{k\rho}\right]. \tag{2.2.11}$$

The last term of the right-hand side that appears from this decomposition is called the dispersion term and represents the effect of the void and momentum flux profiles on the averaging volume. A quantitative study of this term has been made by Zuber and Findlay (1965) in parallel with the analysis of the drift flux model. Pinson (2006) and Drouin et al. (2010) have provided a macroscopic turbulence model that takes into account both turbulence effects and these dispersion effects for an incompressible single-phase flow. However, in most macroscopic codes, this term is neglected.

The volume average of the viscous and turbulent stress tensors leads to an additional term related to the wall:

$$\begin{aligned}\mathbf{c} =&\Phi\left\langle\nabla.\left(\alpha_k\underline{\underline{\tau_m}}_k + \underline{\underline{\tau_T}}_k\right)\right\rangle &(2.2.12)\\ =&\nabla.\left[\Phi\langle\alpha_k\rangle\left\langle\underline{\underline{\tau_m}}_k\right\rangle_k + \Phi\left\langle\underline{\underline{\tau_T}}_k\right\rangle\right] + \frac{1}{V}\int_{A_w}\alpha_k\underline{\underline{\tau_m}}_k.n_w dA + \underbrace{\frac{1}{V}\int_{A_w}\underline{\underline{\tau_T}}_k.n_w dA}_{\text{=0: no turbulence at wall}} &(2.2.13)\end{aligned}$$

For the pressure term, the approach is similar:

$$\begin{aligned}\mathbf{d} + \mathbf{e} &= \Phi\langle-\alpha_k\nabla p_k - P_k\nabla\alpha_k + p_k^I\nabla\alpha_k\rangle &(2.2.14)\\ &= -\Phi\langle\nabla\alpha_k P_k\rangle + \Phi\langle p_k^I\nabla\alpha_k\rangle &(2.2.15)\\ &= \nabla\left(\Phi\langle\alpha_k\rangle\langle P_k\rangle_k\right) + \frac{1}{V}\int_{A_w}\alpha_k P_k\mathbb{I}.\mathbf{n}_w dA + \Phi\langle p_k^I\nabla\alpha_k\rangle &(2.2.16)\end{aligned}$$

For the gravity term, gas-liquid interfacial shear stress, and drag force term, the average operation is basic:

$$\mathbf{f}\mathbf{+}\mathbf{g}\mathbf{+}\mathbf{h} = \Phi\langle\nabla\alpha_k.\underline{\underline{\tau_m}}_k^I\rangle + \Phi\underline{g}\langle\alpha_k\rangle\langle\rho_k\rangle_k + \Phi\langle\Gamma_k\underline{v}_k^{Im}\rangle + \Phi\langle\underline{M}_{ik}\rangle \tag{2.2.17}$$

By combining all these terms, the macroscopic momentum equation is written as:

$$\begin{aligned}
&\Phi \frac{\partial}{\partial t}(\langle\alpha_k\rangle\langle\rho_k\rangle_k\langle\underline{v}_k\rangle_{k\rho}) + \underbrace{\nabla.\left(\Phi\langle\alpha_k\rangle\langle\rho_k\rangle_k\langle\underline{v}_k\rangle_{k\rho}\langle\underline{v}_k\rangle_{k\rho}\right)}_{\text{Convection divergence}} = -\underbrace{\nabla.\left(\Phi\langle\alpha_k\rangle\langle\rho_k\rangle_k\langle\delta\underline{v}_k\delta\underline{v}_k\rangle_{k\rho}\right)}_{\text{Dispersion divergence}} \\
&\quad - \underbrace{\langle\alpha_k\rangle\nabla\left(\Phi\langle P\rangle_k\right)}_{\text{Pressure gradient}} + \underbrace{\nabla.\left[\Phi\left(\langle\alpha_k\rangle\left\langle\underline{\underline{\tau_m}}_k\right\rangle_k + \left\langle\underline{\underline{\tau_T}}_k\right\rangle\right)\right]}_{\text{Diffusion (Laminar + Turbulent)}} + \underbrace{\frac{1}{V}\int_{A_w}(-P\mathbb{I}+\underline{\underline{\tau_m}}_k).\underline{n}_w dA}_{=M^w;\quad \text{Wall contribution}} \\
&\quad + \underbrace{\Phi\langle\alpha_k\rangle\langle\rho_k\rangle_k\underline{g}}_{\text{Gravity}} + \underbrace{\Phi\langle\Gamma_k\underline{\overline{v}}_k^{Im}\rangle + \underbrace{\Phi\langle\underline{M}_{ik}\rangle + \Phi\left(\langle P_k\rangle_k\nabla\langle\alpha_k\rangle - \langle\overline{p}_k^I\nabla\alpha_k\rangle\right) + \Phi\langle\overline{\underline{\underline{\tau_m}}}_k^I.\nabla\alpha_k\rangle}_{=\Phi\langle\underline{M}_k\rangle;\text{Interfacial transfer, part independent of mass transfer}}}_{=\Phi\langle\underline{I}_k\rangle;\quad \text{Interfacial momentum transfer}} .
\end{aligned} \tag{2.2.18}$$

Using the mass balance equation, the momentum equation can also be written in non-conservative form:

$$\begin{aligned}
&\Phi\langle\alpha_k\rangle\langle\rho_k\rangle_k\left[\frac{\partial}{\partial t}\langle\underline{v}_k\rangle_{k\rho} + \langle\underline{v}_k\rangle_{k\rho}\nabla.\langle\underline{v}_k\rangle_{k\rho}\right] = -\nabla.\left(\Phi\langle\alpha_k\rangle\langle\rho_k\rangle_k\langle\delta\underline{v}_k\delta\underline{v}_k\rangle_{k\rho}\right) - \langle\alpha_k\rangle\nabla\left(\Phi\langle P\rangle_k\right) \\
&+ \nabla.\left[\Phi\left(\langle\alpha_k\rangle\left\langle\underline{\underline{\tau_m}}_k\right\rangle_k + \left\langle\underline{\underline{\tau_T}}_k\right\rangle\right)\right] + \frac{1}{V}\int_{A_w}\alpha_k(-P\mathbb{I}+\underline{\underline{\tau_m}}_k).\mathbf{n}_w dA + \Phi\langle\alpha_k\rangle\langle\rho_k\rangle_k\underline{g} \\
&+ \Phi\left[\langle\Gamma_k\underline{\overline{v}}_k^{Im}\rangle - \langle\Gamma_k\rangle\langle\underline{v}_k\rangle_{k\rho}\right] + \Phi\langle\underline{M}_k\rangle.
\end{aligned} \tag{2.2.19}$$

2.2.3 Volume average of energy balance equation

The volume average operation of the local energy balance equation is written as:

$$\begin{aligned}
\lessdot\chi_f\frac{\partial}{\partial t}(\alpha_k\rho_k H_k)\gtrdot + \lessdot\chi_f\nabla.(\alpha_k\rho_k H_k\underline{v}_k)\gtrdot - \lessdot\chi_f\alpha_k\frac{\partial P}{\partial t}\gtrdot = -\lessdot\chi_f\nabla.\left[\alpha_k\left(\underline{q_m}_k + \underline{q_T}_k\right)\right]\gtrdot \\
+ \lessdot\chi_f\Gamma_k\overline{H}_k^{Ie}\gtrdot + \lessdot\chi_f\Pi'_k\gtrdot + \lessdot\chi_f q_{wk}\gtrdot .
\end{aligned} \tag{2.2.20}$$

Using the same rules as those used in the previous sections, this equation becomes:

$$\begin{aligned}
&\Phi\frac{\partial}{\partial t}\left(\langle\alpha_k\rangle\langle\rho_k\rangle_k\langle H_k\rangle_{k\rho}\right) + \nabla.\Phi\left(\langle\alpha_k\rangle\langle\rho_k\rangle_k\langle H_k\rangle_{k\rho}\langle\underline{v}_k\rangle_{k\rho}\right) - \Phi\langle\alpha_k\rangle\frac{\partial\langle P\rangle_k}{\partial t} = \Phi\langle\Pi'_k\rangle + \Phi\langle\Gamma_k H_k^{Ie}\rangle \\
&- \nabla.\Phi\left(\langle\alpha_k\rangle\langle\rho_k\rangle_k\langle\delta H_k\delta\underline{v}_k\rangle_{k\rho}\right) - \nabla.\Phi\left[\langle\alpha_k\rangle\left\langle\left(\underline{q_m}_k + \underline{q_T}_k\right)\right\rangle_k\right] - \frac{1}{V}\int_{A_w}\alpha_k(\underline{q_m}_k + \underline{q_T}_k).\mathbf{n}_w dA
\end{aligned} \tag{2.2.21}$$

In Neptune_CFD, the conductive thermal flux $(\underline{q_m}_k + \underline{q_T}_k)$ is calculated by:

$$\underline{q_m}_k + \underline{q_T}_k = -\lambda_k\nabla T_k \tag{2.2.22}$$

Assuming that the thermal conductivity λ_k varies only slightly in the control volume ($\langle\lambda_k\rangle = \lambda_k$), the conductive thermal flux term and the wall term can be expressed as:

$$-\nabla.\Phi\left[\langle\alpha_k\rangle\left\langle\left(\underline{q_m}_k + \underline{q_T}_k\right)\right\rangle_k\right] - \frac{1}{V}\int_{A_w}\alpha_k(\underline{q_m}_k + \underline{q_T}_k).\mathbf{n}_w dA \tag{2.2.23}$$

$$= \nabla.\left[\langle\alpha_k\rangle\lambda_k\Phi\left\langle\nabla T_k\right\rangle_k\right] + \frac{1}{V}\int_{A_w}\alpha_k\lambda_k\nabla T_k.\mathbf{n}_w dA \tag{2.2.24}$$

$$= \nabla.\left[\langle\alpha_k\rangle\lambda_k\Phi\nabla\left\langle T_k\right\rangle_k\right] + \underbrace{\nabla.\left[\langle\alpha_k\rangle\lambda_k\frac{1}{V}\int_{A_{kw}}\delta T_k.\mathbf{n}_w dA\right]}_{\text{Tortuosity term}} + \underbrace{\frac{1}{V}\int_{A_w}\alpha_k\lambda_k\nabla T_k.\mathbf{n}_w dA}_{\text{Thermal heat flux at wall}} \tag{2.2.25}$$

Moreover, Drouin et al. (2010) have proven that all components of tortuosity tensor are zero in parallel flow, which is the case in all the simulations done in this work. As a result of this study, the tortuosity tensor is neglected in this work.

Therefore, the final form of the statistical-volume averaged energy equation is :

$$\Phi\frac{\partial}{\partial t}\left(\langle\alpha_k\rangle\langle\rho_k\rangle_k\langle H_k\rangle_{k\rho}\right)+\underbrace{\nabla.(\Phi\langle\alpha_k\rangle\langle\rho_k\rangle_k\langle H_k\rangle_{k\rho}\langle\underline{v}_k\rangle_{k\rho})}_{\text{Convection divergence}}-\Phi\langle\alpha_k\rangle\frac{\partial\langle P\rangle_k}{\partial t}=\underbrace{\nabla.[\langle\alpha_k\rangle\lambda_k\Phi\nabla\left\langle T_k\right\rangle_k]}_{\text{Conductive flux}}$$
$$-\underbrace{\nabla.(\Phi\langle\alpha_k\rangle\langle\rho_k\rangle_k\langle\delta H_k\delta\underline{v}_k\rangle_{k\rho})}_{\text{Dispersion divergence}}\underbrace{\frac{1}{V}\int_{A_w}\alpha_k\lambda_k\nabla T_k.\mathbf{n}_w dA}_{=q_{kw};\quad\text{Wall heat flux}}+\underbrace{\Phi\langle\Gamma_k\overline{H}_k^{Ie}\rangle+\Phi\langle\Pi_k'\rangle}_{=\langle\Pi_k\rangle;\text{ Interfacial term}}. \tag{2.2.26}$$

2.2.4 Interfacial jump conditions

The volume-averaged Interfacial Jump Conditions (IJC), already existing at the local scale, come naturally with the application of the volume average:

Volumetric continuity: $$\sum_{k=g,l}\langle\alpha_k\rangle=1, \tag{2.2.27}$$

Mass interface jump condition: $$\sum_{k=g,l}\langle\Gamma_k\rangle=0, \tag{2.2.28}$$

Momentum interface jump condition: $$\sum_{k=g,l}\langle\Gamma_k\underline{v}_k^{Im}\rangle+\langle\underline{M}_k\rangle=0, \tag{2.2.29}$$

Energy interface jump condition: $$\sum_{k=g,l}\langle\Pi_k\rangle=\sum_{k=g,l}\langle\Gamma_k\overline{H}_k^{Ie}\rangle+\langle\Pi_k'\rangle=0. \tag{2.2.30}$$

2.3 Study of the equation system determinism by comparison to existing macroscopic codes

The study of the determinism is mandatory since a new formulation is established in this work, and nothing guarantees a priori the resolvability of the system.

Mathematically, the principle of determinism requires as many equations as there are unknowns. However, Table 2.3.1 shows that the new system of macroscopic equations is insufficient to fully describe the system. Indeed, there are 10 equations, including the balance equations of each phase and the IJC, and 31 unknowns, including 7 dependent variables and 24 auxiliary parameters. Therefore, 21 additional closure relations are required to close the system.

Equations	**DV (No)**	**AP (No)**
Volumetric (1)	$\langle\alpha_k\rangle$ (2)	
Mass (2)	$\langle\underline{v}_k\rangle_{k\rho}$ (2)	$\langle\rho_k\rangle_k$ (2); $\langle\Gamma_k\rangle$ (2); Φ (1)
Momentum (2)	$\langle P\rangle_k$ (1)	$\langle\delta\underline{v}_k\delta\underline{v}_k\rangle_{k\rho}$ (2); $\left\langle\underline{\underline{\tau_T}}_k\right\rangle_k$ (2); $\left\langle\underline{\underline{\tau_m}}_k\right\rangle_k$ (2); $\langle\underline{M}_k\rangle$ (2); $\underline{g}$ (1); M^w (2)
Energy (2)	$\langle H_k\rangle_{k\rho}$ (2)	$\langle\delta H_k\delta\underline{v}_k\rangle_{k\rho}$ (2); $\langle T_k\rangle_k$ (2); $\langle\Pi_k\rangle$ (2); q_{wk} (2)
IJC (3)		
Totals (10)	(7)	(24)

Table 2.3.1: Summary of the number (No) of Dependant Variables (DV) and Auxiliary Parameters (AP) for the macroscopic two-fluid model (statistical-volume averaged model).

This section aims to check if accurate closure relations exist in the literature for 21 unknown terms. For this purpose, this new formulation is compared to the existing macroscopic formulations of the TRACE code and the 3-D module of the CATHARE code. This comparison allows us to link the terms of each formulation among themselves and then to identify the different assumptions and modeling choices done in the existing codes. Based on the assumptions and closure laws usually used in these macroscopic codes, the resolvability of this new system is consequently evaluated.

2.3.1 Analysis of differences between the formulation of existing macroscopic codes and the new one

A summary of the new formulation and of both TRACE (Bajorek, 2008) and 3-D module of CATHARE (Bestion, 1990) formulations is first expressed, and then the formulations are compared together. The equations of the 3-D module of CATHARE are described in detail in section 1.3.1, and the equations of TRACE are expressed in the following. In most macroscopic codes, such as CATHARE and TRACE codes, an important hypothesis is made that the volume average of a product is assumed to be equal to the product of volume averages. As a result of this assumption, all variables in the equations are time and volume averaged. In the following equations, the operator $\tilde{(\,)}$ represents the fact that the variable is a time- and volume-averaged variable. Moreover, the superscript n represents the phase number, $n = 0$ corresponds to the liquid phase and $n = 1$ to the gas phase. In the following, the balance equations of the new (N) formulation are compared to those of CATHARE (C) and TRACE (T) codes. In these equations, the variables in black color correspond to the terms known as dependent variables in Table 2.3.1. These terms are directly calculated by macroscopic codes. The variables in blue represent known constant terms, such as porosity or gravity force. The green terms correspond to variables that are calculated from equations of state or constitutive equations. The red terms correspond to variables that need to be modeled by closure laws.

Mass balance equation

$$(N) \quad \Phi\frac{\partial}{\partial t}\left(\langle\alpha_k\rangle\,\langle\rho_k\rangle_k\right) + \nabla.\left(\Phi\langle\alpha_k\rangle\langle\rho_k\rangle_k\langle\underline{v}_k\rangle_{k\rho}\right) = \Phi\langle\Gamma_k\rangle, \tag{2.3.1a}$$

$$(C) \quad \frac{\partial(\Phi\tilde{\alpha_k}\tilde{\rho_k})}{\partial t} + \nabla.\left(\Phi\tilde{\alpha_k}\tilde{\rho_k}\tilde{\underline{v}_k}\right) = (-1)^n\Phi\tilde{\Gamma}, \tag{2.3.1b}$$

$$(T) \quad \frac{\partial(\tilde{\alpha_k}\tilde{\rho_k})}{\partial t} + \nabla.\left(\tilde{\alpha_k}\tilde{\rho_k}\tilde{\underline{v}_k}\right) = (-1)^n\tilde{\Gamma}. \tag{2.3.1c}$$

Momentum balance equation

$$\begin{aligned}(N) \quad & \Phi\frac{\partial}{\partial t}\left(\langle\alpha_k\rangle\langle\rho_k\rangle_k\langle\underline{v}_k\rangle_{k\rho}\right) + \nabla.\left(\Phi\langle\alpha_k\rangle\langle\rho_k\rangle_k\langle\underline{v}_k\rangle_{k\rho}\langle\underline{v}_k\rangle_{k\rho}\right) + \langle\alpha_k\rangle\nabla\left(\Phi\langle P\rangle_k\right) = \Phi\langle\underline{M}_k\rangle \\ & + \Phi\langle\alpha_k\rangle\langle\rho_k\rangle_k\underline{g} + \frac{1}{V}\int_{A_w}\left(-P\mathbb{I} + \underline{\underline{\tau_m}}_k\right).\underline{n}_w dA + \Phi\langle\Gamma_k\underline{v}_k^{Im}\rangle \\ & - \nabla.\left(\Phi\langle\alpha_k\rangle\langle\rho_k\rangle_k\langle\delta\underline{v}_k\delta\underline{v}_k\rangle_{k\rho}\right) + \nabla.\Big[\Phi\left(\langle\alpha_k\rangle\left\langle\underline{\underline{\tau_m}}_k\right\rangle_k + \left\langle\underline{\underline{\tau_T}}_k\right\rangle\right)\Big],\end{aligned} \tag{2.3.2a}$$

$$\begin{aligned}(C) \quad & \Phi\frac{\partial(\tilde{\alpha_k}\tilde{\rho_k}\tilde{\underline{v}_k})}{\partial t} + \nabla.\left(\Phi\tilde{\alpha_k}\tilde{\rho_k}\tilde{\underline{v}_k}\tilde{\underline{v}_k}\right) + \Phi\tilde{\alpha_k}\nabla\tilde{P} + \Phi P_i\nabla\tilde{\alpha_k} = \Phi(-1)^n\tilde{\underline{\tau}_i} + \Phi\tilde{\alpha_k}\tilde{\rho_k}\tilde{\underline{g}} \\ & - \Phi\frac{2}{D_h}\tilde{\rho_k}C_k\tilde{\underline{v}_k}|\tilde{\underline{v}_k}| - \Phi\frac{K}{2\Delta\underline{X}}\tilde{\alpha_k}\tilde{\rho_k}\tilde{\underline{v}_k}|\tilde{\underline{v}_k}| + \Phi(-1)^n\tilde{\Gamma}\tilde{\underline{v}_i} \\ & + \nabla.\left[\left(\tilde{\nu}_{tk}^{\Phi} + \tilde{\nu}_{dk}^{\Phi}\right)\left(\underline{\nabla}(\Phi\tilde{\underline{v}_k}) + \underline{\nabla}^T(\Phi\tilde{\underline{v}_k}) - \frac{2}{3}\underline{\nabla}.(\Phi\tilde{\underline{v}_k})\underline{\underline{\mathbb{I}}}\right)\right],\end{aligned} \tag{2.3.2b}$$

$$(T) \quad \frac{\partial(\tilde{\alpha_k}\tilde{\rho_k}\tilde{\underline{v}_k})}{\partial t} + \nabla.\left(\tilde{\alpha_k}\tilde{\rho_k}\tilde{\underline{v}_k}\tilde{\underline{v}_k}\right) + \tilde{\alpha_k}\nabla\tilde{P} = (-1)^n\tilde{\underline{f}_i} + \tilde{\alpha_k}\tilde{\rho_k}\tilde{\underline{g}} + \tilde{\underline{f}_{wk}} + (-1)^n\tilde{\Gamma}\tilde{\underline{v}_i}. \tag{2.3.2c}$$

Energy balance equation

$$
\begin{aligned}
(N)\quad & \Phi\frac{\partial}{\partial t}\left(\langle\alpha_k\rangle\langle\rho_k\rangle_k\langle H_k\rangle_{k\rho}\right)+\nabla.\left(\Phi\langle\alpha_k\rangle\langle\rho_k\rangle_k\langle H_k\rangle_{k\rho}\langle\underline{v}_k\rangle_{k\rho}\right)-\Phi\langle\alpha_k\rangle\frac{\partial\langle P\rangle_k}{\partial t}=\Phi\langle\Pi_k'\rangle \\
& +\frac{1}{V}\int_{A_w}\alpha_k\lambda_k\nabla T_k.\mathbf{n}_w dA+\Phi\langle\Gamma_k\overline{H}_k^{Ie}\rangle-\nabla.\left(\Phi\langle\alpha_k\rangle\langle\rho_k\rangle_k\langle\delta H_k\delta\underline{v}_k\rangle_{k\rho}\right) \qquad (2.3.3a)\\
& +\nabla.[\langle\alpha_k\rangle\lambda_k\Phi\nabla\langle T_k\rangle_k],
\end{aligned}
$$

$$
\begin{aligned}
(C)\quad & \frac{\partial(\Phi\tilde{\alpha}_k\tilde{\rho}_k\tilde{H}_k)}{\partial t}+\nabla.\left(\Phi\tilde{\alpha}_k\tilde{\rho}_k\tilde{H}_k\tilde{\underline{v}}_k\right)-\Phi\tilde{\alpha}_k\frac{\partial\tilde{P}}{\partial t}=\Phi\widetilde{q_{ik}}+\chi_c\widetilde{q_{wk}}+\Phi(-1)^n\tilde{\Gamma}\tilde{H}_k \qquad (2.3.3b)\\
& +\nabla.\left(\tilde{\alpha}_k\underline{q}_k^T\right),
\end{aligned}
$$

$$
\begin{aligned}
(T)\quad & \frac{\partial(\tilde{\alpha}_k\tilde{\rho}_k\tilde{H}_k)}{\partial t}+\nabla.\left(\tilde{\alpha}_k\tilde{\rho}_k\tilde{H}_k\tilde{\underline{v}}_k\right)-\tilde{\alpha}_k\frac{\partial P}{\partial t}=\widetilde{q_{ik}}+\widetilde{q_{wk}}+\widetilde{q_{dk}}+(-1)^n\tilde{\Gamma}\tilde{H}_k+\tilde{\alpha}_k\tilde{\rho}_k\tilde{\underline{g}}.\tilde{\underline{v}}_k\\
& \qquad +\left[(-1)^k\underline{\tilde{f}}_i+\widetilde{\underline{f}_{wk}}\right].\tilde{\underline{v}}_k. \qquad (2.3.3c)
\end{aligned}
$$

In order to be able to compare the formulation developed in this chapter and the formulations of the existing codes, some assumptions on the notations of the primary variables need to be made and are described below:

$$
\begin{aligned}
\tilde{\alpha}_k &= \langle\alpha_k\rangle,\\
\tilde{\rho}_k &= \langle\rho_k\rangle_k,\\
\tilde{\underline{v}}_k &= \langle\underline{v}_k\rangle_{k\rho},\\
\tilde{H}_k &= \langle H_k\rangle_{k\rho},\\
\tilde{P} &= \langle P\rangle_k.
\end{aligned}
$$

Using these notations, Table 2.3.2 shows a comparison between the different terms of the formulation developed in this chapter and those already existing.

> **Remark:** In the following chapter, this comparison will allow us to evaluate the terms of existing codes based on an average of the variables generated by CFD simulations. This is called an a priori evaluation.

Based on Table 2.3.2, it can be seen that the different formulations have some similarities and some discrepancies. First, the porosity term is not present in the TRACE formulation, but it is present in both the new and CATHARE 3-D module formulations. Since the porosity is constant axially in the test cases studied in this thesis, the porosity term can be simplified in this study. Therefore, there are no differences whether the porosity is taken into account or not. An important difference in these formulations is that the dispersion and diffusion terms are missing in TRACE, but are modeled in the 3-D module of CATHARE. These models are described in section 1.3.3 and expressed in detail in Appendix IV. Moreover, in the energy conservation equation, the gravity term and the energy coming from interfacial forces are not present in this new formulation since they are already neglected in the RANS formulation given in equations 2.2.1. An interfacial pressure term is present in the CATHARE momentum equation, but in the case of non-stratified flows, this term is simply chosen to provide the hyperbolicity of the system (Bestion, 1990).

The two next sections describe the closure relations for the auxiliary parameters presented in Table 2.3.1 usually postulated in macroscopic codes, and in particular in CATHARE and TRACE codes. The physical laws of the TRACE code are described in detail by Bajorek (2008), and those of the CATHARE code are described by Bestion (1990). The next one focuses on the existing closure relations in the mass and energy equations.

New Formulation	**TRACE**	**CATHARE-3D**
Porosity		
Φ	\	Φ
Mass conservation equation		
Interfacial mass transfer		
$\langle\Gamma_k\rangle$	$(-1)^n\tilde{\Gamma}$	$(-1)^n\tilde{\Gamma}$
Momentum conservation equation		
Convection term		
$\nabla.\,(\Phi\langle\alpha_k\rangle\langle\rho_k\rangle_k\langle\underline{v}_k\rangle_{k\rho}\langle\underline{v}_k\rangle_{k\rho})$	$\nabla.\,(\tilde{\alpha_k}\tilde{\rho_k}\underline{\tilde{v}_k}\underline{\tilde{v}_k})$	$\nabla.\,(\Phi\tilde{\alpha_k}\tilde{\rho_k}\underline{\tilde{v}_k}\underline{\tilde{v}_k})$
Pressure term		
$\langle\alpha_k\rangle\nabla(\Phi\langle P\rangle_k)$	$\tilde{\alpha_k}\nabla(\tilde{P})$	$\Phi\tilde{\alpha_k}\nabla(\tilde{P})+\Phi P_i\nabla(\tilde{\alpha_k})$
Dispersion term		
$\nabla.\,(\Phi\langle\alpha_k\rangle\langle\rho_k\rangle_k\langle\delta\underline{v}_k\delta\underline{v}_k\rangle_{k\rho})$	\	$\nabla.\Big[\tilde{\nu}_{dk}^{\Phi}\Big(\underline{\nabla}(\Phi\underline{\tilde{v}}_k)+\underline{\nabla}^T(\Phi\underline{\tilde{v}}_k)-\frac{2}{3}\underline{\nabla}.(\Phi\underline{\tilde{v}}_k)\underline{\underline{\mathbb{I}}}\Big)\Big]$
Diffusion term		
$\nabla.\Big[\Phi\left(\langle\alpha_k\rangle\left\langle\underline{\underline{\tau_m}}_k\right\rangle_k+\left\langle\underline{\underline{\tau_T}}_k\right\rangle\right)\Big]$	\	$\nabla.\Big[\tilde{\nu}_{tk}^{\Phi}\Big(\underline{\nabla}(\Phi\underline{\tilde{v}}_k)+\underline{\nabla}^T(\Phi\underline{\tilde{v}}_k)-\frac{2}{3}\underline{\nabla}.(\Phi\underline{\tilde{v}}_k)\underline{\underline{\mathbb{I}}}\Big)\Big]$
Wall contribution		
$\frac{1}{V}\int_{A_w}(-P\mathbb{I}+\underline{\underline{\tau_m}}_k).\underline{n}_w dA$	$\underline{f}_{wk}^{\tilde{}}$	$\Phi\frac{2}{D_h}\tilde{\rho}_k C_k\underline{\tilde{v}}_k\lvert\underline{\tilde{v}}_k\rvert+$ $\Phi\frac{K}{2\Delta\underline{X}}\tilde{\alpha_k}\tilde{\rho_k}\underline{\tilde{v}}_k\lvert\underline{\tilde{v}}_k\rvert$
Gravity term		
$\Phi\langle\alpha_k\rangle\langle\rho_k\rangle_k\langle\underline{g}\rangle$	$\tilde{\alpha_k}\tilde{\rho_k}\underline{\tilde{g}}$	$\Phi\tilde{\alpha_k}\tilde{\rho_k}\underline{\tilde{g}}$
Interfacial momentum transfer		
$\Phi\langle\Gamma_k\underline{\overline{v}}_k^{Im}\rangle+\Phi\langle\underline{M_k}\rangle$	$(-1)^n\underline{\tilde{f}}_i+(-1)^n\tilde{\Gamma}\underline{\tilde{v}}_i$	$\Phi(-1)^n\underline{\tilde{\tau}}_i+\Phi(-1)^n\tilde{\Gamma}\underline{\tilde{v}}_i$
Energy conservation equation		
Convection term		
$\nabla.(\Phi\langle\alpha_k\rangle\langle\rho_k\rangle_k\langle H_k\rangle_{k\rho}\langle\underline{v}_k\rangle_{k\rho})$	$\nabla.\left(\tilde{\alpha_k}\tilde{\rho_k}\tilde{H}_k\underline{\tilde{v}_k}\right)$	$\nabla.\left(\Phi\tilde{\alpha_k}\tilde{\rho_k}\tilde{H}_k\underline{\tilde{v}_k}\right)$
Dispersion + Diffusion term		
$\nabla.(\Phi\langle\alpha_k\rangle\langle\rho_k\rangle_k\langle\delta H_k\delta\underline{v}_k\rangle_{k\rho})+$ $\nabla.[\langle\alpha_k\rangle\lambda_k\Phi\nabla\left\langle T_k\right\rangle_k]$	\	$\nabla.\left(\tilde{\alpha_k}\underline{q}_k^T\right)$
Wall heat flux		
$\frac{1}{V}\int_{A_w}\alpha_k\lambda_k\nabla T_k.\mathbf{n}_w dA$	$\tilde{q_{wk}}$	$\chi_c\tilde{q_{wk}}$
Interfacial energy transfers		
$\Phi\langle\Gamma_k\overline{\overline{H}}_k^{Ie}\rangle+\Phi\langle\Pi_k'\rangle$	$\tilde{q_{ik}}+\tilde{q_{dk}}+(-1)^n\tilde{\Gamma}\tilde{H}_k$	$\Phi\tilde{q_{ik}}+\Phi(-1)^n\tilde{\Gamma}\tilde{H}_k$
Gravity term		
\	$\tilde{\alpha_k}\tilde{\rho_k}\underline{\tilde{g}}.\underline{\tilde{v}_k}$	\
Energy from interfacial forces		
\	$\Big[(-1)^k\underline{\tilde{f}}_i+\underline{f}_{wk}^{\tilde{}}\Big].\underline{\tilde{v}_k}$	\

Table 2.3.2: Comparison of macroscopic terms.

2.3.2 Existing closure relations in mass and energy equations

Equations of state

In mass and energy equations, for each phase, some variables can be calculated from equations of state. This is the case of the averaged temperature in the energy balance equation and density in the mass balance equation:

$$\langle T_k \rangle_k = \langle T_k \rangle_k \Big(\langle H_k \rangle_k, \langle P \rangle_k \Big); \quad \langle \rho_k \rangle_k = \langle \rho_k \rangle_k \Big(\langle T_k \rangle_k, \langle P \rangle_k \Big). \tag{2.3.4}$$

Interfacial heat and mass transfer model

Then, the mass (2.2.29) and energy (2.2.30) interfacial jump conditions allow to link the interfacial mass and energy transfers of each phase:

$$\langle \Gamma_l \rangle = -\langle \Gamma_g \rangle \text{ with } \langle \Gamma_l \rangle = \langle \Gamma_l^c \rangle + \langle \Gamma_l^{nuc} \rangle; \quad \langle \Pi_l \rangle = -\langle \Pi_g \rangle. \tag{2.3.5}$$

Γ_l^c is the interfacial mass transfer from the gas phase to the liquid one (bulk transfer), Γ_l^{nuc} represents the mass transfer contribution to phase k induced by wall nucleate boiling and verify:

- $\langle \Gamma_l^{nuc} \rangle + \langle \Gamma_g^{nuc} \rangle = 0$,
- $\langle \Gamma_l^{nuc} \rangle \leq 0$ since steam is produced by nucleation.

Moreover, the interfacial heat transfer between two phases can be divided into two contributions, as it can be seen in the equation (2.2.26):

$$\langle \Pi_k \rangle = \langle \Gamma_k^c H_k \rangle + \langle \Pi_k' \rangle. \tag{2.3.6}$$

Most of the system codes in the nuclear industry, such as the TRACE code (Bajorek, 2008), rewrite the last equation as: $\langle \Pi_k \rangle = \langle \Gamma_k^c \rangle \langle H_k \rangle + \langle \Pi_k' \rangle$, which, using the interfacial jump condition, leads to:

$$\langle \Gamma_k^c \rangle = \frac{\langle \Pi_l' \rangle + \langle \Pi_g' \rangle}{\langle H_g \rangle - \langle H_l \rangle}. \tag{2.3.7}$$

Both heat and mass interfacial transfer terms are then linked, and for each phase, closure models are needed for Π_k', which is the part independent of the mass transfer of the heat transfer rate contributions. The empirical correlation presented by Ranz and Marshall (1952) is often used for the liquid to interface heat transfer term, such as in the TRACE code. In the 3-D module of CATHARE code (Bestion, 1990), the empirical approach developed by Shah (1979) is used and described in detail in section 5.2. The gas to interface heat transfer is usually modeled by a classical laminar forced convection heat transfer (Bestion, 1990). Usually, in sub-cooled boiling conditions, the gas temperature is typically close to saturation; therefore, the liquid to interface heat transfer is predominant compared to the gas to interface one.

Wall heat transfer model

Usually, system codes in the nuclear industry use wall heat transfer models dependent on the flow regime. For sub-cooled nucleate boiling, the wall heat flux q_{wk} is divided into a part related to forced convection q_c, a second one related to the vapor generation q_e (Bajorek, 2008; Bestion, 1990), and sometimes, to a third term related to the quenching phenomena q_q (Kurul and Podowski, 1990).

Diffusion and dispersion term

In several nuclear systems codes such as TRACE (Bajorek, 2008), SPACE (Ha et al., 2011), and ATHLET (Lerchl et al., 2019), the dispersion term is neglected by making the assumption that the volume average of a product is equal to the product of volume averages. The 3-D module of the CATHARE code proposes an option to model these terms, which is described in section 1.3.3 and expressed in detail in Appendix IV. Moreover, Ishii and Mishima (1984) have supported the fact that this energy dispersion term can be neglected. However, no quantitative values are given for these terms in turbulent flows representative of nuclear reactor cores, either for transient or developed flows.

2.3.3 Existing closure relations in momentum equation

Mechanical constitutive equation for viscous stress $\left\langle \underline{\underline{\tau_{m}}}_k \right\rangle_k$

The viscous shear stresses are sometimes neglected in the field equations (Bajorek, 2008) or calculated from the mechanical constitutive equations as:

$$\left\langle \underline{\underline{\tau_{m}}}_k \right\rangle_k = \mu_k \langle \alpha_k \rangle \langle \rho_k \rangle_k \left(\nabla \langle \underline{v}_k \rangle_{k\rho} + \nabla^T \langle \underline{v}_k \rangle_{k\rho} - \frac{2}{3} \nabla . \langle \underline{v}_k \rangle_{k\rho} \underline{\underline{\mathbb{1}}} \right). \tag{2.3.8}$$

Frictional pressure losses M^w

The frictional pressure losses can be divided into two terms: singular friction and regular wall friction. The first term accounts for geometry-specific pressure losses, such as elbow or tee, while the second one corresponds to the friction between the fluid and the wall. In the 3-D module of CATHARE, these terms are modeled as Bestion (1990):

$$M^w = \underbrace{\Phi \frac{2}{D_h} \tilde{\rho}_k C_k \tilde{\underline{v}}_k |\tilde{\underline{v}}_k|}_{M^w_{regular}} + \underbrace{\Phi \frac{K}{2 \Delta \underline{X}} \tilde{\alpha}_k \tilde{\rho}_k \tilde{\underline{v}}_k |\tilde{\underline{v}}_k|}_{M^w_{singular}}. \tag{2.3.9}$$

The regular friction term is described in detail in Appendix III. The variable K is the singular friction coefficient and depends on the flow configuration and the geometry.

Interfacial momentum transfers

The interfacial momentum transfer term $\langle \underline{M}_k \rangle$ can be divided into a few terms as shown in equation (2.2.18). However, only the drag force model is often considered for bubbly flows since it is the preponderant term of $\langle \underline{M}_k \rangle$. This term is expressed in its general form as:

$$\langle \underline{M}_k \rangle = f_i = a_i \rho_l C_i \langle v_r \rangle^2. \tag{2.3.10}$$

The friction coefficient C_i is usually estimated by empirical correlation depending on the geometry and flow regime (Bajorek, 2008; Bestion, 1990). Moreover, these correlations use the volume averaged relative velocity $\langle v_r \rangle$, and it is important to note that:

$$\langle v_r \rangle \neq \langle v_g \rangle_{g\rho} - \langle v_l \rangle_{l\rho}. \tag{2.3.11}$$

In chapter 15 of Ishii and Hibiki (2011) book, the authors say that the differences between these two relative velocities can be very large. Indeed, in one-dimensional formulation, the term present on the right-hand side represents the slip between two phases and is caused by two completely different effects. The first effect is the local relative motion. The second one is an integral effect of the phase and velocity distributions. It arises due to the spatial average and depends on the local profiles of void fractions and velocities. Ishii and Mishima (1984) have suggested a relationship for the volume-averaged relative velocity in a volume that takes the void fraction distribution into account. This relationship is expressed as:

$$\langle v_r \rangle = \frac{1 - C_0 \langle \alpha_g \rangle}{1 - \langle \alpha \rangle} \langle v_g \rangle_{g\rho} - C_0 \langle v_l \rangle_{l\rho}, \tag{2.3.12}$$

with C_0 the volumetric-flux-distribution parameter of the drift flux model defined by Zuber and Findlay (1965) and described in equation (3.2.8). This approach is used in TRACE code (Bajorek, 2008).

In the CATHARE code, the term $\langle v_r \rangle$ is modeled using a coefficient C_{slip} as:

$$\langle v_r \rangle = \langle v_g \rangle_{g\rho} - C_{slip} \langle v_l \rangle_{l\rho}. \tag{2.3.13}$$

Another way to describe the drag force is to write the volume-averaged relative velocity by introducing the sub-grid drift velocity in addition to the phasic mass-weighted averages of the velocity of each phase (Ozel et al., 2013).

Dispersion and turbulence

The physical meaning, as well as the different models of the subgrid terms of dispersion and turbulence, are described in section 1.3.3. A model exist for these terms in CATHARE and is expressed in Appendix IV. As mentioned in section 1.3.3, to the extent of our knowledge, these subgrid terms have never been evaluated on industrial conditions that can be encountered in a nuclear reactor core under different circumstances.

This is why the momentum dispersion and turbulence terms, as well as energy dispersion term, are evaluated in the chapter 3 on experiments with flows similar to those encountered in nuclear reactor cores with several geometries. In fact, a priori simulations are carried out by Neptune_CFD code, and the local variables obtained are averaged in order to estimate those terms and thus validate or not the hypothesis done by some macroscopic codes to neglect these terms.

2.3.4 Determinism

The closure relations presented in section 2.3.2 and 2.3.3 linked with the IJC allow us to determine all the 24 auxiliary parameters presented in Table 2.3.1. There are still six main equations, namely the mass continuity, momentum, and energy balance equations for each phase and six main variables, the void fraction $\langle \alpha_g \rangle = -\langle \alpha_l \rangle$, mean pressure $\langle P \rangle$, liquid and gas velocities $\langle \underline{v}_k \rangle_{k\rho}$ and enthalpies $\langle H_k \rangle_{k\rho}$. Accordingly, the resolvability of the system is proved in this section.

2.4 Discussions

In this chapter, we have established a macroscopic two-fluid model formulation based on the Neptune_CFD equations, which includes some unknown terms and so, needs closure relations to close the system. By comparison of this formulation to the existing macroscopic code equations, some assumptions made by these codes have been highlighted. Moreover, the different terms of the existing codes and the new formulation have been compared, and the corresponding terms have been identified. Therefore, it is now possible to evaluate some terms present or neglected in the existing code formulations based on an average of variables generated by Neptune_CFD. This is called the a priori method.

As a consequence, we would like to evaluate the unknown terms of this formulation in sub-cooled boiling test cases representative of industrial conditions, in order to find out which unknown term needs the most to be modeled. Moreover, this evaluation would permit us to know if the diffusion and dispersion terms are actually negligible. In order to estimate these terms, we would like to develop a validated database using Neptune_CFD, i.e., with a predicted void fraction close to the experimental one, on sub-cooled boiling cases representative of industrial configurations.

Chapter 3

Sub-cooled boiling industrial flows at macroscopic scale: a priori identification of predominant terms

Contents

In this chapter, the terms of the volume-statistic averaged equations developed in chapter 2 are evaluated for industrial subcooled boiling flows. First, RANS CFD simulations are performed using Neptune_CFD. These simulations cover around 80 sub-cooled boiling test cases at high pressure and temperature. From the results of these simulations, an average is applied in order to evaluate the macroscopic terms of the equations thus obtained (cf. chapter 2); this is called a priori evaluation. It is conventionally assumed that turbulence and subgrid dispersion terms are generally neglected in volume-statistic macro-scale codes. It is proposed in this chapter to evaluate these terms specifically, in order to determine whether or not they are really negligible. Finally, the predominant terms of the macroscopic equations in sub-cooled boiling flows are highlighted using the same a priori evaluation method. Part of this chapter has been published in the International Journal of Heat and Mass Transfer, in sections 3 and 4 of Herry et al. (2024b).

3.1 Building a RANS CFD simulation database with Neptune_CFD

In this section, a local database of Neptune_CFD simulations is developed, for which the void fraction predictions are close to the experimental ones, on sub-cooled boiling flows representative of industrial conditions. The accuracy of the predictions can be achieved by the selection of models adapted for this flow type.

In the extreme industrial conditions encountered in nuclear power plants, the pressure can reach 155 bar and the temperature 345°C. In such conditions, it is challenging to take fine measurements locally. Currently, only a few measurements are available for these conditions, such as the local temperature obtained with thermocouples or the average void fraction obtained with γ-ray detectors. In order to obtain complete experimental data, in particular with radial profiles of temperature, velocity, void fraction, and bubble diameter, some experiments have been carried out using other fluids. For example, the DEBORA experiment was carried out using Freon refrigerant 12 (R12) at 14 to 26 bar to simulate the boiling of subcooled water at 100 to 155 bar (Cubizolles, 1996; Garnier et al., 2001; Manon, 2000). These conditions allow more measurements to be made than with water at 155 bar. In addition, numerous numerical studies of this experiment have already been carried out with Neptune CFD (Guelfi et al., 2007; Laviéville et al., 2017; Favre, 2023; Ruyer and Seiler, 2009), in order to validate the code. However, although these experiments were conducted to achieve the same density ratio as water at high pressure, some physical properties of significant importance regarding the boiling process are not reproduced (Favre, 2023), such as surface wetting or bubble contact angle. Other subcooled boiling water flow experiments were carried out at high pressure, between 44 and 169 bars, and at high temperatures. These two experiments are KIT (Sabotinov, 1974) for a cylindrical geometry and PSBT (Rubin et al., 2012) for a sub-channel geometry. In these experiments, only the cross-section averaged void fraction is measured. Validating a code based on a comparison with this single measurement does not make it possible to assert with certainty the predictive nature of the code. Indeed, good mean void fraction predictions do not make it possible to guarantee that the heat transfer coefficient and the interfacial area are correctly modeled due to possible error compensation. However, the objective of these simulations is not to provide a complete validation of the numerical tool on these tests but to ensure that Neptune_CFD is globally consistent and that it is, therefore, able to provide an accurate order of magnitude of subgrid terms. This first estimation of the macroscopic terms aims, qualitatively, to identify the predominant terms in the equations. For these reasons, in this work, simulations with good void fraction predictions on the KIT and PSBT tests are considered sufficiently validated to be incorporated into the database used for macroscopic term evaluation.

This database then allows us to study the effect of geometry on dispersion and turbulence terms in the first part of section 3.2 by an a priori evaluation. Finally, all the terms of macroscopic equations are evaluated using the CFD database to identify the predominant ones.

3.1.1 Selected experiments: real and simplified geometries

The KIT and PSBT experiments are selected due to their similar boundary conditions and their different geometries. The PSBT experiment represents a real geometry encountered in assemblies, while KIT presents a simplified cylindrical geometry. The range of the selected test cases' boundary conditions is given in Table 3.1.1. Moreover, Neptune_CFD's simulations of KIT tests at low inlet mass flow rates, i.e., below 400 $kg/m^2.s$, give rather poor results, especially for the void fraction. For these reasons, these test cases have not been included in the database.

	KIT	PSBT
Pressure (bar)	[44-110]	[50-169]
Wall heat flux ($10^3 W/m^2$)	[430-1720]	[430-1940]
Inlet Mass Flux ($kg/m^2 s$)	[950-2100]	[500-3080]
Inlet sub-cooling (K)	[1-134]	[6-94]

Table 3.1.1: Boundary conditions of both test series KIT and PSBT.

PSBT and KIT experiments are described in detail in the following.

KIT experiment

The KIT experiment (Sabotinov, 1974) consists of sub-cooled boiling. This phenomenon can be encountered in different accident conditions, for instance, a depressurization of the primary or secondary loop or a decrease of coolant velocity in the core. The KIT experiment contains 75 different tests with constant, linearly increasing, and linearly decreasing heat fluxes along a pipe. A scheme of these three test series is shown in Figure 3.1.1.

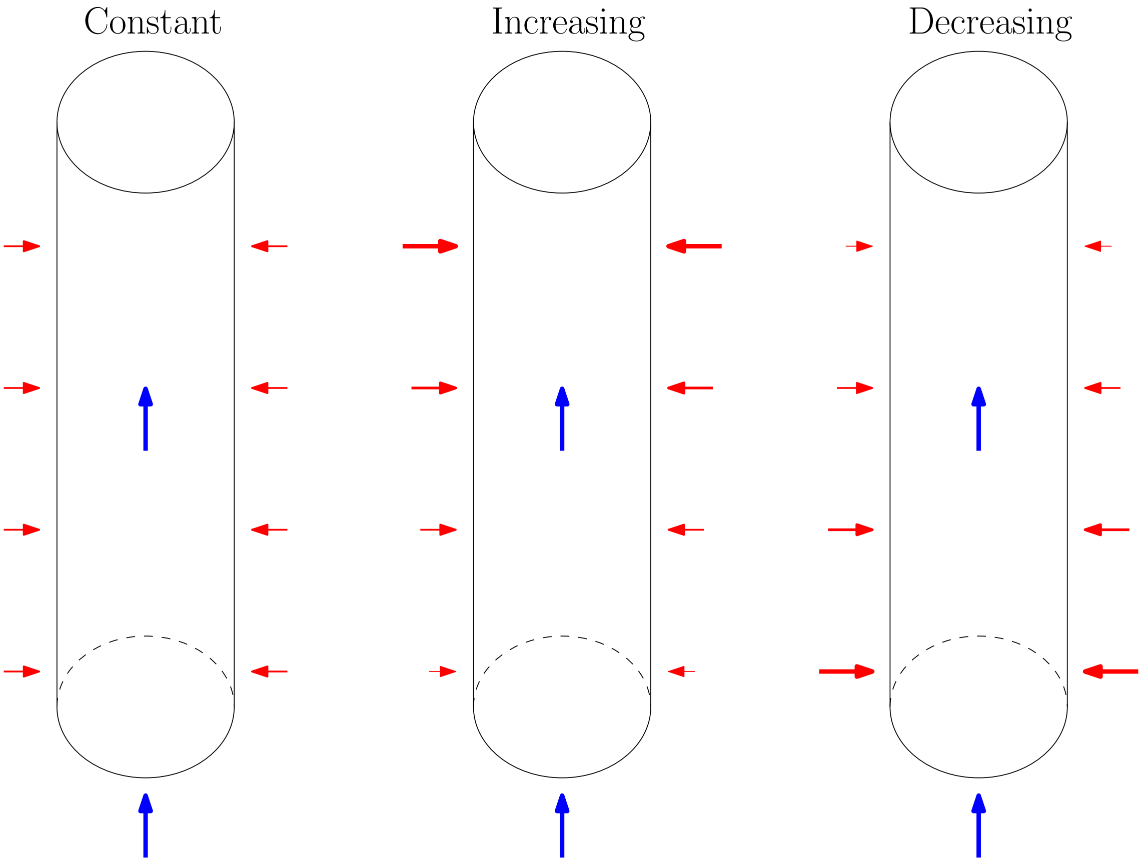

Figure 3.1.1: Scheme of the constant, increasing and decreasing heat fluxes test series.

These tests cover a broad range of pressure, surface heat flux, mass flow, and sub-cooling. The test section is a vertical pipe of a length of 1.5 m and a diameter of 1.17 cm for the constant heat flux tests. For the tests with increasing and decreasing heat flux, the diameter is 1.223 cm. The pipe was manufactured with a wall of variable thickness in order to increase and decrease the heat flux linearly. The outer diameter changes from 1.398 cm to 1.814 cm in 20 steps, which corresponds to a heat flux that changes from 0.3973*q to 1.6027*q, with q the average value of the heat flux. The water is preliminarily heated, and its temperature T_L and mass flowrate G are measured upstream of the test section, while pressure P is measured downstream. The average density of the fluid (and therefore the void fraction) is measured at different heights of the pipe by specially designed γ-rays and γ detectors.

In Figure 3.1.2, a simplified scheme of the KIT test facility is shown, with the main components (Kalitvianski, 2000). The input experimental data are given by Sabotinov (1974) and the data of the constant heat flux test series can also be found in the work of Kolev (1985). The data of the constant heat flux test series are presented in Table 3.1.2. Additionally to the experimental data, the inlet quality $x_{eq,in}$ and outlet quality $x_{eq,out}$ are calculated to have a better view of the experimental conditions. The inlet quality is calculated by:

$$x_{eq,in} = \frac{H_{in} - H_{l,sat}}{H_{lg}}, \tag{3.1.1}$$

with H_{in} the inlet enthalpy calculated from the fluid properties using the inlet liquid temperature. The outlet quality is expressed as:

$$x_{eq,out} = \frac{H_{m,out} - H_{l,sat}}{H_{lg}}, \tag{3.1.2}$$

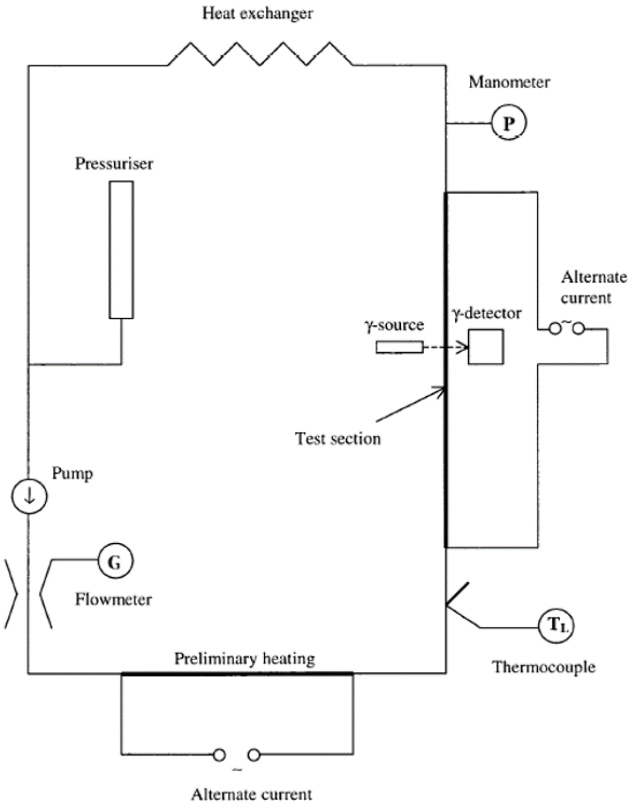

Figure 3.1.2: Simplified scheme of KIT test facility (Kalitvianski, 2000).

with $h_{m,out}$ the calculated outlet mixture enthalpy:

$$H_{m,out} = H_{in} + \frac{\Phi_w}{GS_{in}} = H_{in} + \frac{4L_{heat}q}{GD_h}. \tag{3.1.3}$$

Φ_w is the total heat input in Watt, G is the inlet mass flux ($kg/(m^2s)$), S_{in} is the inlet surface area, q is the wall heat flux (W/m^2), D_h is the hydraulic diameter and L_{heat} is the heated length. In all the test cases, the inlet qualities are negative.

KIT: Constant Heat Flux							
case	P, MPa	q, W/cm^2	G, $kg/(m^2s)$	$T_{in}(°C)$	Sub-cooling (°C)	Inlet Quality	Outlet Quality
1	6.806	113.718	2037	231	52.93	-0.172	0.016
2	6.796	113.02	1980	250	33.84	-0.113	0.080
3	6.806	113.823	1975	266	17.93	-0.061	0.133
4	6.992	136.024	1530	203	82.75	-0.265	0.038
5	6.835	136.722	1547	231	53.22	-0.174	0.125
6	6.786	78.514	2023	246	37.74	-0.125	0.006
7	6.806	78.619	1979	263	20.93	-0.071	0.063
8	6.806	79.317	2089	271	12.93	-0.045	0.084
9	6.786	168.833	962	188	95.74	-0.300	0.293
10	10.768	172.333	1015	183	133.48	-0.519	0.166
11	10.768	172.333	2129	241	75.48	-0.313	0.014
12	10.797	171.833	2109	266	50.69	-0.219	0.110

Table 3.1.2: Input data of Constant heat flux tests.

PSBT experiment

The PSBT benchmark has been created to provide some experimental data for the development and validation of thermal-hydraulic codes (Rubin et al., 2012). Indeed, this experiment has been organized to assess the capabilities of codes to predict detailed void distributions and departure from nucleate boiling in subchannels based on experimental data measured at a full-scale prototypical Pressurized Water Reactor rod bundle in NUPEC (Nuclear Power Engineering Corporation) facility.

Four subchannels configurations (S1, S2, S3, S4) (as shown in Figure 3.1.3) and three rod bundle configurations 5x5 are used. A vertical upward flow is considered. The length of the heated section is 1.555 m and the volume averaged void fraction is measured at 1.4 m.

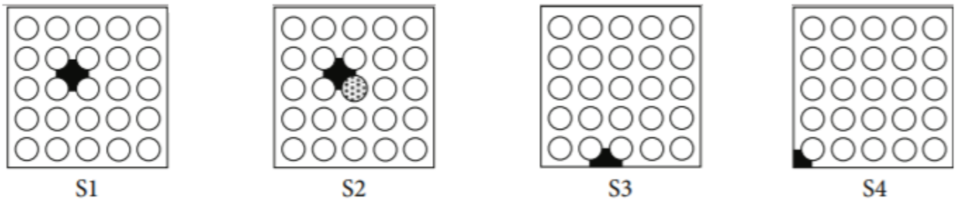

Figure 3.1.3: Configurations of subchannels S1, S2, S3, S4. Black part corresponds to the subchannel, white circles are the heated tubes and circle with points is the non heated tube (guide tube) (Rubin et al., 2012).

Specifically, the test section consists of a titanium alloy pressurized vessel, a test channel adapted according to the configuration (S1, S2, S3, or S4), and several electrodes to provide electricity to the heating elements. Figure 3.1.4 describes the test section geometry. The external diameter of the heated rod is 9.5 mm and the gap between two rods is 3.1 mm. The axial heat flux is constant.

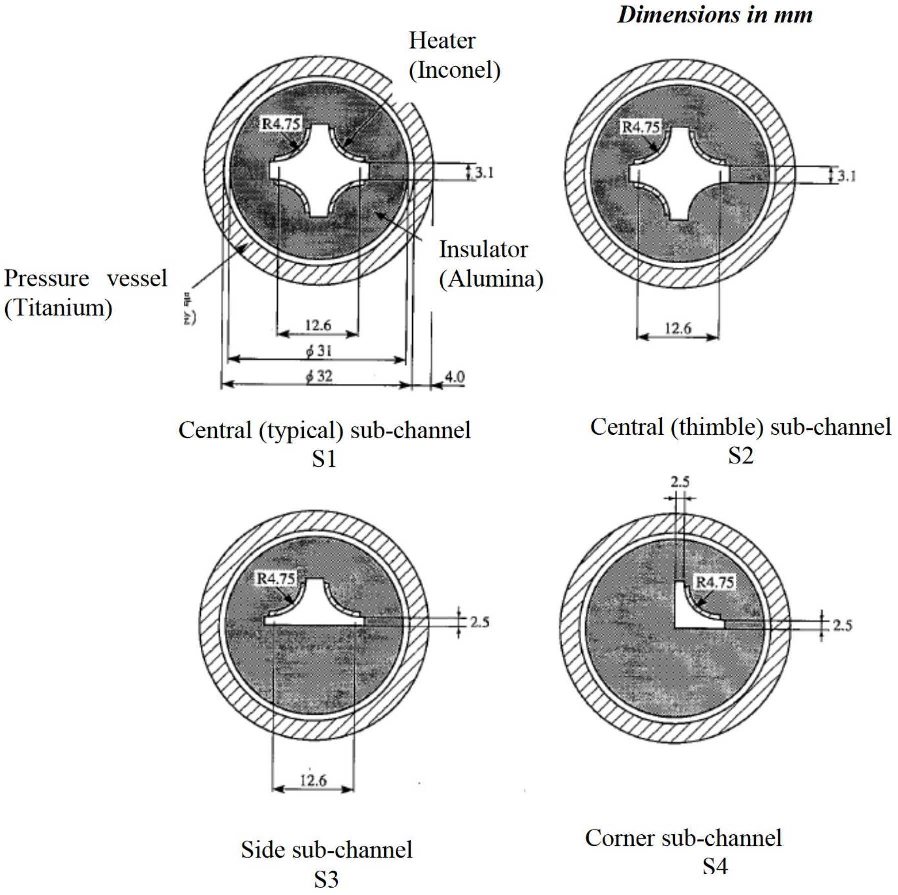

Figure 3.1.4: Dimensions of subchannels S1, S2, S3, S4 (Rubin et al., 2012).

A non-intrusive method of gamma-ray transmission is used to measure the flow density and then the void fraction. This measurement device is shown in Figure 3.1.5.

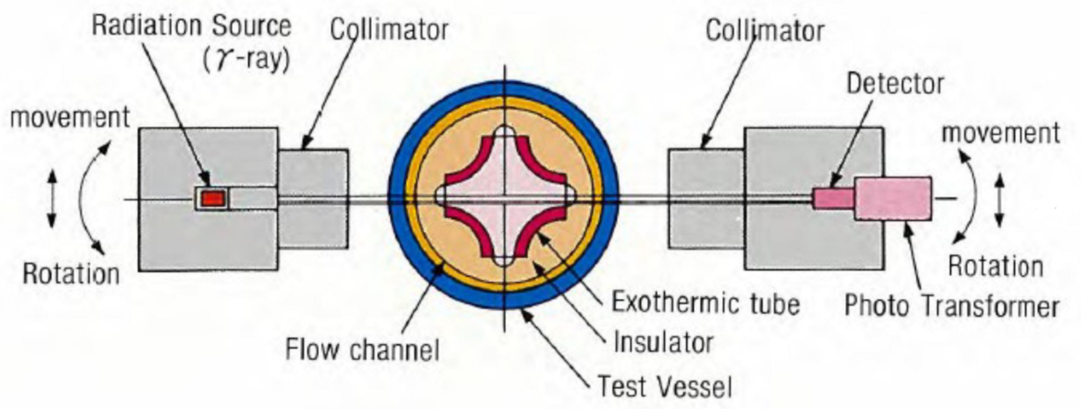

Figure 3.1.5: Void fraction measurement method (Rubin et al., 2012).

The present work aims to establish a database by comparing the numerical results from Neptune_CFD with the experimental results from 43 different test cases of the four PSBT benchmark subchannels configurations and then to carry out the a priori estimation of macroscopic subgrid terms on the validated numerical results.

The data of the four test series are presented in Table 3.1.3. In the same way as for the KIT experiment, the inlet quality $x_{eq,in}$ and outlet quality $x_{eq,out}$ are shown.

PSBT							
case	P, MPa	q, W/cm^2	G, $kg/(m^2s)$	$T_{in}(°C)$	Sub-cooling $(°C)$	Inlet Quality	Outlet Quality
1.1222	16.91	107.7	3050	334.7	17.16	-0.164	0.014
1.1223	16.91	107.6	3056	339.7	12.16	-0.122	0.055
1.2211	15.01	193.9	3031	295.4	46.81	-0.297	-0.020
1.2221	15.01	150.5	3022	299.4	42.81	-0.276	-0.060
1.2223	15.01	150.5	3031	319.6	22.61	-0.159	0.056
1.2237	15.03	129.3	3036	329.6	12.72	-0.096	0.089
1.2422	15.01	129.3	1389	284.1	58.11	-0.357	0.047
1.2423	15.03	129.1	1369	299.3	43.02	-0.277	0.132
1.4311	10.04	172.2	1392	214.2	97.09	-0.373	0.035
1.4312	10.02	172.0	1397	248.9	62.25	-0.249	0.156
1.4325	10.03	128.9	1397	253.8	57.42	-0.232	0.072
1.4326	10.01	129.5	1394	268.8	42.27	-0.175	0.130
1.5221	7.55	107.6	1394	219.2	71.79	-0.241	-0.013
1.5222	7.5	107.7	1394	243.9	46.64	-0.160	0.067
1.6221	5.05	107.7	1392	189.2	75.37	-0.215	-0.010
1.6222	5	107.6	1389	204.2	59.74	-0.172	0.033
2.1231	16.89	107.7	3050	335	16.76	-0.160	-0.027
2.1232	16.88	107.7	3056	340	11.71	-0.118	0.015
2.1233	16.88	107.7	3058	345	6.71	-0.072	0.060
2.3232	12.51	129.6	3031	309.8	18.08	-0.099	0.020

Continued on the next page

Table 3.1.3: Input data of PSBT test cases.

Continued from previous page							
PSBT							
case	P, MPa	q, W/cm^2	G, $kg/(m^2s)$	$T_{in}(°C)$	Sub-cooling $(°C)$	Inlet Quality	Outlet Quality
2.3233	12.5	129.6	3031	319.9	7.92	-0.046	0.074
2.4421	10.04	172.7	1397	244	67.29	-0.268	0.037
2.4422	10.05	172.7	1394	279.2	32.17	-0.136	0.170
2.4551	10.07	43.09	497	274	37.51	-0.158	0.057
2.4552	10.07	43.38	494	294.3	17.21	-0.076	0.141
2.6431	5.06	107.7	1392	209.2	55.49	-0.161	-0.007
2.6432	5.06	107.7	1394	224.2	40.49	-0.119	0.035
2.6433	5.05	108.0	1397	253.9	10.67	-0.032	0.121
3.2231	14.99	174.1	3028	309.4	32.70	-0.219	-0.024
3.2232	14.99	174.5	3028	314.5	27.60	-0.189	0.006
3.2451	15.03	130.1	1378	283.8	58.52	-0.360	-0.039
3.2452	15.05	130.1	1369	299	43.42	-0.280	0.043
3.2453	15.03	130.1	1372	314.3	28.02	-0.192	0.130
3.6431	5.04	173.2	1378	189	75.44	-0.215	0.045
3.6432	5.04	172.8	1381	223.9	40.54	-0.119	0.140
3.6461	5.06	108.6	1378	203.9	60.79	-0.175	-0.012
4.2251	14.99	131.0	3072	319.3	22.80	-0.160	-0.044
4.2253	15	130.1	3072	318.4	23.76	-0.166	-0.051
4.2256	15	130.1	3086	330.5	11.66	-0.088	0.027
4.2257	14.99	130.1	3089	334.5	7.60	-0.059	0.055
4.4455	10.05	131.0	1400	278.8	32.57	-0.138	0.056
4.4456	10.05	131.0	1394	289	22.37	-0.097	0.098
4.6461	5.06	107.7	1397	214	50.69	-0.148	-0.019

Table 3.1.3: Input data of PSBT test cases (continued from previous page).

3.1.2 Choice of adapted meshes and modeling

Boundary conditions

In the simulations of both tests, a zone with unheated walls is created and modeled upstream of the test section in order to have a developed velocity profile at the entrance of the test section. Consequently, on the one hand, the temperature profile is still flat at the entrance of the test section, and on the other hand, the velocity profile is fully developed at the beginning of the test section. A reference pressure is imposed at the outlet. The heated pin is a non-adiabatic wall with imposed heat flux. Symmetry boundary conditions are applied to the symmetry planes. For example, for the test series S1 of PSBT, one-eighth of the domain is computed. In the KIT experiment, because of the symmetrical nature of the experimental facility and the flow, the simulations are carried out in an angular sector (1°) of the pipe section. Moreover, for PSBT tests, the non-heated walls are considered adiabatic, and a no-slip boundary condition is imposed in the same way that Lutsanych et al. (2017). Schemes of the boundary conditions of both PSBT and KIT experiments are shown in Figure 3.1.6.

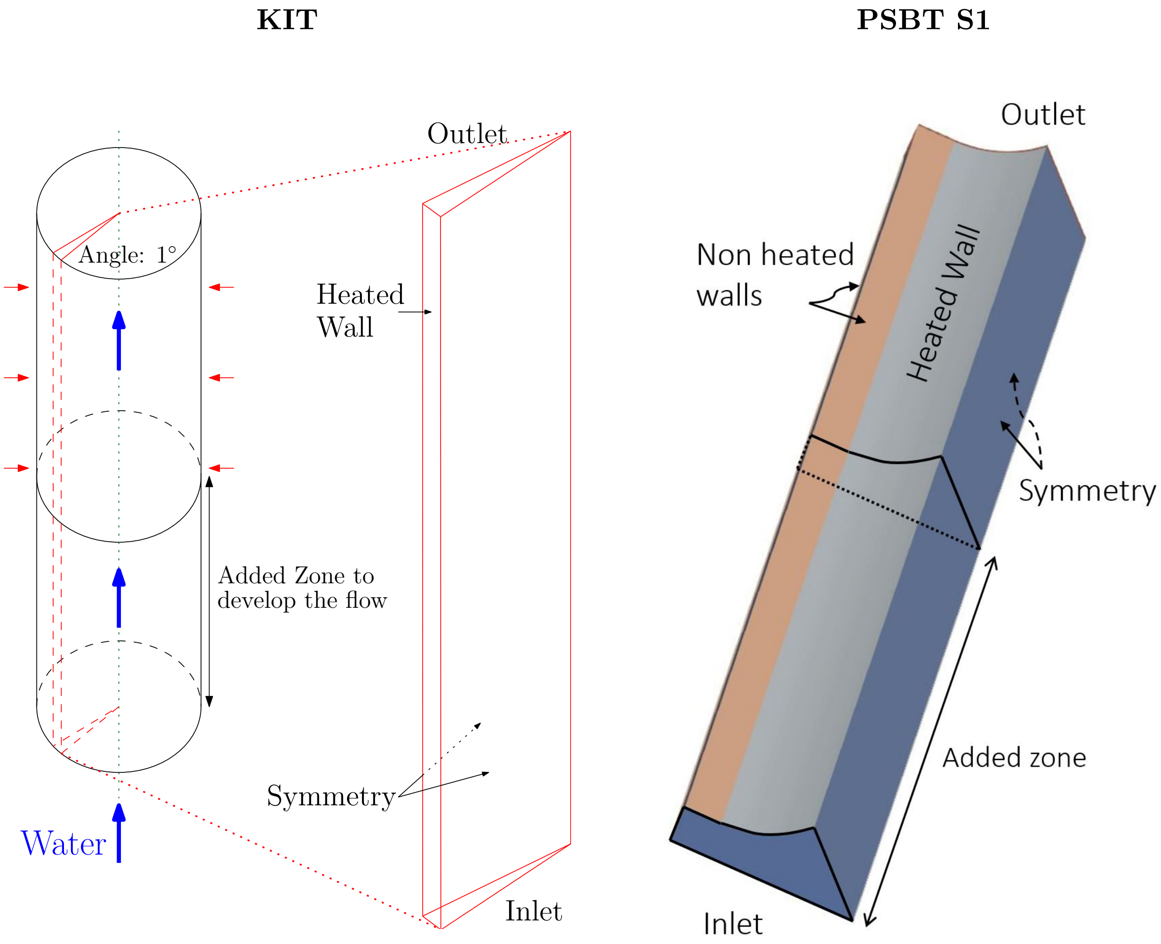

Figure 3.1.6: Scheme of the boundary conditions of KIT (left) and PSBT S1 (right) experiments.

Mesh selection

In the KIT experiment, the meshes are generated as three-dimensional ones, with only one cell in the orthoradial direction. The results are thus calculated in the r, z plane. Three different grids of increasing sizes are used, as shown in Table 3.1.4.

Mesh level	Number of cells in the pipe cross-section	Number of cells in the angular direction	Number of cells along pipe axis
Coarse	30	1	420
Medium	50	1	700
Fine	70	1	840

Table 3.1.4: Description of different mesh refinements of KIT experiment.

The sensitivity to the mesh refinement shows that a slight difference exists between the results with coarse mesh and other meshes at the beginning of the vapor generation. The medium mesh is used in the following because the results do not seem to change compared to those obtained with the fine mesh. The mesh sensitivity is shown in Figure 3.1.7.

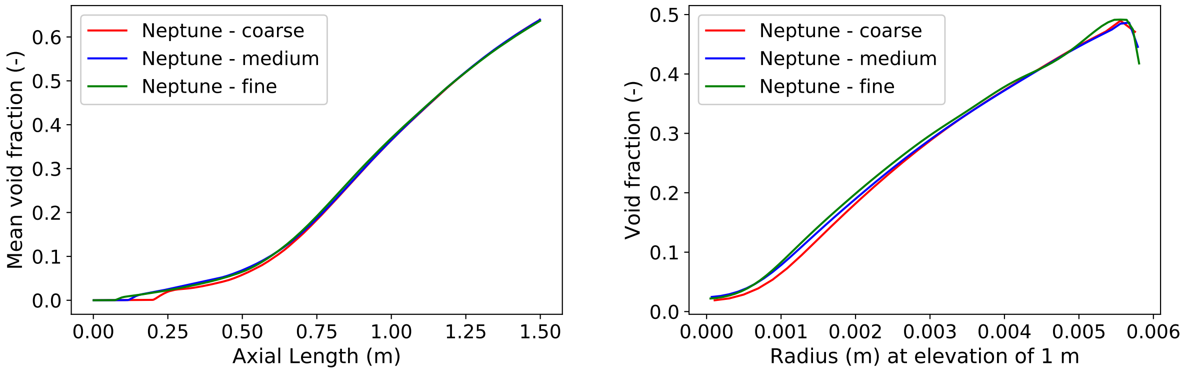

Figure 3.1.7: Sensitivity to the mesh refinement for the KIT experiment on test series ”Constant heat flux”, case n°2.

For the PSBT experiment, the spatial discretization is based on that of Lutsanych et al. (2017), which achieves the mesh convergence. Thus, four fully structured hexagonal meshes are created for the respective configurations S1, S2, S3, and S4, as shown in Figure 3.1.8.

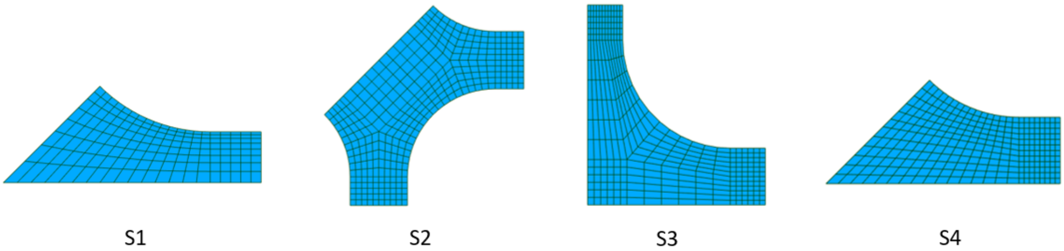

Figure 3.1.8: Meshes of the configurations S1, S2, S3 et S4.

In addition, the cells in the near-wall region are thinner to describe velocity and temperature gradients more accurately. A cell size of 5 *mm* is imposed in the axial direction. The characteristics of the grids are summarized in Table 3.1.5.

	S1	**S2**	**S3**	**S4**
Total number of cells	49760	108850	100764	89568
Cell size in axial direction z (mm)	5	5	5	5
Number of cells in axial direction z	311	311	311	311
Number of cells in a section	160	350	324	288

Table 3.1.5: Characteristics of the grids for the configurations S1, S2, S3 and S4.

For both experiments, the wall-adjacent cells remain in the log region of the wall boundary layer ($30 < y+ < 300$).

Models selection

The models selected in this section are those recommended to study bubbly flows with Neptune_CFD and are described in section 1.2.

Uncertainties evaluation by boundary condition variations

The absolute instrumental uncertainties for both KIT and PSBT experiments are given in Table 3.1.6. On the one hand, for the KIT experiment, the uncertainties are primarily expressed as

	(ΔP)max	**(Δq)max**	**(ΔG)max**	**(ΔT_l)max**	**($\Delta\alpha$)max**
KIT	± 0.08MPa [±0.7%, ±1.8%]	± 2.60 * 10^4 W/m^2 [±1.5%, ±6%]	± 28.8 kg/(m^2s) [±1.3%, ±3.0%]	± 0.9K	± 0.03
PSBT	± 1%	± 1%	± 1.5%	± 1K	± 0.03

Table 3.1.6: Experimental uncertainties (Sabotinov, 1974; Rubin et al., 2012).

absolute change and then converted to a range of relative changes to the boundary conditions. On the other hand, for the PSBT experiment, the uncertainties are directly expressed as relative changes to the boundary conditions. The uncertainties are slightly larger for the KIT experiment, especially for the test cases for which the wall heat flux is the lowest, with relative values of wall heat flux uncertainties up to ±6%.

Lutsanych et al. (2017) have calculated the impact of boundary condition uncertainties on the results of one test case and then have applied it to all the others. In this chapter, the test cases simulated by Herry et al. (2022) are also carried out, and taking into account the uncertainties in boundary conditions. We distinguish between the most favorable and the most unfavorable boundary condition uncertainties to calculate the impact on the void fraction for each test case. This provides an uncertainty band on the void fraction for each test case. In addition, the void fraction measurement uncertainties of ±0.03 for both experiments are also added to the uncertainty band.

3.1.3 Analysis of numerical results and CFD validation

For both experiments, the axial evolution of the predicted cross-section averaged void fraction is shown for one representative test case. Then, the predicted void fraction at 1.4 m from the inlet is compared with the measured one for all the test cases. The uncertainties on predicted void fraction described in section 3.1.2 are added to the comparison figures. Regarding the axial evolution of void fraction, the uncertainties related to boundary conditions and those related to the void fraction measurements are separated. An envelope represents the uncertainties related to the boundary conditions, and those related to the void fraction measurements are added as a band on both sides of the measurement point. Regarding the comparison for all the test cases, both uncertainties are plotted together as an uncertainty band.

Special attention should be given to the simulation validation on cross-section averaged void fractions. Indeed, an accurate prediction of the averaged void fraction does not always imply an accurate validation since error compensation may occur. Unfortunately, to our knowledge, there is no such sub-cooled boiling experiment at high pressure, up to 155 bar, with local measurements, which would allow an increased validation. However, some validations of Neptune_CFD code have already been done on local variables on a sub-cooled boiling experiment of Freon at a limited pressure of 26 bar, corresponding to the density ratio of water at 155 bar (Guelfi et al., 2007; Laviéville et al., 2017; Favre, 2023; Ruyer and Seiler, 2009). Then, the aim of these simulations is not to provide full validation of the numerical tool on these tests but to ensure that Neptune_CFD is broadly consistent and is, therefore, able to provide an accurate order of magnitude of the macroscopic subgrid terms. The emergence of new experimental facilities of sub-cooled boiling flow at high pressure, including local measurements of void fraction, velocity, and bubble diameter, could provide further validation.

Void fraction predictions on KIT experiments

The axial evolution of the predicted cross-section averaged void fraction is compared to the experimental measurements for test case 1 of the constant heat flux test series in Figure 3.1.9. The blue line corresponds to the calculation done with Neptune_CFD using the experimental boundary conditions. Next, the uncertainties are divided into two parts. First, the void fraction measurement uncertainties of ±3% are shown as a vertical band corresponding to 3% above and below the calculation point. The second part corresponds to the boundary condition uncertainties, such as the uncertainties on the inlet flow rate and temperature, outlet pressure, and wall heat flux. The combination of uncertainties that produces the most void fraction is added to the experimental boundary conditions to provide the upper bound. For example, the upper limit consists of the positive uncertainties for the wall heat flux and inlet temperature, and the negative uncertainties for the inlet flow rate and outlet pressure. In the same way, the combination that produces the least void fraction is added to the experimental boundary conditions to provide the lower bound. Afterward, Neptune_CFD calculations are achieved again by taking into account these minimum and maximum boundary conditions, and the numerical results obtained using the minimum are shown in green in Figure 3.1.9, and using the maximum in red.

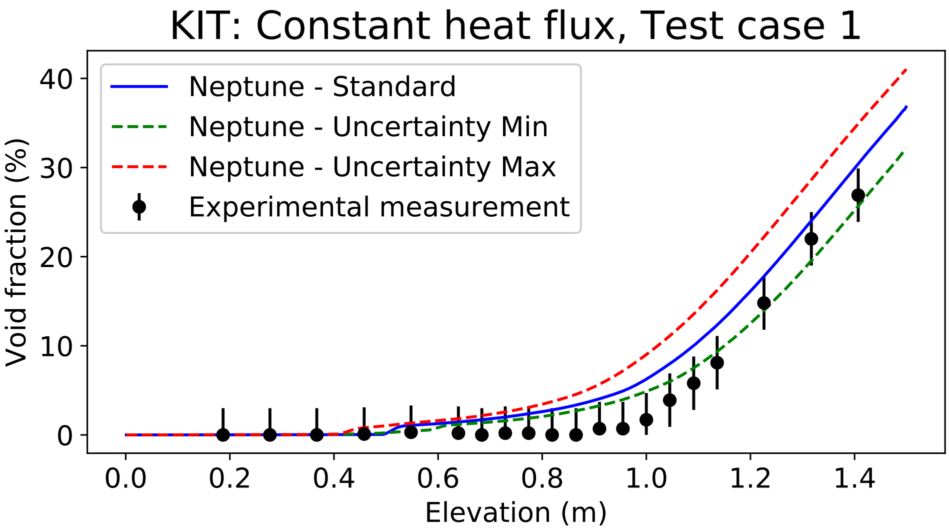

Figure 3.1.9: Void fraction prediction of case n°1 of KIT constant heat flux test series.

For this test case, a part of the predicted void fraction envelope is always inside the measurement band. However, in order to compare the accuracy of all the 52 test cases, only the comparison between the predicted and measured void fraction on the last measurement point, at 1.4 m, is considered. In this comparison, all the uncertainties are shown together.

Simulation results for 52 tests from the KIT experiment are shown in Figure 3.1.10.

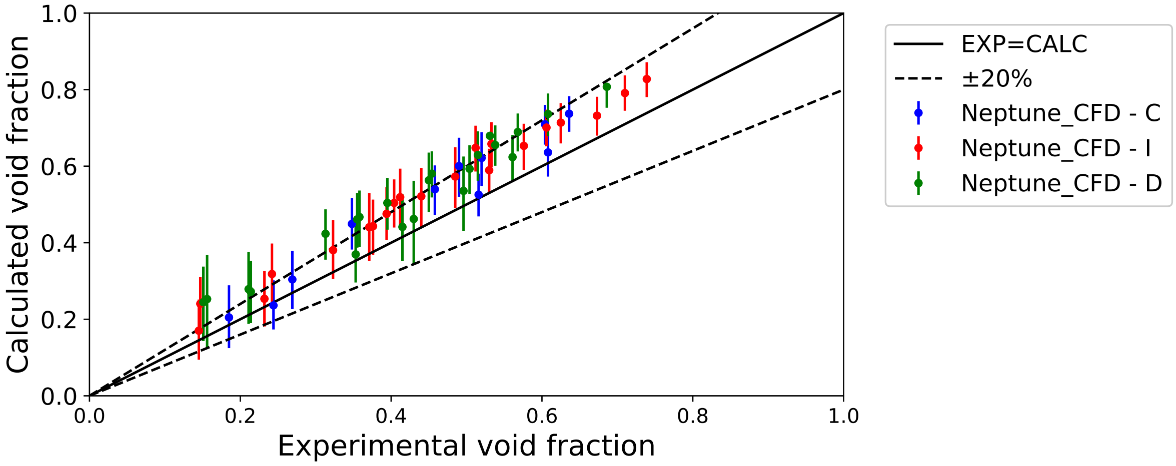

Figure 3.1.10: Comparison between predicted and measured void fraction at $z = 1.4m$ for KIT tests. Blue: Constant heat flux (C); Red: Increasing heat flux (I); Green: Decreasing heat flux (D).

Overall, the code overestimates the void fraction. Some tests are outside the band of uncertainties but are retained in the database used to estimate the subgrid terms of the macroscopic equations. Indeed, our work focuses on up-scaling from CFD simulations using state-of-the-art models such as Neptune_CFD, which uses, for example, a second-order turbulence model. Therefore, improving CFD simulations and models is not an issue in this chapter.

Void fraction predictions on PSBT experiments

In the same way that for the KIT experiment, the axial evolution of the predicted void fraction, as well as the uncertainty envelope, is shown in Figure 3.1.11. There is only one experimental measurement for each test case, at 1.4 *m*.

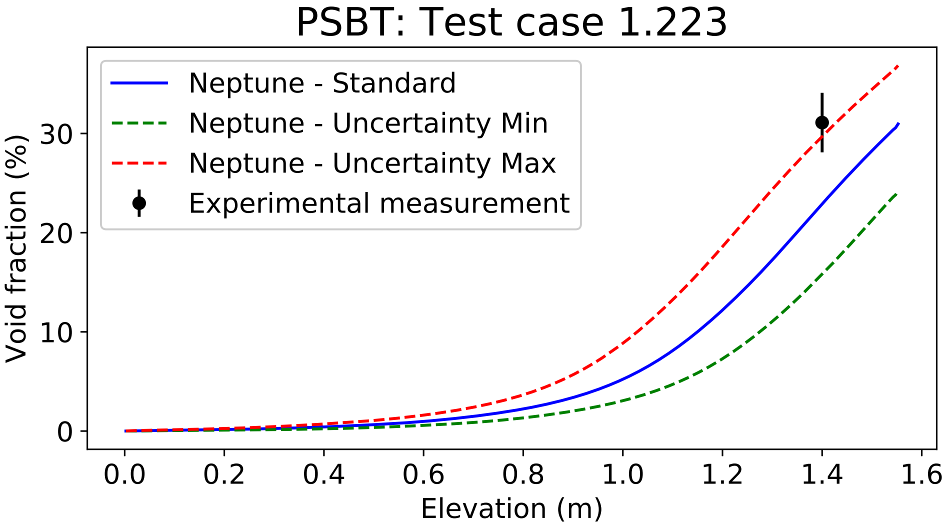

Figure 3.1.11: Void fraction prediction of case n°1.223 of PSBT experiment.

Next, the predicted and measured void fractions of all the 43 PSBT test cases are compared in Figure 3.1.12. 30 of those 43 test cases lie within the uncertainty band and are considered validated in this work. These test cases are those for which the vertical uncertainty band crosses the black line, corresponding to the experimental void fraction. Moreover, the deviations of ±20% are shown in dash lines. These simulations are part of the database for the section 3.2, where sub-grid terms of macroscopic equations are estimated.

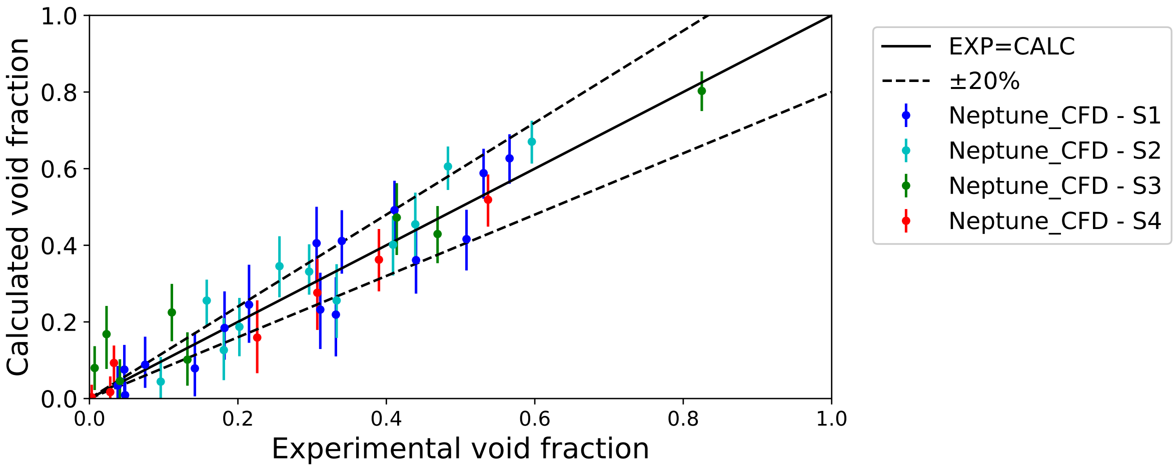

Figure 3.1.12: Comparison between predicted and measured void fraction for PSBT tests.

Discussion

In this section, 86 sub-cooled boiling test cases under industrial conditions have been simulated using the Neptune_CFD code. The void fraction predicted by the numerical tool is sufficiently close to the experimental fraction for the test cases to be considered validated. This database is used in the next section to evaluate all the macroscopic terms in order to identify which are predominant and which are negligible. This will help to clarify the choices made in the macroscopic codes.

3.2 A priori evaluation of predominant terms

In this section, the predominant terms of conservation equations in industrial conditions of sub-cooled boiling flows are identified by an a priori evaluation using the CFD database. This allows us to know which term it would be better to focus on in the rest of the thesis and in future work. Moreover, particular attention is given to the subgrid terms of turbulence and dispersion. Indeed, first, the relative weights of these terms compared to the convection terms are evaluated in order to validate or reject the hypothesis done by existing macroscopic codes to neglect those subgrid terms. Then, some existing correlations to model these subgrid terms are evaluated in these test cases. Finally, all the terms of conservation equations are evaluated to determine the predominant ones.

3.2.1 Macroscopic scale, importance assessment of dispersion and turbulence terms

The relative importance of the subgrid terms of turbulence and dispersion in momentum and energy macroscopic equations are evaluated in comparison to the convection terms. These relative weights are determined from the simulation database, which is composed of 56 and 30 test cases, respectively, from KIT and PSBT experiments. All variables are available at each local cell presented in section 3.1.2, as, for example, the Reynolds stress tensor, velocity, and enthalpy. Moreover, the macroscopic discretization consists of 50 cells in the axial direction and only one cell in the cross-section, regardless of the test section geometry. Some macroscopic cells are presented on the PSBT local mesh in Figure 3.2.1.

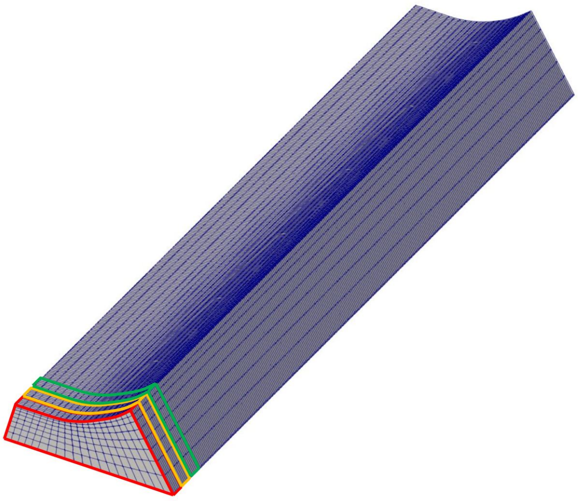

Figure 3.2.1: Three PSBT macroscopic cells (in red, orange and green) overlying the local CFD mesh.

All macroscopic variables are calculated on each macroscopic cell by averaging local variables obtained by CFD simulations. Then, the deviation $\delta\xi$ at each local cell is deducted from the subtraction of the averaged variable $\langle\xi\rangle$ by the local variable ξ. Therefore, all macroscopic terms introduced in table 2.3.1 are calculated at each macroscopic cell. In this section, for each macroscopic cell, the liquid averaged Reynolds stress tensor $\left\langle \underline{\underline{\tau_{T}}}_{l} \right\rangle_{l}$, along with liquid and gas momentum dispersion terms $\langle \delta \underline{v}_l \delta \underline{v}_l \rangle_{l\rho}$, $\langle \delta \underline{v}_g \delta \underline{v}_g \rangle_{g\rho}$ are evaluated and compared with liquid and gas convection terms $\langle \underline{v}_l \rangle_{l\rho} \langle \underline{v}_l \rangle_{l\rho}$, $\langle \underline{v}_g \rangle_{g\rho} \langle \underline{v}_g \rangle_{g\rho}$. The liquid energy dispersion term $\langle \delta \underline{v}_l \delta H_l \rangle_{l\rho}$ is also compared to the liquid energy convection term $\langle \underline{v}_l \rangle_{l\rho} \langle H_l \rangle_{l\rho}$.

By assuming standard turbulent flow profiles for velocity and enthalpy, Ishii and Hibiki (2011) have reached the conclusion that the energy dispersion term is negligibly small for both developing and fully developed flows under normal conditions. We propose here to check if this term is also negligible in flows representative of a nuclear reactor core. Beyond the information on this term, it is rather the magnitude of the divergence of dispersion and turbulence terms that matters since these terms do intervene effectively in momentum and energy equations. Therefore, the values of the dispersion and turbulence divergence terms are also compared to the value of convection divergence terms for all the test cases.

The objective is to check whether the neglect of the dispersion and turbulence divergence terms is justified for flow and thermal-hydraulic conditions encountered in the core of a nuclear power plant. This work also allows these terms to be compared depending on the configuration, either cylinder or subchannel. In order to do so, multiple methodologies can be applied. First, a non-dimensional subgrid term, scaled by the convection term, can be taken at each macroscopic cell. Then, the maximum may be taken to conclude if subgrid terms are effectively negligible compared to convection terms. However, the shape of the convection term according to the axial direction can be parabolic, so its derivative can be null in some locations. Consequently, the non-dimensional subgrid terms would be infinitely large in these cells. Then, it would not be relevant to use this methodology. The other way to do it is to get vectors, for which each component corresponds to the value of a subgrid or convection term at a macroscopic cell. Then, a norm is applied to each vector, and the relative weight of subgrid term norms compared to convection term ones is analyzed.

Estimation of subgrid terms and their derivatives

Estimation of the subgrid terms Only one macroscopic cell per cross-section is used, thus only the axial terms and axial derivative terms $(\frac{\partial}{\partial z})$ are considered. Then, the subgrid and convection terms vectors are introduced in equation (3.2.1). The parameter I corresponds to the macroscopic cell index.

$$\begin{aligned}
T_{disp_l} &= \left(\langle \alpha_l \rangle^I \langle \rho_l \rangle_l^I \langle \delta v_{l_z} \delta v_{l_z} \rangle_{l\rho}^I \right)_{1<I<50}, & T_{disp_g} &= \left(\langle \alpha_g \rangle^I \langle \rho_g \rangle_g^I \langle \delta v_{g_z} \delta v_{g_z} \rangle_{g\rho}^I \right)_{\substack{1<I<50 \\ \langle \alpha_g \rangle^I > 10^{-4}}}, \\
T_{conv_l} &= \left(\langle \alpha_l \rangle^I \langle \rho_l \rangle_l^I \langle v_{l_z} \rangle_{l\rho}^I \langle v_{l_z} \rangle_{l\rho}^I \right)_{1<I<50}, & T_{conv_g} &= \left(\langle \alpha_g \rangle^I \langle \rho_g \rangle_g^I \langle v_{g_z} \rangle_{g\rho}^I \langle v_{g_z} \rangle_{g\rho}^I \right)_{\substack{1<I<50 \\ \langle \alpha_g \rangle^I > 10^{-4}}}, \\
T_{turb_l} &= \left(\langle \alpha_l \rangle^I \langle \rho_l \rangle_l^I \left\langle \tau_{T_{l_{zz}}} \right\rangle_{l\rho}^I \right)_{1<I<50}, & T_{disp_{l_{en}}} &= \left(\langle \alpha_l \rangle^I \langle \rho_l \rangle_l^I \langle \delta v_{l_z} \delta H_l \rangle_{l\rho}^I \right)_{\substack{1<I<50 \\ T_{sat} - \langle T_l \rangle_l^I > 1K}}, \\
T_{conv_{l_{en}}} &= \left(\langle \alpha_l \rangle^I \langle \rho_l \rangle_l^I \langle v_{l_z} \rangle_{l\rho}^I \langle H_l \rangle_{l\rho}^I \right)_{\substack{1<I<50 \\ T_{sat} - \langle T_l \rangle_l^I > 1K}}.
\end{aligned} \tag{3.2.1}$$

The gas dispersion and convection vectors are only composed of cells where there is more than 0.0001 of void fraction in it, since at a lower void fraction, there is almost no more gas remaining, and so, the gas velocity would have no physical meaning. The liquid energy dispersion is null when the liquid temperature is at saturation, so it is not relevant to consider the part of the domain where the liquid is at saturation or very close to it. This is why the energy dispersion and convection terms are only taken for the cells where the mean liquid temperature has a gap of more than $1K$ with the saturation temperature. Different norms can be applied to these vectors, such as the L^{∞}-norm, L^2-norm, and the L^1. The relative weights of subgrid terms obtained are similar, no matter the norm used. Following the work of Fleau (2017), the L^1-norm is used, and the normalized means of subgrid terms are introduced in equation (3.2.2).

$$\tau^*_{turb_l} = \frac{||T_{turb_l}||_1}{||T_{conv_l}||_1} = \frac{\sum\limits_{1<I<50} \left| \langle \alpha_l \rangle^I \langle \rho_l \rangle^I_l \left\langle \tau_{T_{l_{zz}}} \right\rangle^I_l \right|}{\sum\limits_{1<I<50} \left| \langle \alpha_l \rangle^I \langle \rho_l \rangle^I_l \langle v_{l_z} \rangle^I_{l\rho} \langle v_{l_z} \rangle^I_{l\rho} \right|}, \tag{3.2.2a}$$

$$\tau^*_{disp_l} = \frac{||T_{disp_l}||_1}{||T_{conv_l}||_1} = \frac{\sum\limits_{1<I<50} \left| \langle \alpha_l \rangle^I \langle \rho_l \rangle^I_l \langle \delta v_{l_z} \delta v_{l_z} \rangle^I_{l\rho} \right|}{\sum\limits_{1<I<50} \left| \langle \alpha_l \rangle^I \langle \rho_l \rangle^I_l \langle v_{l_z} \rangle^I_{l\rho} \langle v_{l_z} \rangle^I_{l\rho} \right|}, \tag{3.2.2b}$$

$$\tau^*_{disp_g} = \frac{||T_{disp_g}||_1}{||T_{conv_g}||_1} = \frac{\sum\limits_{\substack{1<I<50 \\ \langle \alpha_g \rangle^I > 10^{-4}}} \left| \langle \alpha_g \rangle^I \langle \rho_g \rangle^I_g \langle \delta v_{g_z} \delta v_{g_z} \rangle^I_{g\rho} \right|}{\sum\limits_{\substack{1<I<50 \\ \langle \alpha_g \rangle^I > 10^{-4}}} \left| \langle \alpha_g \rangle^I \langle \rho_g \rangle^I_g \langle v_{g_z} \rangle^I_{g\rho} \langle v_{g_z} \rangle^I_{g\rho} \right|}, \tag{3.2.2c}$$

$$\tau^*_{disp_{len}} = \frac{||T_{disp_{len}}||_1}{||T_{conv_{len}}||_1} = \frac{\sum\limits_{\substack{1<I<50 \\ T_{sat} - \langle T_l \rangle^I_l > 1K}} \left| \langle \alpha_l \rangle^I \langle \rho_l \rangle^I_l \langle \delta v_{l_z} \delta H_l \rangle^I_{l\rho} \right|}{\sum\limits_{\substack{1<I<50 \\ T_{sat} - \langle T_l \rangle^I_l > 1K}} \left| \langle \alpha_l \rangle^I \langle \rho_l \rangle^I_l \langle v_{l_z} \rangle^I_{l\rho} \langle H_l \rangle^I_{l\rho} \right|}. \tag{3.2.2d}$$

$\tau^*_{turb_l}$, $\tau^*_{disp_l}$, $\tau^*_{disp_g}$, and $\tau^*_{disp_{len}}$ are the normalized mean terms of respectively the liquid momentum turbulence, liquid momentum dispersion, gas momentum dispersion, and liquid energy dispersion.

Estimation of the subgrid terms derivatives In the momentum and energy equations, it is the derivatives of the subgrid terms that matter and not the subgrid terms themselves. Indeed a subgrid term can be important but if it is constant axially, then the value of its derivative will be very low and therefore will have a low impact on the conservation equations.

Consequently, the orders of magnitude of those subgrid terms derivatives are evaluated in comparison with the convection terms derivatives. In a similar way to the previous section, the L1-norm of subgrid terms divergences are compared to the L1-norm of the convection terms divergences.

The normalized mean of subgrid terms derivatives are defined in equations 3.2.3 and are plotted in Figures 3.2.5, 3.2.6 and 3.2.9.

$$\tau^{\nabla *}_{turb_l} = \frac{||\nabla . T_{turb_l}||_1}{||\nabla . T_{conv_l}||_1} = \frac{\sum\limits_{1<I<50} \left| \frac{\partial}{\partial z} \left(\langle \alpha_l \rangle^I \langle \rho_l \rangle^I_l \left\langle \tau_{T_{l_{zz}}} \right\rangle^I_{l\rho} \right) \right|}{\sum\limits_{1<I<50} \left| \frac{\partial}{\partial z} \left(\langle \alpha_l \rangle^I \langle \rho_l \rangle^I_l \langle v_{l_z} \rangle^I_{l\rho} \langle v_{l_z} \rangle^I_{l\rho} \right) \right|}, \tag{3.2.3a}$$

$$\tau^{\nabla *}_{disp_l} = \frac{||\nabla . T_{disp_l}||_1}{||\nabla . T_{conv_l}||_1} = \frac{\sum\limits_{1<I<50} \left| \frac{\partial}{\partial z} \left(\langle \alpha_l \rangle^I \langle \rho_l \rangle^I_l \langle \delta v_{l_z} \delta v_{l_z} \rangle^I_{l\rho} \right) \right|}{\sum\limits_{1<I<50} \left| \frac{\partial}{\partial z} \langle \alpha_l \rangle^I \langle \rho_l \rangle^I_l \langle v_{l_z} \rangle^I_{l\rho} \langle v_{l_z} \rangle^I_{l\rho} \right|}, \tag{3.2.3b}$$

$$\tau^{\nabla *}_{disp_g} = \frac{||\nabla . T_{disp_g}||_1}{||\nabla . T_{conv_g}||_1} = \frac{\sum\limits_{\substack{1<I<50 \\ \langle \alpha_g \rangle^I > 10^{-4}}} \left| \frac{\partial}{\partial z} \left(\langle \alpha_g \rangle^I \langle \rho_g \rangle^I_g \langle \delta v_{g_z} \delta v_{g_z} \rangle^I_{g\rho} \right) \right|}{\sum\limits_{\substack{1<I<50 \\ \langle \alpha_g \rangle^I > 10^{-4}}} \left| \frac{\partial}{\partial z} \left(\langle \alpha_g \rangle^I \langle \rho_g \rangle^I_g \langle v_{g_z} \rangle^I_{g\rho} \langle v_{g_z} \rangle^I_{g\rho} \right) \right|}, \tag{3.2.3c}$$

$$\tau^{\nabla *}_{disp_{l_{en}}} = \frac{||\nabla . T_{disp_{l_{en}}}||_1}{||\nabla . T_{conv_{l_{en}}}||_1} = \frac{\displaystyle\sum_{\substack{1<I<50 \\ T_{sat}-\langle T_l\rangle_l^I>1K}} \left|\frac{\partial}{\partial z}\left(\langle\alpha_l\rangle^I \langle\rho_l\rangle_l^I \langle\delta v_{l_z}\delta H_l\rangle_{l\rho}^I\right)\right|}{\displaystyle\sum_{\substack{1<I<50 \\ T_{sat}-\langle T_l\rangle_l^I>1K}} \left|\frac{\partial}{\partial z}\left(\langle\alpha_l\rangle^I \langle\rho_l\rangle_l^I \langle v_{l_z}\rangle_{l\rho}^I \langle H_l\rangle_{l\rho}^I\right)\right|}. \tag{3.2.3d}$$

The axial derivative $\partial/\partial z$ is calculated using a central differencing scheme of second order as follows:

$$\frac{\partial \xi^I}{\partial z} = \frac{\xi^{I+1} - \xi^{I-1}}{2\Delta z}. \tag{3.2.4}$$

A priori evaluation of subgrid terms and derivatives in momentum equation

Subgrid terms in momentum equation The axial evolution of the subgrid and convection terms in the liquid momentum equation is shown in Figure 3.2.2 for a representative test case, the test case 1 of the KIT experiment, in the constant heat flux test series. The void fraction axial evolution of this test case is shown in Figure 3.1.9. The convection, dispersion, and turbulence terms have an overall similar tendency with around two orders of magnitude between the convection and dispersion, and one between the dispersion and turbulence. The axial evolution can be divided into two regions, first between the inlet and the apparition of void fraction at 0.5 m, the evolution of the all terms are fairly constant, with a slight decrease for turbulence and dispersion terms. Above 0.5 m, there is a clear increase of all terms due to void fraction apparition and, consequently, to the velocity increase. This overall evolution is found in all the test cases with different magnitudes.

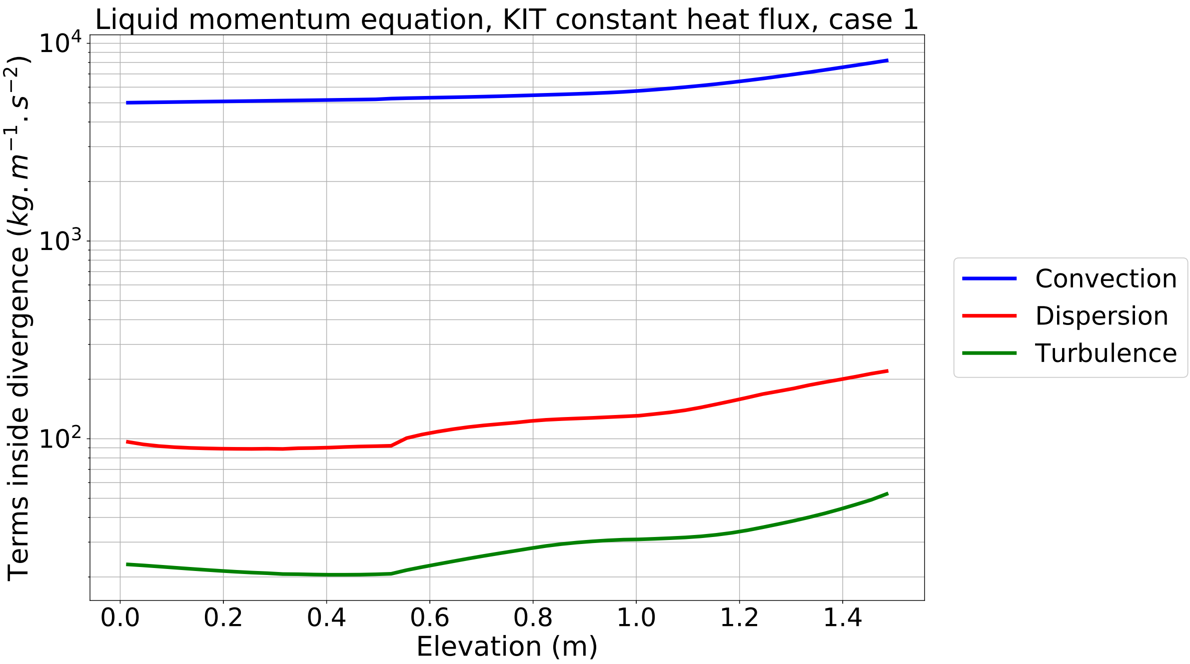

Figure 3.2.2: Axial evolution of the liquid momentum dispersion, turbulence and convection terms, as presented in equation (3.2.1), for KIT constant heat flux, case 1.

In order to compare all test cases of both KIT and PSBT experiments, the normalized mean of liquid momentum turbulence and dispersion terms of all test cases are presented in Figure 3.2.3 according to the inlet conditions.

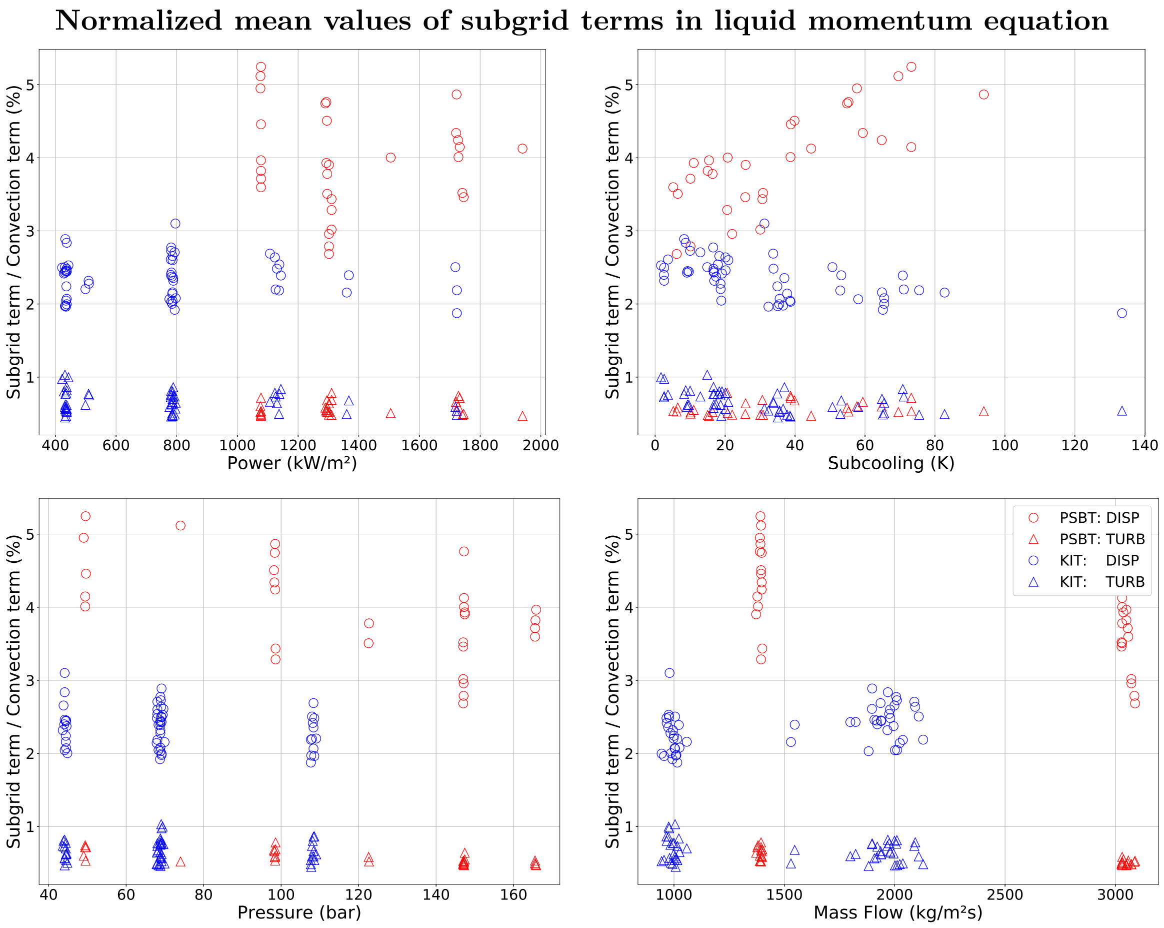

Figure 3.2.3: L1-norm values of subgrid terms normalized by L1-norm values of convection terms in liquid momentum equation. Blue and red colors correspond respectively to KIT and PSBT experiments. ○: $\tau^*_{disp_l}$: normalized mean of liquid dispersion terms (DISP), equation (3.2.2b); △: $\tau^*_{turb_l}$: normalized mean of liquid turbulence terms (TURB), equation (3.2.2a).

For all test cases in both experiments, the subgrid term norms in the momentum equation are lower than the convection term norms ($< 5.5\%$). Moreover, in these a priori simulations, the dispersion terms are always greater than the turbulence terms. For PSBT tests, there is a downward trend of the normalized subgrid terms when the inlet mass flow increases. For KIT tests, there is no clear tendency for the normalized momentum subgrid terms based on inlet conditions.

For PSBT tests, which are representative of nuclear reactor core geometry, the dispersion terms are larger than those for KIT tests. Then, caution should be exercised when using correlations for dispersion in tube bundles while it is based on experiments carried out in cylindrical pipes. In fact, liquid momentum dispersion terms in cylindrical pipes seem smaller than in subchannel geometry. For the PSBT experiment, the L1-norms of dispersion terms are between 2.5 % and 5.5 % of convection terms norms, while for the KIT experiment, these terms are between 1.75 % and 3.25 %. For both experiments, the normalized means of turbulence terms are between 0.25 % and 1.5 %. Thus, these terms are small but not negligible compared to the convection terms.

In the CFD gas momentum equation, there is no turbulence model, given that the flow is assumed to be dispersed. Then, only dispersion terms are compared to the convection terms for the macroscopic momentum equation for all the test cases, using the normalized mean of gas momentum dispersion terms introduced in equation (3.2.2c). These terms are plotted for all test cases as a function of inlet boundary conditions in figure 3.2.4.

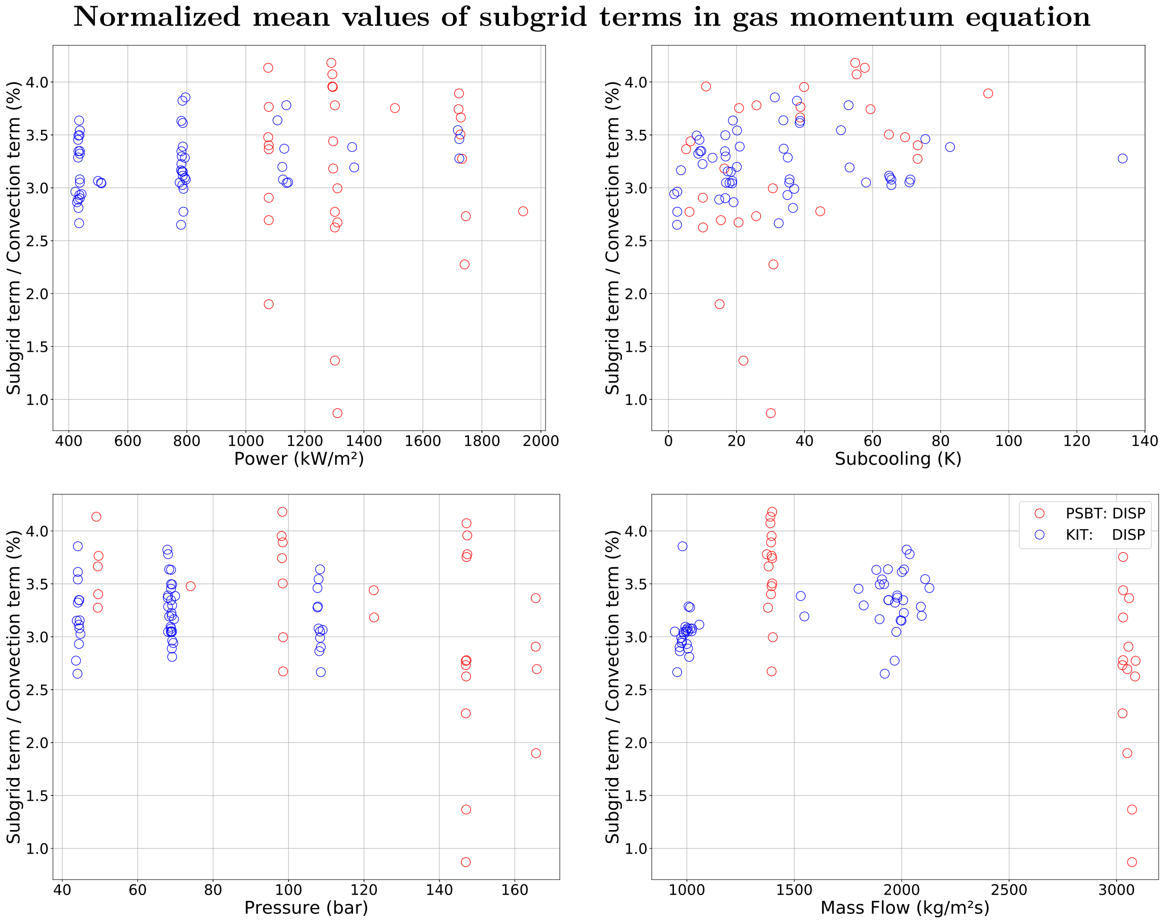

Figure 3.2.4: L1-norm values of subgrid terms normalized by L1-norm values of convection terms in gas momentum equation. Blue and red colors correspond respectively to KIT and PSBT experiments. ○: $\tau^*_{disp_g}$: normalized mean of gas dispersion terms (DISP), equation (3.2.2c).

The differences between both experiments on the normalized mean values of liquid dispersion terms are not found for the gas dispersion. Indeed, the normalized mean values of gas dispersion terms are about the same for both experiments, with few isolated points for the PSBT experiment between 1 % and 2.5 %. Excluding these points, all other terms are in the range of 2.5 %-4.5 %. Therefore, for the KIT experiment, the normalized mean values of gas dispersion terms are slightly higher than the liquid ones while it is the opposite for the PSBT experiment. Overall, these normalized gas dispersion terms have a similar order of magnitude as the liquid phase terms. The same conclusion remains, namely, that the gas dispersion terms are small but not negligible compared to the gas convection terms.

Subgrid terms derivatives in momentum equation The normalized mean values of subgrid terms derivatives in the liquid momentum equation are plotted in figure 3.2.5.

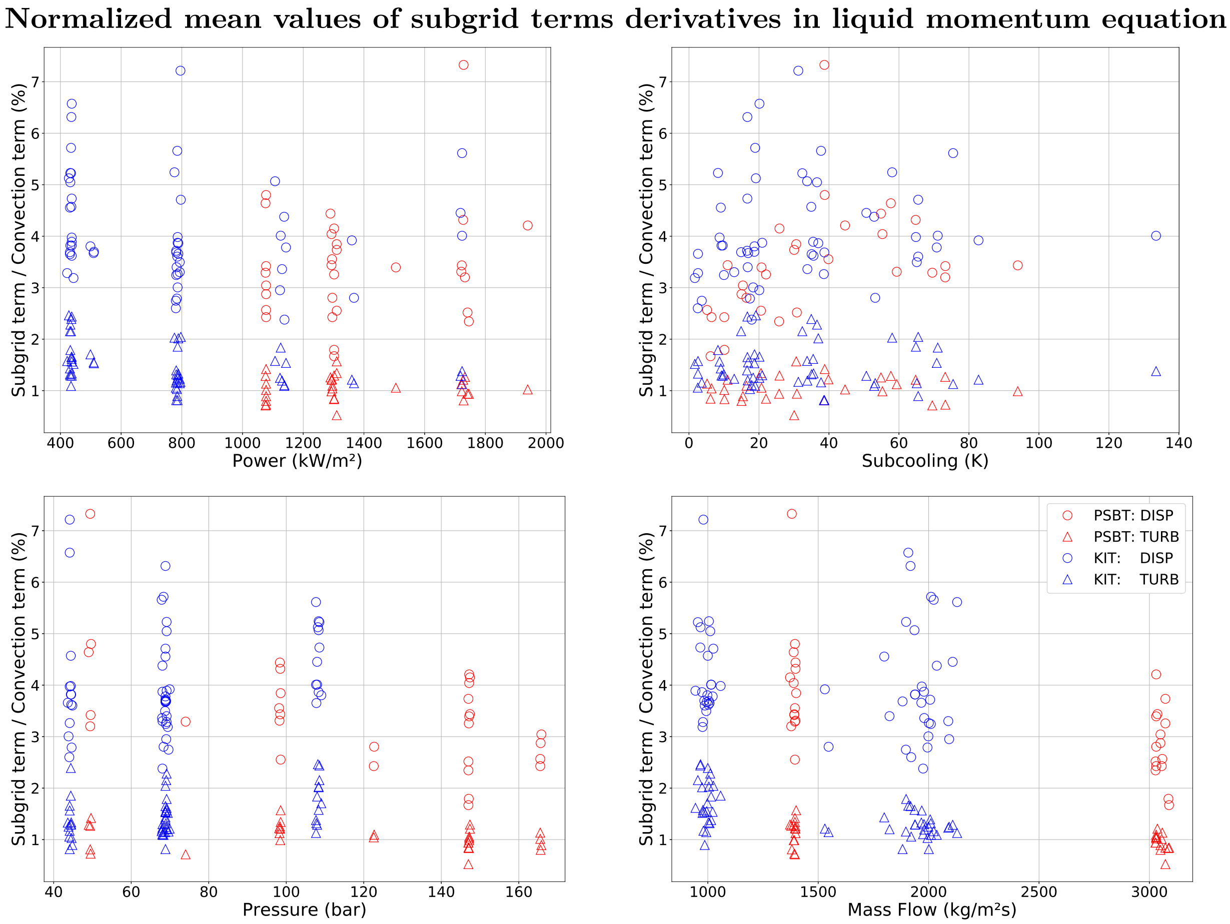

Figure 3.2.5: L1-norm values of subgrid terms derivatives normalized by L1-norm values of convection terms derivatives in the liquid momentum equation. Blue and red colors correspond respectively to KIT and PSBT experiments. ○: $\tau^{\nabla *}_{disp_l}$: normalized mean of liquid dispersion terms derivatives (DISP), equation (3.2.3b); △: $\tau^{\nabla *}_{turb_l}$: normalized mean of liquid turbulence terms derivatives (TURB), equation (3.2.3a).

Overall, the normalized liquid subgrid terms derivatives are slightly greater, but of a similar order of magnitude as the normalized subgrid terms themselves. Indeed, the normalized mean values of turbulence terms derivatives plotted here are in the range of 0.5 %-2.5 %, and the normalized mean values of liquid dispersion derivatives are in the range of 1.5 %-7.5 %. There is no clear pattern of these terms according to any initial condition. This clearly shows that the subgrid terms derivatives appearing in liquid momentum equations are not negligible compared to the convection terms derivatives, which contradicts the hypothesis of neglecting these terms in some system codes.

For the gas phase, the normalized mean values of the dispersion term derivatives are shown in figure 3.2.6.

The dispersion and convection terms in the gas momentum equation have approximately the same axial evolution and the same gap among themselves. This is why, for all cases, the normalized mean values of gas dispersion terms derivatives are near the normalized mean values of the dispersion terms themselves. Indeed, the normalized mean terms values are also in the range 2 %-5 % for most terms, except two isolated points around 1 % and 6 %. So, the same conclusion appears here as with the subgrid term itself, i.e., the gas dispersion term in the momentum equation is small but not negligible compared to the gas convection term.

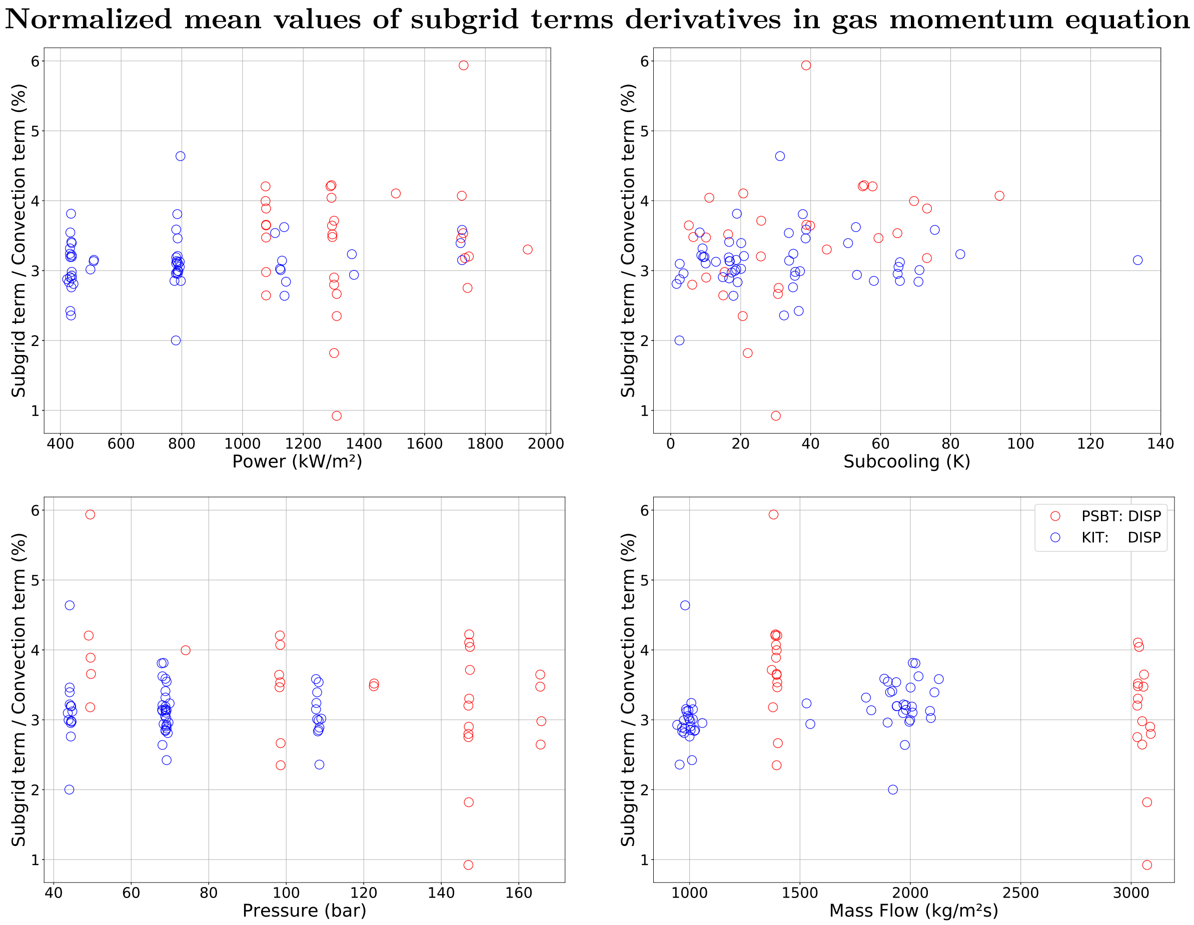

Figure 3.2.6: L1-norm values of subgrid terms derivatives normalized by L1-norm values of convection terms derivatives in gas momentum equation. Blue and red colors correspond respectively to KIT and PSBT experiments. ○: $\tau_{disp_g}^{\nabla *}$: normalized mean of gas dispersion terms derivatives (DISP), equation (3.2.2c).

A priori evaluation of subgrid terms and derivatives in energy equation

Subgrid terms in energy equation The axial evolution of the subgrid dispersion term, as well as the convection term in the liquid energy equation, are shown in Figure 3.2.7 for a representative test case, the test case 1 of the KIT experiment.

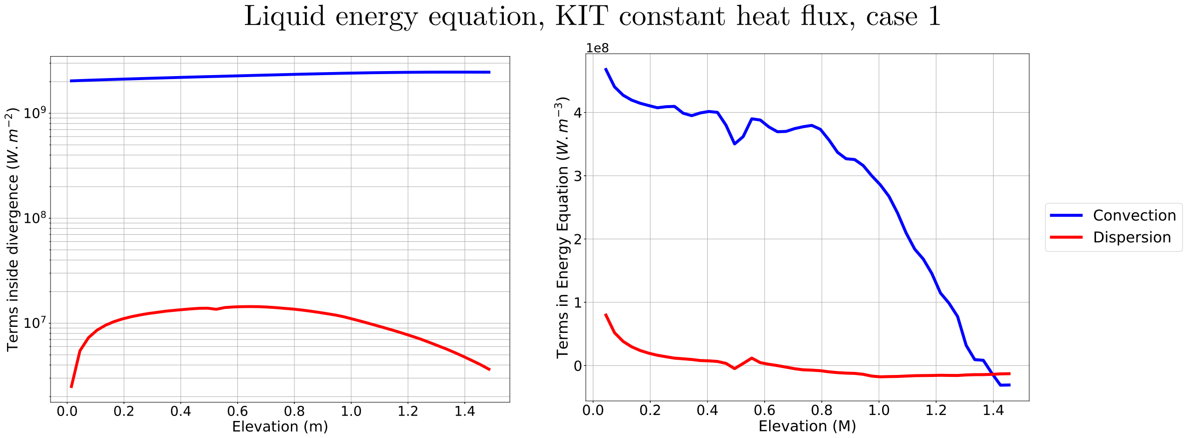

Figure 3.2.7: Axial evolution of the energy dispersion and convection terms, as presented in equation (3.2.1), for KIT, case 1. Left: subgrid terms; right: divergence of the subgrid terms.

In the energy equation, the axial evolutions of convection and dispersion terms are quite different, as shown in the left part of Figure 3.2.7. There are two orders of magnitude between both curves, but there is a sharp increase of dispersion near the inlet, between the inlet and 0.2m, which is not found for the convection term. Indeed, at the inlet, the energy profile is flat, so there is no spatial fluctuation of energy. Therefore, the dispersion term is null at the inlet. However, from the first axial cell, due to the heated wall, the energy increases near the wall. This results in an increase in the energy spatial fluctuations and the dispersion term. Above, the dispersion term becomes flatter and decreases when the liquid temperature approaches the saturation everywhere in the cross-section.

On the other hand, the convection term increases continuously with the increase in enthalpy. However, when a lot of steam is created, the liquid enthalpy decreases due to the decrease in liquid volume fraction. The convection curve is first flattened and can decrease for some test cases due to the decrease in liquid enthalpy. It can be seen on the right part of Figure 3.2.7 that the convection divergence term becomes negative at the end of the pipe. Therefore, although they have different behavior, both terms divergences are first positive before becoming negative at the end of the test section.

The normalized mean values of liquid energy dispersion terms introduced in equation (3.2.2d) are presented in Figure 3.2.8 for all test cases according to the inlet conditions.

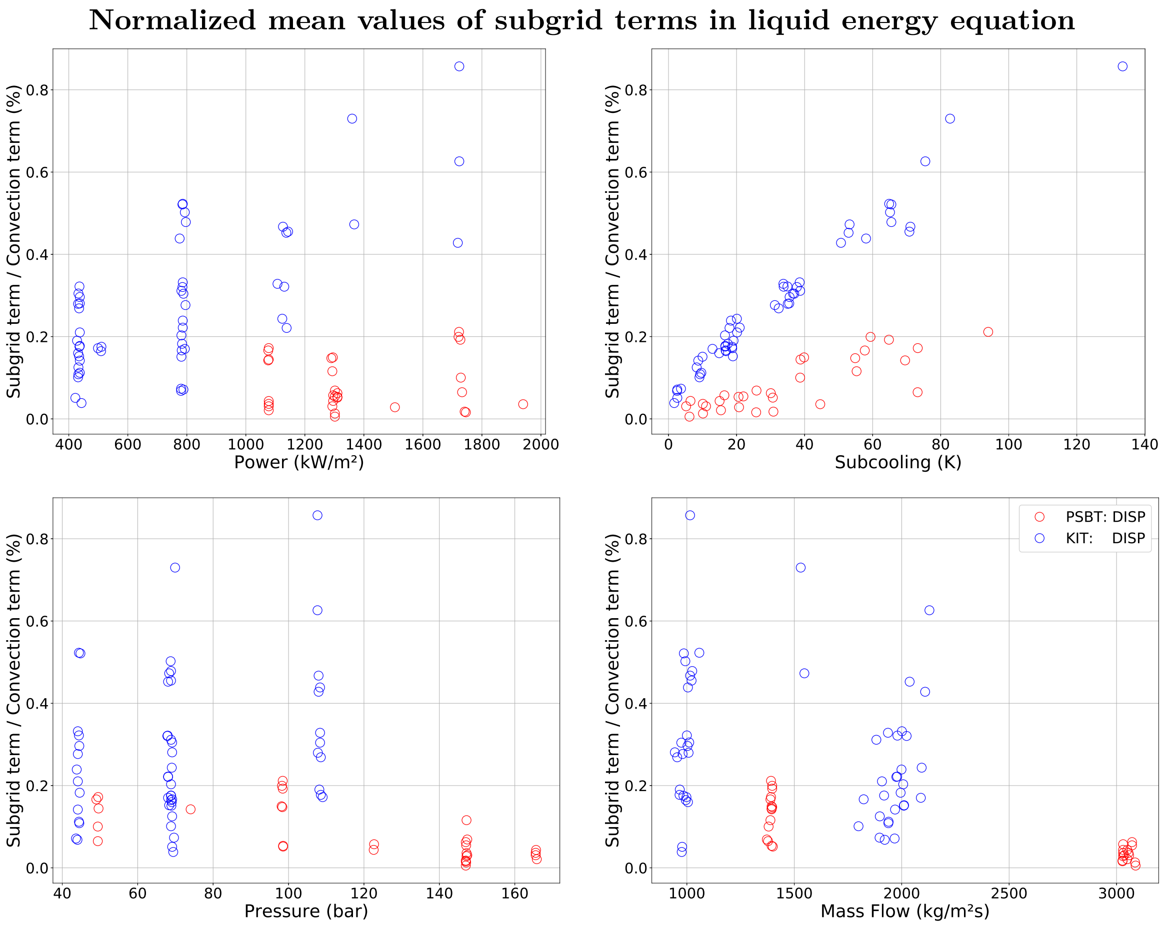

Figure 3.2.8: L1-norm values of subgrid terms normalized by L1-norm values of convection terms in liquid energy equation. Blue and red colors correspond respectively to KIT and PSBT experiments. ○: $\tau^{*}_{disp_{l_{en}}}$: normalized mean of liquid dispersion terms (DISP), equation (3.2.2d).

For all test cases, the normalized liquid energy dispersion terms are lower than the normalized liquid momentum dispersion terms presented in section 3.2.1. For both experiments, the normalized mean values of energy dispersion terms are linearly increasing with increasing inlet sub-cooling, and with decreasing mass flow. However, the growth rate is different between KIT and PSBT tests. Indeed, for both, the dispersion terms are near 0 % of the convection terms for small sub-cooling ($< 10\ K$), but when the sub-cooling increases, the normalized mean values of energy dispersion terms increase faster for KIT tests, around 0.8 % for KIT versus 0.2 % for PSBT tests at sub-cooling of around 80 K. In this type of flow configuration and with high sub-cooling, it might be relevant to model this term and not neglect it.

Subgrid terms derivatives in energy equation There is a clear rise of the order of magnitude of the normalized mean values of dispersion terms derivatives in liquid energy equation compared to the normalized mean values of the dispersion terms themselves, as it can be seen in figure 3.2.9. While for all test cases, the normalized mean values of dispersion terms were below 0.2 % for PSBT and below 0.8 % for the KIT experiment, the values for dispersion terms derivatives are always greater than 1 % for PSBT and 4 % for the KIT experiment, with some mean values up to 16 %. The tendency found in the section 3.2.1 on increasing dispersion according to increasing sub-cooling does not apply to the normalized mean values of dispersion derivatives. Rather, the maximum values of these terms are encountered for low sub-cooling. This may be caused by the fact that the liquid temperature is quickly near saturation, and so, the mean values only apply on the few first cells, where the dispersion is maximum, while for high sub-cooling, the mean is done on more cells, including those with lower values of dispersion derivatives.

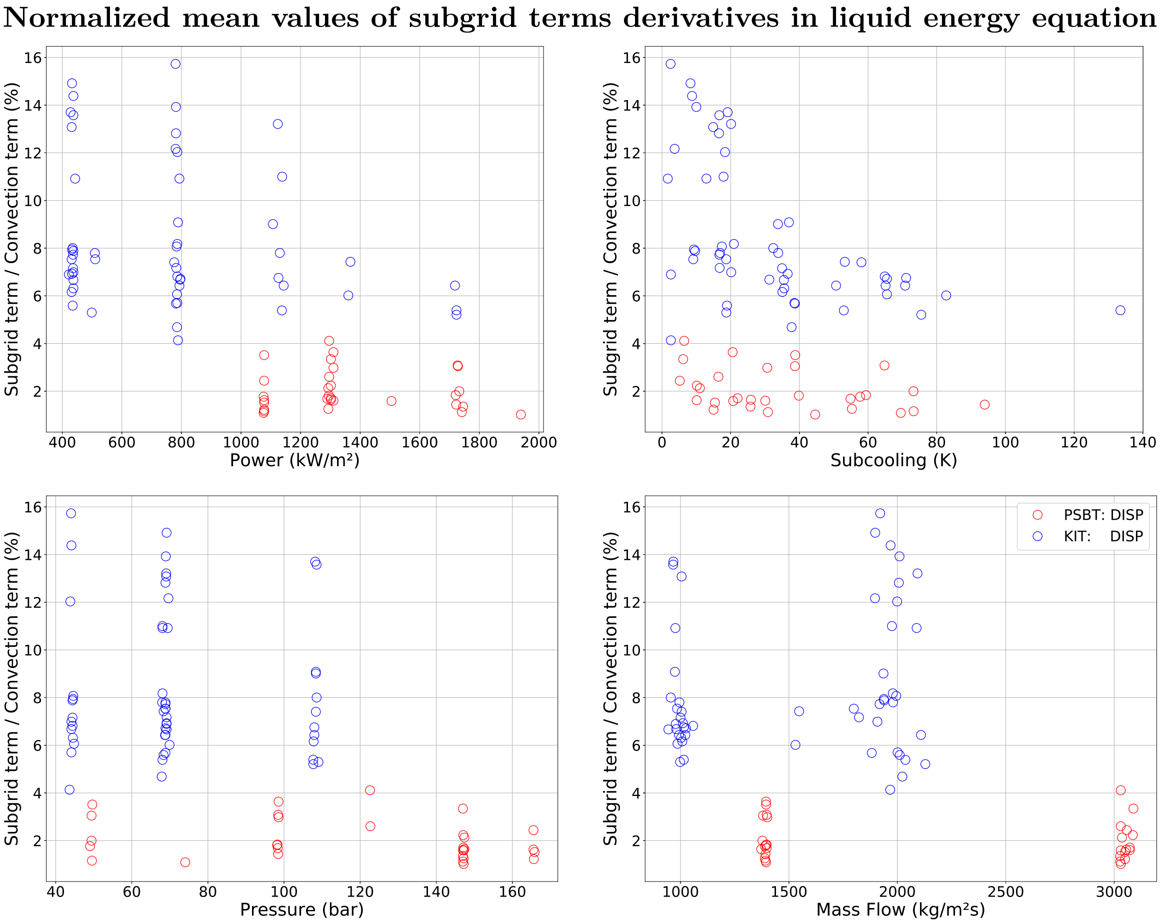

Figure 3.2.9: L1-norm values of subgrid terms derivatives normalized by L1-norm values of convection terms derivatives in liquid energy equation. Blue and red colors correspond respectively to KIT and PSBT experiments. ○: $\tau^*_{disp_{l_{en}}}$: normalized mean of liquid dispersion terms derivatives (DISP), equation (3.2.2d).

Thereby, despite the fact that the energy dispersion term is very small compared to the convection term, lower than 0.8 %, the dispersion term derivatives are no longer as small compared to the convection term derivatives. Indeed, the mean values of the dispersion terms derivatives can reach 16 % of the convection terms derivatives mean values. Therefore, it is very important to take this term into account in system code equations.

3.2.2 Evaluation of existing correlations to model the subgrid terms

The figures 3.2.3 and 3.2.4 show that the subgrid terms in the momentum equation are not negligible compared to the convection terms. This is particularly true for the dispersion term. As mentioned in section 2.3.3, there are very few correlations in the literature to estimate this dispersion term in gas-liquid two-phase flows. In chapter 15 of the book written by Ishii and Hibiki (2011), these effects have been studied in industrial conditions for sub-cooled boiling flows. They have proposed a correlation for the distribution parameter C_{vk}, which is directly related to the dispersion term:

$$C_{vk} = \frac{\langle \alpha_k \rho_k \underline{v}_k \underline{v}_k \rangle}{\langle \alpha_k \rangle \langle \rho_k \rangle_k \langle \underline{v}_k \rangle_{k\rho} \langle \underline{v}_k \rangle_{k\rho}} = 1 + \frac{\langle \delta \underline{v}_k \delta \underline{v}_k \rangle_{k\rho}}{\langle \underline{v}_k \rangle_{k\rho} \langle \underline{v}_k \rangle_{k\rho}}. \tag{3.2.5}$$

The correlation proposed is described in equations (3.2.7) and (3.2.6).

$$C_{vl} = 1 + 1.5(C_0 - 1), \tag{3.2.6}$$
$$C_{vg} = 1 + 0.5(C_0 - 1), \tag{3.2.7}$$

with C_0 the volumetric-flux-distribution parameter of the drift flux model (Zuber and Findlay, 1965) defined as follows:

$$C_0 = \frac{\langle \alpha_g j \rangle}{\langle \alpha_g \rangle \langle j \rangle}, \quad \text{with the mixture volumetric flux j:} \quad j = \alpha_g v_g + \alpha_l v_l. \tag{3.2.8}$$

They have also proposed a simple correlation for the C_0 term as follows:

$$C_0 = 1.2 - 0.2\sqrt{\frac{\rho_g}{\rho_l}}. \tag{3.2.9}$$

Since this work, many studies have been done to improve the prediction of C_0 (Brooks et al., 2014; Ozaki and Hibiki, 2018) but not for the prediction of the distribution parameter C_{vk} in two-phase flows.

It is worth to note that at the macroscopic scale, the parameter C_0 needs to be modeled, but it can be directly calculated from Neptune_CFD results by the equation (3.2.8). Then, the subgrid terms obtained in momentum equations on this database allow us to estimate the existing correlations (3.2.7) and (3.2.6), while avoiding potential deviations linked to the C_0 correlation. Therefore, the distribution parameter for each phase Cvk defined in equation (3.2.5) is calculated at each macroscopic cell for each test case and is shown in blue in the figure 3.2.10. The correlations proposed by Ishii and Hibiki (2011) are also calculated at each macroscopic cell and for each test case, using the calculated C_0, i.e., from Neptune_CFD, and are shown in red in figure 3.2.10.

The distribution parameter of each macroscopic cell is plotted as a function of the macroscopic cell void fraction. Each transparent point corresponds to a C_{vk} value at a macroscopic cell of a test case. Therefore, there are 50 points for each test case. A large part of those points corresponds to $\langle \alpha_g \rangle = 0$, where the gas distribution parameter has no physical meaning. Therefore, those points are not represented in this figure. The blue and red lines represent the mean values of the distribution parameter at each macroscopic void fraction. The dashed lines correspond to the minimum and maximum values of the distribution parameter.

The calculated distribution parameters C_{vk}, directly from CFD simulations, both for liquid and gas phases, lie between 1.0 and 1.1. However, even with C_0 calculated using CFD data, the C_{vk} predicted by correlation is always below 1.0 and converges to 1.0 as the void fraction increases. Our observations suggest that equations (3.2.7) and (3.2.6) are not exact for sub-cooled boiling flows. Then, new correlations for these distribution parameters seem necessary.

Therefore, it is shown that the dispersion terms are not negligible compared to convection terms in both momentum and energy equations and that the existing correlations are insufficient. However, it is also important to evaluate all the terms in momentum and energy equations in order to know if the modeling of some other terms is more critical than the modeling of the dispersion term.

KIT tests

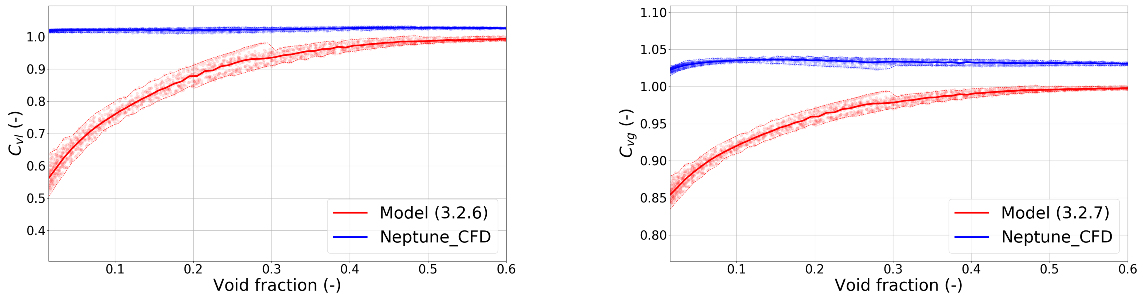

PSBT tests

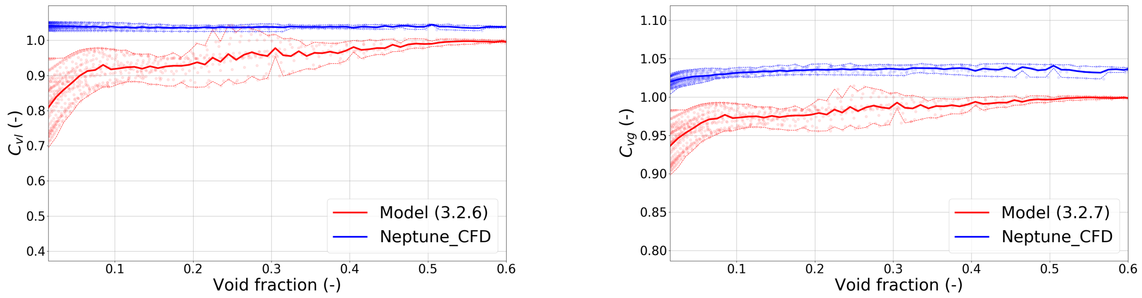

Figure 3.2.10: Distribution parameters of liquid C_{vl} and gas C_{vg} phases as a function of the predicted void fraction, for KIT and PSBT tests. Blue part: calculated values from equation (3.2.5); red part: modeled values from equations (3.2.7) and (3.2.6). Transparent points: values at a macroscopic cell of a test case; dash lines: min and max values; solid lines: mean values.

3.2.3 Identification of the predominant terms

This section aims to identify the predominant terms in the momentum and energy equations by an a priori evaluation of the KIT and PSBT experiments. This evaluation can then provide insights in order to decide on which term it is more relevant to analyze the current models and to propose a new one.

For both momentum and energy equations, first, the axial evolutions of all their terms are analyzed for a representative test case, and then the norms of all the terms in all test cases are compared in one Figure. The axial evolution figures allow us to understand the overall evolution of all the terms and also to verify our average operations. Indeed, the right and left-hand sides of equations need to be equal, and this verification is done by comparing the axial evolution of all terms.

Application on liquid momentum equation

The statistical-volume averaged form of the momentum equation developed in equation (2.2.18) is recalled below for stationary flow:

$$\begin{aligned}\underbrace{\langle\alpha_l\rangle\nabla\left(\Phi\langle P\rangle_l\right)}_{\text{Pressure Gradient (1)}} &= -\underbrace{\nabla.\left(\Phi\langle\alpha_l\rangle\langle\rho_l\rangle_l\langle\underline{v}_l\rangle_{l\rho}\langle\underline{v}_l\rangle_{l\rho}\right)}_{\text{Convection Divergence (2)}} - \underbrace{\nabla.\left(\Phi\langle\alpha_l\rangle\langle\rho_l\rangle_l\langle\delta\underline{v}_l\delta\underline{v}_l\rangle_{l\rho}\right)}_{\text{Dispersion Divergence (3)}} + \underbrace{\Phi\langle\alpha_l\rangle\langle\rho_l\rangle_l\underline{g}}_{\text{Gravity (4)}}\\ &+ \underbrace{\frac{1}{V}\int_{A_w}\left(-P\mathbb{I}+\underline{\underline{\tau_m}}_l\right).\underline{n}_w dA}_{\text{Wall friction (5)}} + \underbrace{\Phi\langle\Gamma_l\overline{\underline{v}}_l^{Im}\rangle}_{\text{Mass transfer (6)}} + \underbrace{\nabla.\left[\Phi\left(\langle\alpha_l\rangle\left\langle\underline{\underline{\tau_m}}_l\right\rangle_l+\left\langle\underline{\underline{\tau_T}}_l\right\rangle\right)\right]}_{\text{Molecular (7) + turbulent diffusion div. (8)}} + \underbrace{\Phi\langle\underline{M}_l\rangle}_{\text{Drag (9)}}.\end{aligned} \tag{3.2.10}$$

The color code is the same as in equation (2.2.18). The variables in black color correspond to the terms known as dependent variables, which are directly calculated by macroscopic codes. The variables in blue represent known constant terms, such as porosity or gravity force. The green terms correspond to variables that are calculated from the equations of state or constitutive equations. The red terms correspond to variables that need to be modeled by closure laws.

Theoretically, all these terms can be determined by an average of local CFD variables. However, given that wall functions are used near walls in CFD calculations, it is difficult to obtain the wall friction term directly from the CFD calculation. Considering that only the overall relative weights of all the terms between themselves are wanted and not the precise values of all terms, a correlation from CATHARE is used to obtain the wall friction term. This correlation is described in the Appendix III. All the other terms are directly calculated from CFD calculations.

Nevertheless, if the sum of all the right hand side terms is equal to the pressure gradient term value, it would simultaneously prove that the wall friction term is well calculated and that the average operations on local variables are also well executed.

The axial evolution of the terms present in the liquid momentum equation for test case 1 of the KIT experiment is shown in Figure 3.2.11. The numbers associated with each term are recalled in this Figure.

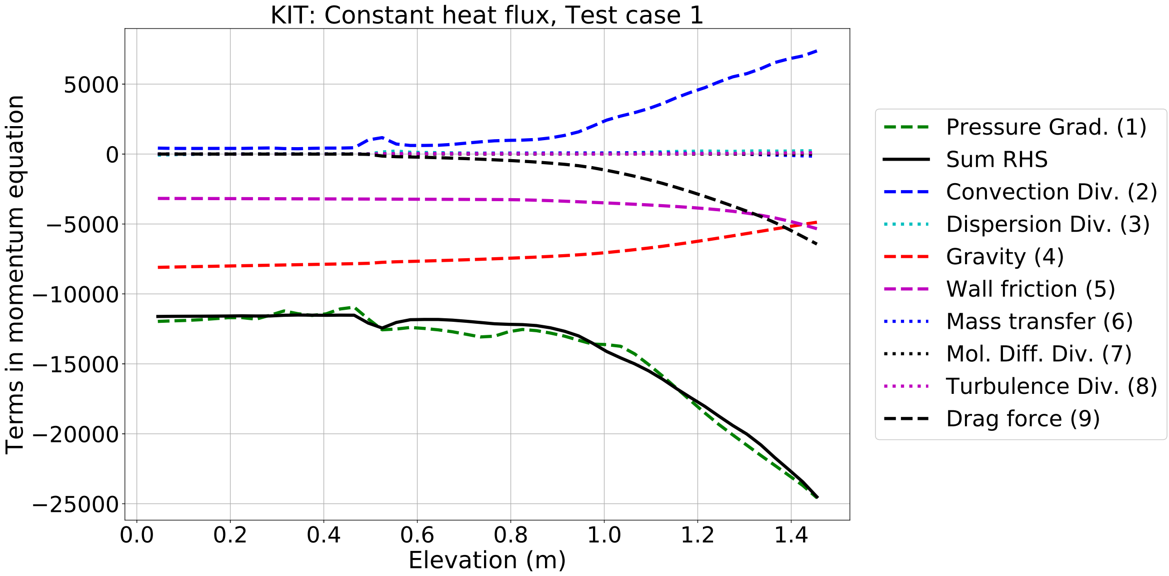

Figure 3.2.11: Axial evolution of all the terms described in liquid momentum equation (3.2.10).

First of all, it can be seen that both the pressure gradient term (green dashed line) and the sum of all the right-hand side terms (black line) of equation (3.2.10) are close but not equal. The fact that the curves are close shows that the average operations are relevant. The slight differences can come from the fact that a correlation is used to obtain the wall friction term. However, since it is only the overall behavior of all terms that are wanted, the accuracy of these results is sufficient.

This section aims to identify the predominant terms in industrial conditions and, in particular, the predominant terms that need to be modeled, in red in equation (3.2.10). This identification allows in the following to choose which term needs the most to be modeled. Therefore, all the absolute values of the terms in red in equation (3.2.10) are shown in a logarithmic scale in Figure 3.2.12. All the terms are normalized by the wall friction value. The choice of the normalization by the wall friction is made since this term value is monotonous with little variation along the axial direction.

First, this Figure can be split into two regions: a one-phase liquid region from the inlet to 0.5m and a sub-cooled boiling region from 0.5m to the outlet. In the first region, the dispersion and turbulence terms are low compared to the wall friction term and the drag force, and mass transfer terms appear only when steam bubbles are created. Therefore, in the one-phase liquid region, the wall friction term is predominant. In the sub-cooled boiling region above 0.5m, the turbulence and mass transfer terms are lower than 3 % of the wall friction term. The dispersion

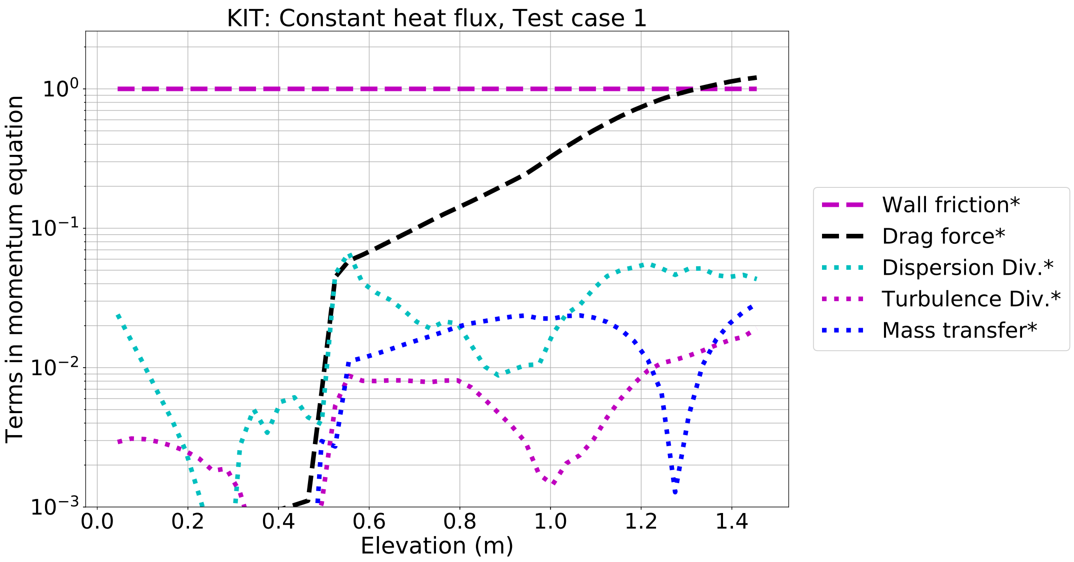

Figure 3.2.12: Axial evolution of all the terms that need to be modeled, in red in equation (3.2.10).

term is lower but not negligible compared to the wall friction term, between 1 % and 7 %. Finally, the drag force term becomes clearly also predominant along with the wall friction term, from 7 % at the onset of nucleate boiling to above 100 % of this wall friction term at the outlet. The sub-cooled boiling region is especially studied in this work. This is why, in the following, only the terms in the sub-cooled boiling region are studied, where $\alpha_g > 0.001$ and $T_l < T_{sat} - 1$.

The momentum equation is usually solved in a non-conservative form, in which the mass transfer term disappears, as shown in equation (2.2.18). For this reason and for clarity, only the dispersion, turbulence, drag and wall friction terms are compared in sub-cooled boiling conditions in the following. The L^1-norm and L^∞-norm of each term, normalized by the norm of the wall friction term, are shown for all the test cases for the KIT experiment in Figure 3.2.13.

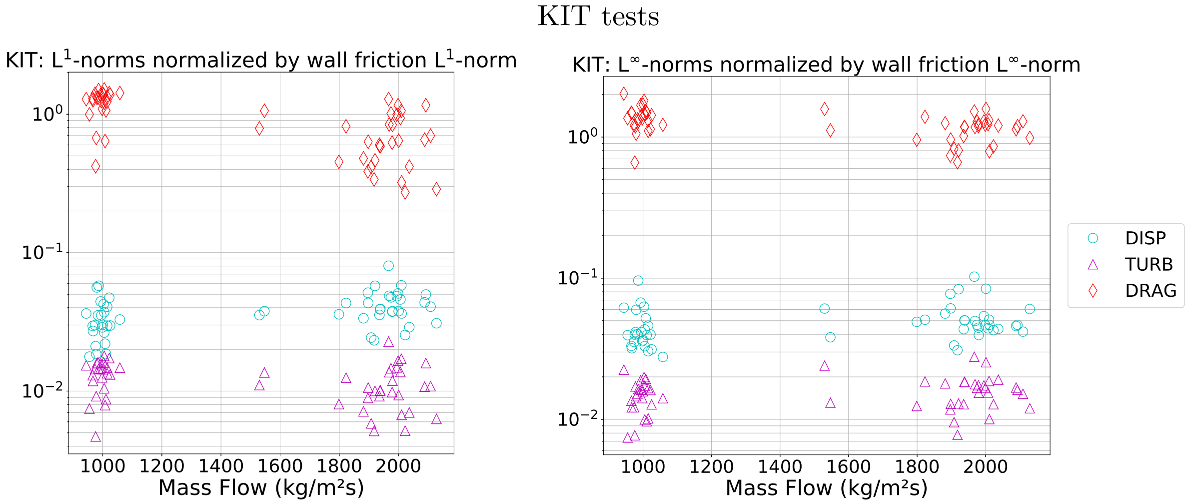

Figure 3.2.13: Norms values of dispersion derivatives (cyan), turbulence derivatives (magenta) and drag (red) terms normalized by wall friction norm values in liquid momentum equation.

This Figure shows that between the terms that need to be modeled, the drag and wall friction terms are predominant. Indeed, the norms of the drag force are, in some cases, greater and, in some cases, lower than the wall friction norms. Therefore, these two terms need to be modeled in priority. However, the dispersion term cannot be neglected since its norms range from 2 %

to 10 % of the wall friction norms. The turbulence is lower, from 0.4 % to 2 %. Nevertheless, these terms cannot be taken independently in two-phase flow conditions since the drag forces, the wall friction and the dispersion term coexist in these conditions. Thus, it seems difficult to find a separate effect test on one of these terms in two-phase flow conditions.

Application on liquid energy equation

The statistical-volume averaged form of the energy equation developed in equation (2.2.26) is recalled below for stationary flow:

$$\begin{aligned}\underbrace{\nabla.(\Phi\langle\alpha_l\rangle\langle\rho_l\rangle_l\langle H_l\rangle_{l\rho}\langle\underline{v}_l\rangle_{l\rho})}_{\text{Convection divergence (1)}} = & -\underbrace{\nabla.(\Phi\langle\alpha_l\rangle\langle\rho_l\rangle_l\langle\delta H_l\delta\underline{v}_l\rangle_{l\rho})}_{\text{Dispersion divergence (2)}} + \underbrace{\frac{1}{V}\int_{A_w}\alpha_l\lambda_l\nabla T_l.\mathbf{n}_w dA}_{\substack{\text{Wall heat flux to liquid (3)}\\ \phi_{conv}+\phi_{quench}}} \\ & + \underbrace{\Phi\langle\Pi'_l\rangle}_{\text{Interfacial transfer (4)}} + \underbrace{\Phi\langle\Gamma_l\overline{H}_l^{Ie}\rangle}_{\substack{\text{Transfer due to mass change (5)}\\ \text{Condensation + Nucleation}}} + \underbrace{\nabla.[\langle\alpha_l\rangle\lambda_l\Phi\nabla\langle T_l\rangle_l]}_{\text{Conductive flux}}.\end{aligned} \tag{3.2.11}$$

All the terms in this equation can be determined from CFD calculations by average operations, and all the variables in red need closure relations to be estimated at the macroscopic scale. In one-direction calculation, the conductive flux is negligible compared to all the other terms, more than 10^6 times lower. For two test cases, the axial evolution of all the terms, except the conductive flux, which is negligible, are shown in Figure 3.2.14.

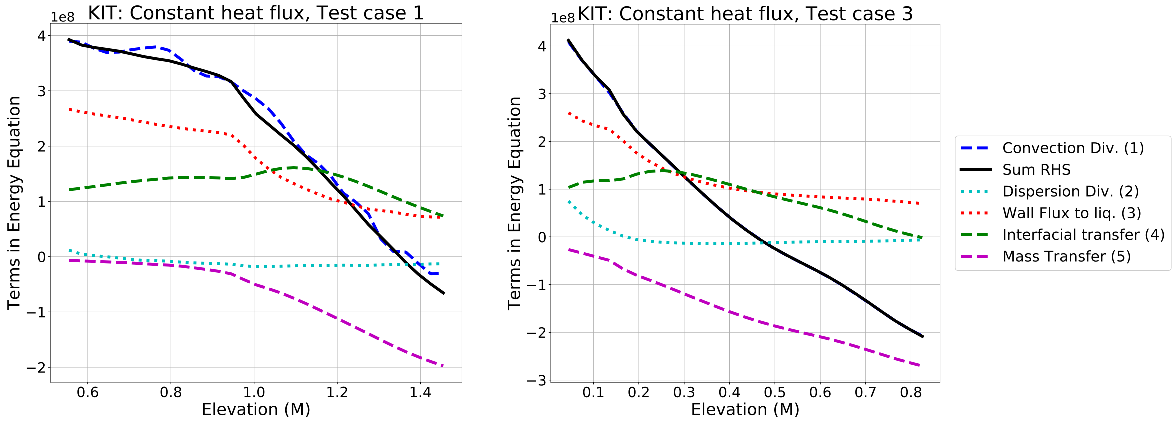

Figure 3.2.14: Axial evolution of all the terms described in liquid energy equation (3.2.3).

First, the convection divergence term is equal to the sum of all the right-hand side terms in test case 3, while it is not exactly equal in test case 1. These deviations, visible only in a few test cases, could result from the numerical scheme used to calculate the divergence, which is a centered scheme of second-order. Nevertheless, the convection and the sum of the right-hand side terms are sufficiently close in all the test cases to be confident in the average operations done on the CFD variables and, therefore, to estimate the order of magnitude of all terms.

Some terms of the liquid energy equation (3.2.3) can be divided in order to highlight some physical phenomena. For example, the mass transfer term can be divided into two terms, one related to the condensation and one related to the nucleation. Moreover, it is important to note that the interfacial transfer term Π'_l is closely related to the mass transfer term of condensation Γ_l^c for steam-water in sub-cooled boiling flow. Indeed, both terms are related by this formula:

$$\Gamma_l^c = \frac{\Pi'_l + \Pi'_g}{H_g - H_l}. \tag{3.2.12}$$

For sub-cooled boiling flow, the term Π'_g is negligible compared to the Π'_l term.

Moreover, the terms of wall heat flux to liquid and nucleation are unknown, but they are directly related. Indeed, the total wall heat flux is known as a boundary condition and is divided into three different categories: convection, quenching, and nucleation, as follows:

$$\phi_{wall} = \phi_{conv} + \phi_{quench} + \underbrace{\Gamma^{nuc}\left(H_g - H_l\right)}_{\phi_{vaporization}} = \phi_{wall\to liq} + \phi_{wall\to gas} \tag{3.2.13}$$

$$\text{with: } \phi_{wall\to liq} = \phi_{conv} + \phi_{quench} - \underbrace{\Gamma^{nuc} H_l}_{\text{Nucleation}} \tag{3.2.14}$$

$$\phi_{wall\to gas} = \Gamma^{nuc} H_g \tag{3.2.15}$$

Therefore, the term $\phi_{wall\to liq}$ is included in the liquid energy equation in two terms, on the one hand in the wall heat flux to liquid term, and on the other hand in the nucleation part of the mass transfer term. Since the total wall heat flux is known and the nucleation term is estimated by a model, the wall heat flux to liquid term $(\phi_{conv} + \phi_{quench})$ can be determined directly from the other terms. Therefore, the unknown terms are the dispersion divergence, the interfacial transfers between bubbles and sub-cooled water, and the mass transfer terms of condensation and nucleation. The orders of magnitude of all these terms are compared for all the test cases of KIT in Figure 3.2.15.

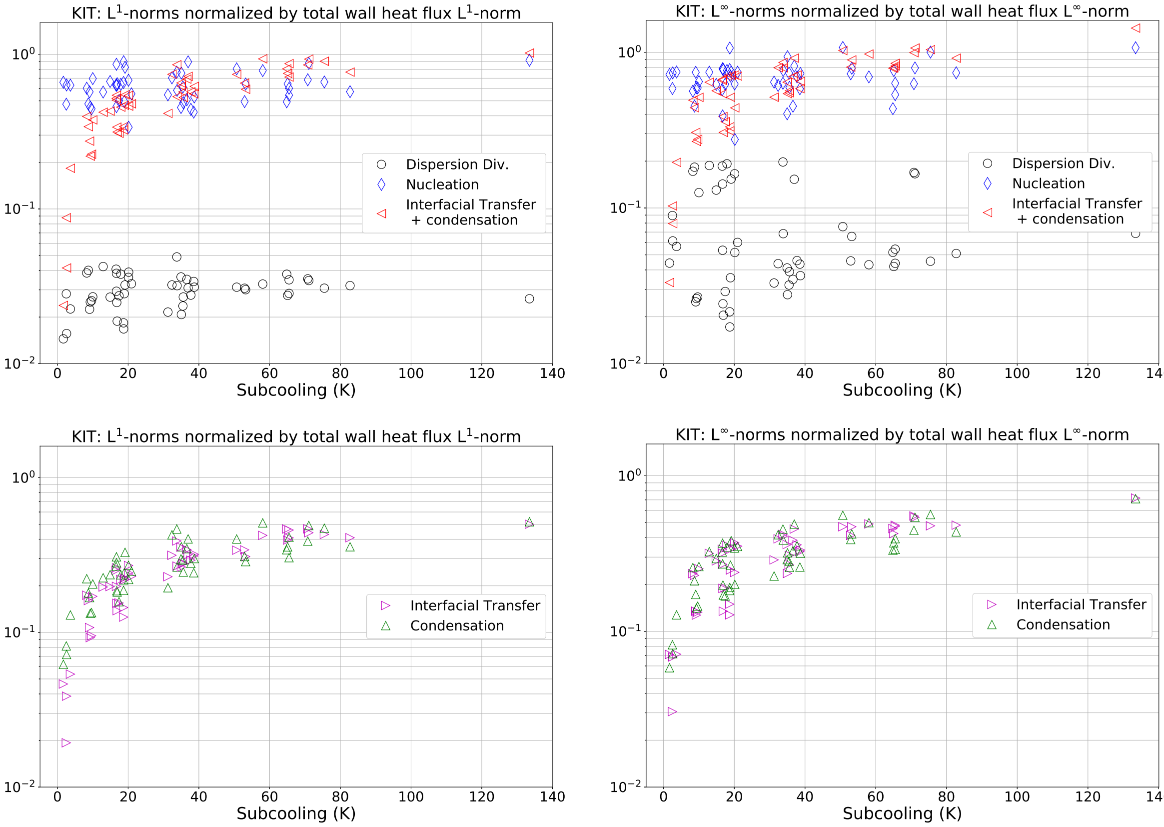

Figure 3.2.15: Upper part: Norms values of dispersion divergence (black), nucleation (blue) and the sum of interfacial transfer and condensation (red) terms normalized by wall friction norm values in liquid energy equation (3.2.3). Lower part: Norms values of normalized interfacial transfer (magenta) and condensation (green) terms.

The results obtained for the PSBT tests are similar. For clarity, the results from PSBT tests are not shown in this Figure. Since in sub-cooled boiling flows, the interfacial energy transfers Π_l' are directly related to the interfacial mass transfers of condensation Γ_l^c, both terms can be modeled in the same way. Consequently, these two terms are represented together as a sum: $\langle \Pi_l' \rangle + \langle \Gamma_l \overline{H}_l^{Ie} \rangle$, in the upper side of the Figure 3.2.15, and are compared between themselves in the lower part. Moreover, the left part corresponds to the L^1-norm of the terms normalized by the L^1-norm of the total wall heat flux, while the right part corresponds to the L^∞-norm.

First, there is a clear link between the inlet liquid sub-cooling and the interfacial transfers and condensation terms. This result is consistent since there is not much condensation and interfacial transfers when the liquid temperature is close to saturation. These relations between the sub-cooling and the normalized norms are not found for the nucleation and dispersion divergence terms. However, there is a clear difference between the normalized L^1 and L^∞ norms of the dispersion divergence terms. This is due to the fact that the dispersion divergence term is important near the inlet and diminishes when the temperature approaches saturation. Indeed, the dispersion term is null at the inlet since there is a flat radial profile of enthalpy, and is high slightly above since the temperature is high near the walls and low at the bulk. Above, when the bulk temperature increases, the spatial fluctuations of enthalpy decrease, and so does the dispersion term also. Therefore, as it can be seen in test case 3 in Figure 3.2.14, the dispersion divergence is important near the inlet, and low above. This is why the L^∞ of this term is not negligible, near 20 % of the wall heat flux norm in some cases, while the L^1-norm of this term is lower, below 5 %.

Either way, the nucleation term is always predominant, and the sum of interfacial transfers and condensation terms also becomes predominant when the sub-cooling is higher than 10K, regardless of the norm operator that is used. Moreover, the energy interfacial transfer and condensation terms are in the same order of magnitude as shown in the lower part of Figure 3.2.15. Therefore, although the dispersion term should not be neglected, the terms linked to the interfacial transfers, namely energy interfacial transfers, condensation and nucleation, are predominant. Consequently, we have chosen to focus on the modeling of interfacial transfers in the following part of the thesis. We have made the choice to model the energy interfacial transfers and the condensation of steam in sub-cooled water since both terms are related. The choice of working on these terms and not the nucleation term is made since in sub-cooled boiling, the ebullition always comes with bulk condensation and some other phenomena, such as coalescence and break-up, etc. However, some separate effect experiments are done concerning the bubble condensation in sub-cooled water, in which only the condensation and the interfacial energy transfers play a predominant role. This is the case of the TOPFLOW experiment, which is used in the following section.

3.3 Discussions

In this chapter, we have developed a local CFD database on sub-cooled boiling test cases of two experiments representative of industrial conditions, namely KIT and PSBT, which consist of, respectively, a pipe and a subchannel geometry. The void fractions predicted by Neptune_CFD are compared to the experimental ones on all the 86 test cases. Although it is difficult to conclude on the full validation of all the test cases only based on the void fraction comparisons, the consistent void fraction predictions obtained allow us to be confident in the overall consistency of all the predicted variables. Either way, the test cases for which the predicted void fractions are sufficiently close to the experimental ones are selected in the CFD database, which is then used for the a priori evaluation. The a priori evaluation consisted of estimating the macroscopic terms by calculating the average of the local simulated variables. The a priori evaluation has been divided into two parts.

First, the subgrid terms of turbulence and dispersion have been compared to the convection term. We have shown that concerning the momentum and energy equations, the dispersion terms reach respectively 7.5 % and 16 % of the convection terms and are therefore not always negligible. Moreover, the geometry has an impact on the dispersion terms, and so, the correlations developed for this term on a geometry should be used carefully on other geometries. The correlations developed by Ishii and Hibiki (2011) for the liquid and gas momentum dispersion terms have been tested and some discrepancies have been observed between the values predicted by these correlations and those calculated by the a priori evaluation. Therefore, some new correlations need to be formulated in order to accurately predict these subgrid terms.

The second part of the a priori evaluation consisted of the comparison of all the terms in momentum and energy equations. In the momentum equation, several terms play a key role and are not negligible. Moreover, these terms are inter-dependent and, therefore, it is challenging to identify separate effect tests where only one of these terms would be predominant. In the liquid energy equation, although the dispersion is non-negligible compared to the convection term, the terms linked to the interfacial transfers, and linked to the transfers due to phase change are predominant. Moreover, the value of the nucleation term is similar to the sum of the interfacial energy transfers and the transfers due to the condensation phenomenon. Therefore, an error of around 15 % of an interfacial term can cause an error of around 100 % of the dispersion term. Consequently, it seems more relevant to focus on the development of a macroscopic model for either the ebullition or the condensation term. The best way to model it would be to use a local CFD database of a separate effect experiment, which would include only the phenomena that we want to model. Unfortunately, in sub-cooled boiling, the ebullition always comes with bulk condensation, and some other phenomena as for example coalescence and break-up. On the other hand, some separate effect experiments exist concerning the bubble condensation in sub-cooled water, in which only the condensation plays a predominant role.

Therefore, the next chapter consists of establishing a validated local CFD database of condensing flows, which will then be used to develop a condensation model at the macroscopic scale. Since the mass transfer term linked to the condensation Γ_l^c is directly linked to the interfacial energy transfer term Π_l', only the interfacial energy transfer term will be modeled at macroscopic scale in chapter 5.

However, the bubbles are usually polydisperse in size, and the local monodisperse assumption, which is currently used, is not always relevant. This is why the polydispersion assumption is adapted to the models related to the condensation, in order to build a CFD database that is fully validated, i.e., which predicts the radial profiles of gas volume fraction, Sauter diameter, velocity, and liquid temperature close to the measurements.

Chapter 4

Creation of a bubble condensation CFD database by the development of a polydisperse modeling

Contents

This chapter presents the modeling that has been implemented in order to accurately treat interfacial transfers in the case of bubble condensation in sub-cooled water. Thus, a CFD database is developed in this chapter with calculated local variables and is validated by comparison to the experimental local data of gas volume fraction, Sauter diameter, velocity, and liquid temperature. These flows are generally highly polydisperse in bubble size, and an appropriate modeling of these flows is therefore necessary.

Currently, two approaches are used to study the phenomenon of bubble condensation. The first considers a monodisperse bubble size distribution, i.e., all bubbles are assumed to have the same size locally. This approach makes it possible to minimize the calculation time, but the results obtained can be imprecise in certain situations. The second uses a polydisperse distribution, which is based on several bubble size groups. It is therefore more relevant but also more costly in terms of calculation time.

The objective is to propose a modeling that makes it possible to precisely simulate the condensation of bubbles while maintaining a reasonable calculation time. To satisfy this objective, we have used the standard method of moments with a quadratic distribution of bubbles. This new method is evaluated and compared to the current one in the case of bubble condensation in this chapter. Moreover, a model is introduced to take into account the bubble collapse phenomena due to condensation.

The work presented in this chapter has been published in the International Journal of Multiphase Flow (Herry et al., 2024a).

4.1 Choice of a highly instrumented condensation experiment

In order to study the bubble condensation phenomenon at the CFD scale, it is better to work on a separate effect test facility of this phenomenon. It is then necessary to find a highly instrumented test facility in which bubble condensation is the only predominant phenomenon. For all these reasons, the TOPFLOW facility has been chosen and is described in the next section.

4.1.1 Interests of the TOPFLOW facility

The TOPFLOW test facility is described in detail by Lucas and Prasser (2007) and Lucas et al. (2013). A scheme of this facility is shown in Figure 4.1.1a.

The test section is a large vertical pipe with an inner diameter of 195.3mm and a length of about 8m. Saturated steam bubbles are injected in sub-cooled water by either 72 or 32 orifices of a diameter of 1mm and 4mm, respectively, equally distributed around the pipe, which assures a rotation-symmetric gas injection.

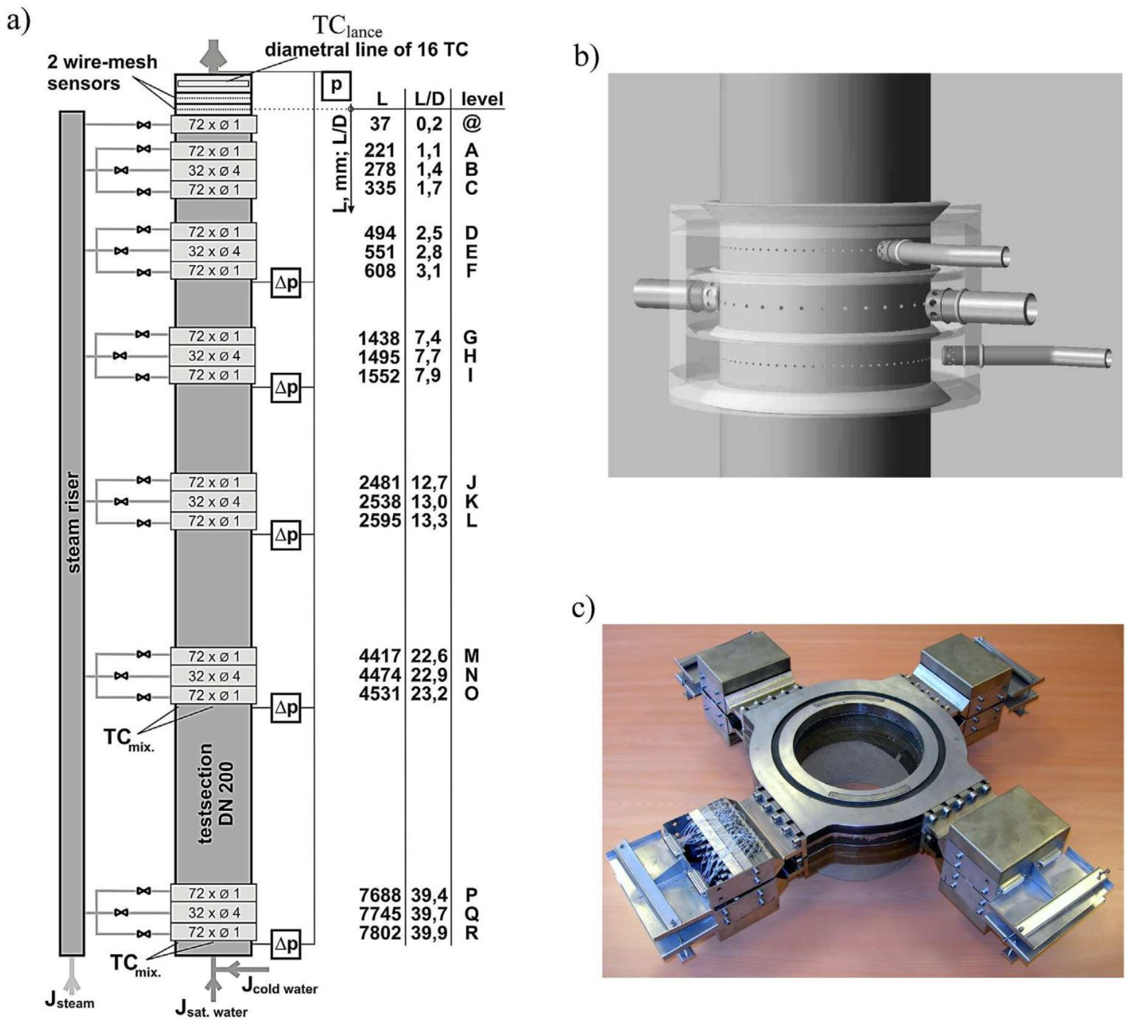

Figure 4.1.1: Variable gas injection: (a) Scheme of the test section, (b) Gas injection device, (c) Wire-mesh sensors (Krepper et al., 2011).

Seven test cases with different pressure, initial sub-cooling and orifice diameters are investigated in this work, the details of these test cases are given in Table 4.1.1.

Case	P [bar]	J_l [m/s]	J_g [m/s]	ΔT_{in} [K]	D_{or} [mm]
1	10	1.017	0.219	3.9	1.0
2	10	1.017	0.219	5.0	1.0
3	20	1.017	0.219	3.7	1.0
4	20	1.017	0.219	6.0	1.0
5	20	1.017	0.219	6.0	4.0
6	40	1.017	0.219	5.0	1.0
7	65	1.017	0.219	7.4	1.0

Table 4.1.1: Selected test cases of the TOPFLOW experiment.

The experimental bubble size distributions which are shown and described in section 4.2.3 indicate that a bubbly flow regime is encountered in these test cases.

Measurements of radial profiles of gas volume fraction, gas velocity, bubble size distribution, and liquid temperature are acquired at different heights using wire-mesh sensors and a lance of thermocouples. The wire-mesh sensors are shown in Figure 4.1.1c. The height position of each level relative to the steam injection for each orifice diameter is given in Table 4.1.2. Liao and Lucas (2016) have claimed that some vortices exist below Levels A/B and disappear before reaching Levels A/B. Therefore, they use Level A or Level B as inlet conditions in their simulations. Following the same approach, Levels A/B are also used as inlet conditions in this work. Moreover, it should be noted that injected bubbles are pretty large, and as a consequence, the bubble Reynolds number Re_b lies in the range $[4,000-30,000]$. This experiment allows us to validate condensation models of CFD codes.

$D_{orifice} = 1.0mm$		$D_{orifice} = 4.0mm$	
Level	Height [m]	Level	Height [m]
A (Inlet)	0.221	B(Inlet)	0.278
C	0.335	E	0.551
F	0.608	H	1.495
I	1.552	K	2.538
L	2.595	N	4.474
O	4.531		
P	7.689		

Table 4.1.2: Heights relative to steam injection position.

4.1.2 Measurement uncertainties

Lucas et al. (2010) have analyzed the uncertainties of the measurements. Systematic and statistical errors are considered, and the authors have stated that the number of measured bubbles is very high; therefore, the statistical errors are much lower compared to the systematic errors. Some interactions between the bubbles and the sensor can result in systematic errors, up to 5% for air-water flow, but it should be lower for steam-water flow due to the lower surface tension. Absolute errors in void fraction could be up to ±1% for bubble flow. But this error evaluation has been done by Prasser et al. (2005) for a cross-section averaged void fraction of about 25%, so this absolute error should be much lower for the test cases investigated in this work, for which the inlet averaged void fraction is around 5%. The error of the temperature measurement is about 1 K. The volume equivalent diameter is measured with an accuracy of ±20%. In the following, simulations are carried out using Neptune_CFD code.

4.2 Choice of a modelization adapted to bubble condensation

It is recalled that the equations used in Neptune_CFD are based on the two-fluid model proposed by Ishii and Hibiki (2011), as it is described in section 1.2. The field equations are given in their primary form with $k = g, l$ denoting gas and liquid phases are recalled below:

$$\frac{\partial}{\partial t}(\alpha_k \overline{\rho}_k) + \underline{\nabla}(\alpha_k \overline{\rho}_k . \overline{\overline{\underline{v}_k}}) = \Gamma_k, \tag{4.2.1a}$$

$$\begin{aligned} \frac{\partial}{\partial t}(\alpha_k \overline{\rho}_k \overline{\overline{\underline{v}_k}}) + \underline{\nabla}(\alpha_k \overline{\rho}_k \overline{\overline{\underline{v}_k}} . \overline{\overline{\underline{v}_k}}) &= \underline{\nabla} . (\alpha_k \overline{\underline{\underline{\tau}}}_k^m + \underline{\underline{\tau}}_k^T) - \alpha_k \underline{\nabla} P + \alpha_k \overline{\rho}_k \underline{g} + \Gamma_k \overline{\overline{\underline{v}_k}}^I \\ &+ \underbrace{\underline{M}_k^D + \underline{M}_k^{AM} + \underline{M}_k^L + \underline{M}_k^T}_{=\underline{M}_k}, \end{aligned} \tag{4.2.1b}$$

$$\frac{\partial}{\partial t}(\alpha_k \overline{\rho}_k \overline{\overline{H}}_k) + \underline{\nabla} . (\alpha_k \overline{\rho}_k \overline{\overline{H}}_k \overline{\overline{\underline{v}_k}}) = -\underline{\nabla} . \left[\alpha_k \left(\overline{\underline{q_m}}_k^k + \overline{\underline{q_T}}_k \right) \right] + \alpha_k \frac{\partial P}{\partial t} + \underbrace{\Gamma_k H_{k,i} + \Pi'_k}_{\Pi_k} + q_{wk}. \tag{4.2.1c}$$

In this work, the gas phase is considered as a dispersed phase. The equations (4.2.1) are written in a general form, and the unknown terms on the right-hand side of the dispersed gas phase equations depend on the bubble size distribution modelization. Two different approaches to model the bubble size distribution are presented in the following, namely the population balance method and the method of moments. In chapter 3, the unknown terms are modeled based on a bubble size monodispersion approach. This approach gives the same formulation as the method of moments using a Dirac function, which is introduced in section 4.2.2.

4.2.1 Existing population balance method (iMUSIG)

The iMUSIG (Krepper et al., 2005) model is based on a multi-fluid Euler-Euler approach, as previously described. The gaseous disperse phase is divided into a number J (j=[1,..., J]) of velocity groups. It assumes a spectrum of bubble size for each velocity group, which is discretized into a number N_j (i=[1, N_j]) of groups. The heat transfer is usually calculated based on the Sauter diameter of the gas phases (or velocity groups) (Liao et al., 2019). Therefore, J momentum and energy equations are resolved for the gas phase. For example, Liao and Lucas (2016) consider two velocity groups with consideration of sign change for the lift force coefficient. As a consequence, small bubbles have a positive coefficient while large bubbles have a negative one (Tomiyama, 1998). Moreover, there are $\sum N_j$ mass balance equations, with, for each group i:

$$\frac{\partial}{\partial t}(\alpha_{g,i}\rho_g) + \underline{\nabla}(\alpha_{g,i}\rho_g.\underline{v}_{g,j}) = S_{ph,i} + S_{nuc,i} + S_{br,i} + S_{coal,i}. \tag{4.2.2}$$

The terms on the right-hand side of the equation (4.2.2) represent sources due to phase change, nucleation, break-up, and coalescence, respectively. In this work, only bubble condensation is considered as phase change, so, in this case, the nucleation term is null. The other balance equations are presented by Lucas et al. (2011).

This approach permits the bubble size change to be taken into account quite naturally during evaporation and condensation. However, this approach is time-consuming since it usually needs to solve two momentum and energy equations for the gas phase, as well as a few dozen mass balance equations.

Simulations results using this method have been obtained by Liao and Lucas (2016) on the bubble condensation experiment TOPFLOW. Then, these results are compared in section 4.5 to the results obtained using the Dirac and the quadratic approaches, which are expressed in the next section.

4.2.2 Choice of the method of moments

The method of moments is applied in this work since the computational cost is much lower than the one obtained using the iMUSIG approach. In this method, the transport equations of the statistic moments of the bubble size distribution are considered. The general idea of this method is to build the PDF (Probability Density Function) based on the knowledge of a finite number of its moments. Therefore, this method differs from the population balance method previously presented, which is based on a discretization in the bubble size space. In the method of moments, it is the integral information that matters and not the distribution shape details.

There are two subcategories to the method of moments, the first is the Standard Method of Moments (SMM), which is developed by Hulburt and Katz (1964) and is used by Kamp et al. (2001); Ruyer and Seiler (2009) and Zaepffel et al. (2012). This approach consists of imposing a law for the bubble size distribution function, such as a log-normal or quadratic law. Given that there are some restrictions to the applicability of the SMM, McGraw (1997) has proposed a second method of moments, which approximates the integrals by using a N-point Gaussian quadrature.

In this work, we will use the first method, the SMM, using simple laws such as a Dirac law (monodisperse approach) and a quadratic law (polydisperse approach) to describe the bubble size distribution. Indeed, by using such simple functions, it is possible to obtain simple relations between the statistic moments and the parameters of the bubble size distribution law f. In this way, it is also possible to get a simple expression of the integrals used to estimate the source terms in the transport equations. However, initially, it is necessary to introduce the mathematical formalism required to describe a bubble population statistically. It should be noted that it is assumed that all bubbles have spherical shape in this work.

Statistical distribution formalism

First of all, a phase space Ω of the bubble population description is introduced and can be divided into external and internal coordinates:

- Externals: the position vector $\underline{x}$ and the time t.
- Internal: the bubble size, given by the diameter ζ_b, the bubble mass center velocity $\underline{c}_b$, and its enthalpy θ_b. We define Ω_{int} the phase subspace corresponding to the internal coordinates.

Then, we introduce the bubble size distribution function $F(kg^{-1}.m^{-9}.s^5)$. Using this variable, $F(\zeta_b, \underline{c}_b, \theta_b, \underline{x}, t)\delta\zeta_b\delta\underline{c}_b\delta\theta_b\delta\underline{x}$ represents the probable number of bubbles with bubble center $x_b(t) \in [x, x+\delta x[$, with bubble diameter $d_b(t) \in [\zeta_b, \zeta_b+\delta\zeta_b[$, bubble velocity $\underline{\omega}_b(t) \in [\underline{c}_b, \underline{c}_b+\delta\underline{c}_b[$, and bubble enthalpy $h_b(t) \in [\theta_b, \theta_b + \delta\theta_b[$.

Using this definition, the bubble number density $n_b(m^{-3})$ is given by:

$$n_b(\underline{x}, t) = \int_{\Omega_{int}} F d\zeta_b \, d\underline{c}_b \, d\theta_b. \tag{4.2.3}$$

In order to describe the flow at the statistical-averaged scale, it is not necessary to precisely know all the dispersed phase distribution functions, but what actually matters is to describe integral quantities. These quantities can be the bubble density number n_b, the mean size of bubbles, the interfacial area between phases, or else the volume fraction of the dispersed phase.

A generic variable $\psi(d_b(t), \underline{u}_b(t), h_b(t), x_b(t); t)$ that depends on the bubble properties is then introduced. Moreover, a conditional expectation is introduced as:

$$\langle \psi|_{\zeta_b, \underline{c}_b, \theta_b} \rangle = \langle \psi|_{d_b=\zeta_b, \underline{\omega}_b=\underline{c}_b, h_b=\theta_b} \rangle. \tag{4.2.4}$$

Next, in order to deduce these integral quantities from the size distribution function F, an average operator of the variable ψ weighted by a variable Y is introduced as:

$$\langle \psi \rangle_Y = \frac{\int_{\Omega_{\text{int}}} F \langle \psi|_{\zeta_b, \underline{c}_b, \theta_b} \rangle Y d\zeta_b \, d\underline{c}_b \, d\theta_b}{\int_{\Omega_{\text{int}}} F Y d\zeta_b \, d\underline{c}_b \, d\theta_b}. \tag{4.2.5}$$

Then, a volumetric quantity can be introduced as:

$$\mu_\psi = \int F \langle \psi|_{\zeta_b, \underline{c}_b, \theta_b} \rangle d\zeta_b \, d\underline{c}_b \, d\theta_b = n_b \langle \psi \rangle_1. \tag{4.2.6}$$

It can be noted that using definitions (4.2.5) and (4.2.6), the following expressions can be obtained:

$$\frac{\mu_{\psi \underline{\omega}_b}}{\mu_\psi} = \langle \underline{\omega}_b \rangle_\psi, \tag{4.2.7}$$

$$\frac{\mu_{\psi \underline{\omega}_b \, \underline{\omega}_b}}{\mu_\psi} = \langle \underline{\omega}_b \, \underline{\omega}_b \rangle_\psi, \tag{4.2.8}$$

If the variable ψ can be written as $\psi = d_b^\gamma$, then this quantity corresponds to the γ-th moment μ of the bubble size distribution function F around 0, as:

$$\mu_{d_b^\gamma} = \int F \langle d_b^\gamma|_{\zeta_b, \underline{c}_b, \theta_b} \rangle d\zeta_b \, d\underline{c}_b \, d\theta_b. \tag{4.2.9}$$

These moments are linked to the integral quantities by these relations:

$$n_b = \mu_{d_b^0}, \tag{4.2.10}$$

$$a_i = \pi \mu_{d_b^2}, \tag{4.2.11}$$

$$\alpha_g = \pi \frac{\mu_{d_b^3}}{6}, \tag{4.2.12}$$

with a_i the interfacial area concentration. The formulation (4.2.10) is direct using equations (4.2.9) and (4.2.3). The two other formulations come from the area and volume formula of a sphere, integrated along the bubble size distribution function. Moreover, the local mean diameters $d_{\gamma1\gamma2}$ are also introduced as:

$$d_{\gamma1\gamma2} = \left(\frac{\mu_{d^{\gamma1}}}{\mu_{d^{\gamma2}}}\right) \quad \text{if} \quad \gamma1 = \gamma2 + 1. \tag{4.2.13}$$

The mean diameter d_{10} and the diameter d_{32} are the most commonly used. Indeed, d_{10} is the arithmetic mean diameter, and d_{32} is interesting because it allows the preservation of the ratio of the exchange surface between phases to the volume fraction of the dispersed phase. Using equations (4.2.11) and (4.2.12), the mean diameter d_{32} can be written:

$$d_{32} = \frac{6\alpha_g}{a_i}. \tag{4.2.14}$$

The formalism described in this section allows us to provide balance equations for the dispersed gas phase that involve the bubble size distribution function. These equations are described in the next section.

Dispersed phase equations

General equations The statistical distribution formalism is expressed in the previous section and so, the dispersed phase equations can now be expressed using the method of moments. Simonin (2000) have shown that an Enskog equation can be obtained from the Liouville equation. This Enskog equation can be written as:

$$\begin{aligned} \frac{\partial \mu_\psi}{\partial t} + \underline{\nabla}\cdot\left(\mu_{\psi\underline{\omega}_b}\right) = & \int \left\langle \frac{\partial \psi}{\partial d_b} \frac{Dd_b}{Dt}\bigg|_{\zeta_b,\underline{c}_b,\theta_b} \right\rangle F d\zeta_b\, d\underline{c}_b\, d\theta_b + \int \left\langle \frac{\partial \psi}{\partial \underline{\omega}_b} \frac{D\underline{\omega}_b}{Dt}\bigg|_{\zeta_b,\underline{c}_b,\theta_b} \right\rangle F d\zeta_b\, d\underline{c}_b\, d\theta_b \\ & + \int \left\langle \frac{\partial \psi}{\partial h_b} \frac{Dh_b}{Dt}\bigg|_{\zeta_b,\underline{c}_b,\theta_b} \right\rangle F d\zeta_b\, d\underline{c}_b\, d\theta_b + \int \psi S d\zeta_b\, d\underline{c}_b\, d\theta_b. \end{aligned} \tag{4.2.15}$$

In this equation, the term S takes into account the source and sink terms linked to the phenomena of coalescence S_{coal}, break-up S_{bk}, nucleation S_{nuc}, and collapse S_{coll}. The variable μ is a statistic moment as defined in equation (4.2.6), and ψ is a variable that can correspond to the term d^γ as introduced above. Moreover, $D./Dt$ represents the Lagrangian derivative associated to the gas phase description along the bubble trajectory.

The variables of equation (4.2.15) in the case of moment of different order γ are provided in Table 4.2.1.

ψ	Order γ	μ_ψ	$\mu_{\psi\underline{\omega}_b}$	$\frac{\partial\psi}{\partial d_b}$	$\frac{\partial\psi}{\partial \underline{\omega}_b}$	$\frac{\partial\psi}{\partial h_b}$
d_b^0	0	n_b	$n_b\langle\underline{\omega}_b\rangle_1$	0	0	0
d_b^2	2	$\frac{a_i}{\pi}$	$\frac{a_i}{\pi}\langle\underline{\omega}_b\rangle_{d_b^2}$	$2d_b$	0	0
d_b^3	3	$\frac{6\alpha_g}{\pi}$	$\frac{6\alpha_g}{\pi}\langle\underline{\omega}_b\rangle_{d_b^3}$	$3d_b^2$	0	0
$\underline{\omega}_b d_b^3$	3	$\frac{6\alpha_g}{\pi}\langle\underline{\omega}_b\rangle_{d_b^3}$	$\frac{6\alpha_g}{\pi}\langle\underline{\omega}_b\,\underline{\omega}_b\rangle_{d_b^3}$	$3\underline{\omega}_b d_b^2$	d_b^3	0
$h_b d_b^3$	3	$\frac{6\alpha_g}{\pi}\langle h_b\rangle_{d_b^3}$	$\frac{6\alpha_g}{\pi}\langle h_b\,\underline{\omega}_b\rangle_{d_b^3}$	$3h_b d_b^2$	0	d_b^3

Table 4.2.1: Variables of equation (4.2.15) using different variables ψ.

By dividing the term $\underline{\omega}_b$ into a mean and a fluctuation part, as done in definition (1.2.1), the following equation can be obtained:

$$\langle\underline{\omega}_b\,\underline{\omega}_b\rangle_{d_b^3} = \langle(\langle\underline{\omega}_b\rangle_{d_b^3} + \underline{\omega}_b')\cdot(\langle\underline{\omega}_b\rangle_{d_b^3} + \underline{\omega}_b')\rangle_{d_b^3} = \langle\underline{\omega}\rangle_{d_b^3}\langle\underline{\omega}\rangle_{d_b^3} + \langle\underline{\omega}_b'\,\underline{\omega}_b'\rangle. \tag{4.2.16}$$

A similar formulation can be obtained using the average of the product of enthalpy and velocity.

Using Table 4.2.1, the transport equations of the bubble number density n_b, the interfacial area a_i, the gas volume fraction α_g, the mean bubble velocity $\langle \underline{\omega}_b \rangle_{d_b^3}$, and the mean bubble enthalpy $\langle h_b \rangle_{d_b^3}$ can be established.

However, it is difficult to solve these equations since the bubble diameter, velocity, and enthalpy are dependent. This is why some assumptions are provided in the following.

Velocity and enthalpy assumptions In this thesis, the assumption that all bubbles have the same velocity and temperature is made. The assumption that all bubbles have the same temperature seems accurate for sub-cooled boiling flow since the gas temperature is always around the saturation temperature. The assumption that all bubbles travel locally at the same velocity is more questionable physically, but it provides an equation system that is easier to solve. Indeed, using this assumption, the distribution function F can be written as the product of three independent functions, namely the bubble size, the velocity, and the enthalpy distributions:

$$F = f(\zeta_b, \underline{x}, t)\,\delta_{\langle \underline{\omega}_b \rangle_{d_b^3}}(\underline{\omega}_b)\,\delta_{\langle h_b \rangle_{d_b^3}}(h_b). \tag{4.2.17}$$

Therefore, due to the assumption that all bubbles are traveling at the same velocity and that the mean gas velocity $\underline{v}_g$ is equal to the bubble mass center mean velocity $\langle \underline{\omega} \rangle_{d^3}$, this relation is obtained: $\underline{v}_g = \langle \underline{\omega} \rangle_{d^2} = \langle \underline{\omega} \rangle_{d^3}$. Using this assumption, the bubbles fluctuation velocities are null, and so the gas turbulence is neglected. Moreover, the mean enthalpy is written $\langle h_b \rangle_{d_b^3} = H_g$ in the following.

In the following, the bubble diameter and bubble density number are written $\zeta_b = d$ and $n_b = n$.

Balance equation establishment From equation (4.2.15) using γ-order of respectively 2 and 3, the hypotheses formulated and the values of Table 4.2.1, the transport equations of a_i, known as IATE, and the transport equation of α_g can be obtained:

$$\frac{\partial a_i}{\partial t} + \underline{\nabla}.\left(a_i \underline{v}_g\right) = \int 2\pi d \frac{Dd}{Dt} f \partial d + \int \pi d^2 (S_{coal} + S_{bk} + S_{nuc} + S_{coll}) \partial d, \tag{4.2.18}$$

$$\frac{\partial \alpha_g \rho_g}{\partial t} + \underline{\nabla}.\left(\alpha_g \rho_g \underline{v}_g\right) = \underbrace{\int \rho_g \frac{\pi d^2}{2} \frac{Dd}{Dt} f \partial d}_{\Gamma_{g,bulk}} + \underbrace{\int \rho_g \frac{\pi d^3}{6} S_{nuc} \partial d}_{\Gamma_{g,nuc}}. \tag{4.2.19}$$

The collapse source term S_{coll} is present in equation (4.2.18) but is neglected in most numerical tools. Moreover, this term is modeled in equation (4.2.19) and in the following balance equations of momentum and energy together with the bulk interfacial mass transfer term $\Gamma_{g,bulk}$. The break-up and coalescence phenomena have a high impact on the interfacial area concentration but not on the void fraction. Similarly, these terms do not impact the momentum and energy balance equations due to the assumption of the same velocity and temperature for all bubbles. It should be noted that in equation (4.2.19), in order to relate to the balance equations of the two-fluid model, the part associated with compressibility and dilatability of the term Dd/Dt is already taken apart from the integral and is included in the left-hand side terms. This is also the case for the momentum and energy balance equations that are presented hereafter. Therefore, the Dd/Dt term presented in these equations only accounts for the bubble diameter change along its trajectory due to phase change.

Then, an equation analog to the momentum balance equation can also be obtained from the method of moments using the variable $\psi = \underline{\omega}_b d_b^3$ (Ruyer and Seiler, 2009):

$$\frac{\partial \alpha_g \rho_g \underline{v}_g}{\partial t} + \underline{\nabla}(\alpha_g \rho_g \underline{v}_g . \underline{v}_g) = \underbrace{\int \rho_g \frac{\pi d^2}{2} \underline{v}_g \frac{Dd}{Dt} f \partial d}_{\underline{v}_g \Gamma_{g,bulk}} + \int \rho_g \frac{\pi d^3}{6} \frac{D\underline{v}_g}{Dt} f \partial d + \underbrace{\int \rho_g S_{nuc} \frac{\pi d^3}{6} \underline{v}_g \partial d}_{\underline{v}_g \Gamma_{g,nuc}}, \tag{4.2.20}$$

with:

$$\frac{D\underline{v}_g}{Dt} = \underline{g} - \frac{1}{\rho_g}\underline{\nabla}P - \frac{\rho_l}{\rho_g}\sum_i \underline{F}_i(d). \tag{4.2.21}$$

The terms $\underline{F}_i$ correspond to the various forces acting on an individual bubble of size d, which are divided in the forces of added mass, drag, lift and dispersion. The bubble diameter appears explicitly in most drag and lift force models but does not appear in added mass and turbulent dispersion models. Therefore, in this work, the drag and lift forces depend on the bubble size distribution, and the added mass and turbulent dispersion forces do not rely on the distribution. Consequently, using the monodispersion assumption in velocity, the equation (4.2.20) is simplified:

$$\begin{aligned}\frac{\partial \alpha_g \rho_g \underline{v}_g}{\partial t} + \underline{\nabla}(\alpha_g \rho_g \underline{v}_g . \underline{v}_g) =& \alpha_g \rho_g \underline{g} - \alpha_g \underline{\nabla} P + \underline{v}_g (\Gamma_{g,bulk} + \Gamma_{g,nuc}) \\ &+ \underline{F}^{AM} + \underline{F}^{TD} + \int \rho_g \frac{\pi d^3}{6} f (\underline{F}^D + \underline{F}^L) \partial d.\end{aligned} \tag{4.2.22}$$

It is worth noting that the terms $\Gamma_{g,bulk}$ and $\Gamma_{g,nuc}$ depend on the size distribution function and are defined in equation (4.2.19). Moreover, despite the fact that only one velocity is assumed for all bubbles, the local polydispersion in bubble size is taken into account in the interfacial forces of drag and lift, and in the terms Γ. Then, the local dispersion is considered in the gas hydrodynamic behavior. Therefore, in this work, the gas velocity directly depends on the local bubble size polydispersion effects.

Finally, the energy balance equation can also be deducted from the method of moments with the variable $\psi = \underline{h_{b_b}} d_b^3$ and is written (Ruyer and Seiler, 2009):

$$\frac{\partial \alpha_g \rho_g H_g}{\partial t} + \underline{\nabla}.(\alpha_g \rho_g \underline{v}_g H_g) = \int \rho_g \frac{\pi d^3}{6} \frac{DH_g}{Dt} f \partial d + \int \rho_g H_g \frac{\pi d^2}{2} \frac{Dd}{Dt} f \partial d + \int \rho_g S_{nuc} \frac{\pi d^3}{6} H_g \partial d. \tag{4.2.23}$$

It is recalled that all bubbles have the same temperature despite possibly different diameters. Then H_g does not depend on the bubble diameter. Moreover, the first source term on the right-hand side of the equation corresponds to the enthalpy change due to bubble collision. Because of the temperature monodispersion hypothesis, H_g can be extracted from the integral, and this first term then corresponds to the gas volume fraction change due to collisions, which is null by definition. Also, resulting from the temperature monodispersion hypothesis, the two last terms are equal to the gas enthalpy multiplied by $\Gamma_{g,bulk}$, and $\Gamma_{g,nuc}$, respectively.

Moreover, the variation of the enthalpy of a bubble along its trajectory is given by its enthalpy balance equation (Ishii and Hibiki, 2011):

$$\int \rho_g \frac{\pi d^3}{6} \frac{DH_g}{Dt} f \partial d = \int \pi d^2 q''_{gi} f \partial d + \alpha_g \left(\frac{\partial P}{\partial t} + \phi_D + \phi_R \right), \tag{4.2.24}$$

where q''_{gi} is the interfacial gas heat flux density, ϕ_D is a dissipation function that is neglected in this study, and ϕ_R is a source term that can be due to radiation or chemical effect and is null in this study. Finally, the enthalpy equation can be formulated:

$$\frac{\partial \alpha_g \rho_g H_g}{\partial t} + \underline{\nabla}.(\alpha_g \rho_g \underline{v}_g H_g) = \int \pi d^2 q''_{gi} f \partial d + \alpha_g \frac{\partial P}{\partial t} + H_g \left(\Gamma_{bulk} + \Gamma_{nuc} \right). \tag{4.2.25}$$

Therefore, all the balance equations are formulated in this section. However, the bubble size distribution function f needs to be defined in order to close the system. A Dirac law and a quadratic law are introduced in the following as bubble size distribution functions, and the accuracy of these laws compared to the experimental data is discussed in the section 4.2.3.

Dirac law (Monodisperse approach)

Size distribution expression The monodisperse approach assumes that all bubbles have the same size locally. Therefore, the PDF is a Dirac law centered in the bubble diameter d_{mono}. The analytic expression of the PDF is:

$$P(d) = \delta_{d_{mono}}(d). \tag{4.2.26}$$

As a consequence, the bubble size distribution function f is written:

$$f = n\delta_{d_{mono}}(d). \tag{4.2.27}$$

Then the moment μ of order γ can be written as:

$$\mu_{d^\gamma} = nd^\gamma_{mono}. \tag{4.2.28}$$

Using equation (4.2.13), the Sauter diameter d_{32} is written:

$$d_{32} = \frac{\mu_{d^3}}{\mu_{d^2}} = \frac{nd^3_{mono}}{nd^2_{mono}} = d_{mono}. \tag{4.2.29}$$

Principal variables Using the expressions previously defined in (4.2.10), (4.2.11) and (4.2.12), the integral quantities can be calculated in the monodisperse approach as follows:

$$a_i = n\pi d^2_{mono} = n\pi d^2_{32}, \tag{4.2.30}$$

$$\alpha_g = \frac{n\pi d^3_{mono}}{6} = \frac{n\pi d^3_{32}}{6}. \tag{4.2.31}$$

Therefore, the interfacial area concentration a_i and the void fraction α_g are linked to the variables describing the distribution function f. From the equations (4.2.30) and (4.2.31), the bubble number density can be calculated by:

$$n = \frac{1}{36\pi}\frac{a_i^3}{\alpha_g^2}. \tag{4.2.32}$$

Quadratic law Q1 (Polydisperse approach)

Ruyer et al. (2007) have proposed to use a one-parameter quadratic law (Q1) to describe the bubble size distribution function f, written as:

$$f = \begin{cases} \frac{3}{4}\frac{nd}{d_{10}^3}\left(2d_{10} - d\right) & \text{if } d < 2d_{10}, \\ 0 & \text{otherwise.} \end{cases} \tag{4.2.33}$$

A scheme of the bubble size distribution function, as a function of the bubble diameter, is shown in Figure 4.2.1.

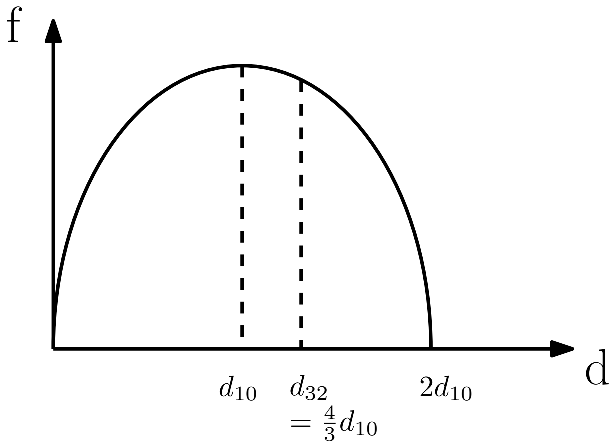

Figure 4.2.1: Scheme of the one-parameter quadratic bubble size distribution function f.

Using this distribution function f, the first moments are written:

$$\mu_{d^0} = n; \quad \mu_{d^1} = nd_{10}; \quad \mu_{d^2} = \frac{6}{5}nd_{10}^2; \quad \mu_{d^3} = \frac{8}{5}nd_{10}^3. \tag{4.2.34}$$

These equations link the Sauter diameter d_{32} to the arithmetic diameter:

$$d_{32} = \frac{\mu_{d^3}}{\mu_{d^2}} = \frac{4}{3}d_{10}. \tag{4.2.35}$$

Generally, using this approach, the moment μ of order γ can be written as:

$$\mu_{d^\gamma} = \frac{6n(2d_{10})^\gamma}{(\gamma+3)(\gamma+2)}. \tag{4.2.36}$$

These moments, together with the relations given in equations (4.2.11) and (4.2.12), allow to calculate the integral quantities:

$$\alpha = \frac{9}{80}\pi n d_{32}^3, \quad a_i = \frac{27}{40}\pi n d_{32}^2, \quad n = \frac{1}{24.3\pi}\frac{a_i^3}{\alpha^2}. \tag{4.2.37}$$

Log-normal law

Habiyaremye et al. (2022) have proposed to use a log-normal law to describe the bubble size distribution function, written as:

$$f = \frac{n}{\sqrt{2\pi}\sigma d}\exp\left[-\frac{log^2\left(\frac{d}{d_{cm}}\right)}{2\sigma^2}\right]. \tag{4.2.38}$$

This log-normal distribution has three degrees of freedom, given by the total bubble number density n, the logarithm of the geometric standard deviation σ, and the count median bubble diameter d_{cm}, and can, therefore, be reconstructed based on three statistic moments. Loosely speaking, n, σ, and d_{cm} can be interpreted as the height, width, and offset of the distribution function, respectively.

Using the log-normal law, the general moment μ or order γ does not have an analytic expression as is the case for Q1 and Dirac approaches. Therefore, these moments need to be approximated by quadrature functions.

4.2.3 Comparisons of bubble size distribution models with experimental data

The PDFs predicted by the different laws are compared to the experimental ones in Figure 4.2.2. It is worth noting that in order to predict the PDF in this Figure, some experimental data are used, such as the Sauter diameter for the Dirac and quadratic laws, the median diameter and the geometric standard deviation for the log-normal law. The iMUSIG approach presented in

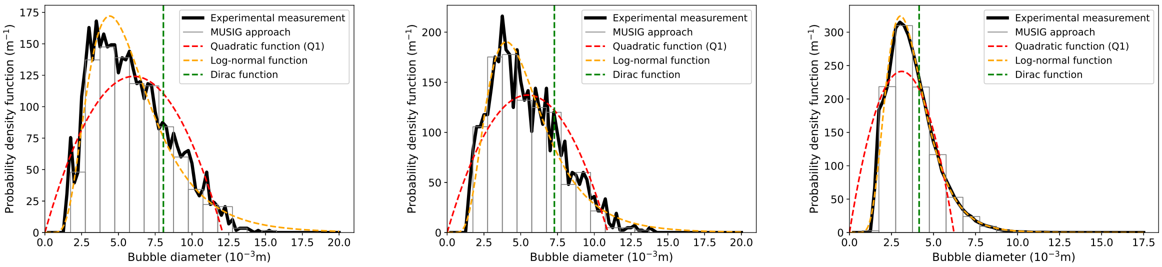

Figure 4.2.2: Experimental and predicted probability density function in the TOPFLOW large diameter experiment at height far from the injection, for the test cases 2 (left), 4 (center) and 7 (right) defined in section 4.1.

section 4.2.1 is also shown in this Figure as a piece-wise constant function of the diameter. The experimental data are also used to define this function.

The law that is closer to the experimental PDF is the log-normal law. The overall shape of the PDF obtained by the one-parameter quadratic (Q1) law is quite different from the experimental PDF. The Dirac function assumes that the entire bubble population is concentrated at the Sauter mean diameter, and so the bubble population is considered monodisperse. Due to its simplicity, this function is unable to characterize a proper PDF.

The bubble size distribution functions of both the Dirac and the quadratic approaches have two degrees of freedom, given by the bubble number density n and the Sauter diameter d_{32}. In fact, the quadratic approach uses the diameter d_{10}, which is directly related to the Sauter diameter. Thanks to the fact that there are only two degrees of freedom, the bubble size distribution functions can be closed with the transport of one additional moment beside the gas fraction. The second moment is usually used, which is equal to the interfacial area concentration a_i divided by π, as presented in equation (4.2.11). Therefore, both Dirac and quadratic functions have the same complexity since they can be solved by an IATE. The advantage of the quadratic approach is that it is able to consider a polydispersion, as shown in Figure 4.2.2, without introducing more complexity.

The log-normal bubble size distribution function has three degrees of freedom, given by the bubble number density n, the logarithm of the geometric standard deviation σ, and the count median bubble diameter d_{cm}. These parameters correspond to, respectively, the height, width, and offset of the bubble size distribution function. Thereby, three size distribution moments must be known. As a consequence, another moment transport equations need to be solved, which leads to more complexity in the system. However, it is still possible to solve it, and Habiyaremye et al. (2023) have proposed a log-normal method of moments which is achieved by solving the transport equations of the zeroth, second, and third diameter-based moments. However, the integral of the log-normal function does not have an analytical solution. So, the integrals need to be approximated using Gauss-Hermite quadrature method for example, at each cell and at each time step.

Since the quadratic function is polynomial and has a finite support $(0, 2d_{10})$, it is possible to obtain an analytic solution of the interfacial terms present in mass and energy conservation equations, as well as the phase change term in IATE. The integrals of drag and lift forces have localized approximations (Ruyer et al., 2007) but can mainly be determined analytically using this quadratic law. It is, therefore, easy to implement it in an Eulerian CFD code such as Neptune_CFD, and this method is less time-consuming than the log-normal method since there is no integral to calculate at each cell and time step. Moreover, the quadratic bubble size distribution function is overall not too far from the experimental one a shown in Figure 4.2.2. Habiyaremye et al. (2023) have stated that the quadratic approach, while being less accurate in predicting the shape of the size distribution, is able to predict the Sauter mean diameter relatively accurately, and with a CPU-time two times lower than using the log-normal approach. For all these reasons, only the quadratic function is used in this work to predict the polydispersion approach.

The section 4.2.2 shows that the models for the mass and energy interfacial transfers, the drag and lift forces, and the right-hand side terms of the IATE depend on the chosen bubble size distribution function. For these terms, the model formulations obtained by the different approaches and the impacts of these approaches on the numerical results are presented in section 4.3. The closure laws independent of the bubble size distribution are described in the next section.

4.2.4 Choice of the closure laws independent of bubble size distribution

This statistical-average approach requires some closure laws since this averaging operation removes information about smaller scale physics such as turbulence, wall-fluid interactions or interfacial exchanges between phases. Indeed, the unknown terms that require closure laws to close the system are shown in section 4.2.2. The closure laws considered as independent of the bubble size distribution function are the liquid turbulence, the added mass and turbulent dispersion forces, and the wall heat flux partitioning. Regarding these closure laws, the set of models already used in chapter 3 is used again in this chapter. These models are described in detail in section 1.2. It is worth mentioning that there are no adjusting parameters in these models.

4.2.5 Mesh and boundary conditions

Because of the axisymmetrical nature of the experimental facility and the flow, the simulations are carried out in an angular sector of 4° of the pipe section. Meshes are generated as three-dimensional ones, with only one cell in the orthoradial direction. The results are thus calculated in the r, z plane, with 25 cells in r direction and 625 cells in z direction, giving an $y+$ around 300. The angular sector and the medium mesh are represented in Figure 4.2.3.

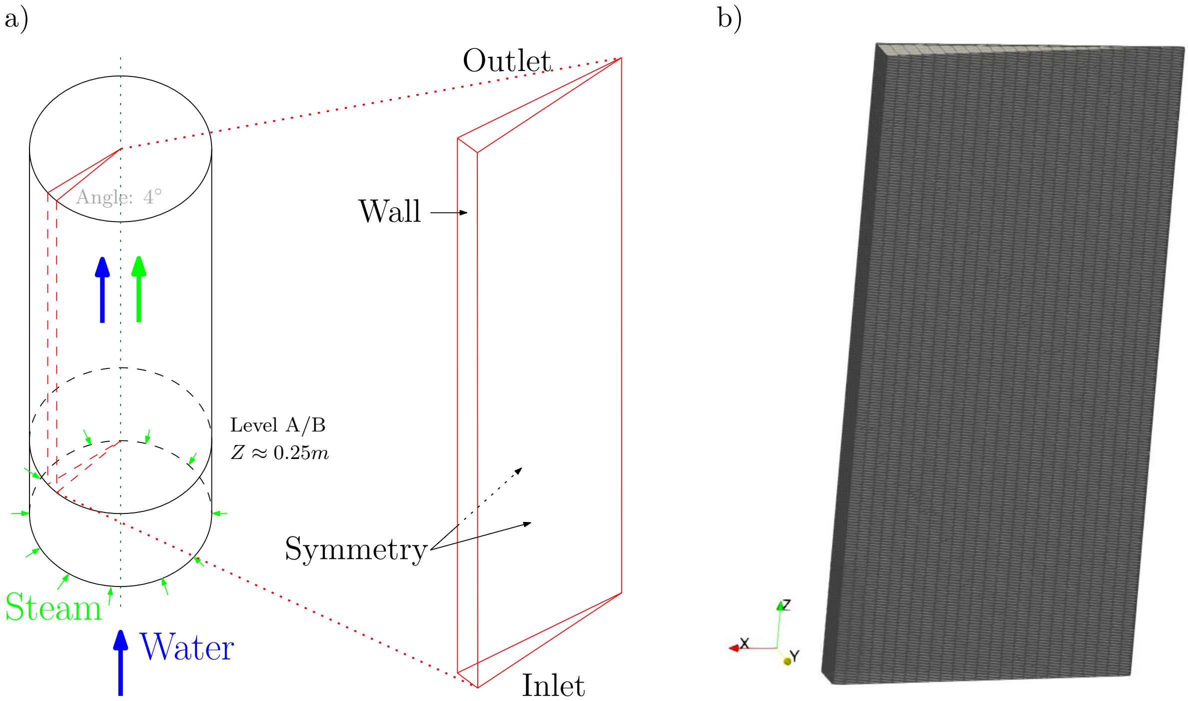

Figure 4.2.3: (a) Sector cut of the pipe geometry; (b) Medium mesh, quasi-2D.

A sensitivity to the mesh refinement is shown in Figure 4.2.4 on the radial profiles of void fraction at different heights.

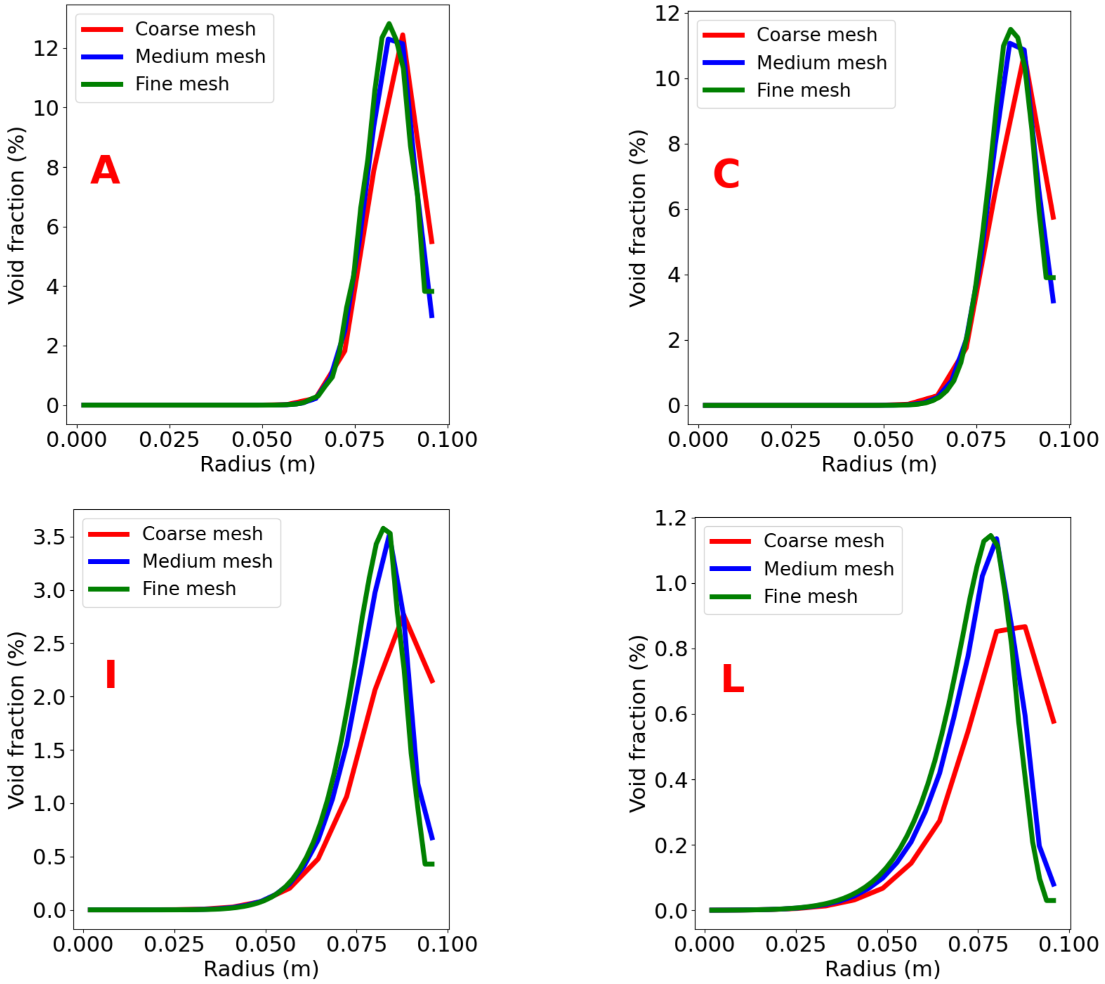

Figure 4.2.4: Mesh convergence study on the test case 1 using the full Dirac approach, as presented in section 4.5.

Two more meshes, a coarse and a fine, are introduced in this Figure, with respectively 13 and 50 cells in r directions, and with 313 and 1250 cells in z direction. Some deviations are found between the results obtained with the coarse mesh and with the others. The results obtained with the medium and fine meshes are similar. For this reason, the medium mesh is used in the following. Moreover, the same mesh has been used by Liao and Lucas (2016) to simulate the same test cases, and the same mesh sensibility has been retrieved. Four different types of boundary conditions are applied in the simulation: inlet, outlet, wall, and symmetry.

The inlet radial profiles of steam volume fraction, velocity, Sauter mean diameter, and liquid temperature are defined according to the experimental data at level A/B. The liquid velocity profile is not measured experimentally, so it is postulated to be identical to the measured gas velocity profile while preserving the inlet liquid flow rate. The solid wall is considered adiabatic and smooth, and the outlet pressure is defined from the measured inlet pressure minus the loss pressure associated with the water column. A symmetry condition is imposed on the remaining faces. The experimental bubble size distributions (Lucas et al., 2013) show that for all the test cases studied in this work, only two phenomena are predominant in the change of interfacial area: condensation and coalescence. Both condensation and coalescence coexist between the inlet and the elevation Z=0.6m. At an elevation above 0.6m, it seems that only condensation exists and has a predominant impact on the interfacial area.

In summary, a description of the general modeling used in this work has been described in this section. The section 4.2.2 shows that the models for the mass and energy interfacial transfers, the drag and lift forces, and the right-hand side terms of the IATE depend on the choice of the bubble size distribution function. The model formulations in different approaches and the impacts of these approaches on the numerical results are presented in section 4.3.

4.3 Study of the impact of bubble size distribution function on interfacial terms (Imposed diameter)

Experimentally, the radial profiles of the Sauter diameter are given at 12 different heights.

> **Note:** In this section, the Sauter diameter is not calculated using the code. The experimental Sauter diameter profiles are imposed at each height in the calculation, and a linear interpolation is done in the cells between two experimental measurement heights.

4.3.1 Models of Mass and Energy interfacial transfers

Considering that there is no nucleation in the TOPFLOW experiment, only the phase change terms at the bulk need to be treated. These terms, which are present in the mass (4.2.19) and energy (4.2.23) balance equations, are written:

$$\Gamma_{g,bulk} = \int \rho_g \frac{\pi d^2}{2} \frac{Dd}{Dt} f \partial d, \tag{4.3.1}$$

$$\Pi'_l + \Pi'_g = \underbrace{\int \pi d^2 q''_{li} f \partial d}_{\Pi'_l} + \underbrace{\int \pi d^2 q''_{gi} f \partial d}_{\Pi'_g} = \int \pi d^2 (q''_{li} + q''_{gi}) f \partial d, \tag{4.3.2}$$

with the bulk part of the bubble diameter Lagrangian derivative:

$$\frac{Dd}{Dt} = -\frac{2}{\rho_g} \frac{(q''_{li} + q''_{gi})}{H_{lg}}, \tag{4.3.3}$$

with H_{lg} the latent heat. Moreover, the heat flux from the liquid q''_{li} and gas q''_{gi} to the interface both need to be modeled. The term q''_{gi} is modeled by a time-step return to saturation, which is written as:

$$q''_{gi} = \alpha_g \frac{\rho_g c_{p_g}}{\Delta t} (T_{sat} - T_g), \tag{4.3.4}$$

with Δt the computational time step and c_{p_g} the heat capacity of the gas phase. However, in sub-cooled flow, the heat flux from the liquid to the interface is largely predominant compared to the heat flux from the gas to the interface. As a consequence, the q''_{li} model is the most important and is treated in detail in this work. By introducing a bubble Nusselt number Nu_b, this term is written:

$$q''_{li} = h_l (T_{sat} - T_l) = \frac{\mathrm{Nu}_b \lambda_l}{d} (T_{sat} - T_l), \tag{4.3.5}$$

with λ_l the thermal conductivity. The Nusselt number is usually written in this form:

$$\mathrm{Nu}_b = C_0 + C_1 \mathrm{Re}_b^{C_2} \mathrm{Pr}^{C_3}. \tag{4.3.6}$$

The coefficients C_0, C_1, C_2, and C_3 are usually estimated by empirical correlations. Some correlations can be found in the literature, and two of them are described below.

Nusselt models for an individual bubble

As a reminder, it has been said in section 4.1 that the TOPFLOW experimental bubble Reynolds number lies in the range $[4,000 - 30,000]$. Most CFD codes use the correlation developed by Ranz and Marshall (1952), but this formulation is based on experiments for evaporating droplets with particle Reynolds numbers below 200. Therefore, its application to bubble condensation with higher particle Reynolds numbers is not direct, and this correlation is evaluated in this work on steam condensation. Indeed, in the following, this correlation is compared to the one developed by Chen and Mayinger (1992), which is based on experiments of gas bubble condensation with larger bubble Reynolds numbers ($400 < \mathrm{Re}_b < 10,000$). These Reynolds numbers are more consistent with those encountered in the test cases investigated in this work, where the bubble

Reynolds number is above 4,000. These two correlations have the same form with different coefficients:

$$\text{Ranz-Marshall:} \quad \mathrm{Nu}_b = 2 + 0.6\mathrm{Re}_b^{0.5}\mathrm{Pr}_l^{1/3}, \tag{4.3.7}$$

$$\text{Chen-Mayinger:} \quad \mathrm{Nu}_b = 0.185\mathrm{Re}_b^{0.7}\mathrm{Pr}_l^{0.5}. \tag{4.3.8}$$

Re_b and Pr_l are, respectively, the bubble Reynolds number and the liquid Prandtl number and are written as:

$$\mathrm{Re}_b = \frac{\rho_l d|\underline{v}_r|}{\mu_l}, \tag{4.3.9}$$

$$\mathrm{Pr} = \frac{\mu_l Cp_l}{\lambda_l}. \tag{4.3.10}$$

Both Ranz-Marshall and Chen-Mayinger correlations are in the form of the equation (4.3.6), with different coefficients.

Model formulation in context of different approaches

Given that in sub-cooled flow, q''_{li} is largely predominant compared to q''_{gi}, only the formulations in different approaches concerning the q''_{li} part of interfacial transfers are compared in this section. Since it is not of fundamental importance, in this work, the term q''_{gi} is always integrated using the monodisperse approach. Using the interfacial mass transfer formulation described in equation (4.3.1) and the Lagrangian derivative of the diameter expressed in equation (4.3.3), the following formulation is obtained:

$$\Gamma_l = \int \pi d^2 \frac{(q''_{li} + q''_{gi})}{H_{lg}} f \partial d = \underbrace{\int \pi d^2 \frac{q''_{li}}{H_{lg}} f \partial d}_{\Gamma_{l,li}} + \underbrace{\int \pi d^2 \frac{q''_{gi}}{H_{lg}} f \partial d}_{\Gamma_{l,gi}}. \tag{4.3.11}$$

Moreover, the interfacial energy transfer term is expressed in equation (4.3.2). Since the enthalpy jump H_{lg} does not depend on the bubble size distribution, the following expression is obtained:

$$\Pi'_l = \Gamma_{l,li} \cdot H_{lg}. \tag{4.3.12}$$

The following paragraphs are dedicated to the calculation of $\Gamma_{l,li}$ and Π'_l terms in both approaches.

Dirac law First, the liquid to interface part $\Gamma_{l,li}$ of interfacial mass transfer rate term is formulated using a Dirac function as bubble size distribution function:

$$\Gamma_{l,li} = \int_0^\infty \left[\pi d^2 \frac{q''_{li}}{H_{lg}} f \partial d\right], \tag{4.3.13a}$$

$$= \int_0^\infty \pi d^2 \frac{q''_{li}}{H_{lg}} n \delta_{d_{32}} \partial d \tag{4.3.13b}$$

$$= n\pi d_{32}^2 \underbrace{\frac{\lambda_l \mathrm{Nu}_b}{d_{32}}}_{=q''_{li}} \frac{1}{H_{lg}} \partial d, \quad \text{using (4.2.30):} \quad \underbrace{a_i = n\pi d_{32}^2}_{\text{Valid for Dirac law}} \tag{4.3.13c}$$

$$\boxed{\Longrightarrow \Gamma_{l,li} = \frac{a_i \mathrm{Nu}_b \lambda_l (T_{sat} - T_l)}{d_{32} H_{lg}}.} \tag{4.3.13d}$$

This formulation obtained using the standard method of moments and a Dirac law is identical to the one used in the standard version Neptune_CFD code, as presented in section 1.2 and used in Chapter 3. Using equation (4.3.12), the interfacial energy transfer term is expressed as:

$$\Pi'_l = \frac{a_i \mathrm{Nu}_b \lambda_l (T_{sat} - T_l)}{d_{32}}. \tag{4.3.14}$$

Quadratic law (Q1) The quadratic bubble size distribution function f is recalled:

$$f = \begin{cases} \frac{3}{4}\frac{nd}{d_{10}^3}\left(2d_{10} - d\right) & \text{if } d < 2d_{10}, \\ 0 & \text{otherwise.} \end{cases} \tag{4.3.15}$$

Based on this function and the equations (4.3.2) to (4.3.6), the formulation of the interfacial mass transfer term, using the quadratic law and a generic formulation of Nusselt number, has been developed in the framework of this thesis, and its establishment is presented as follows:

$$\Gamma_{l,li} = \int_0^\infty \left[\pi d^2 \frac{q''_{li}}{H_{lg}} f \partial d\right], \tag{4.3.16a}$$

$$= \int_0^{2d_{10}} \pi d^2 \frac{q''_{li}}{H_{lg}} \frac{3}{4}\frac{nd}{d_{10}^3}\left(2d_{10} - d\right)\partial d, \tag{4.3.16b}$$

$$= \int_0^{2d_{10}} \left[\frac{3}{4}\frac{\pi n}{H_{lg}} \underbrace{\frac{\lambda_l \mathrm{Nu}_b}{d}\Delta T}_{=q''_{li}} \frac{d^3}{d_{10}^3}(2d_{10} - d)\partial d\right], \tag{4.3.16c}$$

$$= \frac{3}{4}\pi n \frac{\lambda_l \Delta T}{H_{lg}} \int_0^{2d_{10}} \underbrace{\left(C_0 + C_1 \mathrm{Re}_b^{C_2}\mathrm{Pr}^{C_3}\right)}_{=\mathrm{Nu}_b} \frac{d^2}{d_{10}^3}\left(2d_{10} - d\right)\partial d, \tag{4.3.16d}$$

$$= \frac{3}{4}\pi n \frac{\lambda_l \Delta T}{H_{lg}} \left[\int_0^{2d_{10}} \frac{2C_0 d^2}{d_{10}^2}\partial d - \int_0^{2d_{10}} \frac{C_0 d^3}{d_{10}^3}\partial d + C_1 \frac{v_r^{C_2}\mathrm{Pr}^{C_3}}{\nu^{C_2}}\left(\int_0^{2d_{10}} \frac{2d^{2+C_2}}{d_{10}^2}\partial d - \int_0^{2d_{10}} \frac{d^{3+C_2}}{d_{10}^3}\partial d\right)\right], \tag{4.3.16e}$$

$$= \frac{3}{4}\pi n \frac{\lambda_l \Delta T}{H_{lg}} \left[\left[\frac{2C_0 d^3}{3d_{10}^2}\right]_0^{2d_{10}} - \left[\frac{C_0 d^4}{4d_{10}^3}\right]_0^{2d_{10}} + C_1 \frac{v_r^{C_2}Pr^{C_3}}{\nu^{C_2}}\left(\left[\frac{2d^{3+C_2}}{(3+C_2)d_{10}^2}\right]_0^{2d_{10}} - \left[\frac{d^{4+C_2}}{(4+C_2)d_{10}^3}\right]_0^{2d_{10}}\right)\right] \tag{4.3.16f}$$

$$= \frac{3}{4}\pi n \frac{\lambda_l \Delta T}{H_{lg}} \left[\frac{16C_0}{3}d_{10} - \frac{16C_0}{4}d_{10} + C_1 \frac{v_r^{C_2}Pr^{C_3}}{\nu^{C_2}}\left(\frac{2 * 2^{3+C_2}d_{10}^{1+C_2}}{3+C_2} - \frac{2^{4+C_2}d_{10}^{1+C_2}}{4+C_2}\right)\right] \tag{4.3.16g}$$

$$= \frac{3}{4}\pi n \frac{\lambda_l \Delta T}{H_{lg}} \left[\frac{4}{3}C_0 d_{10} + C_1 \frac{v_r^{C_2}\mathrm{Pr}^{C_3}}{\nu^{C_2}} d_{10}^{1+C_2}\left(\frac{(4+C_2)2^{4+C_2} - (3+C_2)2^{4+C_2}}{(3+C_2)(4+C_2)}\right)\right], \quad \text{with: } d_{10} = \frac{3}{4}d_{32}, \tag{4.3.16h}$$

$$= \frac{3}{4}\pi n \frac{\lambda_l \Delta T}{H_{lg}} d_{32}\left[C_0 + C_1\left\{\left(\frac{3}{4}\right)^{1+C_2} \frac{2^{4+C_2}}{(3+C_2)(4+C_2)}\right\}\mathrm{Re}_b^{C_2}\mathrm{Pr}^{C_3}\right], \quad \text{with : } n = \frac{1}{24.3\pi}\frac{a_i^3}{\alpha^2} = \frac{36}{24.3\pi}\frac{a_i}{d_{32}^2}, \tag{4.3.16i}$$

$$\boxed{\Longrightarrow \Gamma_{l,li} = \frac{3}{4}\frac{36}{24.3}\frac{a_i \mathrm{Nu}_{b_{mod}} \lambda_l (T_{sat} - T_l)}{d_{32}H_{lg}}}, \quad \text{with : } \mathrm{Nu}_{b_{mod}} = C_0 + C_1\left\{\left(\frac{3}{4}\right)^{1+C_2} \frac{2^{4+C_2}}{(3+C_2)(4+C_2)}\right\}\mathrm{Re}_b^{C_2}\mathrm{Pr}^{C_3}. \tag{4.3.16j}$$

Remark: The generic formulation (4.3.16j) has been developed in the framework of this thesis.

Therefore, the liquid-to-interface part of the interfacial mass transfer term is derived above. Using the equation (4.3.12), the interfacial energy transfer term is written:

$$\Pi'_l = \Gamma_{l,li} \cdot H_{lg} = \frac{3}{4}\frac{36}{24.3}\frac{a_i \mathrm{Nu}_{b_{mod}} \lambda_l (T_{sat} - T_l)}{d_{32}}. \tag{4.3.17}$$

Note: Analytic expressions are obtained for the mass and energy interfacial transfer terms using the Q1 approach, proving the benefits of this law.

This quadratic law allows us to take into account the experimental bubble polydispersion while keeping an analytic expression of the $\Gamma_{l,li}$ and Π'_l terms. Moreover, the analytic expression is similar to the one in the monodisperse approach; there are just a few additional factors that appear in the formulation.

Simulation results

Both correlations of Ranz-Marshall and Chen-Mayinger are tested using Dirac and quadratic laws functions for all the seven test cases, and the numerical results are shown in Figure 4.3.1.

The simulations performed here clearly show that the Ranz-Marshall correlation underestimates the Nusselt number and, therefore, the heat and mass transfers, resulting in a significant overestimation of the void fraction. On the contrary, the Chen-Mayinger correlation correctly predicts the axial evolution of void fraction and, therefore, the Nusselt number. This result was expected considering that the bubble Reynolds numbers of these test cases are in the range $[4,000 - 30,000]$, which are in the same order of magnitude as those used in the Chen-Mayinger correlation development, but far above those used in the Ranz-Marshall correlation one ($Re_b < 200$).

Figure 4.3.1 also shows that the choice of the bubble size distribution function for the interfacial mass and energy transfer terms does not significantly impact the results. This outcome was, in fact, predictable since the analytic expressions of $\Gamma_{l,li}$ and Π'_l are similar with both Dirac and quadratic approaches. The differences between these expressions lie in some different coefficients. However, overall, these coefficient values are very close in both approaches.

At the inlet, a slight difference can be seen between the averaged void fraction obtained from the Neptune_CFD code and from the experimental measurements, despite the fact that the same void fraction is imposed. This difference is caused by a gas velocity imposed at the inlet, which is instantly slowed down by the numerical tool due to the velocity difference between both phases and the drag force that is used. This issue is analyzed in detail in the next section.

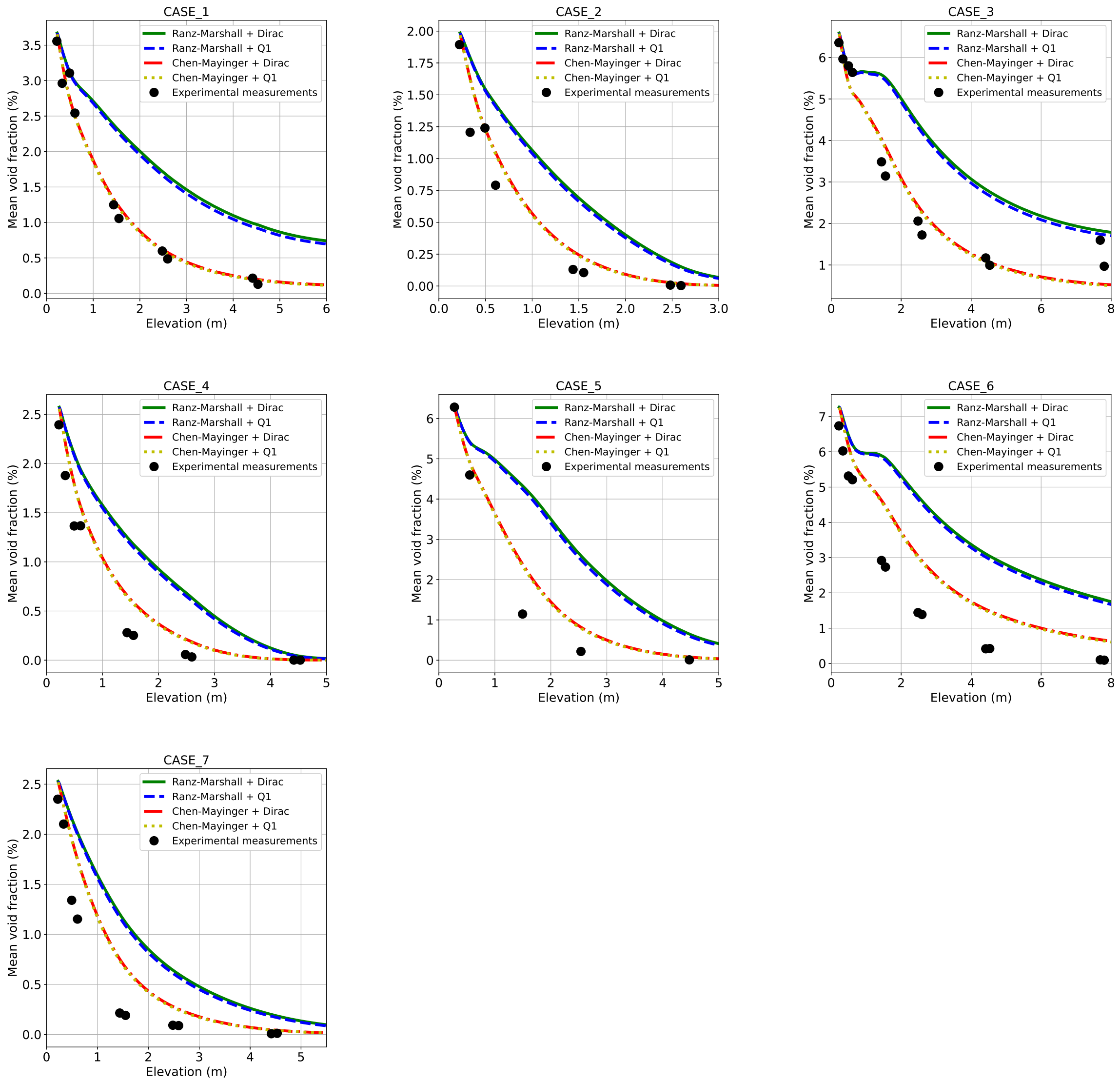

Figure 4.3.1: Axial evolution of the predicted averaged void fraction with imposed experimental Sauter diameter, compared to the experimental measurements (black dots). Simulations are done either using Ranz-Marshall correlation with the Dirac (green) or quadratic (blue) laws functions or using Chen-Mayinger with the Dirac (red) or quadratic laws functions (yellow).

4.3.2 Models of Drag and Lift interfacial forces

In this section, the drag and lift forces are expressed for an individual bubble and then using Dirac and quadratic approaches. Next, the simulation results obtained using both approaches are analyzed.

Drag force model for an individual bubble

The drag force is expressed in its general form as:

$$\underline{F}_D = \rho_l \int \frac{\pi d^3}{6} \frac{3}{4d} C_D |\underline{v}_r| \underline{v}_r f \partial d. \tag{4.3.18}$$

The widely used Ishii and Zuber (1979) drag coefficient is applied in this work. This coefficient, for an individual bubble of size d, is written as:

$$C_D = Max \left\{ \left(24 Re_b^{-1} + 2.4 Re_b^{-1/4} \right) ; \left[\frac{2}{3} \sqrt{Eo} \left(\frac{1 + 17.67 \left(\alpha_l^{1.5} \right)^{6/7}}{18.67 \alpha_l^{1.5}} \right)^2 \right] \right\}, \tag{4.3.19}$$

with Eo the Eötvös number, which uses a capillary length λ_c:

$$Eo = \left(\frac{d}{\lambda_c}\right)^2 \quad \text{with:} \quad \lambda_c = \sqrt{\frac{\sigma}{(\rho_l - \rho_g)g}}, \tag{4.3.20}$$

with σ the surface tension.

Lift force model for an individual bubble

The lift force is expressed in its general form as:

$$\underline{F}_L = \rho_l \left(\int \frac{\pi d^3}{6} C_L f \partial d \right) \underline{v}_r \times rot(\underline{v}_l). \tag{4.3.21}$$

The Tomiyama et al. (2002) lift coefficient is applied in this work and uses a modified Eötvös number, defined as:

$$Eo_H = \frac{(\rho_l - \rho_g) g d_H^2}{\sigma} \quad \text{with: } d_H = d_{32} \left(1 + 0.163 Eo^{0.757}\right)^{1/3}. \tag{4.3.22}$$

This modified Eötvös number is similar to the one defined in equation (4.3.20), but it uses d_H, the maximum horizontal dimension of the deformed bubble. This d_H number has been established by Wellek et al. (1966).

The Tomiyama et al. (2002) lift coefficient for an individual bubble of size d is then written:

$$C_L = \begin{cases} Min\left\{\overline{C}_L(Re_b); \tilde{C}_L(Eo_H)\right\} & \text{if } Eo_H < 4, \\ \tilde{C}_L(Eo_H) & \text{if } 4 \geq Eo_H < 10.7, \\ -0.278 & \text{if } Eo_H \geq 10.7, \end{cases} \tag{4.3.23}$$

with :

$$\overline{C}_L(Re_b) = 0.288 \tanh(0.121 Re_b), \tag{4.3.24}$$

$$\tilde{C}_L(Eo_H) = 0.00105 Eo_H^3 - 0.0159 Eo_H^2 - 0.0204 Eo_H + 0.474. \tag{4.3.25}$$

Drag model formulation in context of different approaches

Dirac law Using the Dirac law, the drag force is expressed as:

$$\underline{F}_D = \frac{3}{4} \frac{\rho_l \alpha_g}{d_{32}} C_D |\underline{v}_r| \underline{v}_r, \tag{4.3.26}$$

with the bubble size diameter d being replaced by the Sauter diameter d_{32} in the drag coefficient formulation.

Quadratic law Ruyer et al. (2007) have expressed the drag force in the context of a quadratic law:

$$\underline{F}_D = -\rho_l \frac{3\pi}{4} 1.06 a_i |\underline{v}_r| \underline{v}_r N_D. \tag{4.3.27}$$

N_D is a coefficient that depends on the Sauter diameter and the variables presented in equation (4.3.19). This coefficient, expressed by Ruyer et al. (2007), is described in Appendix II.

Lift model formulation in context of different approaches

Dirac law The lift force obtained using the Dirac law is written:

$$\underline{F}_L = C_L \alpha_g \rho_l \underline{v}_r \times rot(\underline{v}_l), \tag{4.3.28}$$

using also the Sauter diameter d_{32} in the lift coefficient formulation.

Quadratic law The lift force obtained using the quadratic law is written as:

$$\underline{F}_L = 9.55\pi N_L \alpha_g \rho_l \underline{v}_r \times rot(\underline{v}_l). \tag{4.3.29}$$

The term N_L has been developed and is expressed by Ruyer et al. (2007). This term is also described in Appendix II.

Simulation results

The Chen-Mayinger correlation is used to predict the Nusselt number since it shows accurate results in the previous section. The drag and lift forces, formulated in both Dirac and quadratic approaches, are evaluated in Figure 4.3.2. The green line corresponds to calculations done in the context of both lift and drag forces formulated using the Dirac bubble size distribution function. The red line corresponds to calculations done with both forces formulated using the quadratic function. Finally, the blue line corresponds to calculations done with the lift force formulated using the Dirac function and drag force using the quadratic function, in order to analyze the influence of the approach on each force.

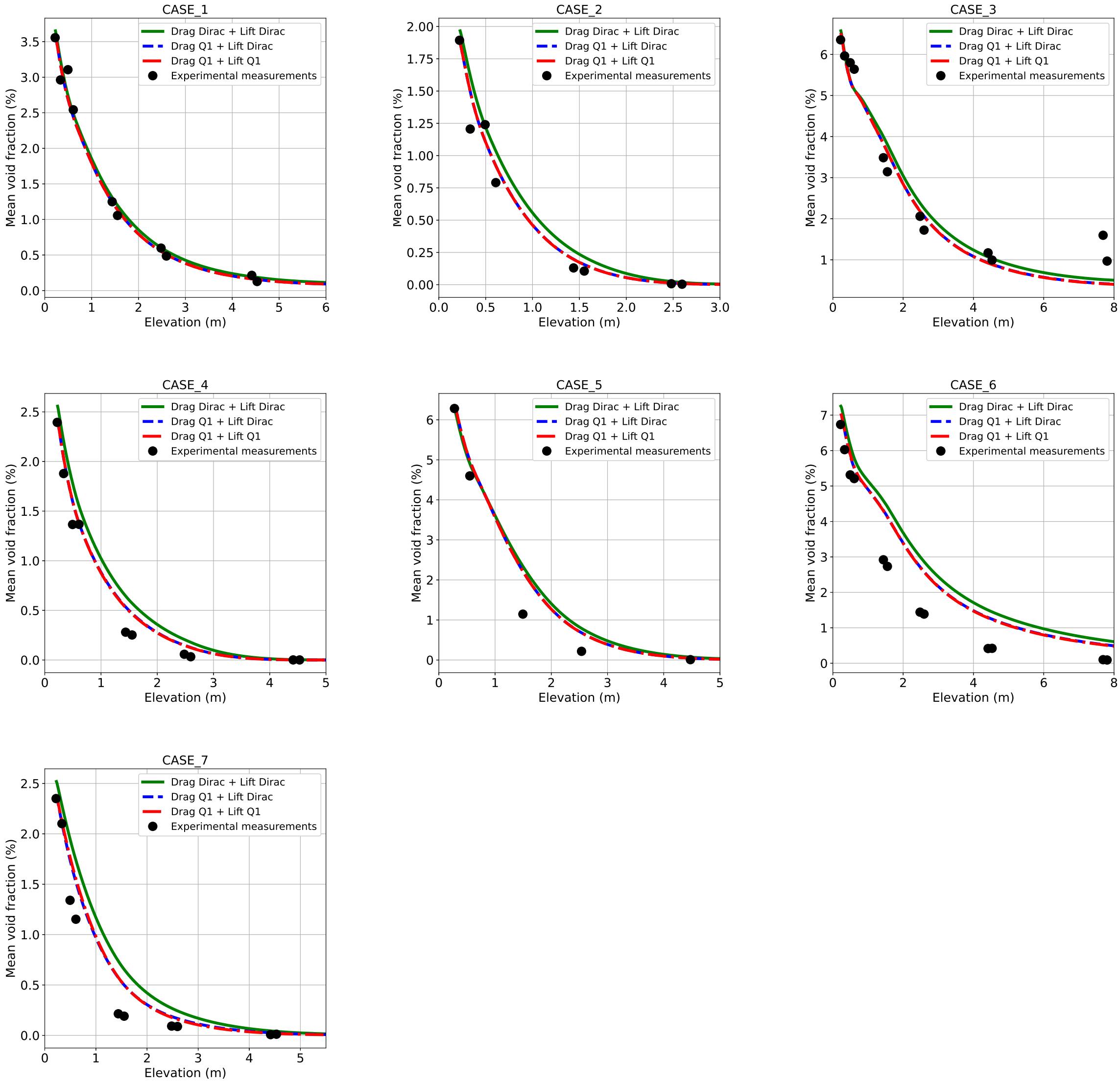

Figure 4.3.2: Axial evolution of the predicted averaged void fraction with imposed experimental Sauter diameter and using Chen-Mayinger correlation, compared to the experimental measurements (black dots). Simulations are done either using Dirac function for lift and drag forces (green), quadratic function for both forces (red) or quadratic for drag and Dirac for lift force (blue).

Overall, the axial evolution of the averaged void fraction is slightly improved using the quadratic approach for the drag force since the blue and red lines are closer to the experimental measurements. Moreover, the approach used for the lift force does not seem to influence the mean void fraction since the blue and red lines are superposed.

It is important to note that the void fraction overestimation at the inlet, which exists for the calculations done using the Dirac approach for the drag force term, is no longer observable for the calculations done using the quadratic approach for the drag force term.

This overestimation of the void fraction is linked to an underestimation of the gas velocity, as it can be seen in Figure 4.3.3.

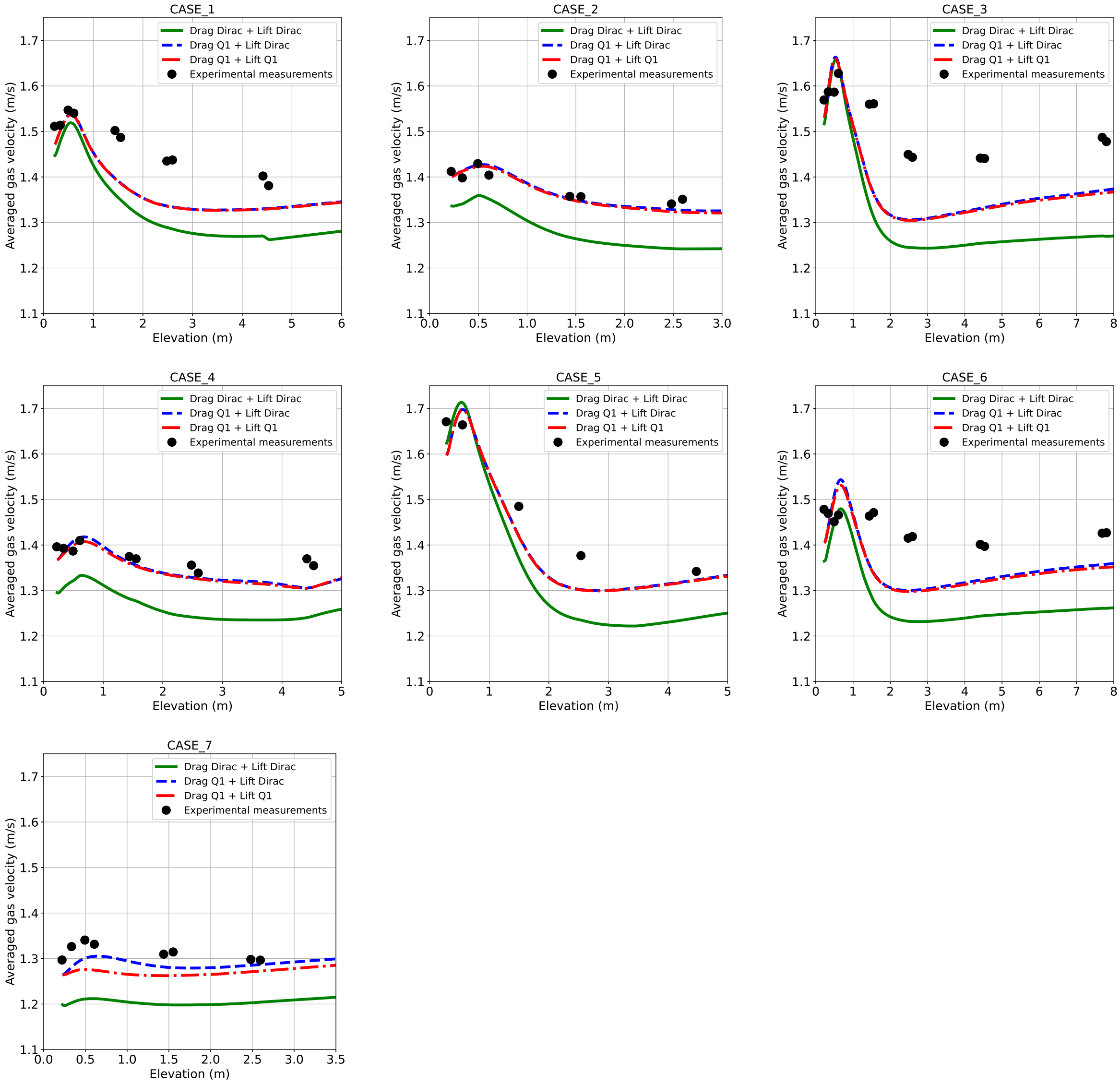

Figure 4.3.3: Axial evolution of the predicted averaged velocity with imposed experimental Sauter diameter and using Chen-Mayinger correlation, compared to the experimental measurements (black dots). Simulations are done either using Dirac function for lift and drag forces (green), quadratic function for both forces (red) or quadratic for drag and Dirac for lift force (blue).

Indeed, in order to study the axial evolution of the mean gas velocity, an average operator, weighted by the void fraction, is introduced:

$$\langle v_g \rangle_g = \frac{\langle \alpha_g v_g \rangle}{\langle \alpha_g \rangle} = \frac{\frac{2}{R^2}\int_0^R \alpha_g(r) v_g(r) r dr}{\frac{2}{R^2}\int_0^R \alpha_g(r) r dr}, \tag{4.3.30}$$

with R the radius of the tube. This form reflects the fact that a 2D axisymmetrical mesh is used. The experimental radial profile of gas volume fraction and velocity is imposed numerically on inlet faces, leading to an inlet gas flow rate. Moreover, the axial gas velocities are plotted in Figure 4.3.3 as long as $\langle \alpha_g \rangle > 0.001$, i.e., as long as it remains gas in the cross-section. This is why, for example, test case 7 ends at 3.5 m in Figure 4.3.3 while it ends at 5 m in Figure 4.3.2.

The experimental gas velocities are different between the test cases, as it is shown in Figure 4.3.3. Indeed, the gas velocity can reach 1.7m/s in test cases 3 and 5, while it does not reach 1.4m/s in test case 7. These differences are related to two main variables: the void fraction and the Sauter diameter. Indeed, a low Sauter diameter, as in test case 7, involves a high drag force and, therefore, a lower gas velocity, and vice-versa. Moreover, a high void fraction involves a lower liquid area and, thus, a higher liquid velocity. This higher liquid velocity reduces the relative velocity and, therefore, the drag force, increasing the gas velocity.

As shown in Figure 4.3.3, even though the experimental gas velocity profile is set at inlet faces, the numerical gas velocity at the first cell is lower than the experimental one due to an overestimation of the drag force. This underestimation of the gas velocity is much more pronounced when the Dirac approach is used for the drag force than when the quadratic approach is used.

This outcome is also actual for the gas velocity prediction along the entire length of the pipe. Indeed, while the gas velocity results in an underestimation of the predicted gas velocity of around 10% compared to the measurements using the Dirac approach, this underestimation drops to less than 5% if the quadratic approach is used for the drag force term. Also, a slight difference can be seen in test case 7 when using either the Dirac or quadratic approach for the lift force term.

Overall, the gas velocity increases both experimentally and numerically from the inlet to 0.6m in most of the test cases, probably due to the coalescence that causes the reduction of the interfacial area concentration. The predicted gas velocity increase is more significant than the measured one. Next, between 0.6m and 3m, there is a decrease in the gas velocity that can be due to the reduction of both Sauter diameter and void fraction. This decrease is sharper numerically than experimentally. Beyond that, the curve shape is flatter, with a slight increase for some test cases both experimentally and numerically from 3.5m. This increase could come from the gas expansion due to pressure change, or even from the fact that the gas phase shifts from the wall to the pipe center, where the water velocity is higher.

To conclude, in this section, the models for the drag and lift forces developed by Ruyer and Seiler (2009) using a quadratic bubble size distribution function have been tested and compared to models using Dirac law and to experimental measurements on condensation test cases. Indeed, these comparisons have been made on separate effect test cases, on which the main phenomena are only the condensation and the interfacial forces, as drag and lift forces, which allows us to confidently evaluate the different models, which has not been the case in previous studies. Actually, the previous studies using these models have been done on test cases where several phenomena have happened simultaneously, such as coalescence, break-up, and nucleation, in addition to condensation and interfacial forces.

> **Remark:** In this section, we have demonstrated that the quadratic approach provides a clear improvement in drag force prediction and so, in the averaged gas velocity.

Using the correlation developed by Chen and Mayinger (1992) and the quadratic approach for both drag and lift forces terms, the predictions are highly accurate.

> **Note:** It is worth mentioning that calculations done in this section are not fully predictive since the experimental Sauter diameter is imposed in the calculation.

In order to have a predictive calculation, the last step is to predict the Sauter diameter, which is directly linked to the interfacial area concentration a_i:

$$d_{32} = \frac{6\alpha_g}{a_i} \tag{4.3.31}$$

The objective of the next section is to get a fully predictive calculation.

4.4 Study of the impact of bubble size distribution function and bubble collapse model on IATE (Calculated diameter)

In order to predict the Sauter diameter, an analysis of the experimental bubble size distribution at each height and for each test case is done. It reveals that coalescence and condensation coexist below the height F (see Table 4.1.1), at 0.6m from the steam injection, and above, the condensation is the only predominant phenomenon. No break-up structures are found. Therefore, the critical section in order to evaluate the capability of our numerical tool to predict the condensation begins at 0.6m. This is why it has been decided to still impose the experimental Sauter diameter profiles from inlet to point F and then to predict it with the IATE, where coalescence and break-up models are turned off, since these phenomena do not happen in the experiment.

4.4.1 IATE formulation in context of the different approaches

First, the IATE is recalled in the context of the method of moments:

$$\frac{\partial a_i}{\partial t} + \underline{\nabla}.\left(a_i \underline{v}_g\right) = \underbrace{\int 2\pi d \frac{Dd}{Dt} f \partial d}_{\phi_{PC}+\phi_{PV}} + \underbrace{\int \pi d^2 S_{\{b,c,n,co\}} \partial d}_{\phi_{BB}+\phi_{BC}+\phi_{BN}+\phi_{CO}}\,, \tag{4.4.1}$$

where the diameter variation is due to phase change and compressibility/dilatability phenomena:

$$\frac{Dd}{Dt} = -\frac{2(q''_{li}+q''_{gi})}{\rho_g H_{lg}} - \frac{d}{3\rho_g}\frac{D\rho_g}{Dt}. \tag{4.4.2}$$

The IATE obtained from the method of moments can be linked to the form obtained by Park et al. (2007):

$$\frac{\partial a_i}{\partial t} + \underline{\nabla}.\left(a_i \underline{v}_g\right) = \phi_{PC} + \phi_{PV} + \phi_{BB} + \phi_{BC} + \phi_{BN} + \phi_{CO}, \tag{4.4.3}$$

with ϕ_{PC} and ϕ_{PV} mean the source and sink terms of an expansion or shrinkage due to a phase change and a pressure change, respectively. ϕ_{BB} and ϕ_{BC} correspond to the source term due to a bubble break-up and the sink term due to a bubble coalescence, respectively, and ϕ_{CO} corresponds to the sink term linked to the bubble collapse due to condensation. Finally, ϕ_{BN} is related to the bubble nucleation. As mentioned, the coalescence and break-up models are turned off in this work. Since the walls are adiabatic in the TOPFLOW experiment, the wall nucleation model is turned off as well. Therefore, in the following formulations: $\phi_{BB} = \phi_{BC} = \phi_{BN} = 0$. Moreover, in most numerical tools, the term ϕ_{CO} is not taken into account. Initially, this term is not considered in the IATE. Then, a model based on the work of Park et al. (2007) is adapted to Dirac and quadratic approaches for this collapse term and is implemented into Neptune_CFD code. Therefore, the assumption that this term is not considered is going to be assessed, and the impact of this term on the results is going to be evaluated. In the following paragraphs, the source terms of the IATE are expressed using either Dirac or quadratic laws.

Dirac law Using the Dirac law and the assumptions given previously, the IATE is written:

$$\frac{\partial a_i}{\partial t} + \underline{\nabla}.\left(a_i \underline{v}_g\right) = -\int \cdot 2\pi f d \cdot \frac{2(q''_{li}+q''_{gi})}{\rho_g H_{lg}} \partial d - \int 2\pi f d \cdot \frac{d}{3\rho_g}\frac{D\rho_g}{Dt} \partial d, \tag{4.4.4a}$$

$$\frac{\partial a_i}{\partial t} + \underline{\nabla}.\left(a_i \underline{v}_g\right) = -n\pi d_{32}^2 \cdot \frac{4}{d_{32}\rho_g}\frac{(q''_{li}+q''_{gi})}{H_{lg}} - n\pi d_{32}^2 \frac{2}{3\rho_g}\frac{D\rho_g}{Dt}, \quad \text{with: } a_i = \pi d_{32}^2 \tag{4.4.4b}$$

$$\frac{\partial a_i}{\partial t} + \underline{\nabla}.\left(a_i \underline{v}_g\right) = -\frac{4}{d_{32}\rho_g}\frac{a_i(q''_{li}+q''_{gi})}{H_{lg}} - a_i \frac{2a_i}{3\rho_g}\frac{D\rho_g}{Dt}, \quad \text{with: } d_{32} = \frac{6\alpha_g}{a_i} \tag{4.4.4c}$$

$$\frac{\partial a_i}{\partial t} + \underline{\nabla}.\left(a_i \underline{v}_g\right) = -\frac{2a_i}{3\alpha_g \rho_g}\frac{a_i(q''_{li}+q''_{gi})}{H_{lg}} - \frac{2a_i}{3\rho_g}\frac{D\rho_g}{Dt}, \text{using (1.2.13): } \Gamma_l = a_i \frac{(q''_{li}+q''_{gi})}{H_{lg}} \tag{4.4.4d}$$

$$\frac{\partial a_i}{\partial t} + \underline{\nabla}.\left(a_i \underline{v}_g\right) = -\frac{2}{3}\frac{a_i}{\alpha_g \rho_g}\Gamma_{l,i} - \frac{2}{3}\frac{a_i}{\rho_g}\frac{d\rho_g}{dt} \tag{4.4.4e}$$

Quadratic law The general form of the IATE is presented in equation (4.4.5).

$$\frac{\partial a_i}{\partial t}+\underline{\nabla}\cdot\left(a_i\underline{v}_g\right)=-\underbrace{\int 4\pi d\frac{q''_{li}}{\rho_g H_{lg}}f\partial d}_{\phi_{PC,li}}-\underbrace{\int 4\pi d\frac{q''_{gi}}{\rho_g H_{lg}}f\partial d}_{\phi_{PC,gi}}-\underbrace{\int 2\pi d\frac{d}{3\rho_g}\frac{D\rho_g}{Dt}f\partial d}_{\phi_{PV}},\tag{4.4.5}$$

In the case of bubble condensation without nucleation, the gas is constantly near saturation, and therefore, the term $\phi_{PC,gi}$ is negligible compared to $\phi_{PC,li}$. Moreover, in the TOPFLOW conditions, the pressure change term ϕ_{PV} is low compared to $\phi_{PC,li}$. Indeed, the calculations have shown that the term ϕ_{PV} is more than two orders of magnitude lower than the $\phi_{PC,li}$ term. For these reasons, the bubble size distribution law applied to the term ϕ_{PV} would have no significant impact on the results. This is why the term ϕ_{PV} is expressed in the Dirac approach, even in the quadratic section.

The phase change term $\phi_{PC,li}$ has been developed using the quadratic law in the framework of this thesis. The establishment of this term is presented as follows:

$$\phi_{PC,li}=\int 4\pi d\frac{q''_{li}}{\rho_g H_{lg}}f\partial d,\tag{4.4.6a}$$

$$=\int_0^{2d_{10}}4\pi d\frac{q''_{li}}{\rho_g H_{lg}}\frac{3}{4}\frac{nd}{d_{10}}\left(2d_{10}-d\right)\partial d,\tag{4.4.6b}$$

$$=\int_0^{2d_{10}}\frac{3\pi n}{\rho_g H_{lg}}\frac{\lambda_l\mathrm{Nu}_b\Delta T}{d}\frac{d^2}{d_{10}^3}\left(2d_{10}-d\right)\partial d,\tag{4.4.6c}$$

$$=3\pi n\frac{\lambda_l\Delta T}{\rho_g H_{lg}}\int_0^{2d_{10}}\frac{d}{d_{10}^3}\left(C_0+C_1\mathrm{Re}^{C2}\mathrm{Pr}^{C3}\right)\left(2d_{10}-d\right)\partial d,\tag{4.4.6d}$$

$$\begin{aligned}=3\pi n\frac{\lambda_l\Delta T}{\rho_g H_{lg}}\Bigg[\int_0^{2d_{10}}\frac{2C_0 d}{d_{10}^2}\partial d-\int_0^{2d_{10}}\frac{C_0 D^2}{d_{10}^3}\partial d+\frac{C_1 v_r^{C_2}\mathrm{Pr}^{C_3}}{\nu^{C2}}\Bigg(\int_0^{2d_{10}}\frac{2d^{1+C_2}}{d_{10}^2}\partial d\\-\int_0^{2d_{10}}\frac{d^{2+C_2}}{d_{10}^3}\partial d\Bigg)\Bigg],\end{aligned}\tag{4.4.6e}$$

$$\begin{aligned}=3\pi n\frac{\lambda_l\Delta T}{\rho_g H_{lg}}\Bigg[\left[\frac{C_0 d^2}{d_{10}^2}\right]_0^{2d_{10}}-\left[\frac{C_0 d^3}{3d_{10}^3}\right]_0^{2d_{10}}+\frac{C_1 v_r^{C_2}Pr^{C_3}}{\nu^{C2}}\Bigg(\left[\frac{2d^{2+C_2}}{(2+C_2)d_{10}^2}\right]_0^{2d_{10}}\\-\left[\frac{d^{3+C_2}}{(3+C_2)d_{10}^3}\right]_0^{2d_{10}}\Bigg)\Bigg],\end{aligned}\tag{4.4.6f}$$

$$=3\pi n\frac{\lambda_l\Delta T}{\rho_g H_{lg}}\left[4C_0-\frac{8}{3}C_0+\frac{C_1 v_r^{C_2}Pr^{C_3}}{\nu^{C2}}\left(\frac{2^{3+C_2}d_{10}^{C_2}}{(2+C_2)}-\frac{2^{3+C_2}d_{10}^{C_2}}{(3+C_2)}\right)\right]\tag{4.4.6g}$$

$$=3\pi n\frac{\lambda_l\Delta T}{\rho_g H_{lg}}\left[\frac{4}{3}C_0+\frac{C_1 v_r^{C_2}d_{32}^{C_2}\mathrm{Pr}^{C_3}}{\nu^{C2}}\left(\frac{3}{4}\right)^{C_2}\frac{2^{3+C_2}}{(2+C_2)(3+C_2)}\right],\tag{4.4.6h}$$

$$=\frac{4\pi n\lambda_l\Delta T}{\rho_g H_{lg}}\underbrace{\left(C_0+C_1\left[\left(\frac{3}{4}\right)^{1+C_2}\frac{2^{3+C_2}}{(2+C_2)(3+C_2)}\right]\left(\frac{v_r d_{32}}{\nu}\right)^{C_2}\mathrm{Pr}^{C_3}\right)}_{\mathrm{Nu}_{b,modif,\phi_c}},\tag{4.4.6i}$$

$$=\frac{4\pi n\lambda_l\Delta T\mathrm{Nu}_{b,modif,\phi_c}}{\rho_g H_{lg}}\quad\text{with: }n=\frac{1}{24.3\pi}\frac{a_i^3}{\alpha^2}=\frac{6}{24.3\pi}\frac{a_i}{d_{32}\alpha_g},\tag{4.4.6j}$$

$$\boxed{\Longrightarrow\phi_{PC,li}=\frac{24}{24.3}\frac{a_i}{\alpha_g\rho_g}\Gamma_{l,mod,\phi_c},\quad\text{with : }\Gamma_{l,mod,\phi_c}=\frac{a_i\lambda_l\Delta T\mathrm{Nu}_{b,modif,\phi_c}}{d_{32}H_{lg}}.}\tag{4.4.6k}$$

Therefore, the phase change term in the IATE provided in equation (4.4.5) is derived in equation (4.4.6k). Using the quadratic law, the obtained IATE is written:

$$\frac{\partial a_i}{\partial t} + \nabla(a_i v_g) = -\frac{24}{24.3}\frac{a_i}{\alpha_g \rho_g}\Gamma_{l,mod,\phi_c} - \frac{2}{3}\frac{a_i}{\rho_g}\frac{d\rho_g}{dt}, \quad \text{with: } \Gamma_{l,mod,\phi_c} = \frac{a_i \lambda_l \Delta T Nu_{b,mod,\phi_c}}{d_{32} H_{lg}}, \quad (4.4.7)$$

with:

$$Nu_{b,mod,\phi_c} = C_0 + C_1 \left(\frac{3}{4}\right)^{1+C_2} \frac{2^{3+C_2}}{(2+C_2)(3+C_2)} Re_b^{C_2} Pr^{C_3} \quad (4.4.8)$$

> **Remark:** The form of the IATE is the same for both approaches, but some coefficients are different.

4.4.2 Simulation results without bubble collapse model

In this section, the Chen-Mayinger correlation is used to predict the Nusselt number, and the quadratic approach is used to model the terms of interfacial mass and energy transfer as well as the terms of drag and lift forces. Thereby, the influence of the distribution function on the IATE is evaluated. The axial evolution of the predicted Sauter diameter is shown in Figure 4.4.1.

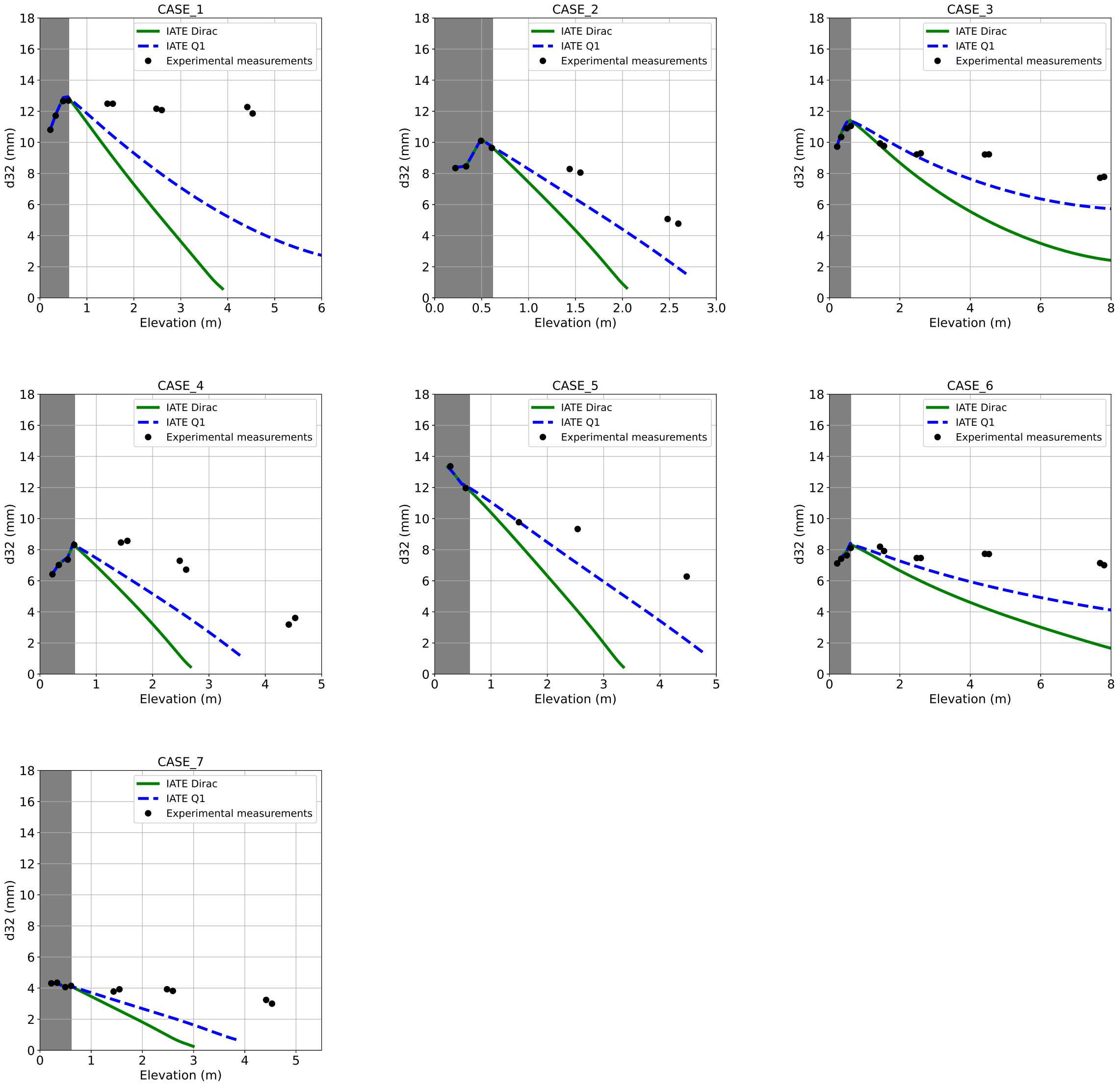

Figure 4.4.1: Axial evolution of the predicted averaged Sauter diameter using Chen-Mayinger correlation, compared to the experimental measurements (black dots). Simulations are done using either Dirac (green) or quadratic (blue) laws functions for the IATE formulation.

An apparent influence of the bubble size distribution function can be seen. Indeed, the Sauter diameter obtained using the Dirac approach to formulate the IATE is much smaller than the one obtained using the quadratic approach. But overall, the Sauter diameter predicted is underestimated by the IATE compared to the experimental measurements, no matter the approach used.

This underestimation can be explained by the fact that the bubble collapse is not currently taken into account, and these results demonstrate the importance of modeling this phenomenon. Indeed, experimentally, the bubble size distribution is highly polydispersed, and when the bubble population moves upward in sub-cooled liquid, all the bubbles shrink in size, and the smallest bubbles collapse. This collapse phenomenon results in an increase in the mean bubble size since the smallest bubbles disappear. Park et al. (2007) have proposed a model to take into account this phenomenon. This model is described in detail in the next section and is adapted for each approach.

4.4.3 Introduction of bubble collapse model

The model proposed by Park et al. (2007) is based on the consideration that the condensing region for a sub-cooled condition can be divided into two parts: the heat transfer-controlled region and the inertia-controlled region. In their view, in the first region, the Nusselt number approach is appropriate. In the second one, the bubbles are collapsed by the inertia of the surrounding liquid during a short period. The part of the condensation related to the first region can be characterized by the sink term ϕ_{PC}. In contrast, the part associated with the second region can be described by the last term ϕ_{CO}. The boundary between both regions is determined using the time history of a collapsing single bubble in a sub-cooled liquid, using the Rayleigh (1917) solution as well as Zwick and Plesset (1955) one, as shown in figure 4.4.2. Indeed, Rayleigh (1917) used a hydrodynamic approach and obtained the expression (4.4.9) for a non-dimensional time t^* as a function of the non-dimensional bubble diameter β, which is defined as $\beta = d/d_0$.

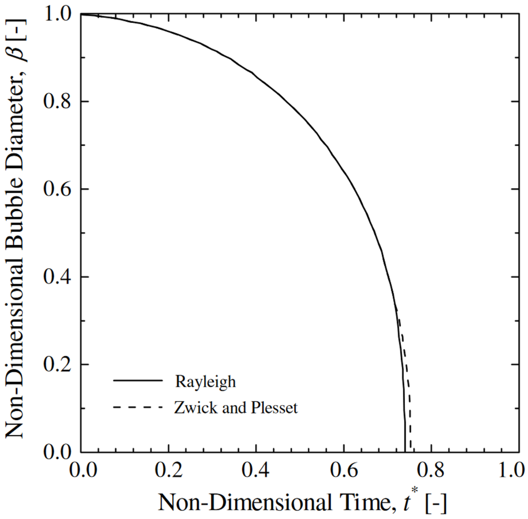

Figure 4.4.2: Time history of the collapsing bubble in a sub-cooled liquid. (Rayleigh, 1917; Zwick and Plesset, 1955)

$$t^* = \frac{t}{d_0\sqrt{\frac{3\rho_l}{8P}}} = \int_{\beta}^{1} \sqrt{\frac{\beta^3}{1-\beta^3}} d\beta = f(\beta). \tag{4.4.9}$$

The variable d_0 is the initial bubble diameter, which is assumed to be equal to the Sauter mean bubble diameter d_{32}. Moreover, $f(\beta)$ can be calculated from the curve in figure 4.4.2 or by an approximation of the integral (4.4.9). The residence times of the collapsing bubbles in both the heat transfer-controlled and the inertia-controlled regions can be calculated separately. To this aim, these regions are separated using the boundary bubble size. The non-dimensional bubble diameter at the boundary is defined as $\beta_b = d_b/d_{32}$. The residence times both in the heat transfer-controlled region $\Delta t_{c,th}$ and in the inertia-controlled region $\Delta t_{c,in}$ can be calculated by using equations (4.4.10) and (4.4.11).

$$\Delta t_{c,th} = d_0 \sqrt{\frac{3\rho_l}{8P}} \int_{\beta_b}^{1} \sqrt{\frac{\beta^3}{1-\beta^3}} d\beta = d_0 \sqrt{\frac{3\rho_l}{8P}} \cdot f(\beta_b), \tag{4.4.10}$$

$$\Delta t_{c,in} = d_0 \sqrt{\frac{3\rho_l}{8P}} \left(\int_{0}^{1} \sqrt{\frac{\beta^3}{1-\beta^3}} d\beta - \int_{\beta_b}^{1} \sqrt{\frac{\beta^3}{1-\beta^3}} d\beta \right) = d_0 \sqrt{\frac{3\rho_l}{8P}} \cdot [f(0) - f(\beta_b)] \tag{4.4.11}$$

The boundary is found when there is a rapid change in the non-dimensional bubble diameter β. Park et al. (2007) have assumed that the non-dimensional bubble diameter is 0.4 on the edge of the region. As a consequence, the boundary diameter can be defined as $d_b = 0.4 d_{32}$.

In this work, the interfacial area change in the heat transfer-controlled region is modeled in the same way as the models presented in section 4.4.1. However, this interfacial area change is done only for the bubbles inside the heat transfer controlled region, i.e., for the bubbles larger than the boundary diameter d_b. It is why Park et al. (2007) have introduced the fraction of bubbles with a smaller size than the d_b as:

$$p_c = \text{probability}(d < d_b) = \frac{\Delta t_{c,in}}{\Delta t_{c,th} + \Delta t_{c,in}}, \tag{4.4.12}$$

with $\Delta t_{c,th}$ and $\Delta t_{c,in}$ the residence times, respectively, in the heat transfer-controlled region and the inertia-controlled region.

As a reminder, the term ϕ_{PC} corresponding to the interfacial area change due to the phase change is modeled in the previous section without considering the inertia-controlled region. Therefore, this term is multiplied by $(1 - p_c)$, which is the fraction of bubbles larger than d_b.

The interfacial area sink term due to condensation in the inertia-controlled region is formulated by Park et al. (2007) as follows:

$$\phi_{CO} = -\pi d_b^2 \cdot \frac{n_b}{t_c}, \tag{4.4.13}$$

with n_b the bubble number density and t_c the residence time in the heat-transfer controlled region, expressed as:

$$t_c = \frac{d_{32}^2 - d_b^2}{4} \frac{\rho_g H_{lg}}{Nu_b \lambda_f \Delta T_{sub}}. \tag{4.4.14}$$

The term t_c is independent of the approach used, but it is crucial to note that the bubble number density depends on the approach. In both approaches, these numbers are set out below:

- Dirac law:

$$n_b = \frac{1}{36\pi} \frac{a_i^3}{\alpha_g^2}. \tag{4.4.15}$$

- Quadratic law

$$n_b = \frac{1}{24.3\pi} \frac{a_i^3}{\alpha_g^2}. \tag{4.4.16}$$

Therefore, the collapse source term (4.4.13) is expressed using only known variables. The new IATE formulation using this new collapse model is written as follows:

$$\frac{\partial a_i}{\partial t} + \nabla(a_i v_g) = -(1 - p_c) \underbrace{\frac{24}{24.3} \frac{a_i}{\alpha_g \rho_g} \Gamma_{l,mod,\phi_c}}_{\phi_{PC}} - \underbrace{\frac{2}{3} \frac{a_i}{\rho_g} \frac{d\rho_g}{dt}}_{\phi_{PV}} - \underbrace{\pi d_b^2 \cdot \frac{n_b}{t_c}}_{\phi_{CO}}. \tag{4.4.17}$$

The term Φ_{CO} is implemented in Neptune_CFD code using both approaches, and the predictions of the Sauter diameter using both approaches are compared in the following section.

4.4.4 Simulation results using bubble collapse model

The models presented in the previous section for the ϕ_{PC} and the ϕ_{CO} terms are implemented in the Neptune_CFD code, and the simulation results are presented in Figure 4.4.3.

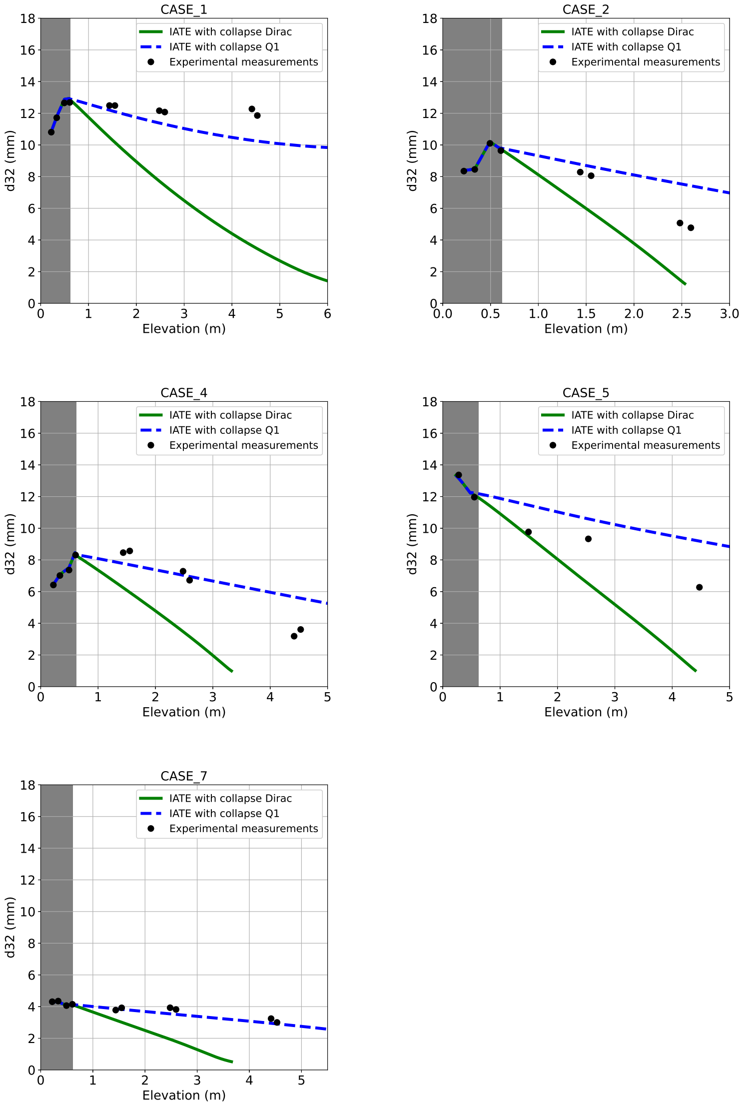

Figure 4.4.3: Axial evolution of the predicted averaged Sauter diameter using Chen-Mayinger correlation, compared to the experimental measurements (black dots). Simulations are done using either Dirac (green) or quadratic (blue) law functions for the IATE formulation, which includes a bubble collapse model.

The Sauter diameter predicted using the IATE with bubble collapse models and the Dirac approach is still underestimated compared to the measurements. On the contrary, the IATE with the collapse model and the quadratic approach tends to slightly overestimate the Sauter diameter on some tests, as in test cases 2 to 5. Nevertheless, the predicted Sauter diameter is close to the experimental one.

The slight differences can be explained by the fact that the boundary diameter d_b has been formulated empirically using this form: $d_b = \beta_b d_{32}$. The value $\beta_b = 0.4$ has been taken since it provides the best results in the simulation done by Park et al. (2007). Thus, another value for the parameter β_b could be chosen.

A sensitivity to the β_b parameter in the quadratic approach is done in the following section.

4.4.5 Sensitivity of the collapse model to the β_b parameter

The sensitivity to the β_b parameter in the quadratic approach is shown in Figure 4.4.4.

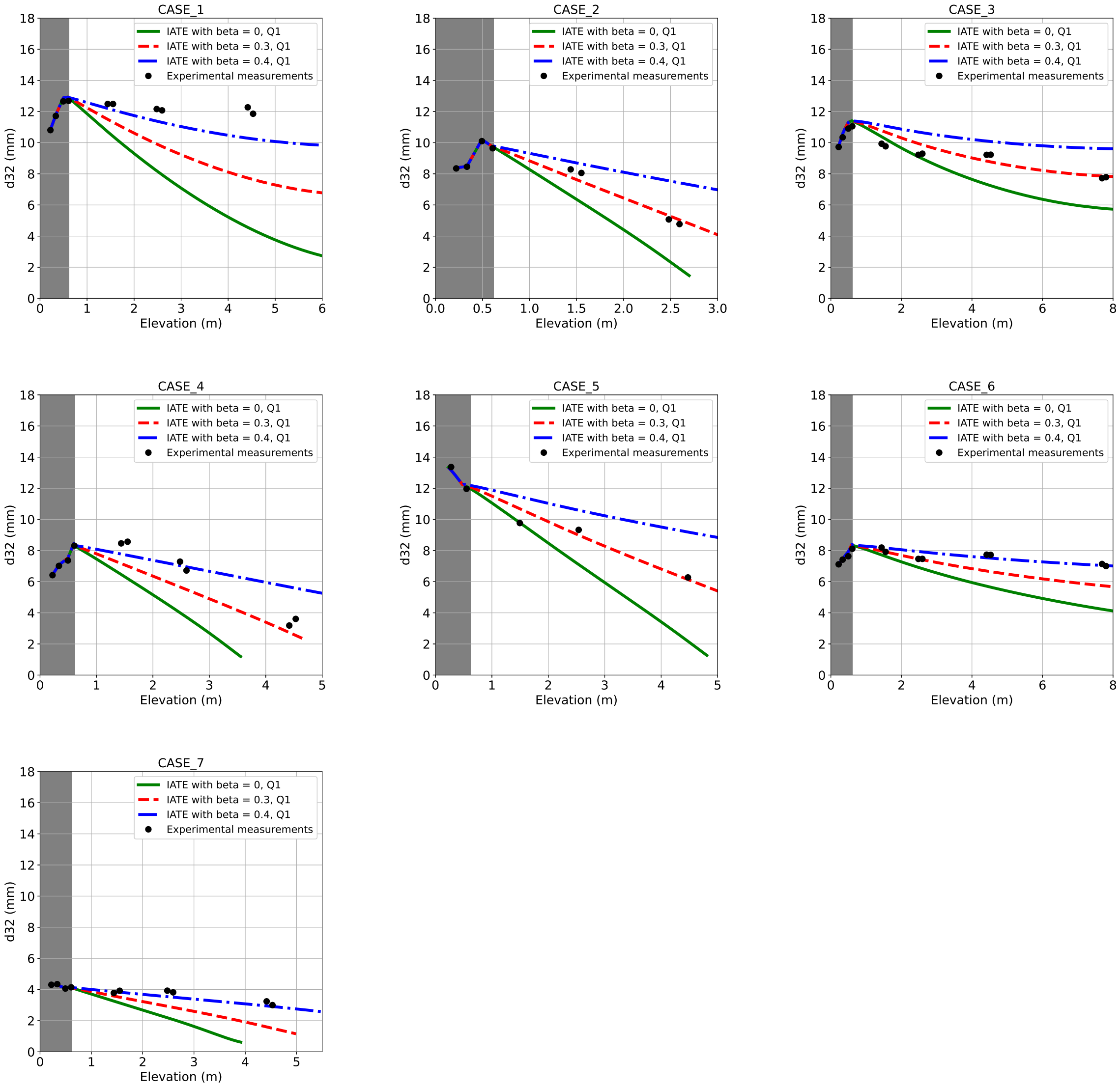

Figure 4.4.4: Axial evolution of the predicted averaged Sauter diameter, compared to the experimental measurements (black dots). Simulations are done using IATE in the quadratic approach with the bubble collapse model using different β_b parameters, respectively $\beta_b = 0, 0.3, 0.4$ (green, red, blue).

First, this Figure definitely shows that a bubble collapse model is necessary when a polydisperse bubble population is moving inside a sub-cooled liquid flow. Indeed, the Sauter diameter predicted without the bubble collapse model ($\beta_b = 0$) is constantly underestimated compared to the measurements. The predictions are much more accurate using the bubble collapse model, either with $\beta_b = 0.3$ or $\beta_b = 0.4$.

However, it does not seem that there is an ideal β_b value that predicts the best Sauter diameter for all the test cases. Indeed, besides test case 1, which appears to be different, the ideal value seems to be $\beta_b = 0.3$ for the test cases at the lowest pressure, of $P = \{10, 20\}$bar (Test cases 2-5). At the highest pressure, of $P = \{40, 65\}$bar, the best value seems to be $\beta_b = 0.4$.

Therefore, the pressure could affect the β_b parameter, but other experiments and other numerical simulations are necessary to confirm this hypothesis.

However, the results obtained with either $\beta_b = 0.3$ or $\beta_b = 0.4$ are really accurate using the quadratic approach, and since the parameter $\beta_b = 0.4$ also shows better results on the work of Park et al. (2007), this value is kept in this work. As a consequence, the results obtained with the full Dirac and quadratic approaches using the bubble collapse model with $\beta_b = 0.4$ are compared to the measurements and the iMUSIG results of Liao and Lucas (2016) in the next section.

4.5 Evaluation of the full quadratic and monodisperse approaches' capabilities to model condensation flow, in comparison to iMUSIG approach

The results obtained using the iMUSIG approach, introduced in section 4.2.1, are compared to those obtained using the method of moments with Dirac and quadratic approaches in Figure 4.5.1. The results obtained using the iMUSIG approach are provided by Liao and Lucas (2016).

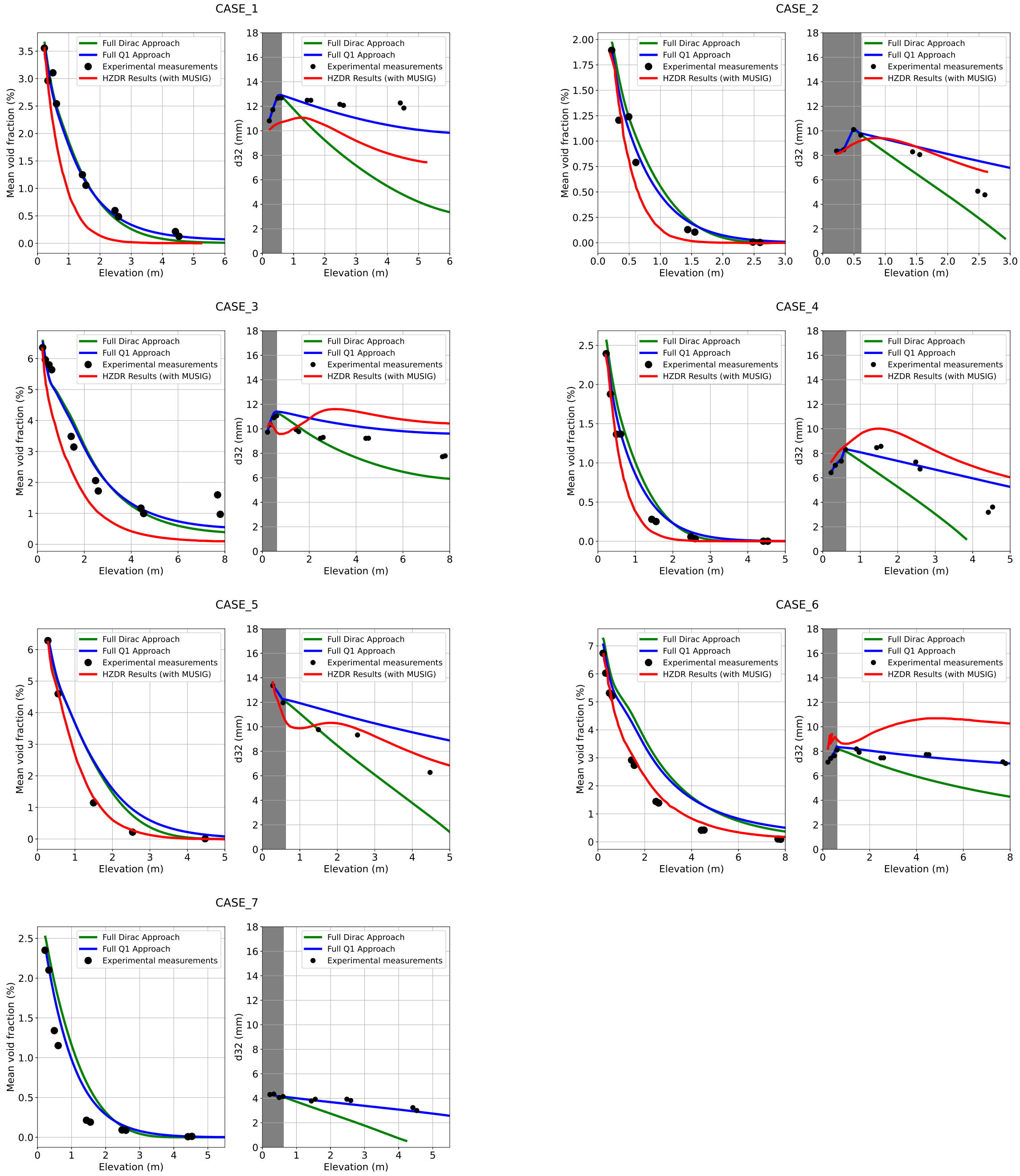

Figure 4.5.1: Axial evolution of the predicted averaged void fraction (left) and Sauter diameter (right) using, compared to the experimental measurements (black dots). Simulations are done either using a full Dirac (green) or quadratic (blue) approach, or using the iMUSIG approach (red) (Liao and Lucas, 2016).

First, it is worth noting that the iMUSIG calculations are done using a different Nusselt correlation than the Chen-Mayinger correlation used for the full Dirac and quadratic approach. Indeed, the correlation developed by Tomiyama (2009) is used for the iMUSIG approaches, which causes larger Nusselt number at high bubble Reynolds number compared to the Chen-Mayinger correlation. The use of this correlation explains the fact that the void fraction predicted by the iMUSIG approach is always lower than the one calculated by the full Dirac and quadratic approaches. However, it is challenging to decide definitively which Nusselt correlation is better since the results obtained using the Chen-Mayinger correlation are better for cases 1 to 4 and poorer for cases 5 and 6. Comparisons on new test cases should be made to give the final judgment on which correlation gives the best results. Either way, both correlations give satisfactory results on all the test cases, especially if they are compared to the Ranz-Marshall correlation presented in section 4.3.1.

Moreover, both iMUSIG and quadratic approaches give good predictions of the void fraction near the inlet, while the Dirac approach sometimes overestimates it at the inlet, especially in test cases 4, 6, and 7. This is a consequence of the drag force model, as explained in section 4.3.2. It suggests that both iMUSIG and quadratic approaches better predict the drag force than the Dirac approach.

The Sauter diameter predictions are quite heterogeneous between the approaches. As it was analyzed in the previous section, the Dirac approach always underestimates the experimental Sauter diameter despite the use of the bubble collapse model. The consideration of the collapse of small bubbles is direct in the iMUSIG approach since the small bubbles, included in the smallest size group, naturally disappear when they are subjected to condensation.

The Sauter diameter predicted by the iMUSIG and quadratic approaches tends to slightly overestimate the experimental one from test cases 2 to 5. The quadratic approach really well predicts the Sauter diameter of test cases 1, 6, and 7. In contrast, the iMUSIG approach underestimates the Sauter diameter of test case 1 and overestimates the Sauter diameter of test case 7.

However, it is essential to note that for the iMUSIG approach, the Sauter diameter is not imposed in the first 0.6m and that the break-up and coalescence models are not frozen in these test cases. This can explain the fact that in test case 6, the predicted Sauter diameter increases using the iMUSIG approach while it slightly decreases experimentally and using the quadratic approach. The last test case has not been simulated by Liao and Lucas (2016).

Overall, the quadratic approach gives at least as good results as the iMUSIG approach in these test cases, either on void fraction or Sauter diameter evolution. Moreover, Habiyaremye et al. (2023) compared the CPU-time using either quadratic or iMUSIG approach for the Sauter diameter prediction for adiabatic test cases in this TOPFLOW large diameter test section, and showed that the CPU-time using quadratic approach is six times lower than using a multiple size group approach. Therefore, in these test cases, the quadratic approach is able to take into account the polydispersion effects on the mean flow in a low CPU-time. Indeed, as proved, it shows far better results than using the Dirac approach, and a reduced CPU-time compared to the iMUSIG approach.

However, Habiyaremye et al. (2023) have shown that the iMUSIG approach seems slightly better than the quadratic approach when predicting break-up and coalescence effects. They also showed that the log-normal method of moments gives really good results, similar to those obtained by the iMUSIG approach.

This shows that there is still work to be done to improve the quadratic approach so that it can be as good as the iMUSIG approach in all circumstances. Moreover, the log-normal method of moments could also be used in condensing flows to evaluate its capacities to predict the void fraction and Sauter diameter.

Moreover, these comparisons are done on cross-section averaged variables, and it is also essential to evaluate the new models on local variables as well. Indeed, the local evaluation can allow us to prove the accuracy of the new modeling and its limits.

4.6 Validation based on local profiles

This section aims to evaluate the accuracy of the full polydisperse modeling on local variables such as the radial profile of void fraction, gas velocity, bubble Sauter diameter, and liquid temperature. Moreover, this evaluation can highlight the limits of our modeling, especially in terms of transverse forces, such as the lift and turbulent dispersion forces.

Indeed, the previous sections of this chapter have allowed us to evaluate the accuracy of the Nusselt number correlation, the advantages of using the method of moments with a quadratic approach on the drag force and the mean Sauter diameter prediction, and also the benefits of introducing a bubble collapse model. All this work has been possible by analyzing the evolution of the cross-section average of the void fraction, Sauter diameter, and gas velocity. However, the evaluation of transverse forces is not possible using only cross-section variables.

This is why the radial profiles are evaluated in this section. In order to be brief and concise, only the radial profiles of test cases 2, 3, and 7 are shown in this section. The other profiles are shown in the Appendix I. However, the profiles of test cases 1 and 3 are similar; the profiles of test cases 2 and 4 are also alike; as well as test cases 6 and 7. Therefore, the three test cases that are represented in this section are representative of all the test cases considered in this work.

In this section, the void fraction profiles are normalized by their own cross-sectional average values. This normalization allows us to separate the effects of condensation rate, which are already discussed in the previous sections, from the effects of transverse forces, such as lift and turbulent dispersion forces. The normalization is defined by:

$$\alpha_g^* = \frac{\alpha_g(r)}{\alpha_{av}}, \tag{4.6.1}$$

where the cross-section mean void fraction α_{av} is the same as the one presented in previous sections, and is defined by:

$$\alpha_{av} = \frac{2}{R^2}\int_0^R \alpha_g(r) r dr. \tag{4.6.2}$$

The radial profiles of the normalized void fraction are presented in the left columns of the next Figures. The second, third, and last columns represent, respectively, the radial profiles of the steam velocity, the Sauter diameter, and the liquid temperature. The different lines represent the measurements at various heights. The various measurement heights are recalled in the Table 4.6.1.

$D_{orifice} = 1.0mm$		$D_{orifice} = 4.0mm$	
Level	Height [m]	Level	Height [m]
A (Inlet)	0.221	B(Inlet)	0.278
C	0.335	E	0.551
F	0.608	H	1.495
I	1.552	K	2.538
L	2.595	N	4.474
O	4.531		
P	7.689		

Table 4.6.1: Heights relative to steam injection position.

The measured profiles at Level A are used as inlet conditions for the simulation, which explains the superposition of the curves at Level A for Figure 4.6.1, 4.6.2, and 4.6.3. Moreover, the experimental Sauter diameter is imposed from Level A to Level F.

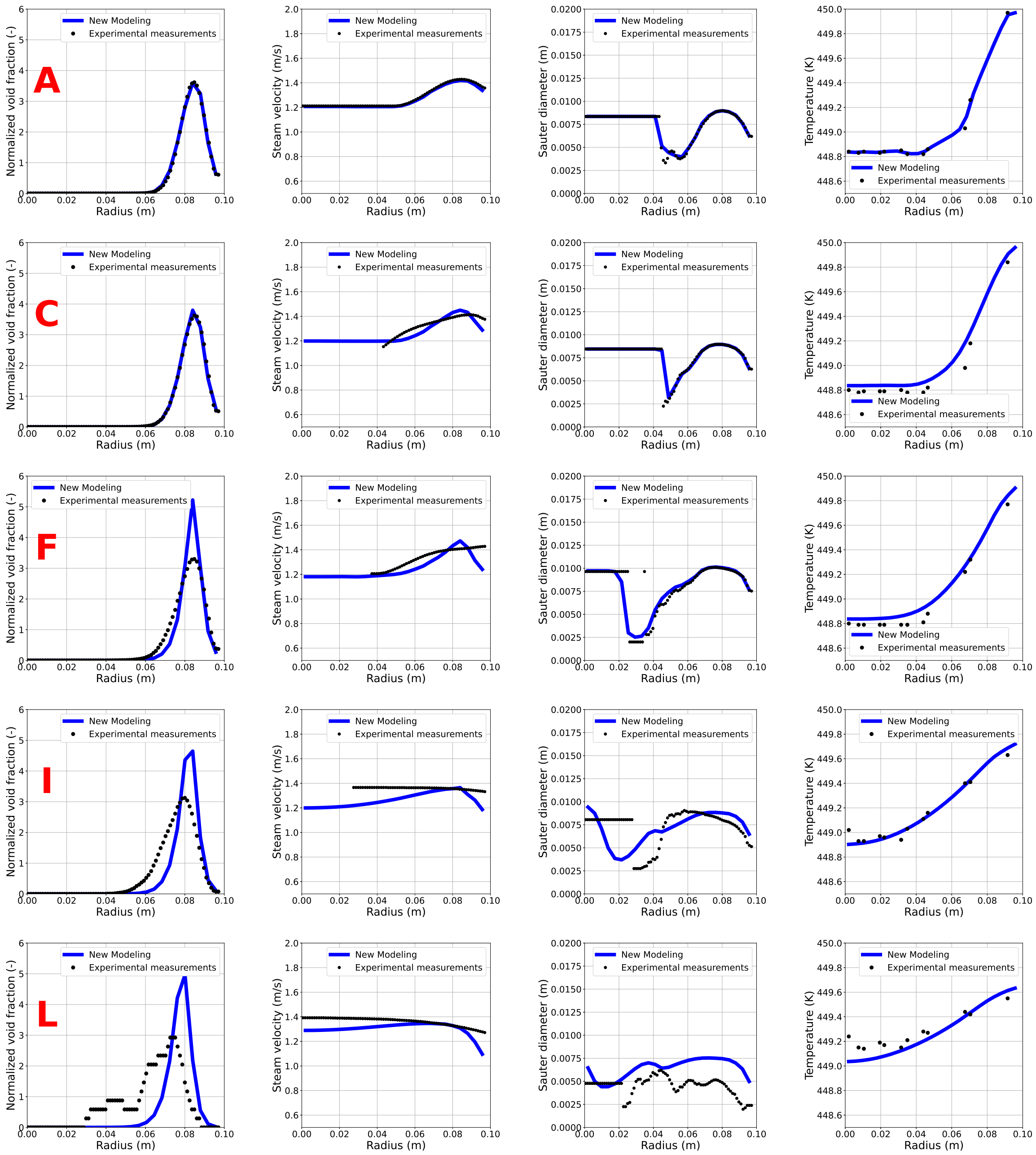

Figure 4.6.1: Case 2

First, it can be notice that since the steam bubbles are injected from the pipe wall, a wall-peak profile is found for all the test cases near the injection. Above, the profile peak moves gradually towards the pipe center. Moreover, experimentally, the peak is gradually spreading, from a sharp to a wide peak. This is due to both the lift and turbulent dispersion forces. The peak motion is credited to the lift force, and the thickness of the peak is attributed to the turbulent dispersion force.

It can be seen at Level I of case 2 in Figure 4.6.1 and especially at Level O of case 3 in Figure 4.6.2 that the numerical void fraction peak moves slightly slower to the pipe center than the experimental one. This can be due to an underestimation of the lift force by the model developed by Tomiyama et al. (2002), which is used in this work. Indeed, a higher lift force would cause the void fraction peak to move more quickly, therefore closer to the experimental one. However, the discrepancies shown are sufficiently low so that the model developed by Tomiyama et al. (2002) would still be used in the following.

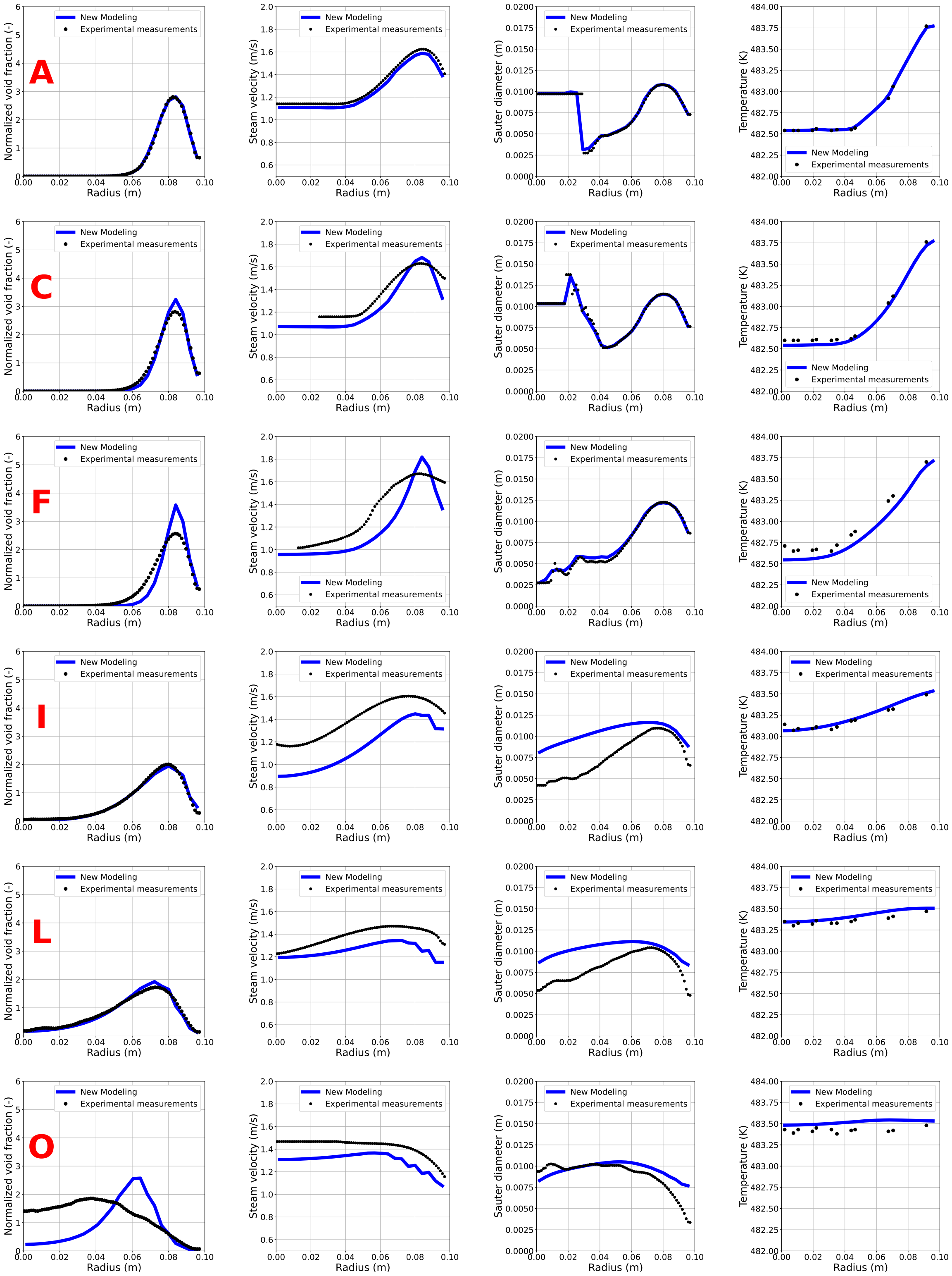

Figure 4.6.2: Case 3

Moreover, it is shown on Figure 4.6.1 that at Level F and I, the predicted profile peak is sharper and higher than the experimental one. This can be explained by a slight lack of accuracy of the turbulent dispersion force. Indeed, this force tends to increase the width of the void fraction peak, and so, a larger turbulent dispersion force would induce a better predicted void fraction. This too sharp and high peak is also particularly observable in the Figure 4.6.2 at Level F, but not in the Figure 4.6.3. It is interesting to note that the good predictions of the peak thickness are obtained in the test case 7, where the Sauter diameter are the lowest. And Mimouni et al. (2017b) have shown on CHAPTAL experiment that the experimental liquid Reynolds stress increases with the bubble diameter at same void fraction. Moreover, the turbulent dispersion is directly proportional to the turbulent kinetic energy. Therefore, due to the low Sauter diameter in the test case 7, the experimental liquid Reynolds stress and turbulent dispersion should be low, while they should be higher for the other test cases, with higher Sauter diameter.

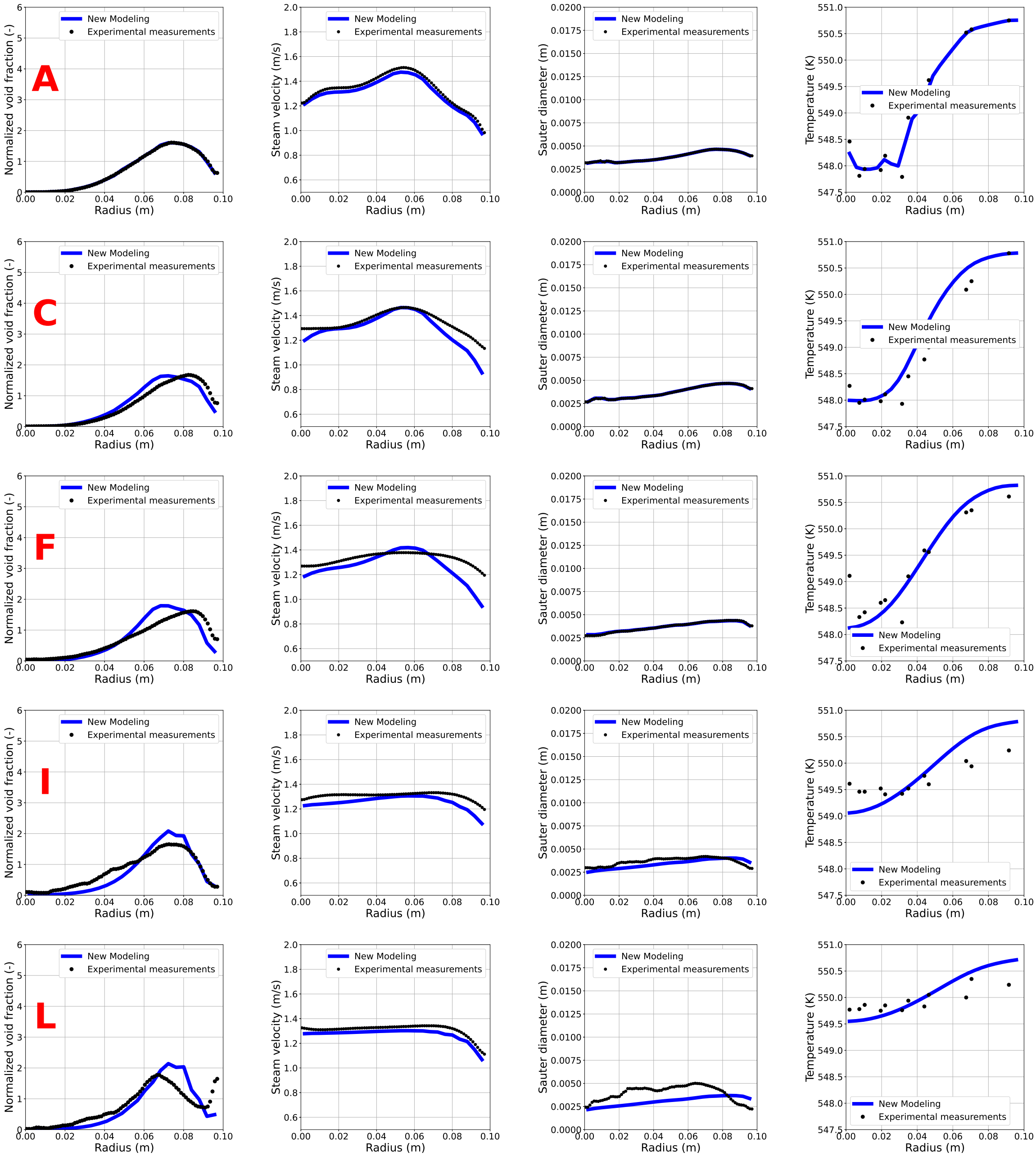

Figure 4.6.3: Case 7

The fact that the peak thickness is well predict for test case where the turbulence is expected to be low, and not so well in other, could indicate that the Reynolds stress predicted by Neptune_CFD is underestimated. Therefore, a higher turbulence intensity for the test cases where the bubbles are large would imply a wider peak, and a better estimation of the void fraction peak.

> **Note:** Further improvements on the void fraction peak thickness predictions could be achieved by improvements on the turbulence predictions.

However, these discrepancies noticeable on the peak thickness are sufficiently small so that both the current $R_{ij} - SSG$ turbulence model and the Generalized Turbulent Dispersion (GTD) model developed by Haynes (2004) and presented by Laviéville et al. (2017) are still used in the following.

Concerning the gas velocity profile, a peak is found at the inlet near the wall, similar to the void fraction peak. This is due to the acceleration effect brought by the steam injection. Above in the pipe, where the steam spreads from the near-wall region to the pipe center, the velocity decreases near the wall and increases in the center part. These simulations predict well this evolution tendency. However, the calculated gas velocity is usually underestimated compared to the experimental measurements. This issue has already been discussed in the section 4.3.2, on the discussion about the drag force. Indeed, it has been shown that this velocity underestimation is much lower in this modeling, using the quadratic approach, than using the Dirac approach.

The Sauter diameter is imposed from Level A to Level F. Above, the Sauter diameter profile is predicted overall well. There are a few discrepancies, which have already been discussed in detail regarding the cross-section averaged Sauter diameter evolution in the previous sections.

Finally, the radial profiles of the liquid temperatures are well predicted in all test cases and at all Levels.

4.7 Discussions

In this chapter, an accurate modeling of the bubble condensation in sub-cooled water phenomena is established using only one dispersed phase and one IATE. Indeed, using a quadratic bubble size distribution function, the Nusselt model developed by Chen and Mayinger (1992), and a bubble collapse model, the numerical results obtained on TOPFLOW test cases are comparable to the experimental ones.

First, the equations of the dispersed phase are described using the standard method of moments. As a result, equations similar to the equations of the two-fluid model are obtained. However, using this method, the interfacial terms are expressed as integrals that depend on a bubble size distribution function. In addition, this method also provides an IATE, and the terms on the right-hand side of this equation also rely on the distribution function. Next, two distribution functions are introduced. The first is the Dirac function, which assumes a local monodispersion of bubble size, and the second is a quadratic function, which assumes a local polydispersion of bubble size.

These functions lead to different formulations for interfacial exchanges, whether in terms of mass and energy exchange, interfacial forces, or interfacial area concentration. The influence of these functions on each model of interfacial terms is evaluated by analyzing the results of TOPFLOW simulations. The distribution function, whether Dirac or quadratic, has a limited impact on interfacial mass and energy exchange. This study also confirms that the Ranz-Marshall correlation underestimates condensation, as observed by Liao and Lucas (2016) using the iMUSIG approach. The principal implication of this study is that the Ranz-Marshall correlation, developed for low bubble Reynolds numbers below 200, should be used with caution for larger bubble Reynolds numbers.

Nevertheless, this work helped to identify a more generic correlation: the Chen and Mayinger (1992) one, developed for larger bubble Reynolds numbers, between 400 and $10,000$. The results obtained using this correlation are accurate, even for test cases with larger bubble Reynolds numbers, up to $Re_b = 30,000$.

Remark: Therefore, we recommend using this Chen-Mayinger correlation instead of the Ranz-Marshall one in order to simulate condensing flows with expected bubble Reynolds numbers higher than 400.

In contrast to the mass and energy exchanges, the distribution function used has a significant impact on the drag force model. The quadratic function gives the best results in modeling the drag force. Using the Dirac function, the void fraction was overestimated near the inlet due to an overestimation of the drag force and, therefore, an underestimation of the gas velocity. This behavior was not observable when using the quadratic function. The improvements on the drag force predictions achieved using the quadratic function are not limited to the inlet region but can also be observed throughout the pipe.

The IATE has also been developed using Dirac and quadratic functions, producing different formulations for the source terms in each approach. The Sauter diameter obtained using each approach was different, with a higher Sauter diameter in the case of a quadratic function. However, in both approaches, the Sauter diameter was underestimated compared to the experimental diameter. This is due to the phenomenon of collapse of small bubbles, which is significant experimentally and which has not been taken into account in the IATE at first. Therefore, the model proposed by Park et al. (2007) has been then implemented in the IATE, following both Dirac and quadratic approaches. The predicted Sauter diameter is more accurate using this model and is slightly better using the quadratic approach. A sensitivity to the β_b parameter of the model has been done for the quadratic approach. Initially, the value $\beta_b = 0.4$ has been used from empirical considerations by Park et al. (2007). The sensitivity shows that for some test cases, namely 1, 6, and 7, the value $\beta_b = 0.4$ is better, but for the other test cases, the value $\beta_b = 0.3$ gives better results. Overall, the Sauter diameter is still accurate with both values $\beta_b = 0.3$ and $\beta_b = 0.4$. A more theoretical value may be found for this β_b parameter. Nevertheless, the $\beta_b = 0.4$ value defined by Park et al. (2007) is still accurate for test cases with pressure between $P = 10$ bar to $P = 65$ bar, even if it was initially formulated for test cases at atmospheric pressure.

Next, the axial evolution of the predicted void fraction and Sauter diameter obtained using Dirac and quadratic approaches have been compared to those obtained by the iMUSIG approach, from Liao and Lucas (2016) numerical simulations. It shows accurate results, whether for the quadratic or iMUSIG approach, demonstrating that the quadratic approach can also take into account the bubble size polydispersion to predict the axial evolution of the mean void fraction and Sauter diameter well. Therefore, this approach permits obtaining better results than the Dirac approach, and similar results as the iMUSIG approach with a lower CPU-time.

Finally, the experimental radial profiles of void fraction, gas velocity, Sauter diameter and liquid temperature are compared for all test cases at all measurement heights to the profiles predicted by the new quadratic modeling. Overall, the numerical results are in agreements with the measurements, even if small discrepancies exist on the void fraction peak motion, that could be due to errors on the turbulent dispersion model.

Conclusion

A new modeling using the standard method of moments with quadratic bubble size distribution function, the Chen and Mayinger correlation, and a bubble collapse model has been used to create a database of CFD simulations of bubble condensation flows. The following chapter describes the work associated with the use of this database to develop a macroscopic model for the bubble condensation phenomenon.

Chapter 5

Development and evaluation of a bubble condensation model at macroscopic scale using CFD database

Contents

The chapter 3 has proven that the mass and energy interfacial transfer terms related to bubble condensation are predominant at the macroscopic scale in sub-cooled boiling industrial flows. Next, in chapter 4, a validated database has been developed on bubble condensation separate effect tests. Indeed, by introducing a new modeling, all the predicted radial profiles of void fraction, gas velocity, bubble mean diameter, and liquid temperature are close to the experimental ones.

This chapter aims to evaluate the existing macroscopic models of the interfacial heat and mass transfer terms and develop a new one based on the local CFD database developed in chapter 4.

Since the macroscopic models are compared to the averaged variables of the CFD database and not directly to the experiment, it is necessary to quantify the deviations between CFD predictions and experimental measurements initially. This quantification is done in section 5.1.

Later, the models of the macroscopic codes CATHARE and TRACE are expressed, and next, they are evaluated using the CFD database. Actually, in this chapter, the CATHARE code that is called corresponds to the 3-D module of CATHARE, which is described in 1.3.1. The mean absolute percentage errors (MAPE) of the models are studied, as well as their bias and standard deviations.

Afterward, in section 5.3, new macroscopic models are proposed and evaluated.

First, in section 5.3.1, two different models are introduced based on the correlation developed by Chen and Mayinger (1992), which has been used at the CFD scale. It is important to note that using this model at the macroscopic scale, the variables used in the correlation are spatially averaged and not local as in CFD, which may involve large deviations, that we are going to evaluate.

Next, in section 5.3.2, a statistic approach is used to find a macroscopic Nusselt number that minimizes the error between the energy interfacial terms predicted by the model and calculated from the CFD database.

Then, in section 5.3.3, studies are done to get closer to a fully mechanistic model based on a spatial average of the local correlation. Therefore, some averages of products of local variables appear. This section aims to identify for which variables the hypothesis of an average of product equal to a product of average ($\langle a.b \rangle = \langle a \rangle.\langle b \rangle$) is reasonable and for which it is not. The idea is to reduce to a minimum the number of variables that need to be modeled in order to propose models for the few variables that remain in future works and obtain a fully mechanistic macroscopic model.

Finally, some insights are given about an a priori evaluation on alternative experiments in section 5.3.4, and about an a posteriori evaluation that needs to be done in the future in section 5.4. Indeed, the work done in this thesis consists of a priori evaluation, i.e., evaluations done using averaged CFD variables. In order to apply the models at the macroscopic scale, some a posteriori evaluations, i.e., using directly the macroscopic code, need to be done, and the errors between the a priori and a posteriori evaluations need to be assessed.

5.1 Evaluation of CFD database

5.1.1 Creation of the reference term

The CFD database obtained in chapter 4 provides several variables at each local cell, presented in blue in Figure 5.1.1.

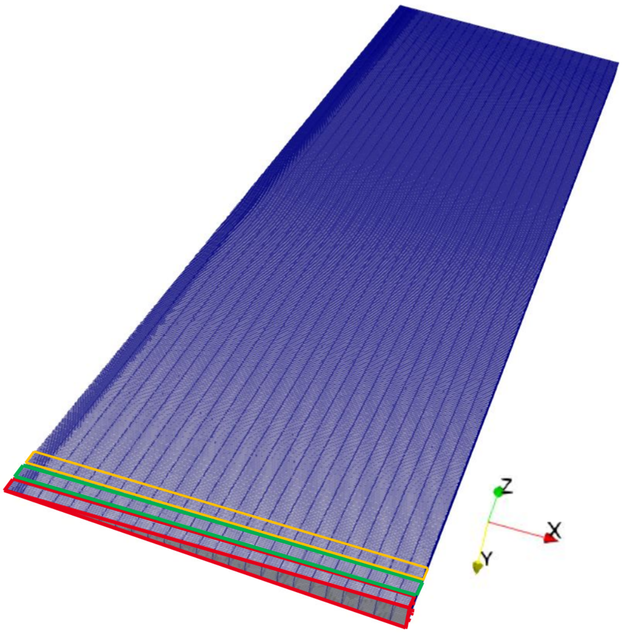

Figure 5.1.1: TOPFLOW local mesh (blue), and first three macroscopic cells (red, green and orange).

Then, all the variables are spatially averaged on macroscopic cells. The first three macroscopic cells are represented in red, green, and orange in Figure 5.1.1. Using the CFD database, it is also possible to calculate the average of the product of local variables or the average of the product of spatial deviations of some terms on the macroscopic cells. These averages are helpful in understanding the phenomena that happen at the subgrid scale and in formulating new models.

The spatially averaged energy interfacial transfer term due to condensation $\langle \Pi_l' \rangle$ can be directly calculated from the CFD database by the averaging of local terms Π_l'. Moreover, this term is directly related to the mass interfacial transfer term :

$$\Gamma_l = \frac{\Pi_l' + \Pi_g'}{H_{lg}}. \tag{5.1.1}$$

In the case of bubble condensation: $\Pi_l' >> \Pi_g'$. All the other macroscopic variables can also be averaged from the CFD database. The reference term $\langle \Pi_l' \rangle_{CFD}$ is calculated from the CFD database as:

$$\langle \Pi_l' \rangle_{CFD} = \Big\langle a_i h_l (T_{sat} - T_l) \Big\rangle; \quad \text{with:} \tag{5.1.2a}$$

$$a_i = \frac{6\alpha_g}{d_{32}}; \quad h_l = \frac{\mathrm{Nu}_b \lambda_l}{d_{32}}; \quad \mathrm{Nu}_b = 0.185 \mathrm{Re}_b^{0.7} \mathrm{Pr}_l^{0.5}; \quad \mathrm{Re}_b = \frac{\rho_l |v_r| d_{32}}{\mu_l}; \quad \mathrm{Pr}_l = \frac{\mu_l C_{p_l}}{\lambda_l}. \tag{5.1.2b}$$

Therefore, the correlations from existing macroscopic codes, as well as the new ones developed in this chapter, can be evaluated by an a priori method. Indeed, at each macroscopic cell, the correlations can be calculated using the values of the averaged variables. Next, the errors between the CFD averaged energy interfacial transfer term $\langle \Pi_l' \rangle_{CFD}$ and the correlations can be calculated.

In order to compare the correlations to the reference term, some statistical operators are introduced in the next section. Moreover, it should be noted that the correlations are compared to the averaged values of the CFD database, and not directly to the experiment. Consequently, the deviations between the CFD database and the experimental measurements are studied in section 5.1.3. In the same way, the potential deviations linked to the experimental uncertainties are also discussed in this section 5.1.3. For this, some statistical operators are introduced in the next section.

5.1.2 Introduction of statistical operators

In order to evaluate a term ξ_{eval} in comparison to a reference term ξ_{ref}, some new statistical operators are introduced. First, the Mean Error (ME) and Mean Absolute Error (MAE) between the term that needs to be evaluated and the reference one are defined as:

$$\mathrm{ME} = \frac{1}{N} \cdot \sum_{I=1}^{N} \left(\xi_{eval}^{I} - \xi_{ref}^{I} \right), \quad \mathrm{MAE} = \frac{1}{N} \cdot \sum_{I=1}^{N} \left| \xi_{eval}^{I} - \xi_{ref}^{I} \right|. \tag{5.1.3}$$

The variable N corresponds to the number of points on which the term is evaluated.

Next, the Mean Absolute Percentage Error (MAPE) is defined to measure the prediction accuracy of the term as:

$$\mathrm{MAPE} = 100 \cdot \frac{1}{N} \cdot \sum_{I=1}^{N} \left(\frac{\left| \xi_{eval}^{I} - \xi_{ref}^{I} \right|}{\left| \xi_{ref}^{I} \right|} \right). \tag{5.1.4}$$

Therefore, error quantification can be done using the MAPE because it represents the mean relative error, expressed in percentage, between the evaluated term and the reference one. This MAPE is going to be used in the next section to evaluate the deviations of the CFD in comparison to the experiment, based on all the experimental measurement points. Moreover, this MAPE will also be used in section 5.2 to evaluate the existing correlations on all the macroscopic cells.

Finally, the Relative Statistical Bias (RSB), Relative Percentage Statistical Bias (RPSB), and Relative Percentage Standard Deviations (RPSD) are also introduced in equations (5.1.5) and (5.1.6).

$$\mathrm{RSB} = \frac{1}{N} \cdot \sum_{I=1}^{N} \left(\frac{\xi_{eval}^{I} - \xi_{ref}^{I}}{\xi_{ref}^{I}} \right), \quad \mathrm{RPSB} = 100 \cdot \frac{1}{N} \cdot \sum_{I=1}^{N} \left(\frac{\xi_{eval}^{I} - \xi_{ref}^{I}}{\xi_{ref}^{I}} \right), \tag{5.1.5}$$

$$\mathrm{RPSD} = 100 \cdot \sqrt{\frac{1}{N} \sum_{I=1}^{N} \left(\frac{\xi_{eval}^{I} - \xi_{ref}^{I}}{\xi_{ref}^{I}} - \mathrm{RSB} \right)^{2}}. \tag{5.1.6}$$

This relative statistical bias is used to calculate the relative bias between the term that is evaluated and the reference. Indeed, a negative bias indicates that the term ξ_{eval} tends to underestimate the ξ_{ref} value, while a positive bias suggests the reverse. This value is related to the accuracy of the evaluation. The standard deviation is a measure of the amount of variation of the relative error around the relative statistical bias defined in equation (5.1.5). A low standard deviation indicates that the values tend to be close to the mean of the set, while a high standard deviation indicates that the values are spread out over a wider range.

5.1.3 Deviations between the CFD database and the experimental flow

The deviations between the CFD database and the experimental flow can come from two different sources. On the one hand, these deviations can come from the local deviations between the CFD results and the experimental measurements. On the other hand, they can come from the experimental uncertainties.

The lack of experimental data makes it impossible to directly estimate the deviations in the energy interfacial transfer term Π_l'. However, since there are local measurements of the void fraction and the liquid temperature, it is possible to calculate experimentally the product $\zeta = \alpha_l \rho_l C_{p_l} T_l$. The liquid density and heat capacity are calculated from water thermodynamic properties tables using the temperature and pressure. The pressure is not measured at each experimental point, but the inlet pressure is measured and used to calculate both the liquid density and heat capacity. Therefore, it is possible in the following to calculate, at each measurement point, the experimental term $\zeta = \alpha_l \rho_l C_{p_l} T_l$, as well as the minimum and maximum terms using the minimum and maximum uncertainties on the void fraction and liquid temperature. Finally, the experimental term can also be compared to the CFD variables that are interpolated at the same measurement points.

These comparisons are treated separately in the following.

Errors linked to experimental uncertainties

The measurement uncertainties of the TOPFLOW experiment are described in section 4.1.2. The error of the temperature measurement is about $\pm 1\ K$, and the absolute error in void fraction could be up to ± 0.01.

It is worth mentioning that some experimental points are positioned where there is only liquid, or where the temperature is close to the saturation temperature. Therefore, the positive uncertainties are limited since $T_l \leq T_{sat}$ and $\alpha_l \leq 1$. Moreover, it is recalled that both the density and heat capacity are calculated from water thermodynamic properties tables using inlet pressure and measured liquid temperature. The uncertainties related to each variable of ζ are expressed in equation (5.1.7).

$$\Delta\alpha_l = [-0.01, \min(0.01, 1-\alpha_l)], \quad \Delta T_l = [-1, \min(1, T_{sat} - T_l)], \tag{5.1.7a}$$

$$\Delta\rho_l = [\rho_l\,(T_l - 1, P) - \rho_l\,(T_l, P)\,,\ \rho_l\,(\min(T_l + 1, T_{sat}), P) - \rho_l\,(T_l, P)]\,, \tag{5.1.7b}$$

$$\Delta C_{p_l} = [C_{p_l}\,(T_l - 1, P) - C_{p_l}\,(T_l, P)\,,\ C_{p_l}\,(\min(T_l + 1, T_{sat}), P) - C_{p_l}\,(T_l, P)]\,. \tag{5.1.7c}$$

Based on the experimental uncertainties of each variable, the total uncertainty is given in equation (5.1.8).

$$\begin{aligned}\Delta\zeta = \rho_l(T_l, P)\cdot C_{p_l}(T_l, P)\cdot T_l\cdot|\Delta\alpha_l| + \alpha_l\cdot C_{p_l}(T_l, P)\cdot T_l|\Delta\rho_l| \\ + \alpha_l\cdot\rho_l(T_l, P)\cdot T_l\cdot|\Delta C_{p_l}| + \alpha_l\cdot\rho_l(T_l, P)\cdot C_{p_l}(T_l, P)\cdot|\Delta T_l|.\end{aligned} \tag{5.1.8}$$

There are two uncertainties $\Delta\zeta_{min}$ and $\Delta\zeta_{max}$ related to the left and right boundaries of the uncertainties defined in equation (5.1.7). Moreover, the reference term ζ_{ref} is expressed as:

$$\zeta_{ref} = \alpha_{l_{exp}}\cdot\rho_l(T_{l_{exp}}, P_{in})\cdot C_{p_{l,exp}}(T_{l_{exp}}, P_{in})\cdot T_{l_{exp}}. \tag{5.1.9}$$

It is important to note that the void fraction and temperature measurements are not done at the same radial positions, as it can be seen in Figure 4.6.1. Indeed, there are 80 radial measurement points for the void fraction but only 12 measurement points for the liquid temperature. Therefore, the void fraction measurements are interpolated at the same radial positions as the liquid temperature. Consequently, there are 12 measurement points for the variables ζ_{ref}, $\Delta\zeta_{min}$, and $\Delta\zeta_{max}$ at each measurement height, corresponding to a total of 504 points. Based on all the measurement points, the MAPE for both $\Delta\zeta_{min}$ and $\Delta\zeta_{max}$ in comparison to ζ_{ref} are calculated as:

$$\text{MAPE} = 100\cdot\frac{1}{504}\sum_{I=1}^{504}\frac{\Delta\zeta^I}{|\zeta^I_{exp}|}. \tag{5.1.10}$$

The MAPE obtained with both the minimum and maximum uncertainty values are expressed in Table 5.1.1.

	$\Delta\zeta_{min}$	$\Delta\zeta_{max}$
MAPE	1.54%	0.81%

Table 5.1.1: Evaluation of the MAPE linked to the experimental uncertainties on ζ variable.

The MAPE obtained when using the negative uncertainties, i.e., characterized by the term ζ_{min} is 1.54%, while it is 0.81% for ζ_{max}, corresponding to the positive uncertainties. As mentioned above, the error related to the positive uncertainties is lower because some experimental points are positioned where there is only liquid phase, or where the temperature is close to the saturation temperature.

Errors linked to the deviations between the CFD database and the measurements

The deviations between the CFD results and the measurements on the variable $\zeta = \alpha_l\rho_l C_{p_l} T_l$ are now considered. The CFD variables are also interpolated on the same radial positions as the temperature probes. For each test case, the results obtained by the code are compared to the measurements at 12 radial positions of all the heights measurements, with the exception of the first one, which corresponds to the inlet, where the experimental profiles are imposed into the calculation boundary condition. The measurement heights are described in Table 4.6.1. Therefore, the comparison is done on 420 points. The MAPE is then expressed as:

$$\text{MAPE} = 100\cdot\frac{1}{420}\cdot\sum_{I=1}^{420}\left(\frac{\left|\zeta^I_{CFD} - \zeta^I_{ref}\right|}{\left|\zeta^I_{ref}\right|}\right). \tag{5.1.11}$$

The operators of relative percentage statistic bias (RPSB) and relative percentage standard deviations (RPSD) are also used following their definitions in equation (5.1.6). In the same way as for the experimental variables, the CFD density and heat capacity variables are deduced from the water thermodynamic properties tables using the predicted temperature and the inlet pressure.

	MAPE	RPSB	RPSD
ζ_{CFD}	0.38%	-0.01%	0.9%

Table 5.1.2: Evaluation of the CFD deviations of the ζ variable compared to the measurements.

The MAPE, RPSB, and RPSD of the CFD in comparison to the measurements for the variable ζ are expressed in Table 5.1.2.

The error on the ζ variable between the CFD predictions and the measurements is relatively low, with a MAPE below 0.5% in comparison to the measurements. Moreover, the RPSB is almost zero, which means that the predictions are centered. Finally, the RPSD is reasonably low, with a value of 0.9%, which means that the errors are not widely dispersed.

Although the variable considered in this section is not directly the energy interfacial transfer term Π'_l, the fact that the error linked to the variable ζ between the CFD and measurements is quite low shows that the CFD results are relatively close to the experimental ones, at least within a few percents.

5.2 Evaluation of existing macroscopic models

This section focuses on the liquid energy interfacial transfer term Π'_l. Moreover, in most macroscopic codes such as CATHARE (Bestion, 1990) or TRACE (Bajorek, 2008), flow regime maps are used and different correlations are used depending on the flow regime which is assumed. In this section, only the models used for bubbly flows are described.

First, an empirical model is used in the CATHARE code. This model is described in detail in the following.

5.2.1 Description of CATHARE correlation

The model used in CATHARE for bubbly flows is adapted from the correlation developed by Shah (1979). Indeed, Shah (1979) has developed a correlation for the heat flux density $\tilde{\Psi}$ for condensing flow due to wall cooling in the form:

$$\tilde{\Psi} = \tilde{h}_{shah} \cdot (\tilde{T}_{sat} - \tilde{T}_w). \tag{5.2.1}$$

However, heat flux density can also be expressed as:

$$\tilde{\Psi} = \tilde{h}_{li} \cdot (\tilde{T}_{sat} - \tilde{T}_l) = \tilde{h}_{wl} \cdot (\tilde{T}_l - \tilde{T}_w), \quad \Longrightarrow \frac{\tilde{h}_{shah}}{\tilde{h}_{wl}} = \frac{\tilde{T}_l - \tilde{T}_w}{\tilde{T}_{sat} - \tilde{T}_w}. \tag{5.2.2}$$

This leads to:

$$\tilde{h}_{shah} \cdot (\tilde{T}_{sat} - \tilde{T}_w) = \tilde{h}_{li} \cdot \left(\tilde{T}_{sat} - \tilde{T}_w\right) + \tilde{h}_{li} \cdot \left(\tilde{T}_w - \tilde{T}_l\right), \tag{5.2.3}$$

$$\Longleftrightarrow \quad \tilde{h}_{shah} = \tilde{h}_{li} \left(1 - \frac{\tilde{T}_l - \tilde{T}_w}{\tilde{T}_{sat} - \tilde{T}_w}\right), \tag{5.2.4}$$

$$\Longleftrightarrow \quad \tilde{h}_{li} = \tilde{h}_{shah} \left(1 - \frac{\tilde{h}_{shah}}{\tilde{h}_{wl}}\right)^{-1}. \tag{5.2.5}$$

The coefficient $\tilde{h}_{wl}$ corresponds to the wall-to-liquid heat flux. The parameter $\left(1 - \frac{\tilde{h}_{shah}}{\tilde{h}_{wl}}\right)^{-1}$ is approximated by the function $\tilde{F}_1$ in the following relation. Indeed, the energy interfacial transfer term due to condensation $\tilde{\Pi}'_{l_{CATHARE}}$ is written in the form:

$$\tilde{\Pi}'_{l_{CATHARE}} = 4 \cdot \tilde{F}_1 \cdot \tilde{Nu} \cdot \tilde{F}_2 \cdot \frac{\tilde{\lambda}_l}{\tilde{D_h}^2} \cdot (\tilde{T}_{sat}(\tilde{P}_g) - \tilde{T}_l). \tag{5.2.6}$$

With:

$$\tilde{F}_2 = 1 + 3.8\left[\frac{\tilde{\alpha}_g\tilde{\rho}_g}{(1-\tilde{\alpha}_g)\tilde{\rho}_l}\right]^{0.76}\cdot\left[\frac{\tilde{P}_{cr}}{\tilde{P}}\right]^{0.38}, \tag{5.2.7}$$

$$\tilde{Nu} = 4 + 0.023\tilde{Re}_l^{0.8}\cdot\tilde{Pr}_l^{0.4}, \tag{5.2.8}$$

$$\tilde{Re}_k = \frac{\tilde{\alpha}_k\tilde{\rho}_k\tilde{D}_h\cdot|\underline{\tilde{v}}_k|}{\mu_k} + \tilde{Re}_0, \quad \tilde{Pr}_k = \frac{\tilde{\mu}_k\cdot\tilde{c}_{p_k}}{\tilde{\lambda}_k}. \tag{5.2.9}$$

$\tilde{P}_{cr}$ is the critical pressure of the water ($\tilde{P}_{cr} = 22.1$ MPa) and $\tilde{Re}_0 = 10$. The function $\tilde{F}_1$ approximates the $\left(1 - \frac{\tilde{h}_{shah}}{\tilde{h}_{wl}}\right)^{-1}$ coefficient and reduces condensation when $\tilde{\alpha}_g$ approaches the residual value:

$$\tilde{F}_1 = \frac{30(\tilde{\alpha}_g - \tilde{\alpha}_0\tilde{X}_g) + 1800(\tilde{\alpha}_g - \tilde{\alpha}_0\tilde{X}_g)^2}{\left[1 + 30(\tilde{\alpha}_g - \tilde{\alpha}_0\tilde{X}_g)\right]\cdot\left[1 + 60\tilde{\alpha}_g^2 - 0.081\tilde{P}^{0.38}\tilde{\alpha}_g^{1.76}(1-\tilde{\alpha}_g)^{0.3}\right]}, \tag{5.2.10}$$

with $\alpha_0 = 10^{-5}$ and $\tilde{X}_g$ the gas mass fraction. The Shah correlation has been validated for void fraction lower than 0.85.

All the terms expressed in equations (5.2.6) are composed of averaged variables and can be calculated from CATHARE calculations. They can also be calculated by an average of local variables from the CFD database. In order to evaluate this correlation, all the macroscopic variables from the correlation (5.2.6) are calculated by an average of CFD variables. Then, the term $\tilde{\Pi}'_{l_{CATHARE}}$ can be compared to the reference term $\langle\Pi'_l\rangle_{CFD}$. This comparison is done in section 5.2.3.

5.2.2 Description of TRACE correlation

In the TRACE code, the model used is inspired by the correlation developed by Ranz and Marshall (1952), which is widely used at the CFD scale and is presented in section 1.2, in equations (1.2.14) and (1.2.15). However, it should be noted that the model developed at the RANS scale uses local variables, while the model developed in TRACE uses only spatially averaged variables. The TRACE model is expressed below.

The subscript DB corresponds to dispersed bubbles. In this section, only the model used for dispersed bubbly flows is described. The interface to liquid heat transfer term is written as follows:

$$\tilde{\Pi}'_{l_{TRACE}} = \tilde{a}_i\tilde{h}_{li,DB}(T_{sat} - \tilde{T}_l). \tag{5.2.11}$$

The variable $\tilde{T}_l$ is calculated by the code, and the interfacial area concentration $\tilde{a}_i$ is calculated as:

$$\tilde{a}_i = \frac{6\tilde{\alpha}_g}{\tilde{d}_{DB}}. \tag{5.2.12}$$

The diameter of the dispersed bubbles is calculated as a function of the capillary length λ_c, namely:

$$\tilde{d}_{DB} = 2\lambda_c = 2\cdot\sqrt{\frac{\tilde{\sigma}}{g(\tilde{\rho}_l - \tilde{\rho}_g)}}. \tag{5.2.13}$$

It is important to note that the bubble diameter is estimated in the TRACE code, while it is not the case in the CATHARE code. Indeed, the bubble diameter does not appear in any CATHARE correlation. The heat transfer coefficient $\tilde{h}_{li,DB}$ is expressed as:

$$\tilde{h}_{li,DB} = \frac{\tilde{\lambda}_l\tilde{\mathrm{Nu}}_{DB}}{\tilde{d}_{DB}}. \tag{5.2.14}$$

The macroscopic bubble Nusselt number $\tilde{\mathrm{Nu}}_{DB}$ is calculated in TRACE code using the correlation from Ranz and Marshall (1952), which is expressed as:

$$\tilde{\mathrm{Nu}}_{DB} = 2.0 + 0.6\,\tilde{\mathrm{Re}}_{DB}^{1/2}\,\tilde{\mathrm{Pr}}_l^{1/3}. \tag{5.2.15}$$

The macroscopic bubble Reynolds number $\tilde{\mathrm{Re}}_{DB}$ and Prandtl number $\tilde{\mathrm{Pr}}_l$ are expressed as:

$$\tilde{\mathrm{Re}}_{DB} = \frac{\tilde{\rho}_l \, \tilde{v}_{r,DB} \, \tilde{d}_{DB}}{\tilde{\mu}_l}, \tag{5.2.16}$$

$$\tilde{\mathrm{Pr}}_l = \frac{\tilde{\mu}_l \, \tilde{c}_{p_l}}{\tilde{\lambda}_l}. \tag{5.2.17}$$

At the macroscopic scale, the dispersed bubble relative velocity $\tilde{v}_{r,DB}$ cannot simply be assumed to be given by the phasic relative velocity, $|\tilde{v}_g - \tilde{v}_l|$, that results from the solution of the two-fluid momentum equations. This is due to the effect of the void fraction distribution. In order to get a more accurate estimation of the dispersed bubble relative velocity, the TRACE relative velocity $\tilde{v}_{r,DB}$ is calculated as:

$$\tilde{v}_{r,DB} = \min\left[|\tilde{v}_g - \tilde{v}_l|, \tilde{v}_{DB,term}\right], \tag{5.2.18}$$

where $\tilde{v}_{DB,term}$ is the dispersed bubble terminal velocity calculated by:

$$\tilde{v}_{DB,term} = \tilde{v}_{r,\infty} \cdot (1 - \tilde{\alpha}_g)^{2.39}, \qquad \text{with:} \quad \tilde{v}_{r,\infty} = \sqrt{2}\left(\frac{\tilde{\sigma} g \left(\tilde{\rho}_l - \tilde{\rho}_g\right)}{\tilde{\rho}_l^2}\right)^{1/4}. \tag{5.2.19}$$

In the same way as for CATHARE, all the variables expressed in equations (5.2.11) are averaged variables and can be calculated from TRACE calculations. However, TRACE and CATHARE correlations are quite different. On one hand, the CATHARE code uses an empirical model, while TRACE uses a model that is widely used at the RANS scale. Moreover, the interfacial area concentration, and thus the mean bubble diameter, are modeled by TRACE and used in the $\tilde{\Pi}_l'$ correlation from TRACE. In contrast, these variables are not used in the CATHARE correlation.

These models are going to be evaluated on the CFD database in the next section.

Since the TRACE correlation is more generic, it is possible to evaluate the capabilities of this correlation by overcoming the errors linked to the bubble diameter predictions. Indeed, a simple algebraic correlation is developed to predict the mean bubble diameter, while a more sophisticated approach could be proposed by using an IATE, for example. Therefore, two evaluations are done for TRACE correlation in the next section, one using the correlation (5.2.11), and one using the same correlation with the variable $\langle a_i \rangle$ calculated from the CFD database, and the relation $\tilde{d}_{DB} = 6\langle \alpha_g \rangle / \langle a_i \rangle_{CFD}$. This separation allows us to evaluate the accuracy of the correlation and to know if the errors are coming from the mean bubble diameter prediction or from the global correlation itself.

5.2.3 A priori evaluation

First, the MAPE, RPSB, and RPSD between the correlation term $\Pi'_{l,cor}$ and the reference term $\langle \Pi_l' \rangle_{CFD}$ are defined as:

$$\mathrm{MAPE} = 100 \cdot \frac{1}{N} \cdot \sum_{I=1}^{N} \left(\frac{\left|\Pi'^{I}_{l,cor} - \langle \Pi_l' \rangle^I_{CFD}\right|}{|\langle \Pi_l' \rangle^I_{CFD}|} \right), \; \mathrm{RSB} = \frac{1}{N} \cdot \sum_{I=1}^{N} \left(\frac{\Pi'^{I}_{l,cor} - \langle \Pi_l' \rangle^I_{CFD}}{\langle \Pi_l' \rangle^I_{CFD}} \right), \tag{5.2.20a}$$

$$\mathrm{RPSB} = 100 \cdot \mathrm{RSB}, \quad \mathrm{RPSD} = 100 \cdot \sqrt{\frac{1}{N} \sum_{I=1}^{N} \left(\frac{\Pi'^{I}_{l,cor} - \langle \Pi_l' \rangle^I_{CFD}}{\langle \Pi_l' \rangle^I_{CFD}} - \mathrm{RSB} \right)^2}. \tag{5.2.20b}$$

Here, the variable N corresponds to the number of macroscopic cells in the CFD database. Considering that there are seven test cases with 50 macroscopic cells each, there is a total of 350 macroscopic cells. However, since an interfacial term is studied, only the cells where the void fraction is non-negligible are considered. Therefore, we have chosen an arbitrary limit at $\langle \alpha_g \rangle = 0.1\%$, and the cells with a void fraction lower than this limit are not taken into account. So, in fact, 199 cells are considered.

	MAPE	RPSB	RPSD
CATHARE	44.5%	-44.1%	18.3%
TRACE ($\langle a_i \rangle$ from CFD)	62.5%	-62.5%	4.50%
TRACE (full)	35.5%	29.2%	29.0%

Table 5.2.1: Evaluation of existing Π'_l correlations

The evaluations of the correlations from CATHARE, from TRACE using the variable $\langle a_i \rangle$ calculated from CFD, and from TRACE using the variable $\tilde{a}_i$ calculated by equation (5.2.12), are given in Table 5.2.1.

First, it can be seen that the CATHARE correlation tends to underestimate the interfacial energy transfer term since the RPSB is negative. Moreover, the error is quite high, with a MAPE of 44.5%. This means that, on average, the value of $\langle \Pi'_l \rangle$ calculated from the CFD is 1.82 times higher than the value predicted by the CATHARE correlation (1/(1-0.445) = 1.82). Moreover, the RPSD value is 18.3%, which means the values are neither widely dispersed nor very constricted.

Moreover, for all cells, a histogram of the percentage errors, a comparison between the correlation and the reference term, and a representation of the relative errors as a function of the pressure and the gas velocity are shown in Figure 5.2.1.

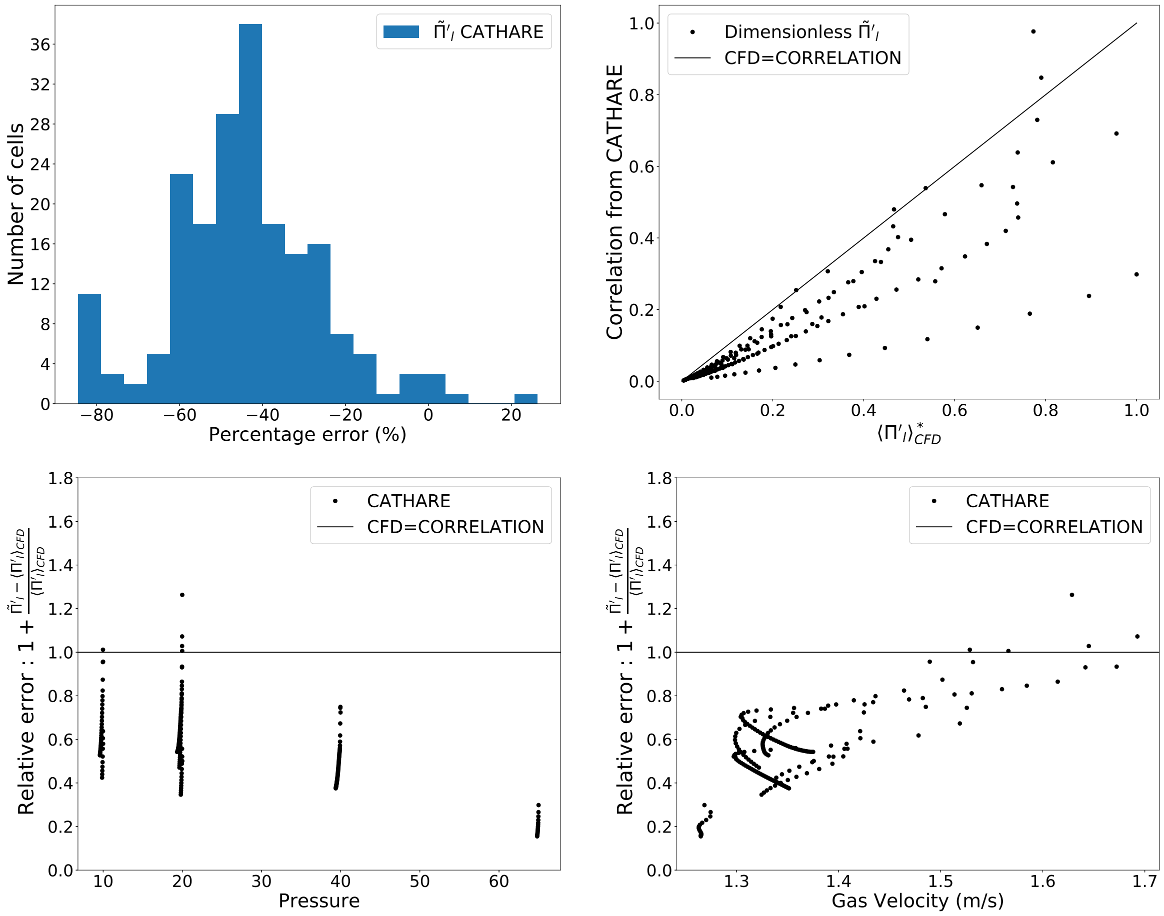

Figure 5.2.1: Representations of the CATHARE correlation evaluation. Upper-left: a histogram of the relative percentage errors; upper-right: values predicted by CATHARE correlation as a function of the calculated values; lower part: relative errors as a function of the pressure (left) and gas velocity (right).

It can be seen in the histogram that in almost all cells, the percentage error is negative, and so, the correlation under-predicts the calculated value in these cells. Moreover, an impact of the pressure can be seen since the relative error is higher for the test cases at 65 bar. In addition, there is a correlation between the gas velocity and the relative error. Indeed, the relative error is negative and high for the low gas velocities and becomes positive for high gas velocities.

The errors obtained from the correlation of the TRACE code are pretty different whether the mean interfacial area concentration $\langle a_i \rangle$ is calculated from the CFD or predicted by the correlation (5.2.12). First, using a_i from CFD, the MAPE is larger than CATHARE, at 62.5%. In the same way as CATHARE, the TRACE correlation underestimates the calculated values with a negative RPSB. This result is substantial since it shows on this database that an empirical correlation as the CATHARE's one provides lower MAPE than a correlation as the one developed by Ranz and Marshall (1952), adapted from CFD scale, using only macroscopic variables. However, it is worth noting that despite the high MAPE, the RPSD is very low, indicating that there is a low dispersion of the relative error values. This means that this correlation provides a low accuracy but a high precision. A histogram of the percentage errors, a comparison between the correlation and the reference terms, and a representation of the relative errors as a function of the pressure and the gas velocity are shown in Figure 5.2.2.

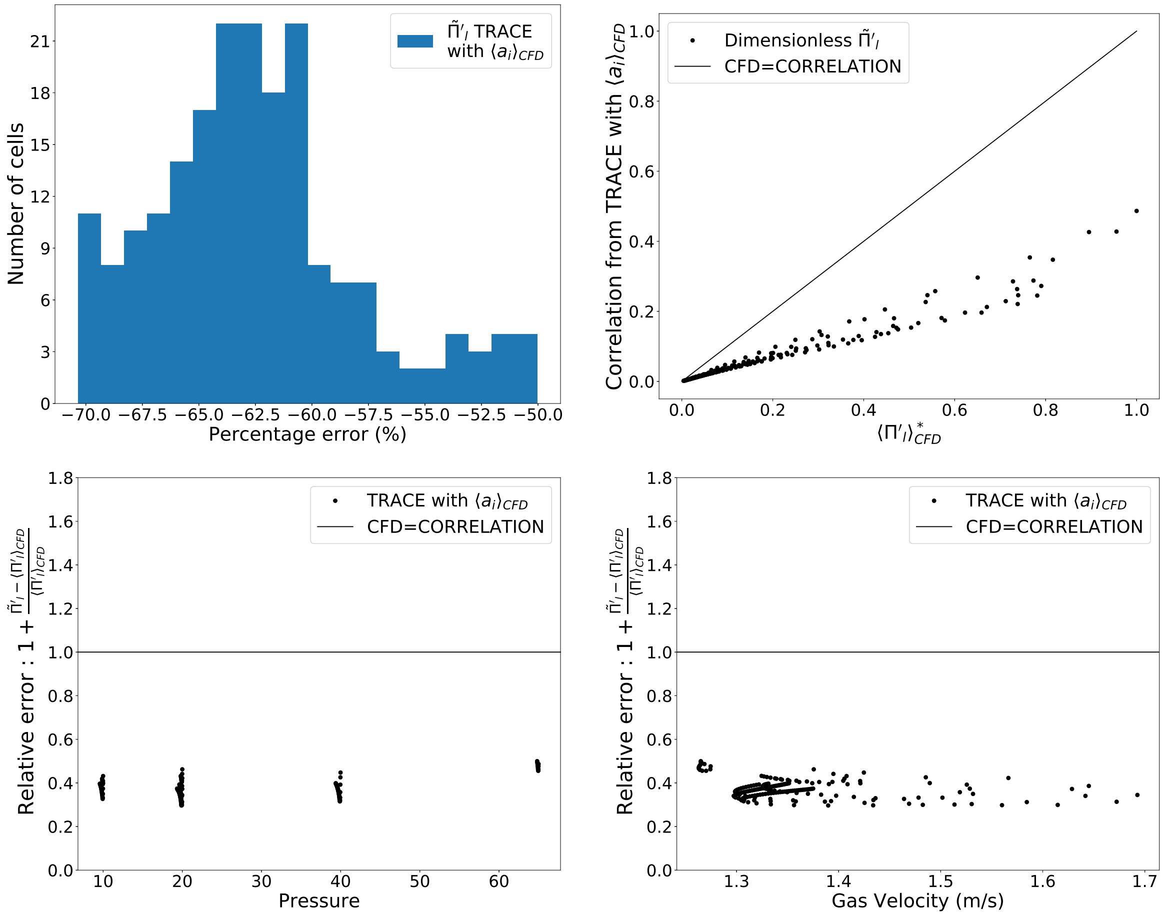

Figure 5.2.2: Representations of the TRACE correlation evaluation, with $\tilde{a}_i$ calculated from the CFD. Upper-left: a histogram of the relative percentage errors; upper-right: predicted values as a function of the calculated values; lower part: relative errors as a function of the pressure (left) and gas velocity (right).

Here, all the relative errors are between -50% and -70%. Therefore, as mentioned above, the error is high, but the dispersion of the relative errors is low. For this correlation, there are no clear impacts of the pressure or gas velocity on the relative error.

The error behavior of the TRACE correlation drastically changes if $\tilde{a}_i$ is predicted by the correlation in equations (5.2.12) and (5.2.13). Indeed, using the correlation for $\tilde{a}_i$, the correlation for $\tilde{\Pi}'_l$ now overestimates the calculated values on this database, with a positive RPSB, and the MAPE is equal to 35.5%. The lower MAPE comes from an error compensation since the interfacial area is poorly predicted. The errors on the predicted interfacial area are shown in the lower-right part of Figure 5.2.3. Moreover, a histogram of the percentage errors, a comparison between the correlation and the reference terms, and a representation of the relative errorq as a function of the pressure are also shown in Figure 5.2.3.

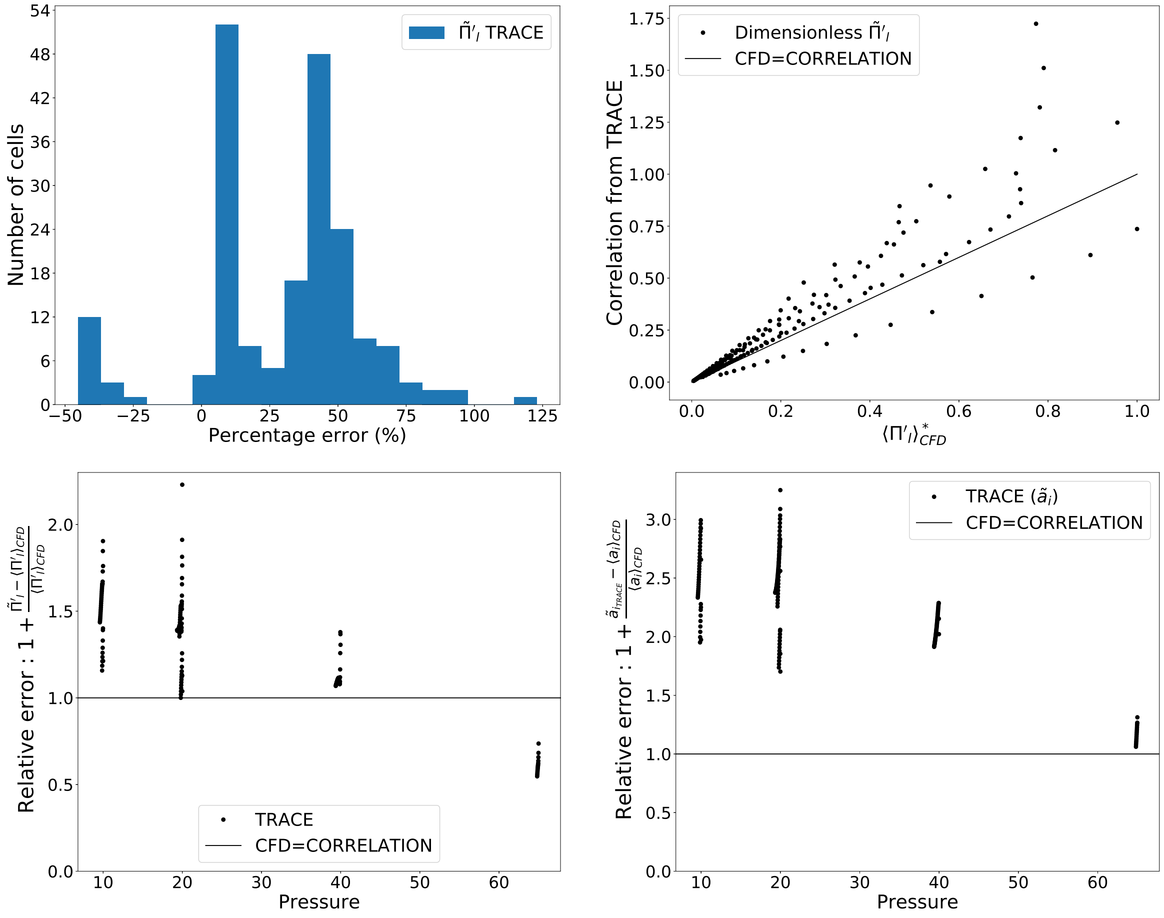

Figure 5.2.3: Representations of the full TRACE correlation evaluation, with $\tilde{a}_i$ calculated by equation (5.2.12). Upper-left: a histogram of the relative percentage errors; upper-right: predicted values as a function of the calculated values; lower-left: relative errors as a function of the pressure; lower-right: relative errors of the interfacial area as a function of the pressure.

Based on the lower-right part of Figure 5.2.3, it can be seen that the predicted interfacial area concentrations are two to three times higher than the ones calculated from the CFD database in the test cases at 10, 20, and 40 bar. However, it is worth noting that in the test cases at 65 bar, the interfacial area concentrations are better predicted, and therefore, the values of the interfacial transfers predicted by the full TRACE correlation are closer to those obtained with TRACE correlation and $\tilde{a}_i$ from CFD. This strong interfacial area overestimation at 10, 20, and 40 bar provides an overestimation of the interfacial transfers. This effect can be directly seen in the lower-left part of Figure 5.2.3. Therefore, the correlation may be adapted to high pressure flows, but this work shows that this a_i correlation is not adapted for flows lower than 40 bar.

This evaluation shows room for improvement in condensation correlation at the macroscopic scale. Therefore, the following section aims at developing a condensation macroscopic model using the CFD database.

5.3 Development of a new macroscopic model

This section aims at developing a model for the energy interfacial transfer term $\tilde{\Pi}_l'$ by three different ways, with increasing complexity.

The first way to model $\tilde{\Pi}_l'$, proposed in section 5.3.1, is based on the correlation from Chen and Mayinger (1992) given in equations 5.1.2, which provides accurate results at RANS scale. The difference here is that the variables of the model are spatially averaged and not local.

The section 5.3.2 proposes two models based on a statistical approach. Indeed, in the same way as the up-scaling methods from the literature described in section 1.1.2, the models are developed based on macroscopic variables and optimization coefficients. Next, a statistic tool is used to find the optimal coefficients that minimize the correlation errors. The difference between the two different models proposed in this section is based on the prediction of the macroscopic relative velocity. Moreover, on the 199 points of the database, the optimizations are done on 159 points, and the evaluations on the 40 other points.

Finally, the section 5.3.3 aims to develop a fully mechanistic model. The first step is to compare the values of the average of the product of variables to the values of the product of the average of the same variables. This work allows us to minimize the number of variables to model. The remaining variables that need to be modeled have a physical meaning and represent phenomena that happen at the subgrid scale. These variables are not modeled in this work, and therefore, the mechanistic model is not complete. However, this section allows us to prove that this mechanistic model significantly reduces the error if these remaining variables are accurately modeled. Moreover, some insights are given about an a priori evaluation of these models on alternative experiments in section 5.3.4.

5.3.1 Model based on the local Chen-Mayinger correlation

This section aims to adapt the correlation developed by Chen and Mayinger (1992) at the macroscopic scale. Indeed, it has been shown in chapter 4 that this correlation is accurate at the local scale, and therefore, the aim is to adapt this correlation using only averaged variables.

It is important to note that in this section, in order to separate the uncertainties, the interfacial area concentration is calculated from CFD ($\tilde{a}_i = \langle a_i \rangle_{CFD}$) and not by an interfacial area correlation. This strategy allows us to evaluate the global correlation errors and not the deviations linked to the interfacial area correlation. If the results obtained are accurate, it would prove the interest in improving the predictions of the interfacial area concentration in macroscopic codes as TRACE, and also in taking into account this a_i variable in CATHARE.

The model based on the correlation of Chen and Mayinger (1992) is written as:

$$\tilde{\Pi}_{l_{CHEN}}' = \tilde{a}_i \tilde{h}_{li} (T_{sat} - \tilde{T}_l), \quad \text{with: } \tilde{h}_{li} = \frac{\langle \lambda_l \rangle_l \tilde{\mathrm{Nu}}_b}{\tilde{d}_{32}}; \quad \tilde{d}_{32} = \frac{6 \langle \alpha_g \rangle}{\tilde{a}_i}, \text{ and :} \tag{5.3.1a}$$

$$\tilde{\mathrm{Nu}}_b = 0.185\, \tilde{\mathrm{Re}}_b^{0.7}\, \tilde{\mathrm{Pr}}_l^{0.5}; \quad \tilde{\mathrm{Re}}_b = \frac{\langle \rho_l \rangle_l \, |\tilde{v}_r| \, \tilde{d}_{32}}{\langle \mu_l \rangle_l}, \quad \tilde{\mathrm{Pr}}_l = \frac{\langle \mu_l \rangle_l \, \langle c_{p_l} \rangle_l}{\langle \lambda_l \rangle_l}. \tag{5.3.1b}$$

It is important to note that the macroscopic relative velocity $|\tilde{v}_r|$ is not always equal to the difference between the macroscopic gas and liquid velocities, as mentioned in section 2.3.3. Indeed, the macroscopic relative velocity is due to two different effects: the local relative motion and an integral effect of the phase and velocity distributions. Two different models are proposed, one with the basic assumption that the macroscopic relative velocity is equal to the difference between gas and liquid velocities, while the second considers the relative velocity model from the TRACE code. These two relative velocities are expressed in equations (5.3.2) and (5.3.3).

$$\text{Chen-Mayinger 1 : } |\tilde{v}_r| = |\langle v_g \rangle_{g\rho} - \langle v_l \rangle_{l\rho}| \tag{5.3.2}$$

$$\text{Chen-Mayinger 2 : } |\tilde{v}_r| = \min\left[|\tilde{v}_g - \tilde{v}_l|, \tilde{v}_{DB,term} \right], \text{ with: } \tilde{v}_{DB,term} = \tilde{v}_{r,\infty} \left(1 - \tilde{\alpha}_g\right)^{2.39}, \\ \text{and: } \tilde{v}_{r,\infty} = \sqrt{2} \left(\frac{\tilde{\sigma} g \left(\tilde{\rho}_l - \tilde{\rho}_g\right)}{\tilde{\rho}_l^2} \right)^{1/4}. \tag{5.3.3}$$

For both models, except the interfacial area concentration, all the other variables present are macroscopic. Therefore, they can be directly calculated using a macroscopic code or by an a priori evaluation using the averaged CFD variables. Using the statistical operators defined in equations (5.2.20), the evaluation of this correlation is shown in Table 5.3.1.

	MAPE	RPSB	RPSD
Chen-Mayinger 1	11.5%	2.28%	17.1%
Chen-Mayinger 2	29.9%	-29.9%	5.9%

Table 5.3.1: Evaluation of $\tilde{\Pi}'_l$ model based on correlation from Chen and Mayinger (1992).

The results obtained by the two models are quite different between themselves. The first model has a low MAPE due to a relatively small statistical bias but has a high relative standard deviation of 17.1%. On the contrary, the second model, which uses TRACE correlation for the relative velocity, has a higher MAPE of 29.9%, linked to a high statistical bias, but has a low relative standard deviation of 5.9%. Therefore, both correlations result in errors significantly reduced in comparison to the errors obtained with the correlations from CATHARE (44.5%) and TRACE (62.5%). These correlations seem largely more adapted to bubble condensation flows between 10 and 65 bar, especially the first model, which has a mean relative error of 11.5%.

A histogram of the percentage errors, a comparison between the correlation and the reference terms, and a representation of the relative errors as a function of the pressure and gas velocity are represented in Figure 5.3.1.

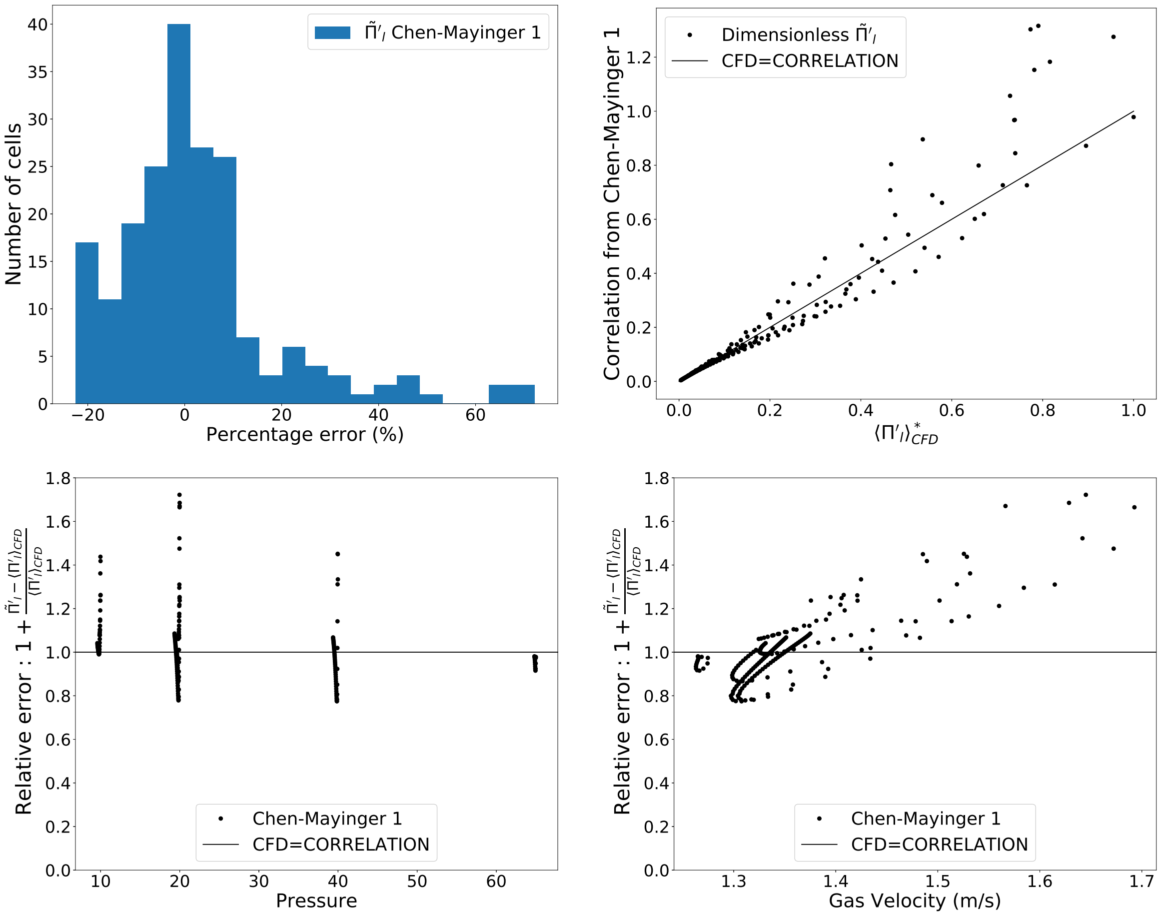

Figure 5.3.1: Representations of the "Chen-Mayinger 1" correlation evaluation. Upper-left: a histogram of the relative percentage errors; upper-right: predicted values as a function of the CFD calculated values; lower part: relative errors as a function of the pressure (left) and gas velocity (right).

First, it can be seen in the upper-right part of Figure 5.3.1 that the predictions are well-centered but with high dispersion, which is consistent with the calculated low RPSB and high RPSD. Moreover, it is noticeable that the dispersion is especially visible for high energy interfacial transfer terms. Furthermore, the results obtained at 65 bar are well predicted, with low bias and low dispersion, while the results obtained at other pressures are pretty dispersed. Finally, we can note that there seems to be a correlation between the relative errors and the gas velocities. Indeed, the relative error increases alongside the increase in gas velocity.

In the same way for the second model, a histogram of the percentage errors, a comparison between the correlation and the reference terms, and a representation of the relative errors as a function of the pressure and gas velocity are represented in Figure 5.3.2.

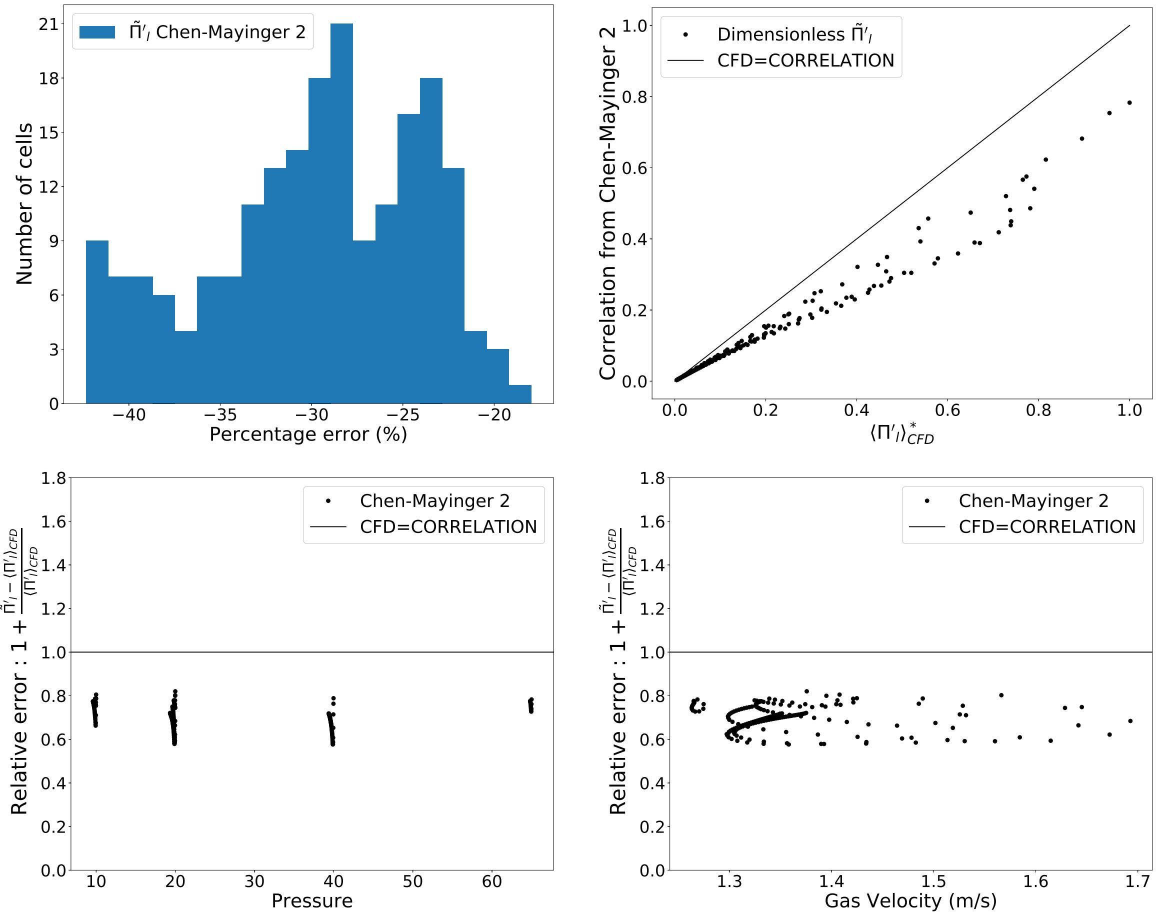

Figure 5.3.2: Representations of the "Chen-Mayinger 2" correlation evaluation. Upper-left: an histogram of the relative percentage error; upper-right: predicted values as function of the CFD calculated values, lower part: relative error as function of the pressure (left) and gas velocity (right).

These Figures confirm that the second correlation underestimates the energy interfacial transfer term, with a relative statistic bias of -29.9%, but with a relatively low dispersion. All the relative errors are between -19% and -42%. Moreover, with this correlation, there is no clear impact of the pressure and gas velocity on the relative errors.

Accordingly, these correlations are reasonably accurate, but both have a deficiency, in the standard deviation for the first correlation, and in the statistical bias for the second one. Since the Nusselt numbers are usually modeled by the generic form of relation (5.3.4) and the coefficients are optimized to match the experiment, we propose in the following section to use the same methodology by optimizing these $\{C_0, C_1, C_2, C_3\}$ terms on the CFD database.

$$Nu_b = C_0 + C_1 Re_b^{C_2} Pr_l^{C_3}. \tag{5.3.4}$$

5.3.2 New model using statistic approach based on coefficient optimization

In this section, the URANIE platform (Gaudier, 2010; Blanchard et al., 2018) is used. This platform has multiple applications, such as uncertainty propagation, sensitivity analysis, optimization, parameters calibration, surrogate models (AI approach), etc. In this work, the optimization module is selected to develop new models for the energy interfacial transfer term $\tilde{\Pi}'_l$.

In order to achieve an optimization, some items need to be defined:

- One or several **criteria** to be minimized (or maximized).
- Several **parameters** which influence the criteria.
- Possibly, some **constraints** can be applied to the values of these parameters.
- An optimization **algorithm**, i.e., a method to decide which new values of the parameters are chosen in order to improve the criteria.

First of all, the criteria, parameters, and constraints need to be defined. Next, the URANIE platform offers various optimization algorithms that are more or less suitable according to the situation.

In this study, a single criterion is chosen, which is the MAPE between the optimized model and the CFD database. Using the generic Nusselt number, this criterion is written as:

$$\text{criterion} = \text{MAPE} = \frac{100}{N}\sum_{I=1}^{N}\left(\frac{\left|\Pi'^{I}_{l,opt} - \langle\Pi'_l\rangle^{I}_{CFD}\right|}{\left|\langle\Pi'_l\rangle^{I}_{CFD}\right|}\right), \tag{5.3.5a}$$

$$\text{with}: \tilde{\Pi}'_{l_{opt}} = \tilde{a}_i\tilde{h}_{li}(T_{sat} - \tilde{T}_l), \quad \tilde{h}_{li} = \frac{\langle\lambda_l\rangle_l\tilde{\mathrm{Nu}}_b}{\tilde{d}_{32}}; \quad \tilde{d}_{32} = \frac{6\langle\alpha_g\rangle}{\tilde{a}_i}, \quad \text{and}: \tag{5.3.5b}$$

$$\tilde{\mathrm{Nu}}_b = C_0 + C_1 Re_b^{C_2} Pr_l^{C_3}; \quad \tilde{\mathrm{Re}}_b = \frac{\langle\rho_l\rangle_l\,|\tilde{v}_r|\,\tilde{d}_{32}}{\langle\mu_l\rangle_l}, \quad \tilde{\mathrm{Pr}}_l = \frac{\langle\mu_l\rangle_l\,\langle c_{pl}\rangle_l}{\langle\lambda_l\rangle_l}. \quad \text{With:} \tag{5.3.5c}$$

$$\text{Optimization 1}: |\tilde{v}_r| = |\langle v_g\rangle_{g\rho} - \langle v_l\rangle_{l\rho}|, \quad \text{and:} \tag{5.3.5d}$$

$$\text{Optimization 2}: |\tilde{v}_r| \text{ calculated from (5.3.3).} \tag{5.3.5e}$$

In the same way as in the previous section, two different models are proposed, the first with the basic assumption that the macroscopic relative velocity is equal to the difference between gas and liquid velocities, while the second considers the relative velocity model from the TRACE code.

The parameters are the coefficients C_0, C_1, C_2 and C_3. By comparison to the existing Nusselt correlations, these constraints are added to the parameters:

$$0 < C_0 < 4; \quad 0.01 < C_1 < 1.0; \quad 0.2 < C_2 < 1.0; \quad 0.2 < C_3 < 0.7. \tag{5.3.6}$$

Therefore, the optimization aims to find the optimal set of parameters $\{C_0, C_1, C_2, C_3\}$ that minimize the MAPE defined in (5.3.5).

The next step is to select an optimization algorithm. URANIE offers various optimization algorithms that can be divided into two categories: the local methods and the global methods. On the one hand, the local methods allow only mono-criterion optimizations, with or without constraints. They are generally computationally efficient but are not parallelized and tend to be trapped in local optima. Two types of local optimization methods exist: the *Simplex*, a direct algorithm insensitive to local optima but without guarantee of convergence, and the *Migrad*, a relatively sophisticated gradient descent algorithm, able to escape some local optima. On the other hand, the global methods allow multi-criteria optimization, with or without constraints. They are suitable for problems with many local optima but are computationally expensive. However, they are easily parallelized.

In the MAPE calculation as a function of the parameter set $\{C_0, C_1, C_2, C_3\}$, several local optima can be expected. Moreover, the database is relatively small, with 199 optimization points. In order to handle several local optima, and because the database is sufficiently small, the global methods seem to be the most suitable methods to deal with this optimization.

Three different global methods are available in URANIE: a genetic algorithm using a diploid representation, a particle swarm algorithm, and a *Nelder Mead Simplex* variant, adapted to work with a population and to deal with multi-objective problems. Since there is only one objective in this study, which is to minimize the MAPE, the genetic algorithm seems the most suitable.

The genetic algorithm, which is based on the way the genes are organized in a living being and the way they might evolve through time and future generations, is schematized in Figure 5.3.3.

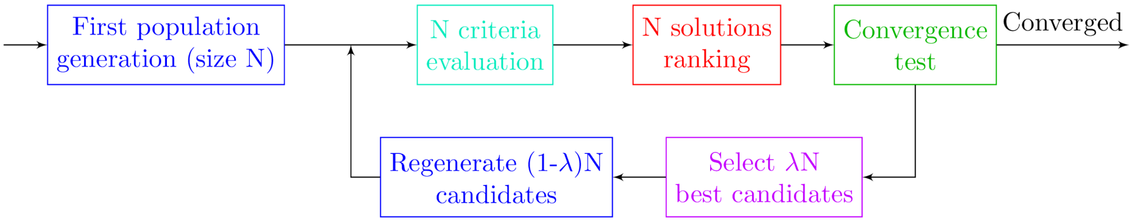

Figure 5.3.3: Genetic algorithm from URANIE platform (Gaudier, 2010).

The first step is to generate a population of size N, which means N sets of parameters $\{C_0, C_1, C_2, C_3\}$ taken in the range defined in (5.3.6). Next, the MAPEs obtained using all sets are calculated and ranked according to the value of the MAPE. Based on this ranking, URANIE performs a convergence test. If the convergence is reached, the ranking done in the last step is given to the user, with the final population of size N and the corresponding MAPE. Then, it is possible to select the set of parameters that minimize the MAPE. If convergence is not reached, new populations are generated based on the genetic approach. First, a survival rate is set, which defines the rate of population items that survive at each generation. It corresponds to the parameter λ in Figure 5.3.3, and the default value of this parameter is 40%. The other candidates are generated based on the selected candidates, on the homozygote rate, and on the mutation rate. Indeed, in a similar manner as in genetics, a rate of the population is considered homozygote, and the others are considered heterozygote. In this algorithm, these homozygotes and heterozygotes are two different ways to obtain a new candidate from two existing candidates. By default, the homozygote rate is set at 50%. Moreover, to keep on exploring the research space, some new candidates mutate, with a mutation probability set by default to 1%. In this way, a new population of N sets of parameters is developed. The first steps are done again to evaluate this new population and test the convergence. If the convergence is not reached at this point, new candidates are created until the convergence or the maximum number of evaluations is reached.

In order to separate the optimization and the evaluation, 80% of the calculated points are randomly taken for the optimization, corresponding to 159 points, and the other 20%, 40 points, are selected for the evaluation of the optimized correlation. It is important to note that the 199 calculated points are not totally independent, and therefore, the evaluation database is not entirely independent of the optimization one. However, due to the small number of test cases considered, this is the best way to optimize and evaluate a model.

The results of the optimization on both types of models on the 159 calculated points are given in Table 5.3.2.

	C_0	C_1	C_2	C_3	MAPE
Optimization 1	0	0.51	0.59	0.35	10.20%
Optimization 2	1.71	0.087	0.81	0.20	5.43%

Table 5.3.2: Set of parameters obtained using URANIE to minimize the MAPE.

The MAPE obtained with the optimized set of parameters is lower using the second optimization, i.e., with the relative velocity obtained from the TRACE correlation, than using the first model. Moreover, on this optimization dataset of 159 points, the RPSB and RPSB of the first model are -0.06% and 14.34%. Therefore, the bias is quasi-null, but the standard deviation is still high. This means that using the simple macroscopic relative velocity defined in (5.3.5d), no set of parameters permits a decrease in the standard deviation. For the second model, the RPSB and RPSB are respectively -1.85% and 6.87%, so the optimization based on the relative velocity correlation from TRACE is able to produce simultaneously a low bias and a low standard deviation. Nevertheless, it is worth mentioning that these results are obtained using the optimization dataset. The next step is to evaluate them using the evaluation dataset, which consists of the other 40 calculated points. The results of this evaluation are shown in Table 5.3.3.

	MAPE	RPSB	RPSD
Optimization 1	10.42%	1.63%	14.34%
Optimization 2	5.40%	-0.56%	7.06%

Table 5.3.3: Evaluation of the optimized correlations of the Π'_l variable on the evaluation dataset.

For the ”Optimization 1” model, a histogram of the percentage errors, a comparison between the correlation and the reference terms, and a representation of the relative errors as a function of the pressure and gas velocity are represented in Figure 5.3.4.

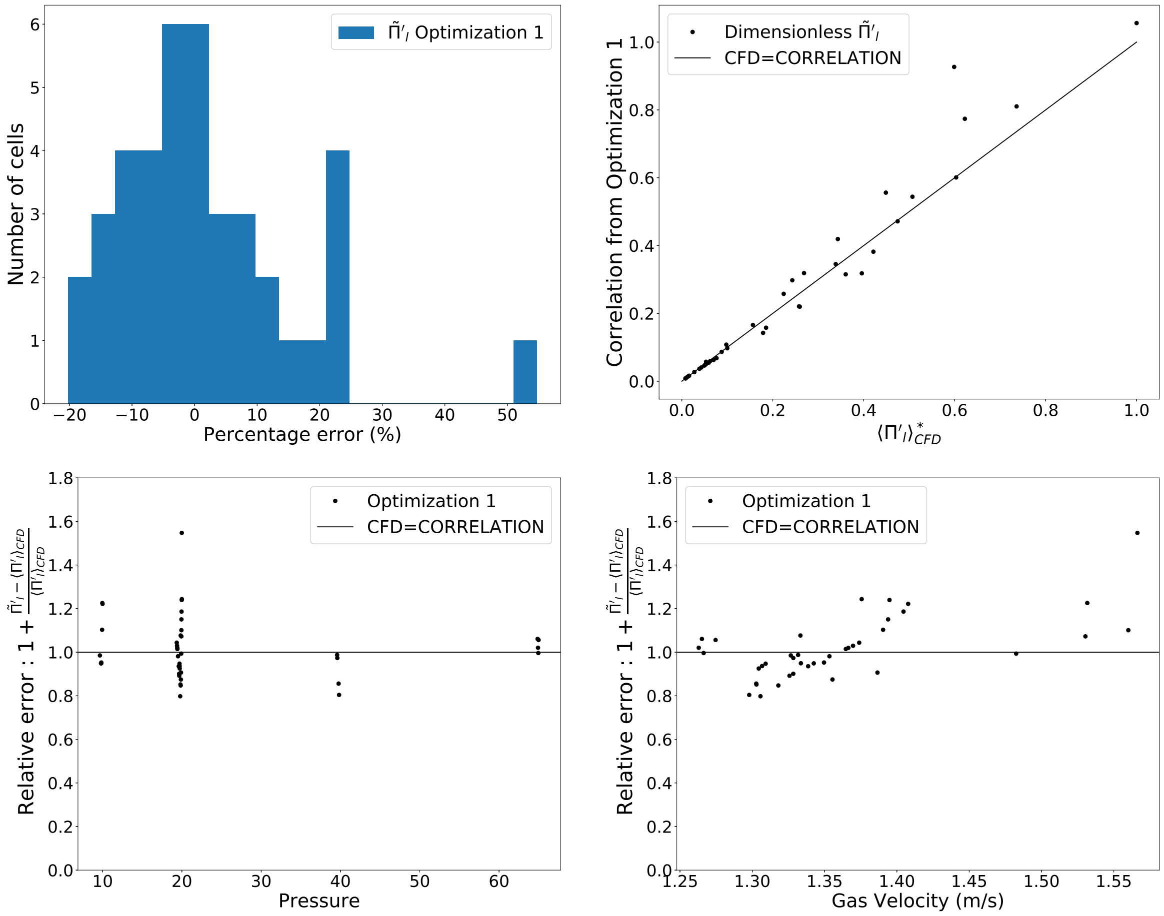

Figure 5.3.4: Representations of the ”Optimization 1” correlation on the evaluation dataset. Upper-left: a histogram of the relative percentage errors; upper-right: predicted values as a function of the CFD calculated values; lower part: relative error as a function of the pressure (left) and gas velocity (right).

Since the evaluation dataset is limited, with only 40 calculated points, it is more difficult to highlight the tendencies. Still, the dispersion between the calculated and predicted values can be seen, especially for the test cases at 20 bar. A slight correlation can be seen between the relative error and the gas velocity in the lower-right Figure, with a slight tendency to underestimate the calculated values at low gas velocities and a tendency to overestimate them at higher gas velocities. The results are pretty similar to the ones obtained using correlation from Chen and Mayinger (1992) with the simple macroscopic relative velocity, so the interest in this new correlation is minimal.

For the "Optimization 2" model also, a histogram of the percentage errors, a comparison between the correlation and the reference terms, and a representation of the relative errors as a function of the pressure and gas velocity are represented in Figure 5.3.5.

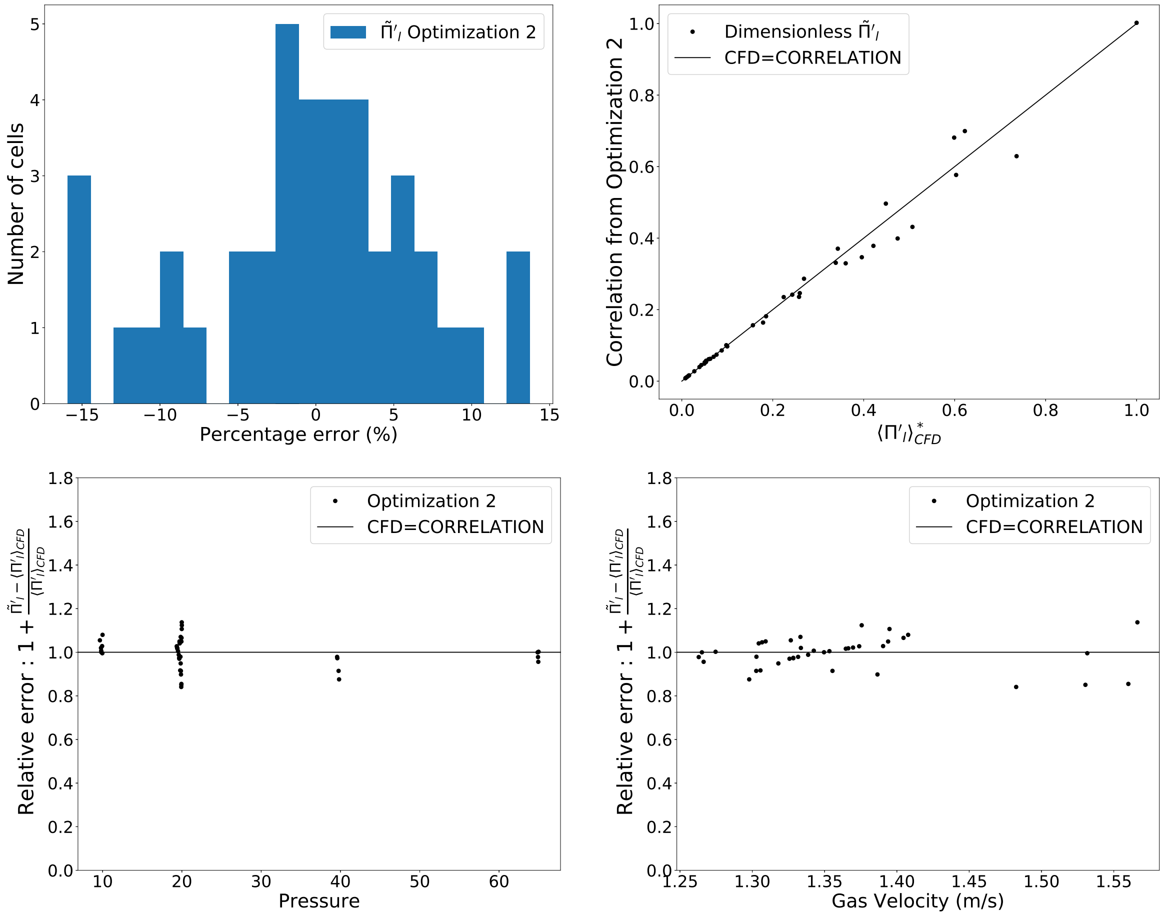

Figure 5.3.5: Representations of the "Optimization 2" correlation on the evaluation dataset. Upper-left: a histogram of the relative percentage errors; upper-right: predicted values as a function of the CFD calculated values; lower part: relative errors as a function of the pressure (left) and gas velocity (right).

These graphs confirm that the predicted values are pretty close to the calculated ones, with a low dispersion. There is no evident influence of the pressure or the gas velocity on the relative errors.

Remark: The excellent predictions obtained using the "Optimization 2" model allow us to recommend this model.

This new model is summarized below:

$$\tilde{\Pi}'_{l_{opt}} = \tilde{a}_i \tilde{h}_{li}(T_{sat} - \tilde{T}_l), \quad \tilde{h}_{li} = \frac{\langle\lambda_l\rangle_l \tilde{\mathrm{Nu}}_b}{\tilde{d}_{32}}, \quad \tilde{d}_{32} = \frac{6\langle\alpha_g\rangle}{\tilde{a}_i}, \quad \text{and :} \tag{5.3.7a}$$

$$\tilde{\mathrm{Nu}}_b = 1.71 + 0.087 Re_b^{0.81} Pr_l^{0.2}, \quad \tilde{\mathrm{Re}}_b = \frac{\langle\rho_l\rangle_l \, |\tilde{v}_r| \, \tilde{d}_{32}}{\langle\mu_l\rangle_l}, \quad \tilde{\mathrm{Pr}}_l = \frac{\langle\mu_l\rangle_l \, \langle c_{p_l}\rangle_l}{\langle\lambda_l\rangle_l}, \tag{5.3.7b}$$

$$\text{With: } |\tilde{v}_r| = \min\left[|\tilde{v}_g - \tilde{v}_l|, \tilde{v}_{DB,term}\right], \text{ with: } \tilde{v}_{DB,term} = \tilde{v}_{r,\infty}\left(1 - \tilde{\alpha}_g\right)^{2.39}, \tag{5.3.7c}$$

$$\text{and:} \quad \tilde{v}_{r,\infty} = \sqrt{2}\left(\frac{\tilde{\sigma} g\left(\tilde{\rho}_l - \tilde{\rho}_g\right)}{\tilde{\rho}_l^2}\right)^{1/4}. \tag{5.3.7d}$$

Naturally, this model should be first tested on a larger database. This more extensive database could consist of new CFD simulations on additional bubble condensation experiments. The section 5.3.4 is dedicated to offering some insights about the experiments that could be simulated. Moreover, some error compensation can exist in this model since only the global behavior of this model is studied and not the behavior of each variable.

This is why, in parallel to the model developed by an optimization method, a mechanistic model is going to be developed in the next section. This model will be created based on a homogenization of the CFD model, and could permit error compensation in the model to be avoided.

5.3.3 Perspectives towards a fully mechanistic model

This section aims to develop a macroscopic model for the energy interfacial transfer based on a homogenization of the local model. Indeed, the section 5.1.3 has shown that the CFD results are close to the experimental results, which means that the local model is accurate. The spatial average of the energy interfacial transfer term is expressed in equation (5.3.8).

$$\langle\Pi'_l\rangle = \Big\langle a_i h_l (T_{sat} - T_l)\Big\rangle; \quad \text{with: } a_i = \frac{6\alpha_g}{d_{32}}; \quad h_l = \frac{\mathrm{Nu}_b\lambda_l}{d_{32}}; \tag{5.3.8a}$$

$$\mathrm{Nu}_b = 0.185\mathrm{Re}_b^{0.7}\mathrm{Pr}_l^{0.5}; \quad \mathrm{Re}_b = \frac{\rho_l|v_r|d_{32}}{\mu_l}; \quad \mathrm{Pr}_l = \frac{\mu_l c_{p_l}}{\lambda_l}. \tag{5.3.8b}$$

This formulation consists of a spatial average of a product of several local variables. However, at the macroscopic scale, only spatial averaged variables are available, and the averages of products of local variables need to be modeled. The first aim of this section is to reduce to a minimum the number of spatial averages of products. For this, the term $\langle\Pi'_l\rangle$ is taken as the starting point, and the objective is to express this term as a function of other variables by involving as few errors as possible. Next, these other variables, which are not necessarily macroscopic at first, are also expressed by alternative variables that can themselves be described, after a few steps, by macroscopic variables available in macroscopic codes. Therefore, the first step is described in Table 5.3.4.

Reference	Prediction	MAPE
$\langle\Pi'_l\rangle$	$\langle a_i\rangle\langle h_{li}\rangle_{a_i}\left(T_{sat} - \langle T_l\rangle_{a_i}\right)$	0.04%

Table 5.3.4: Representation of the MAPE related to the separation of the $\langle\Pi'_l\rangle$ term.

Table 5.3.4 shows that the mean relative error between the reference term and the prediction term is 0.04%. Both terms are calculated from the CFD database, and it is essential to note that, at this point, the prediction term cannot be calculated using a macroscopic code since h_{li} is composed of a product of local variables. Moreover, $\langle T_l\rangle_{a_i}$ is not necessarily equal to the macroscopic liquid temperature calculated by a macroscopic code, which corresponds to $\langle T_l \rangle_l$. Indeed, $\langle T_l \rangle_{a_i}$ is expressed in equation (5.3.9).

$$\langle T_l \rangle_{a_i} = \frac{\langle a_i T_l \rangle}{\langle a_i \rangle}. \tag{5.3.9}$$

Moreover, it is worth noting that the interfacial area concentration $\langle a_i \rangle$ needs to be modeled at the macroscopic scale, and that the macroscopic Sauter diameter is related to this variable by:

$$\tilde{d}_{32} = \frac{6\langle \alpha_g \rangle}{\langle a_i \rangle}. \tag{5.3.10}$$

Next, the variable $\langle h_{li} \rangle_{a_i}$ is decomposed into alternative variables in Table 5.3.5, and the corresponding MAPE is given.

Reference	Prediction	MAPE
$\langle h_{li} \rangle_{a_i}$	$\frac{\langle Nu_b \rangle_{a_i} \langle \lambda_l \rangle}{\tilde{d}_{32}}$	0.06%
$\langle Nu_b \rangle_{a_i}$	$0.185 \langle Re_b \rangle_{a_i}^{0.7} \langle Pr_l \rangle_{a_i}^{0.5}$	0.04%
$\langle Pr_l \rangle_{a_i}$	$\langle Pr_l \rangle = \frac{\langle \mu_l \rangle_l \langle C_{p_l} \rangle}{\langle \lambda_l \rangle_l}$	0.03%
$\langle Re_b \rangle_{a_i}$	$\frac{\langle \rho_l \rangle_l \langle \lvert v_r \rvert \rangle_{g\rho} \tilde{d}_{32}}{\langle \mu_l \rangle_l}$	0.04%

Table 5.3.5: Representation of the MAPE related to the separation of the $\langle h_{li} \rangle_{a_i}$ term.

These few steps show that the variable $\langle h_{li} \rangle$ can be decomposed in a product of averaged variables with a total MAPE lower than 0.2%. Indeed, besides $\tilde{d}_{32}$, which is related to $\langle a_i \rangle$, there is only one variable that still cannot be calculated by a macroscopic code, which is the average of relative velocity weighted by the gas mass, which is expressed as:

$$\langle \lvert v_r \rvert \rangle_{g\rho} = \frac{\langle \alpha_g \rho_g \lvert v_r \rvert \rangle}{\langle \alpha_g \rho_g \rangle}. \tag{5.3.11}$$

For the test cases for which the gas velocity is always higher than the liquid velocity, such as the TOPFLOW test cases considered in this work, this relation can be written as:

$$\langle \lvert v_r \rvert \rangle_{g\rho} = \frac{\langle \alpha_g \rho_g (v_g - v_l) \rangle}{\langle \alpha_g \rho_g \rangle} = \langle v_g \rangle_{g\rho} - \frac{\langle \alpha_g \rho_g v_l \rangle}{\langle \alpha_g \rho_g \rangle} = \langle v_g \rangle_{g\rho} - \langle v_l \rangle_{g\rho}. \tag{5.3.12}$$

Therefore, if the gas velocity is always higher than the liquid velocity, the term that needs to be modeled is the liquid velocity weighted by the void fraction and the gas density. Finally, Table 5.3.6 shows that the reference $\langle \Pi'_l \rangle$ term can be divided into macroscopic variables and three unknown terms: $\langle a_i \rangle$, $\langle \lvert v_r \rvert \rangle_{g\rho}$, and $\langle T_l \rangle_{a_i}$.

Reference	Prediction	MAPE
$\langle \Pi'_l \rangle$	$\langle a_i \rangle \left(0.185 \left(\frac{\langle \rho_l \rangle_l \langle \lvert v_r \rvert \rangle_{g\rho} \tilde{d}_{32}}{\langle \mu_l \rangle_l} \right)^{0.7} \left(\frac{\langle \mu_l \rangle_l \langle C_{p_l} \rangle}{\langle \lambda_l \rangle_l} \right)^{0.5} \cdot \frac{\langle \lambda_l \rangle_l}{\tilde{d}_{32}} \right) (T_{sat} - \langle T_l \rangle_{a_i})$	0.06%

Table 5.3.6: Evaluation of the mechanistic model of $\langle \Pi'_l \rangle$, which still includes three unknown variables: $\langle a_i \rangle$, $\langle \lvert v_r \rvert \rangle_{g\rho}$, and $\langle T_l \rangle_{a_i}$.

The MAPE linked to the variables $\langle |v_r| \rangle_{g\rho}$ and $\langle T_l \rangle_{a_i}$ in comparison to the variables that can be obtained by a macroscopic code are summarized in Table 5.3.7.

Reference	Prediction	MAPE	RPSB	RPSD
$\langle T_l \rangle_{a_i}$	$\langle T_l \rangle_l$	4.55%	-4.55%	4.91%
$\langle \lvert v_r \rvert \rangle_{g\rho}$	$\lvert \langle v_g \rangle_{g\rho} - \langle v_l \rangle_{l\rho} \rvert$	12.88%	-3.19%	17.85%
$\langle \lvert v_r \rvert \rangle_{g\rho}$	$v_{r_{DB}}$	43.3%	-43.25%	6.7%
$\langle \lvert v_r \rvert \rangle_{g\rho}$	$v_{r_{DB,opt}} = 1.715\, v_{r_{DB}}$	8.7%	-2.68%	11.47%

Table 5.3.7: Evaluation of $\langle a_i \rangle$ and $\langle |v_r| \rangle_{g\rho}$ in comparison to variables available at the macroscopic scale, $v_{r_{DB}}$ is the relative velocity correlation from TRACE (5.3.3).

The MAPE between the liquid temperature weighted by the interfacial area and the liquid temperature weighted by the liquid volume fraction is equal to 4.55%. The temperature weighted by the liquid volume fraction corresponds to the liquid temperature calculated by a macroscopic code. Moreover, the associated bias is negative, which means that the predicted temperature is too low. This is consistent since, due to the interfacial exchanges, the temperature at the interface is higher than the temperature far from the interface, where the liquid phase is dominant. Additionally, there is no wall heat flux in these test cases in contrast to sub-cooled boiling test cases. Therefore, in sub-cooled boiling test cases, the subgrid temperature gradient should be higher, and we could expect a higher MAPE compared to the 4.55% calculated here. Consequently, it is crucial to model the term $\langle T_l \rangle_{a_i}$ in order to provide a mechanistic model.

The mean relative error using the relative velocity predicted by the TRACE correlation is way higher than using the simple subtraction, with a MAPE of 43%, against 13%, but the standard deviation is lower. Due to the high bias and low dispersion, an optimization is introduced in order to reduce the bias and, therefore, the MAPE. This optimization allows us to decrease the MAPE to 8.7%, but this optimization is not generic and may induce more significant errors in other test cases. In any case, this highlights the need for a new correlation for this macroscopic relative velocity. In addition, this macroscopic relative velocity is also used in other models, such as for the drag force. Therefore, an improvement of this term could simultaneously improve the energy and mass interfacial transfer terms, as well as the drag force term.

Finally, the macroscopic interfacial area concentration needs to be modeled, whether by an algebraic correlation or by an IATE.

> **Remark:** The macroscopic energy interfacial transfer term $\langle \Pi_l' \rangle$ has been divided into macroscopic variables and three unknown variables that need to be modeled ($\langle a_i \rangle$, $\langle |v_r| \rangle_{g\rho}$, and $\langle T_l \rangle_{a_i}$), by introducing a relative error lower than 0.1%.

The modeling of these variables is not considered in this thesis, but new studies in this way could largely improve the accuracy of macroscopic codes.

Indeed, for example, the macroscopic relative velocity could be modeled based on the relation proposed by Ishii and Mishima (1984) and expressed in relation (2.3.12) on page 63. Next, the variable C_0 present in this relation could be optimized in the same way as in section 5.3.2.

The interfacial area concentration could be modeled by an IATE, and its source terms could also be optimized on specific experiments for each term. For example, the source terms linked to the condensation on this TOPFLOW experiment, the source terms of coalescence and break-up on adiabatic test cases, and finally, the nucleation source terms on boiling experiments.

Finally, to the extent of our knowledge, the term $\langle T_l \rangle_{a_i}$ has never been modeled. The first step would be to find the macroscopic variables that influence this variables, and then to express this term as a product of these macroscopic variables and optimization coefficients. Afterward, an optimization could be done on these coefficients.

5.3.4 Perspectives towards an a priori evaluation of the new models on additional bubble condensation experiments

The models developed in this chapter, as well as the existing models, are evaluated in this thesis on only seven test cases, corresponding to a total of 199 evaluation points. Moreover, in section 5.3.2, the optimizations are done on 159 points, and the evaluations on the 40 other points. Therefore, there is a lack of evaluation points, and, in addition, the optimization and evaluation points are not totally independent. In order to have more confidence in the models developed in this work, the models should be evaluated using a new bubble condensation database.

First, there are 40 test cases in the test matrix of the TOPFLOW experiment (Lucas et al., 2013), but only seven have been considered here. Indeed, in the 33 other test cases, the bubble condensation phenomenon is no longer the only predominant phenomenon since break-up and coalescence patterns are visible on the experimental bubble size distribution profiles. This is why these test cases have not been considered in this work in order to study only the bubble condensation. Nevertheless, it could be relevant to evaluate the new models on a CFD database consisting of these 33 other test cases.

Additionally, some other bubble condensation experiments could be considered (Zeitoun, 1994; Ozar et al., 2013; Kumar et al., 2019). Indeed, these studies provide local void fraction and bubble size measurements for vertical annular channels. In these experiments, the test section is divided into two main parts: a heated section, where steam bubbles are created, and a non-heated section, where the steam bubbles condense and the measurements are done. The strategy used in these test cases is different than the one used in the TOPFLOW experiment, where the steam bubbles are injected into subcooled water by orifices. The pressures considered are lower than those considered in TOPFLOW, around atmospheric pressure for the datasets of Zeitoun (1994), between 5 and 10 bar for Ozar et al. (2013), and between 2 and 10 bar for Kumar et al. (2019). Different values of inlet sub-cooling and mass flux are considered. A total of 60 test cases are available in these three experiments. Despite the fact that the pressures considered in these test cases are lower than in TOPFLOW, and so, further from the industrial conditions, it would still be interesting to evaluate the macroscopic models from a CFD database developed on these test cases. Finally, if the CFD results are sufficiently validated on all these experiments, some purely numerical test cases could be considered for other boundary conditions but still in the same range as these experiments. The CFD database would be greatly expanded by this method. However, this method should be used with caution since some phenomena that are not present in the experimental conditions could exist in these new test cases, and could not be validated.

5.4 Perspectives towards an a posteriori evaluation

Once the accuracy of the models has been confirmed on additional bubble condensation experiments by a priori evaluations, as suggested in the previous section, the last step is to assess the models by an a posteriori evaluation.

This step consists of evaluating the models directly in a macroscopic code as CATHARE. The results could be different since all the variables are calculated by the macroscopic code and not by an average of the local variables obtained by CFD simulations. First of all, the models need to be implemented in the macroscopic code. Next, numerical simulations need to be done using the macroscopic code on the same test cases as for the a priori evaluation. Since the interfacial area concentration appears in the correlations proposed in this thesis, two different types of simulations should be done. On the first hand, simulations with imposed interfacial area concentrations from the CFD database. On the other hand, simulations with a prediction of the interfacial area. The first strategy can be referred to as a semi a posteriori evaluation, while the second one is a full a posteriori evaluation.

Based on the simulations done using the first strategy and the existing CFD database, a quite interesting comparison could be made between $\langle \Pi_l' \rangle_{CFD}$, $\tilde{\Pi}_l'$ predicted by the a priori evaluation, and $\tilde{\Pi}_l'$ predicted by the a posteriori evaluation, so by the macroscopic code. A comparison can also be made with other variables, such as the mass interfacial transfer term, the Nusselt number, the bubble Reynolds number, the Prandtl number, the liquid and gas velocities, temperature, volume fraction, etc. It should be interesting to analyze the differences between the values predicted by the a priori and the a posteriori evaluations. Two possible situations can be encountered. First, only a few variations exist between the a priori and a posteriori evaluations. In this optimal scenario, the models developed in the previous sections can be directly used in macroscopic codes. The second possible situation is that significant deviations exist between the variables predicted by the a priori and a posteriori evaluations. In this case, some new optimizations can be done by combining the URANIE platform and CATHARE calculations. Indeed, using the same genetic algorithm as in section 5.3.2, it is possible to generate a set of parameters $\{C_0, C_1, C_2, C_3\}$ and to perform CATHARE calculation using these parameters, and then to calculate the MAPE between the calculated values and the a priori ones. If the genetic algorithm is too computationally expensive, an algorithm based on a local method could be used instead. In the same way as in section 5.3.2, a new set of parameters that minimize the error could be found.

In order to perform a full a posteriori evaluation, the interfacial area concentration needs to be predicted by the macroscopic code. A few different approaches can be considered. The most basic way is to use an algebraic correlation which depends on macroscopic variables. This approach is already used in TRACE code, but as shown in section 5.2.3, significant deviations exist between the interfacial area concentration calculated from CFD and predicted by TRACE. Some other algebraic correlations have been developed at the macroscopic scale for a_i, such as Zeitoun (1994), Dejesus and Kawaji (1990), and Chung et al. (2010). Moreover, Schlegel and Hibiki (2015) have proposed a model with a complexity between a simple algebraic model and an IATE. They have proposed to separate the gas phase into two groups, one for the smallest and one for the largest bubbles, and then have proposed an algebraic correlation for each group. Finally, the most extensive way to model the interfacial area concentration is to model it by an IATE, in the same way as it is done at the RANS scale. A few studies have been done to propose a one- or two-group IATE at the macroscopic scale (Hibiki and Ishii, 2000; Brooks et al., 2012; Smith et al., 2012). Moreover, a literature review has been done on the progress of IATE at RANS and macroscopic scales by Kim et al. (2021). Therefore, several models already exist at the macroscopic scale to model the interfacial area concentration, from the most basic, with an algebraic relation, to the most complex, with a two-group IATE.

The last step would be to evaluate the code using the new models on integral effect tests to see the influence of these models on the predictions of industrial scenarios.

5.5 Discussions

This chapter allowed us to evaluate two models from existing macroscopic codes for the interfacial energy transfer term $\tilde{\Pi}_l'$ and to develop new ones.

Since this evaluation is done in comparison to the CFD database developed in chapter 4, the first step has been to evaluate the deviations between the CFD and the experiment, and also the potential deviations linked to the experimental uncertainties. The section 5.1.3 has shown that these deviations are relatively small, with a relative absolute error below 2% in total.

Next, the correlations from the CATHARE and TRACE codes are evaluated. These two correlations are quite different. On the one hand, CATHARE uses an empirical correlation based on condensation due to wall cooling, and optimized on bubble condensation test cases. On the other hand, TRACE uses a model based on the correlation of Ranz and Marshall (1952), using more physical concepts, such as the interfacial area concentration which is modeled. Nevertheless, the deviations obtained by both correlations are high, above 40% for the mean absolute relative error. Moreover, an error compensation appears in the TRACE correlation due to the errors linked to the interfacial area correlation. However, it is worth noting that the relative percentage standard deviation obtained using the TRACE correlation for $\tilde{\Pi}_l'$ and $\langle a_i \rangle$ from the CFD database is very low, below 5%. Accordingly, there are several ways to evaluate a correlation, such as based on the mean absolute error or the standard deviation on a database, or else on the approach used to develop the correlation, such as a purely empirical formulation or a formulation based on physical insights. It seems that it is relevant for a correlation to have a low standard deviation, since it is possible to reduce the mean absolute error by optimizing some coefficients, while it is more challenging if the standard deviation is high. Moreover, the best is to propose a correlation based on physical insights since it is more likely to have a coherent results beyond the validity range using this approach than using a purely empirical approach.

After the evaluation of the existing correlations, some new models have been introduced in the section 5.3. First, a model based on the correlation from Chen and Mayinger (1992), adapted to the macroscopic scale, is used with the simple assumption that the macroscopic relative velocity is equal to the difference between the macroscopic gas and liquid velocities. The mean relative error obtained is around 11.5%, which is much lower than those obtained using the correlations of CATHARE and TRACE. However, the standard deviation is relatively high, around 17%. Using the same model with the TRACE correlation for the macroscopic relative velocity, the relative error is higher (30%), but the standard deviation is lower (6%). Next, a statistical approach has been used to optimize the coefficients of the Nusselt number. Two models have been proposed, one with the simpler approach for the relative velocity and one with the TRACE correlation. The relative error obtained using the first approach is 10.2%, which is really close to the error obtained using the correlation from Chen and Mayinger (1992). This shows that using the simpler relative velocity approach, the error cannot be reduced below 10%, even using optimized Nusselt coefficients. However, using the relative velocity correlation from TRACE and the Nusselt coefficient optimization, the relative error is reduced to 5.5%, which is adequate. It is worth noting that, due to the limited database, the evaluation dataset is not totally independent of the one used to optimize the coefficients. Therefore, it is necessary to assess this correlation by an a priori evaluation on additional bubble condensation experiments, such as those mentioned in section 5.3.4. Also, a baseline towards a fully mechanistic model has been developed in order to avoid error compensation, and is described in section 5.3.3. Indeed, a model based on macroscopic variables and only three unknown variables has been proposed, and the development of models for these three terms in the future could largely improve the accuracy of macroscopic codes.

Finally, a baseline towards an a posteriori evaluation of the models introduced in this chapter is given in section 5.4. This evaluation is based on the implementation of the new models in macroscopic codes and on numerical simulations of the same database presented previously. Then, the simulation results are compared to the a priori results, and if the results are different, an optimization needs to be done again. Moreover, a model needs to be used for the interfacial area, whether with an algebraic correlation or by an IATE. Once it is done, the effects of the new models can also be analyzed on integral effect tests.

Therefore, an up-scaling strategy has been developed and applied in the chapters 1 to 5. Indeed, this up-scaling method has permitted to identify the condensation as predominant in sub-cooled test cases representative of industrial conditions and to propose some models for this phenomenon. A summary and a feedback on this up-scaling strategy is given in the following chapter.

Feedback on the up-scaling strategy for industrial two-phase flows

The industrial context presented in the introduction has shown that sub-cooled boiling flows are encountered in accidental conditions in both PWR and BWR. Moreover, at the system or component scale, the smallest pattern is the sub-channel in the fuel assembly of a nuclear reactor core. The sub-channel is the fluid space in the area around four heating rods, and some correlations are developed based on experiments achieved in pipe or sub-channel geometries. They are based on measurements of the liquid temperature or the critical heat flux, for example. Therefore, in this thesis, we have chosen to study the sub-cooled boiling flows with flow conditions that can be encountered in the PWR core in accidental conditions in sub-channel and pipe geometries. These flow conditions consist of high temperature, flow rate, pressure, and wall heat flux.

Moreover, the numerical simulations at the macroscopic scale are used to ensure reactor safety under all circumstances. These codes are usually calibrated based on designed experiments. However, due to the extreme conditions that are dealt with, only limited experimental data can be obtained. It is, therefore, not possible to reconstruct an averaged variable based on these measurements to compare with an average value calculated with the system code.

This is why we have chosen in this thesis to develop an up-scaling method to benefit from correlations and numerical simulations at the local scale of CFD-grade experiments, in order to identify and model the prominent physical phenomenon at the macroscopic scale under industrial sub-cooled boiling conditions.

This up-scaling method is described in 17 steps in Figure 7.

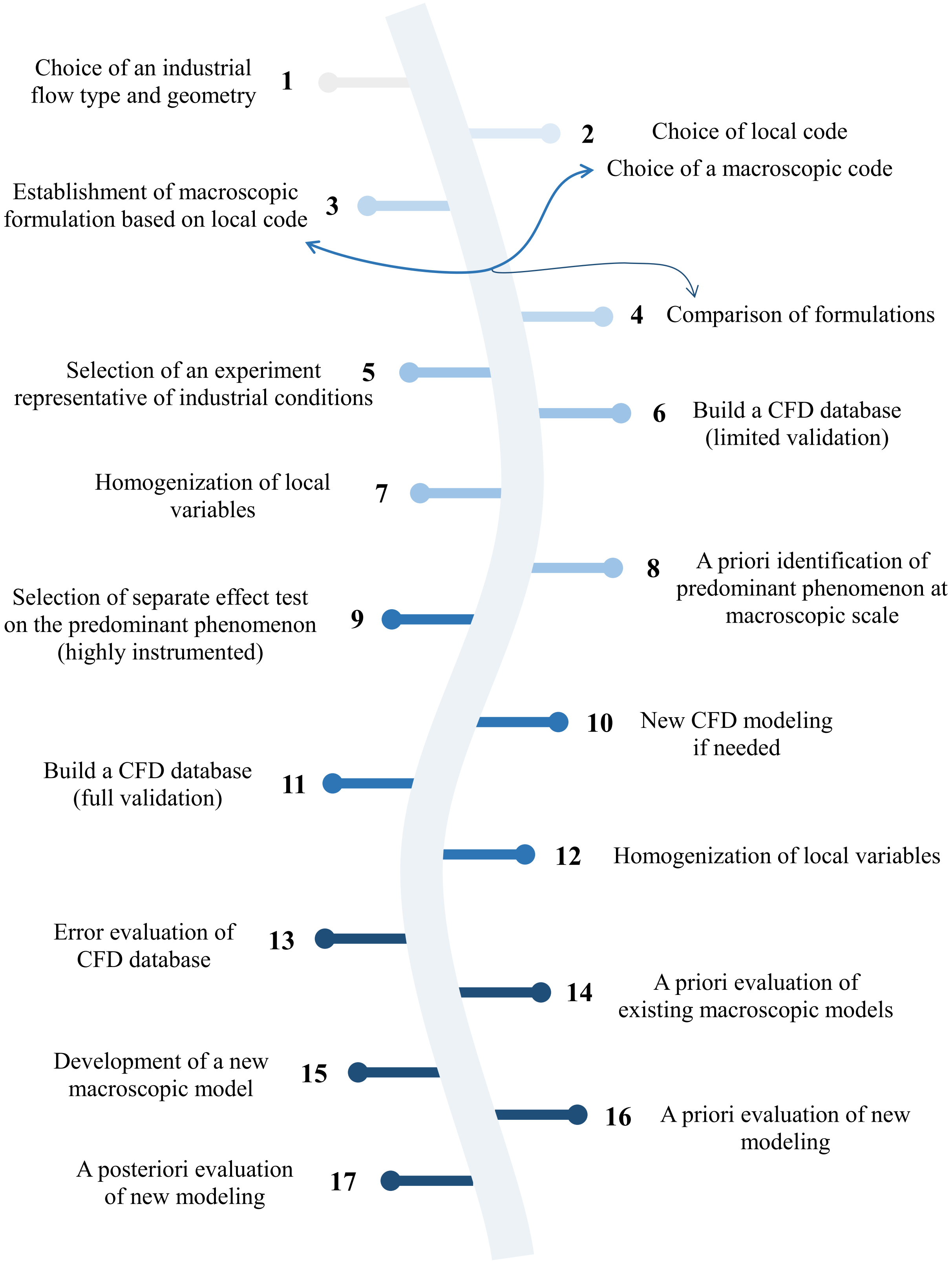

Figure 7: Up-scaling method developed in this thesis

The up-scaling method described in Figure 7 has been applied and discussed in the different chapters of this thesis.

The first step is based on discussions from the introduction, the second step is discussed in the chapter 1, the steps 3 and 4 are treated in chapter 2. Next, steps 5-8 are considered in chapter 3, steps 9-12 are treated in chapter 4, and finally, steps 13-17 are regarded in chapter 5. These steps are explained in detail below.

1. As discussed above, based on the industrial context, the industrial sub-cooled boiling flows in pipe and sub-channel geometries are considered in this thesis.

2. CATHARE is the code used in France to demonstrate the safety of a nuclear reactor under all conditions, and Neptune_CFD is currently in France the most commonly used code in the nuclear field at RANS scale to simulate two-phase flows. Then, the up-scaling method has been used in this thesis from the Neptune_CFD code to the CATHARE one. These codes are described in detail in chapter 1.

3. In chapter 2, we have established a macroscopic two-fluid model formulation based on the Neptune_CFD equations. This new macroscopic formulation includes some unknown terms and, therefore, needs closure relations to close the system.

4. The new formulation developed in step 3 is compared to the existing macroscopic code equations. This comparison has allowed us to highlight some assumptions made by these codes. Moreover, the different terms of the existing codes and the new formulation are compared, and the corresponding terms are identified. Therefore, this step has made it possible to evaluate some terms present or neglected in the existing code equations based on an average of variables generated by Neptune_CFD. This is called the a priori evaluation method.

In chapter 3, corresponding to steps 5-8, we decided to apply this a priori method to evaluate the unknown terms of the new formulation in sub-cooled boiling test cases representative of industrial conditions. This evaluation aims to find out which unknown term needs to be modeled the most and to what extent the diffusion and dispersion terms are actually negligible.

5. We have selected two experiments representative of industrial conditions, namely KIT and PSBT with respectively a pipe and a subchannel geometry. These experiments consist of sub-cooled boiling at conditions representative of industrial conditions in terms of pressure, flow rate, temperature, and wall heat flux. It is worth noting that in these experiments at such conditions, only mean void fractions measurements are available.

6. In section 3.1, we have developed a CFD database on the KIT and PSBT experiments using Neptune_CFD simulations. The predicted void fractions of all test cases are compared to the experimental ones. Although it is difficult to conclude on the complete validation of all the test cases only based on the void fraction comparisons, the consistent void fraction predictions obtained allow us to be confident in the overall consistency of all the predicted variables. Therefore, the test cases for which the predicted void fraction is sufficiently close to the experimental one are selected in the CFD database.

7. The calculated variables from the CFD database are averaged on representative macroscopic cells. In this work, the test section is divided into 50 macroscopic cells.

8. All the terms of the formulation established in step 3 are evaluated by an a priori method on the CFD database. Indeed, they are calculated on all the 50 macroscopic cells of all the test cases. The a priori evaluation has been divided into two parts.

    (a) First, the subgrid terms of turbulence and dispersion have been compared to the convection term. We have shown that concerning the momentum and energy equations, the dispersion terms are not always negligible. Moreover, it has been shown that the geometry has an impact on the dispersion terms. Finally, an existing dispersion correlation has been tested, and some discrepancies have been observed between the values predicted by these correlations and those calculated by the a priori evaluation.

(b) The second part of the a priori evaluation consisted of the comparison of all the terms in momentum and energy equations. It has been shown that, although the dispersion is non-negligible compared to the convection term or the sum of the interfacial transfer terms, the condensation and nucleation taken individually are much larger than the dispersion term, especially for high subcooling. Therefore, it seems more relevant to focus on the development of a macroscopic model for an interfacial term, which can be the ebullition or the condensation term.

The best way to model a phenomenon, such as ebullition or condensation, is to use a local CFD database of a separate effect experiment where only the phenomenon that we want to model is present. Unfortunately, in sub-cooled boiling flows, the ebullition comes with bulk condensation and some other phenomena, such as coalescence and break-up. On the other hand, some separate effect experiments exist concerning the bubble condensation in sub-cooled water, in which only the condensation plays a predominant role. This is why we have decided in chapter 4 to build a validated local CFD database of condensing flows, which will then be used to develop a condensation model at the macroscopic scale. However, the bubbles are usually polydisperse in size, and the local monodisperse assumption, which is used in the standard version of Neptune_CFD, is then not always relevant. Consequently, the chapter 4, corresponding to steps 9-12, has been aimed to develop a new CFD modeling in order to provide a fully validated CFD database, i.e., which predicts a gas volume fraction, Sauter diameter, velocity, and a liquid temperature close to the measurements.

9. The TOPFLOW facility (Lucas et al., 2013) has been selected. In this experiment, saturated steam is injected into a pipe where sub-cooled water is flowing upward. Seven test cases have been selected, for which the condensation phenomena is predominant in comparison to coalescence and break-up. Moreover, this experiment is highly instrumented, with radial profile measurements of void fraction, gas velocity, bubble size distribution, and liquid temperature at different heights.

10. An accurate modeling of the bubble condensation in sub-cooled water is established using a quadratic bubble size distribution function, the Nusselt model developed by Chen and Mayinger (1992), and a bubble collapse model. The numerical simulations done with this modeling are compared to those obtained with a monodisperse assumption and with the iMUSIG approach by Liao and Lucas (2016). The results show that this new modeling provides better results than the monodisperse approach and similar results with a lower CPU time than the iMUSIG approach on these test cases. Indeed, the iMUSIG approach presents a more sophisticated modeling at a higher computational cost, which may give better results in other conditions, where break-up and coalescence are predominant for example, but gives equivalent results to our new modeling in the test cases considered in this thesis.

11. Using the new modeling developed in step 10, a CFD database on separate effect tests has been developed and fully validated by comparison to the measurements on radial profiles of void fraction, gas velocity, Sauter diameter, and liquid temperature. This database consists of seven test cases with 50 macroscopic cells each.

12. The local variables obtained in the CFD database are averaged in the same way as in step 7.

The chapter 5, corresponding to steps 13-17, has been dedicated to the development of new macroscopic models, based on the CFD database of step 11, for the interfacial energy transfer terms of condensation $\tilde{\Pi}_l'$. In order to investigate the potentialities of these new models, they are compared to the CFD database and the existing models of CATHARE and TRACE codes.

13. Since the existing and new models are assessed by an a priori evaluation on the CFD database developed in step 11, the deviations between the CFD and the experiment, as well as the potential deviations linked to the experimental uncertainties, are quantified. We have proven that these deviations are relatively small, within a few percent.

14. The $\tilde{\Pi}_l'$ correlations of TRACE and CATHARE are evaluated by the a priori method based on the CFD database. The deviations obtained by both correlations are high, with an underestimation of the energy interfacial exchanges by approximately a factor of two. Moreover, error compensations appear in the TRACE correlation due to the errors linked to the interfacial area correlation.

15. Since the existing models show room for improvement, some new models have been introduced for the interfacial energy transfer terms of condensation $\tilde{\Pi}_l'$. A model based on the correlation from Chen and Mayinger (1992) and adapted to the macroscopic scale provides a mean relative error of 11.5%, much lower than those obtained from correlations of CATHARE and TRACE. Next, a statistical approach has been used to optimize the coefficients of the Nusselt number to minimize the error on the $\tilde{\Pi}_l'$ term. A model based on the relative velocity correlation from TRACE and the Nusselt coefficient optimization provides a relative error of 5.5%, which is adequate. Also, a baseline towards a fully mechanistic model is provided in order to avoid error compensation.

16. Due to the fact that the database is limited, the evaluation and optimization datasets are not totally independent. Therefore, it is necessary to assess these new models by an a priori evaluation on additional bubble condensation experiments, such as those mentioned in section 5.3.4.

17. A baseline towards an a posteriori evaluation of the new models has been introduced. This evaluation is based on the implementation of the latest models in a macroscopic code and numerical simulations on the same database presented previously. Then, the simulation results are compared to the a priori results, and if the results are different, an optimization needs to be done. Moreover, a model needs to be used for the interfacial area, whether with an algebraic correlation or by an IATE. Once it is done, the effects of the new models can also be analyzed on integral effect tests.

Therefore, the up-scaling method described in Figure 7 has been applied in this thesis on industrial sub-cooled boiling test cases in sub-channel and pipe geometries. Indeed, the condensation phenomenon has been identified as predominant in these flow configurations, and some models adapted to the macroscopic code CATHARE have been developed in this study based on the local code Neptune_CFD.

> **Remark:** The method developed in this thesis is generic and can be adapted to different industrial flow configurations and different geometries. The local and macroscopic codes can also be diverse, depending on the scale studied (DNS to RANS; RANS to component/system) and on the available codes. Finally, depending on the flow configurations, the phenomenon identified as predominant and chosen to be modeled can also be diversified.

Conclusions and Perspectives

Conclusions

The main goal of this thesis was to develop an up-scaling method to identify and model the main physical phenomenon at the macroscopic scale in industrial conditions based on local simulations. Moreover, the aim was to apply this method to sub-cooled boiling flows that can be encountered in accidental conditions in nuclear reactor cores, i.e., at high pressure, temperature, flow rate, and wall heat flux.

This generic method is summarized in 17 steps in Figure 7, and the manner in which this method is applied to industrial sub-cooled boiling flow conditions in this thesis is summarized in the previous chapter. While the chapter 1 aimed to conceive an up-scaling strategy adapted to industrial two-phase flows on the basis of the State of the Art, the chapters 2-5 applied this strategy on sub-cooled boiling flows representative of nuclear reactor core subjected to different conditions. Three main parts emerge from this work.

The first part aims to identify, by an a priori evaluation method, the predominant term in the macroscopic formulation for industrial sub-cooled boiling flows. The work done in this part has been published in the International Journal of Heat and Mass Transfer (Herry et al., 2024b). This part can be divided into three sub-parts. First, in chapter 2, a macroscopic formulation has been established based on the local code (Neptune_CFD) equations using a spatial average operator. This formulation is then only based on averaged local variables, which can be calculated from CFD calculations by spatial averages of local variables. Moreover, the macroscopic formulation developed has also been compared to the formulations of existing macroscopic codes CATHARE and TRACE in order to identify the assumptions made by these codes and to link the terms from the existing formulation to those of the new one. Consequently, the terms of the existing codes can be calculated from the spatial average of local CFD variables. The second sub-part, in section 3.1, has consisted of building a RANS CFD simulation database with Neptune_CFD on industrial sub-cooled boiling flows experiments in pipe and sub-channel geometries, namely KIT and PSBT. In the third sub-part, in section 3.2, we have evaluated by an a priori method all the terms of the macroscopic formulation established in the first sub-part on the variables from the CFD database developed in the second sub-part, which are spatially averaged. This evaluation has permitted us to determine which terms are predominant and which are negligible. Moreover, some existing correlations have been evaluated by the a priori method. The principal results of this part are:

- The terms linked to the statistical and spatial deviations, named turbulence and dispersion, are present in the new macroscopic formulation but not in the standard version of many existing macroscopic codes, which highlights that most of them neglect these terms.
- The Neptune_CFD code is able to simulate sub-cooled boiling flows subjected to conditions representative of different scenarios in the nuclear reactor core. Indeed, the relative deviations in the void fraction prediction of most test cases from KIT and PSBT experiments are in the range of ±20 %.
- The dispersion subgrid terms reach, respectively, 7.5 % of the convection term in the liquid and gas momentum equations and 16 % of the convection terms in the liquid energy

equation for some test cases. They are, therefore, not always negligible. Moreover, the turbulence terms reach 2.5 % of the convection term in the liquid momentum equation.

- In the liquid energy equation, the dispersion terms obtained in the sub-channel geometry experiment (PSBT) are four times lower than those obtained in the pipe geometry experiment (KIT). Accordingly, the configuration clearly affects the macroscopic dispersion terms.
- The existing correlations developed by Ishii and Hibiki (2011) are not able to accurately predict the dispersion terms in these test cases.
- In the momentum equation, many different phenomena are non-negligible in these sub-cooled boiling test cases, and it is difficult to identify a predominant term.
- In the energy equation, the interfacial transfer terms of nucleation and bubble condensation are predominant.

Based on these results, the dispersion terms should not be neglected in the balance equations, especially in energy equations. It is worth noting that this work also addresses a request of the NEA, which states on the macroscopic turbulent-diffusion terms that 'it would be better to quantify such terms than qualitatively neglecting them' (NEA, 2024). Moreover, it has been proven that the geometry impacts the dispersion terms. Therefore, modeling the dispersion terms using a correlation established on a cylindrical configuration might not be appropriate to simulate a nuclear reactor core, where sub-channel configurations are found. Some new models for these terms are therefore needed. Finally, it has been proven that in the liquid energy balance equation, the predominant terms are not the dispersion but the interfacial transfer terms of nucleation and bubble condensation.

However, some limitations have been identified in this part and are summarized below:

- The PSBT and KIT measurements are not CFD-grade. This means that the measurements are not local but averaged on the cross-section, which makes it difficult to ensure the accuracy of the CFD simulation with confidence.
- The Neptune_CFD code tends to overestimate the void fraction compared to the measurements, especially in the KIT experiment.

Although the CFD database developed in this part is able to estimate the order of magnitude of all the terms, these limitations highlight that the CFD database is insufficiently validated to form the basis of the macroscopic model development. Therefore, in order to confidently ensure the accuracy of the CFD database, a local CFD database of a separate effect experiment, which includes only the phenomenon that we want to model, needs to be developed. Since a separate effect experiment exists concerning the bubble condensation in sub-cooled water (Lucas et al., 2013), we have decided to focus on the modeling of the bubble condensation phenomena. Therefore, the second part consists of establishing a validated local CFD database of condensing flows, which will then be used to develop a condensation model at the macroscopic scale in the third part. Since some deviations exist between the predictions and measurements, some new models are also introduced to obtain a fully validated CFD database.

The second main part, corresponding to the chapter 4, focuses on the development of a fully validated CFD database of the bubble condensation phenomena in sub-cooled water on TOPFLOW experiment (Lucas et al., 2013) using only one dispersed phase and one IATE (Interfacial Area Transport Equation). Indeed, a more complex strategy based on a multi-size group approach is often used in the literature but results in a high computational cost, which makes it challenging to simulate industrial two-phase flows in tube bundles, for example. The work done in this part has been published in the International Journal of Multiphase Flow (Herry et al., 2024a).

First, the RANS equations of the dispersed phase are described using the standard method of moments. As a result, equations similar to the two-fluid model equations are obtained. However, using this method, the interfacial terms are expressed as integrals that depend on a bubble size distribution function. In addition, this method provides an IATE, which also relies on the distribution function. Next, two distribution functions are introduced. The first is the Dirac function, which assumes a local monodispersion of bubble size, and the second is a quadratic function, which assumes a local polydispersion of bubble size. It is important to note that the equations obtained with the Dirac function correspond to the ones used in the first part and that the quadratic function is adapted from Ruyer and Seiler (2009) in this work.

These functions lead to different formulations for interfacial exchanges, whether in terms of mass and energy exchange, interfacial forces, or interfacial area concentration. The influence of these functions on each model of interfacial terms is evaluated by analyzing the results of TOPFLOW simulations with Dirac and quadratic functions. Moreover, the widely used correlation for the Nusselt number developed by Ranz and Marshall (1952) is assessed and compared to other correlations, such as the one proposed by Chen and Mayinger (1992). In order to eliminate the uncertainties due to the bubble diameter prediction, the experimental Sauter diameter is imposed in the numerical simulations during the evaluation of both the Nusselt number correlations and the impact of bubble size distribution functions on interfacial terms.

Next, two IATEs have also been developed using the standard method of moments with both Dirac and quadratic distribution functions. Moreover, a model for the bubble collapse phenomenon due to condensation developed by Park et al. (2007) has been introduced and adapted to both Dirac and quadratic functions. Finally, the full Dirac and full quadratic modeling have been compared to the experiments and to the results obtained by Liao and Lucas (2016) using the multi-size group modeling. The key findings of this part are given below:

- The distribution function, whether Dirac or quadratic, has a limited impact on interfacial mass and energy exchange. However, it has a significant influence on the drag force model. The quadratic function gives the best results in modeling the drag force.
- In the test cases considered, using the experimental Sauter diameter, the Ranz-Marshall correlation largely underestimates the condensation, while the results obtained using the correlation from Chen and Mayinger (1992) are accurate.
- Using the IATE with the bubble collapse model from Park et al. (2007), the predicted Sauter diameters are well predicted using the quadratic function but are greatly underestimated using the Dirac function.
- The axial evolution predictions of the void fraction and Sauter diameter using the method of moments with the quadratic function, Chen-Mayinger correlation, and bubble collapse model are in the same order of magnitude as the results obtained by Liao and Lucas (2016) using a multi-size group approach, while being considerably less computational demanding.
- Using the new modeling, a high accuracy is obtained on the radial profiles of void fraction, gas velocity, bubble Sauter diameter, and liquid temperature.

Therefore, this study has shown that the Ranz-Marshall correlation, developed for low bubble Reynolds numbers below 200, should be used with caution for larger bubble Reynolds numbers. Nevertheless, the correlation proposed by Chen and Mayinger (1992) and developed for bubble Reynolds numbers between 400 and $10,000$ gives accurate predictions, even for test cases with larger bubble Reynolds numbers, up to $30,000$. Moreover, it is crucial to take into account the bubble collapse phenomenon that results from condensation since this phenomenon is predominant, and its non-consideration results in a significant underestimation of the Sauter diameter. This work has shown that the correlation from Park et al. (2007), developed at atmospheric pressure, is still accurate for test cases with pressure between 10 and 65 bar. In conclusion, a fully validated database is obtained in this part by the TOPFLOW simulations using the standard method of moments with a quadratic function, the Chen-Mayinger correlation, and the Park bubble collapse model.

Nevertheless, it is worth to mention that some limitations have been identified in this part and are summarized below:

- The database is limited, with only seven test cases. Indeed, only the TOPFLOW test cases where the coalescence and break-up do not play a predominant role are considered.

- The standard method of moments is only applied to distribution functions that have low computational cost, namely the Dirac and quadratic functions. In contrast, other functions that are slightly more computationally demanding exist, such as the log-normal law.

- In the bubble collapse model developed by Park et al. (2007), the parameter β_b, which characterizes the boundary between the heat transfer-controlled and the inertia-controlled regions, is taken at 0.4 to optimize the results and is therefore not developed by a theoretical approach, as the rest of the model. Considering that this value also gives accurate results in TOPFLOW test cases, this value is kept in this work.

The database developed in this part is then used in the last part to propose a macroscopic model for the energy interfacial transfer term.

The last part, corresponding to chapter 5, aims to propose a new macroscopic model for the condensation energy interfacial transfer term. First, the deviations between the CFD database developed in the second part and the experiment have been quantified. Next, the correlations from the macroscopic codes CATHARE and TRACE have been evaluated. Afterward, new models are developed in three different ways. First of all, a model based on the correlation from Chen and Mayinger (1992), adapted to the macroscopic scale, is used. In the second step, a statistical approach has been used to optimize the coefficients of the Nusselt number. Two models have been proposed, one with a simple approach for the relative velocity and one with the TRACE correlation. For the third way, a baseline towards a fully mechanistic model is introduced in order to avoid error compensation. Finally, a baseline towards an a posteriori evaluation of these models is introduced. The main insights of this part are given below:

- The mean relative deviations on the parameter $\zeta = \alpha_l \rho_l C_{p_l} T_l$ are relatively small, 0.38 % due to the CFD errors and a maximum of 1.5 % due to the experimental uncertainties.

- The mean relative errors of the energy interfacial transfer term due to condensation using CATHARE and TRACE correlations compared to the CFD database are 44.5 % and 62.5 %, respectively. However, it is worth noting the low relative standard deviation using the TRACE correlation of 4 %, while it is 18 % using the CATHARE correlation.

- The mean relative error using correlation based on Chen and Mayinger (1992) is 11.5% using the simple relative velocity ($\tilde{v}_r = |\tilde{v}_g - \tilde{v}_l|$) and is 30 % using TRACE correlation for $\tilde{v}_r$. However, the standard deviation is higher using simple relative velocity (17 %) than using TRACE correlation (6 %).

- Using the relative velocity correlation from TRACE and a statistical approach to find optimal coefficients for the Nusselt number, the mean relative error is equal to 5.5 % and the relative standard deviation to 7%, which is adequate.

Accordingly, the new models developed in this thesis permit the reduction of the relative errors in comparison to the correlations from CATHARE and TRACE. Therefore, it would be interesting to implement these models in a macroscopic code to evaluate them by an a posteriori approach.

In this part also, some limitations have been identified and are summarized below:

- It is not possible to obtain the experimental energy interfacial transfer term. For this reason, the CFD deviations and the experimental uncertainties are evaluated on the variables $\zeta = \alpha_l \rho_l C_{p_l} T_l$.

- In the same way as the TRACE correlation and unlike the CATHARE one, the models developed in this thesis need a model for the interfacial area.

- Due to the small CFD database, the optimization and evaluation datasets are not totally independent.

In conclusion, the up-scaling method developed in this thesis has permitted us to identify the bubble condensation as predominant in industrial sub-cooled boiling flows and to propose a model for this phenomenon at the macroscopic scale based on fine-scale simulations.

Perspectives

The application of the up-scaling method developed in this work on sub-cooled boiling flows has highlighted plenty of perspectives toward future works. We propose to divide them into three categories: experiments, models, and simulations.

Experiments:

- To the extent of our knowledge, there are currently no sub-cooled steam-water experiments that are CFD-grade (i.e., with radial measurements) at pressure, flow rate, and wall heat flux representative of a nuclear reactor core. Therefore, new steam-water experiments with local measurements of void fraction, gas velocity, bubble diameter, and liquid temperature at pressure up to 155 bar, wall heat flux up to 2000 kW/m^2, inlet mass flux between 500 and 3000 kg/m^2s would allow to have more confidence on the capabilities of the CFD code to predict these flows.

- These experiments with such fine measurements could be done in different test sections to analyze the effect of the geometry. For example, first in a pipe, then in a sub-channel, and ideally next in a rod bundle first without and later with mixing vanes.

- Regarding the separate effect tests on the bubble condensation phenomenon, the experiments done by Lucas et al. (2013) have allowed us to evaluate our new modeling on test cases with pressure up to 65 bar. However, only seven test cases present bubble condensation alone, without coalescence and break-up. Some other experiments where only bubble condensation is involved exist but at a pressure lower than 10 bar (Zeitoun, 1994; Ozar et al., 2013; Kumar et al., 2019). Therefore, new test cases that involve only bubble condensation at high pressure and with different boundary conditions would permit us to extend the validity domain of our new condensation modeling.

Models:

RANS scale:

- The bubble collapse model adapted in this work demonstrated promising performance. However, as mentioned, the value of the parameter which characterizes the boundary between the heat transfer-controlled and the inertia-controlled regions is taken at 0.4 to optimize the results. Nevertheless, it represents a physical boundary that, in our opinion, could be developed theoretically. Moreover, a theoretical model of this parameter would also allow the use of this bubble collapse model for other ranges of boundary conditions, such as high pressure up to 155 bar.

- The standard method of moments could be applied to other bubble size distribution functions, which are more complex than those used in this work, such as the log-normal law. Since there is no analytic solution to the different integrals using this law, a quadrature method is needed to approximate these integrals.

- Next, in order to consider more test cases, a modeling effort could be done on the coalescence and break-up phenomena. Once these phenomena are sufficiently well modeled, all the 45 bubble condensation test cases of TOPFLOW, where condensation, break-up, and coalescence simultaneously play a dominant role, could be simulated. Finally, the heat flux partitioning, as well as the interfacial forces models, could be improved in order to have complete confidence in the sub-cooled boiling flow predictions.

Macroscopic scale:

- This work highlighted that the subgrid terms of turbulence and especially dispersion are not negligible and thus should be modeled and not neglected. It could be enriching for macroscopic codes to apply this up-scaling method in order to develop a model for these terms in industrial conditions. Indeed, some up-scaling methods for these terms already exist but are established based on academic test cases.

- The mechanistic model developed in this thesis shows promising potential. Two unknown variables, representative of local phenomena, need to be modeled. The development of models for these terms would permit the use of this mechanistic model in macroscopic codes.

- Finally, a model is needed for the interfacial area concentration term, which appears in the mass and energy interfacial transfer models. We recommend the development of an IATE using an up-scaling method since the IATE at the local scale provides accurate results, and the evaluation of the algebraic correlation from TRACE has highlighted large deviations.

Simulations:

RANS scale:

- Simulations could be performed on other bubble condensation experiments (Zeitoun, 1994; Ozar et al., 2013; Kumar et al., 2019) in order to expand the CFD database. Moreover, it would enlarge the validity domain of our modeling since these experiments are done at pressures below 10 bar and in annulus geometries.

- If the break-up and coalescence models are improved, the entire TOPFLOW database could be simulated. Moreover, if sufficient confidence is given to the heat flux partitioning and interfacial transfer models, the KIT and PSBT experiments could be simulated again in comparison to the simulations done in this work. Finally, simulations could also be done on the sub-cooled boiling DEBORA experiment, which uses boiling Freon at 26 bar to imitate the steam-water flow behavior at 150 bar. This facility is highly instrumented and provides radial measurements of void fraction, Sauter diameter, gas velocity, and liquid temperature.

Macroscopic scale:

- In order to evaluate the models developed in this work using an a posteriori method, numerical simulations by macroscopic codes such as CATHARE should be performed. If the results obtained are different from those obtained by the a priori evaluation, some optimizations should be carried out on the proposed model. The a posteriori simulations could also be done on the test cases developed by Zeitoun (1994), Ozar et al. (2013), and Kumar et al. (2019).

- Once the new model is validated by the a posteriori evaluation, numerical simulations could be conducted on PSBT and KIT experiments, with and without the new model, in order to assess it on test cases where several phenomena intervene.

- Finally, numerical simulations with the new model could be performed on integral effect tests, which are reduced-scale experimental facilities representative of accidental scenarios in the reactor system. They are carried out to investigate the behaviors, phenomena, and processes of the entire system, or the interactions between two or more components.

Beyond these perspectives, the up-scaling method developed in this thesis could be applied to many different industrial flow configurations. For example, it could be applied to water jet flows due to Emergency Core Cooling (ECC) in case of Loss Of Coolant Accident (LOCA).

Bibliography

Anderson, T.B., Jackson, R., 1967. Fluid mechanical description of fluidized beds. Equations of motion. Industrial & Engineering Chemistry Fundamentals 6, 527–539. ISBN: 0196-4313 Publisher: ACS Publications.

Bajorek, S., 2008. TRACE V5. 0 Theory manual, field equations, solution methods and physical models. United States Nuclear Regulatory Commission .

Barré, F., Dor, I., Sun, C., 1995. The multi-dimensional module of CATHARE 2. Description and application, in: Nureth 7, September 10-15 1995, Saratoga Springs, NY, United States.

Bensoussan, A., Lions, J.L., Papanicolaou, G., 2011. Asymptotic analysis for periodic structures. volume 374. American Mathematical Soc.

Bestion, D., 1990. The physical closure laws in the CATHARE code. Nuclear Engineering and Design 124, 229–245. URL: https://linkinghub.elsevier.com/retrieve/pii/0029549390902948, doi:doi: 10.1016/0029-5493(90)90294-8.

Bestion, D., 2012. Applicability of two-phase CFD to nuclear reactor thermalhydraulics and elaboration of Best Practice Guidelines. Nuclear Engineering and Design 253, 311–321. URL: https://linkinghub.elsevier.com/retrieve/pii/S0029549311006935, doi:doi: 10.1016/j.nucengdes.2011.08.068.

Blanchard, J.B., Damblin, G., Martinez, J.M., Arnaud, G., Gaudier, F., 2018. The Uranie platform: an open-source software for optimisation, meta-modelling and uncertainty analysis. arXiv preprint arXiv:1803.10656 .

Bois, G., 2021. Derivation of a macroscopic mixture model for two-phase turbulent flows. International Journal of Heat and Mass Transfer 178, 121500. URL: https://linkinghub.elsevier.com/retrieve/pii/S0017931021006037, doi:doi: 10.1016/j.ijheatmasstransfer.2021.121500.

Brooks, C.S., Liu, Y., Hibiki, T., Ishii, M., 2014. Effect of void fraction covariance on relative velocity in gas-dispersed two-phase flow. Progress in Nuclear Energy 70, 209 – 220. URL: https://www.scopus.com/inward/record.uri?eid=2-s2.0-84887060797&doi=10.1016%2fj.pnucene.2013.10.006&partnerID=40&md5=38030e616cbc4f1d4c31974286da3b9a, doi:doi: 10.1016/j.pnucene.2013.10.006. type: Article.

Brooks, C.S., Paranjape, S.S., Ozar, B., Hibiki, T., Ishii, M., 2012. Two-group drift-flux model for closure of the modified two-fluid model. International Journal of Heat and Fluid Flow 37, 196 – 208. URL: https://www.scopus.com/inward/record.uri?eid=2-s2.0-84865571181&doi=10.1016%2fj.ijheatfluidflow.2012.04.002&partnerID=40&md5=d3b635353ff10e0c4172ee8e09d59bd1, doi:doi: 10.1016/j.ijheatfluidflow.2012.04.002. type: Article.

Brun, B., Parent, M., Spindler, B., 1990. Three-Dimensional two phase flow module of the code CATHARE 2, in: International Conference on Super Computing in Nuclear Applications, Tokai-Mura, Japan.

Chandesris, M., 2006. Modélisation des écoulements turbulents dans les milieux poreux et à l'interface avec un milieu libre. Ph.D. thesis. Paris 6.

Chen, Y., Mayinger, F., 1992. Measurement of heat transfer at the phase interface of condensing bubbles. International Journal of Multiphase Flow 18, 877 – 890. URL: https://www.scopus.com/inward/record.uri?eid=2-s2.0-0026947293&doi=10.1016%2f0301-9322%2892%2990065-O&partnerID=40&md5=10691b56be433c78c6406ae855d46cfe, doi:doi: 10.1016/0301-9322(92)90065-O. type: Article.

Chung, B.D., Bae, S.W., Lee, S.W., Yoon, C., Hwang, M.K., Kim, K.D., Jeong, J.J., 2010. MARS Code Manual Volume V: Models and Correlations. Technical Report. Korea Atomic Energy Research Institute.

Ciechocki, A., 2023. New developments of a scaling analysis methodology for nuclear reactors complex thermal-hydraulic transients with calculation of the distortion associated with the full-scale transposition. Ph.D. thesis. université Paris-Saclay.

Cubizolles, G., 1996. Etude stéréologique de la topologie des écoulements diphasiques à haute pression. Ph.D. thesis. Ecully, Ecole centrale de Lyon.

D'Auria, F., 2017. Thermal-hydraulics of water cooled nuclear reactors. woodhead publishing.

Dejesus, J.M., Kawaji, M., 1990. Investigation of interfacial area and void fraction in upward, cocurrent gas-liquid flow. The Canadian Journal of Chemical Engineering 68, 904–912. URL: https://onlinelibrary.wiley.com/doi/10.1002/cjce.5450680603, doi:doi: 10.1002/cjce.5450680603.

Delhaye, J., 1977. Space/time and time/space-averaged equations. Hemisphere Publishing Corp, United States. URL: http://inis.iaea.org/search/search.aspx?orig_q=RN:15059134.

Delhaye, J.M., 1968. Equations fondamentales des écoulements diphasiques. Service central de documentation du CEA [Distributed by Clearinghouse for ....

Delhaye, J.M., Giot, M., Mahias, L., Raymond, P., Rénault, C., 2008. Thermohydraulique des réacteurs. EDP sciences.

Drouin, M., 2010. Modélisation des écoulements turbulents anisothermes en milieu macroporeux par une approche de double filtrage. PhD Thesis.

Drouin, M., Grégoire, O., Simonin, O., 2013. A consistent methodology for the derivation and calibration of a macroscopic turbulence model for flows in porous media. International Journal of Heat and Mass Transfer 63, 401–413. URL: https://linkinghub.elsevier.com/retrieve/pii/S0017931013002676, doi:doi: 10.1016/j.ijheatmasstransfer.2013.03.060.

Drouin, M., Grégoire, O., Simonin, O., Chanoine, A., 2010. Macroscopic modeling of thermal dispersion for turbulent flows in channels. International Journal of Heat and Mass Transfer 53, 2206–2217. URL: https://linkinghub.elsevier.com/retrieve/pii/S0017931009006723, doi:doi: 10.1016/j.ijheatmasstransfer.2009.12.012.

Du Cluzeau, A., 2019. Modélisation physique de la dynamique des écoulements à bulles par remontée d'échelle à partir de simulations fines. PhD Thesis. Université de Perpignan.

Favre, L., 2023. Modeling and simulation of the boiling crisis within PWR at CFD scale. Ph.D. thesis. Institut National Polytechnique de Toulouse-INPT.

Fleau, S., 2017. Multifield approach and interface locating method for two-phase flows in nuclear power plant. PhD Thesis. Université Paris-Est.

Flick, D., Leslous, A., Alvarez, G., 2003. Modélisation semi-empirique des écoulements et des transferts dans un milieu poreux en régime turbulent. International journal of refrigeration 26, 349–359. ISBN: 0140-7007 Publisher: Elsevier.

Garnier, J., Manon, E., Cubizolles, G., 2001. Local measurements on flow boiling of refrigerant 12 in a vertical tube. Multiphase Science and Technology 13. ISBN: 0276-1459 Publisher: Begel House Inc.

Gaudier, F., 2010. URANIE: the CEA/DEN uncertainty and sensitivity platform. Procedia-Social and Behavioral Sciences 2, 7660–7661. ISBN: 1877-0428 Publisher: Elsevier.

Guelfi, A., Bestion, D., Boucker, M., Boudier, P., Fillion, P., Grandotto, M., Hérard, J.M., Hervieu, E., Péturaud, P., 2007. NEPTUNE: A New Software Platform for Advanced Nuclear Thermal Hydraulics. Nuclear Science and Engineering 156, 281–324. URL: `https://www.tandfonline.com/doi/full/10.13182/NSE05-98`, doi:doi: 10.13182/NSE05-98.

Ha, S.J., Park, C.E., Kim, K.D., Ban, C.H., 2011. Development of the SPACE code for nuclear power plants. Nuclear Engineering and Technology 43, 45–62. ISBN: 1738-5733 Publisher: Korean Nuclear Society.

Habiyaremye, V., Komen, E., Kuerten, J., Frederix, E., 2022. Modeling of bubble coalescence and break-up using the Log-normal Method of Moments. Chemical Engineering Science 253, 117577. URL: `https://linkinghub.elsevier.com/retrieve/pii/S0009250922001610`, doi:doi: 10.1016/j.ces.2022.117577.

Habiyaremye, V., Kuerten, J., Frederix, E., 2023. Comparison of population balance models for polydisperse bubbly flow. Chemical Engineering Science 278. URL: `https://www.scopus.com/inward/record.uri?eid=2-s2.0-85160794515&doi=10.1016%2fj.ces.2023.118932&partnerID=40&md5=7c29fd2d2be79194aedf446f07049b0d`, doi:doi: 10.1016/j.ces.2023.118932. type: Article.

Haynes, P.A., 2004. Contribution à la modélisation de la turbulence pour les écoulements à bulles: proposition d'un modèle (k-epsilon) multi-échelles diphasique. Ph.D. thesis. Toulouse, INPT.

Herry, T., Raverdy, B., Mimouni, S., Vincent, S., 2024a. Modeling and simulation of bubble condensation using polydisperse approach with bubble collapse model. International Journal of Multiphase Flow , 104846URL: `https://linkinghub.elsevier.com/retrieve/pii/S0301932224001241`, doi:doi: 10.1016/j.ijmultiphaseflow.2024.104846.

Herry, T., Raverdy, B., Mimouni, S., Vincent, S., 2024b. Volume average of two-fluid RANS equations and a priori estimation of subgrid terms on subcooled boiling experiments. International Journal of Heat and Mass Transfer 223, 125232. URL: `https://linkinghub.elsevier.com/retrieve/pii/S0017931024000644`, doi:doi: 10.1016/j.ijheatmasstransfer.2024.125232.

Herry, T., Raverdy, B., Nguyen, E., Mimouni, S., 2022. Two-phase flow upscaling method in a macroporous medium, in: Proceedings of Advances in Thermal Hydraulics (ATH 2022), Anaheim, USA. pp. 575–588. URL: `https://www.ans.org/pubs/proceedings/article-51619/`, doi:doi: 10.13182/t126-38104.

Hibiki, T., Ishii, M., 2000. One-group interfacial area transport of bubbly flows in vertical round tubes. Int. J. Heat Mass Transfer , 16.

Howes, F.A., Whitaker, S., 1985. The spatial averaging theorem revisited. Chemical Engineering Science 40, 1387–1392. URL: `https://linkinghub.elsevier.com/retrieve/pii/0009250985800786`, doi:doi: 10.1016/0009-2509(85)80078-6.

Hulburt, H., Katz, S., 1964. Some problems in particle technology. Chemical Engineering Science 19, 555–574. URL: `https://linkinghub.elsevier.com/retrieve/pii/0009250964850478`, doi:doi: 10.1016/0009-2509(64)85047-8.

IAEA, 2023. Nuclear Power Reactors in the World. INTERNATIONAL ATOMIC ENERGY AGENCY, Vienna. URL: `https://www.iaea.org/publications/15485/nuclear-power-reactors-in-the-world`. book.

IEA, 2021. World electricity generation mix by fuel, 1971-2019. Technical Report. Paris. URL: https://www.iea.org/data-and-statistics/charts/world-electricity-generation-mix-by-fuel-1971-2019.

Ishii, M., Hibiki, T., 2011. Thermo-Fluid Dynamics of Two-Phase Flow. Springer New York, New York, NY. URL: http://link.springer.com/10.1007/978-1-4419-7985-8, doi:doi: 10.1007/978-1-4419-7985-8.

Ishii, M., Mishima, K., 1984. Two-fluid model and hydrodynamic constitutive relations. Nuclear Engineering and Design 82, 107–126. URL: https://linkinghub.elsevier.com/retrieve/pii/0029549384902073, doi:doi: 10.1016/0029-5493(84)90207-3.

Ishii, M., Zuber, N., 1979. Drag coefficient and relative velocity in bubbly, droplet or particulate flows. AIChE Journal 25, 843–855. URL: https://onlinelibrary.wiley.com/doi/10.1002/aic.690250513, doi:doi: 10.1002/aic.690250513.

Jeong, J.J., Ha, K.S., Chung, B.D., Lee, W.J., 1999. Development of a multi-dimensional thermal-hydraulic system code, MARS 1.3. 1. Annals of Nuclear Energy 26, 1611–1642. ISBN: 0306-4549 Publisher: Elsevier.

Kalitvianski, V., 2000. Qualification of CATHARE 2 v1.5 rev. 6 on subcooled boiling experiments (KIT tests). Technical Report.

Kamp, A., Chesters, A., Colin, C., Fabre, J., 2001. Bubble coalescence in turbulent flows: A mechanistic model for turbulence-induced coalescence applied to microgravity bubbly pipe flow. International Journal of Multiphase Flow 27, 1363–1396. URL: https://linkinghub.elsevier.com/retrieve/pii/S0301932201000106, doi:doi: 10.1016/S0301-9322(01)00010-6.

Kenich, A., 2019. Atomistic simulation of fission products in zirconia polymorphs. Ph.D. thesis. Imperial College London.

Kim, S., Ishii, M., Kong, R., Wang, G., 2021. Progress in two-phase flow modeling: Interfacial area transport. Nuclear Engineering and Design 373. URL: https://www.scopus.com/inward/record.uri?eid=2-s2.0-85099144693&doi=10.1016%2fj.nucengdes.2020.111019&partnerID=40&md5=1943d1a9631de983160b2b40d7535f13, doi:doi: 10.1016/j.nucengdes.2020.111019. type: Article.

Kolev, N., 1985. Comparisons of the RALIZA-2/02 two-phase flow model with experimental data. Nuclear Engineering and Design 85, 217–237. URL: https://linkinghub.elsevier.com/retrieve/pii/0029549385902882, doi:doi: 10.1016/0029-5493(85)90288-2.

Krepper, E., Beyer, M., Lucas, D., Schmidtke, M., 2011. A population balance approach considering heat and mass transfer—Experiments and CFD simulations. Nuclear Engineering and Design 241, 2889–2897. URL: https://linkinghub.elsevier.com/retrieve/pii/S0029549311004031, doi:doi: 10.1016/j.nucengdes.2011.05.003.

Krepper, E., Lucas, D., Prasser, H.M., 2005. On the modelling of bubbly flow in vertical pipes. Nuclear Engineering and Design 235, 597–611. URL: https://linkinghub.elsevier.com/retrieve/pii/S0029549304003322, doi:doi: 10.1016/j.nucengdes.2004.09.006.

Kumar, V., Ooi, Z.J., Brooks, C.S., 2019. Forced convection steam-water experimental database in a vertical annulus with local measurements. International Journal of Heat and Mass Transfer 137, 216–228. URL: https://linkinghub.elsevier.com/retrieve/pii/S0017931018362604, doi:doi: 10.1016/j.ijheatmasstransfer.2019.03.099.

Kurul, N., Podowski, M.Z., 1990. Multidimensional effects in forced convection subcooled boiling, in: International Heat Transfer Conference Digital Library, Begel House Inc.

Lahey, R.T., Drew, D.A., 1988. The Three-Dimensional Time and Volume Averaged Conservation Equations of Two-Phase Flow, in: Lewins, J., Becker, M., Lewins, J., Becker, M. (Eds.), Advances in Nuclear Science and Technology. Springer US, Boston, MA. volume 20, pp. 1–69. URL: http://link.springer.com/10.1007/978-1-4613-9925-4_1, doi:doi: 10.1007/978-1-4613-9925-4_1. series Title: Advances in Nuclear Science and Technology.

Laviéville, J., Mérigoux, N., Guingo, M., Baudry, C., Mimouni, S., 2017. A Generalized turbulent dispersion model for bubbly flow numerical simulation in NEPTUNE_cfd. Nuclear Engineering and Design 312, 284–293. URL: https://linkinghub.elsevier.com/retrieve/pii/S0029549316304332, doi:doi: 10.1016/j.nucengdes.2016.11.003.

Lee, S.Y., Hibiki, T., Ishii, M., 2009. Formulation of time and volume averaged two-fluid model considering structural materials in a control volume. Nuclear Engineering and Design 239, 127–139. URL: https://linkinghub.elsevier.com/retrieve/pii/S0029549308004755, doi:doi: 10.1016/j.nucengdes.2008.09.008.

Lerchl, G., Austregesilo, H., Langenfeld, P., 2019. ATHLET 3.2 User's Manual. Technical Report. Gesellschaft fuer Anlagen- und Reaktorsicherheit (GRS) gGmbH, 1, Rev. 8.

Liao, Y., Krepper, E., Lucas, D., 2019. A baseline closure concept for simulating bubbly flow with phase change: A mechanistic model for interphase heat transfer coefficient. Nuclear Engineering and Design 348, 1–13. URL: https://www.scopus.com/inward/record.uri?eid=2-s2.0-85063948217&doi=10.1016%2fj.nucengdes.2019.04.007&partnerID=40&md5=ff5b30e87135f0595fcb500e0aef86bb, doi:doi: 10.1016/j.nucengdes.2019.04.007. type: Article.

Liao, Y., Lucas, D., 2016. Poly-disperse simulation of condensing steam-water flow inside a large vertical pipe. International Journal of Thermal Sciences 104, 194–207. URL: https://linkinghub.elsevier.com/retrieve/pii/S1290072916000296, doi:doi: 10.1016/j.ijthermalsci.2016.01.016.

Lucas, D., Beyer, M., Szalinski, L., 2010. Experimental data on steam bubble condensation in poly-dispersed upward vertical pipe flow, in: CFD4NRS-3, International Workshop on Experimental Validation and Application of CFD and CMFD Codes to Nuclear Reactor Safety Issues, pp. 14–16.

Lucas, D., Beyer, M., Szalinski, L., 2013. Experimental database on steam water flow with phase transfer in a vertical pipe. Nuclear Engineering and Design 265, 1113–1123. URL: https://linkinghub.elsevier.com/retrieve/pii/S0029549313005463, doi:doi: 10.1016/j.nucengdes.2013.10.002.

Lucas, D., Frank, T., Lifante, C., Zwart, P., Burns, A., 2011. Extension of the inhomogeneous MUSIG model for bubble condensation. Nuclear Engineering and Design 241, 4359–4367. URL: https://linkinghub.elsevier.com/retrieve/pii/S0029549311003037, doi:doi: 10.1016/j.nucengdes.2010.10.039.

Lucas, D., Prasser, H.M., 2007. Steam bubble condensation in sub-cooled water in case of co-current vertical pipe flow. Nuclear Engineering and Design 237, 497–508. URL: https://linkinghub.elsevier.com/retrieve/pii/S0029549306005103, doi:doi: 10.1016/j.nucengdes.2006.09.004.

Lutsanych, S., Moretti, F., D'Auria, F., 2017. Validation of NEPTUNE CFD two-phase flow models against OECD/NRC PSBT subchannel experiments. Nuclear Engineering and Design 321, 82–91. URL: https://linkinghub.elsevier.com/retrieve/pii/S0029549317300535, doi:doi: 10.1016/j.nucengdes.2017.02.005.

Manon, E., 2000. Contribution à l'analyse et à la modélisation locale des écoulements bouillants sous-saturés dans les conditions des réacteurs à eau sous pression. Ph.D. thesis. Châtenay-Malabry, Ecole centrale de Paris.

McGraw, R., 1997. Description of Aerosol Dynamics by the Quadrature Method of Moments. Aerosol Science and Technology 27, 255–265. URL: http://www.tandfonline.com/doi/abs/10.1080/02786829708965471, doi:doi: 10.1080/02786829708965471.

Mimouni, S., Fleau, S., Vincent, S., 2017a. CFD calculations of flow pattern maps and LES of multiphase flows. Nuclear Engineering and Design 321, 118–131. URL: https://linkinghub.elsevier.com/retrieve/pii/S0029549316304964, doi:doi: 10.1016/j.nucengdes.2016.12.009.

Mimouni, S., Guingo, M., Lavieville, J., Mérigoux, N., 2017b. Combined evaluation of bubble dynamics, polydispersion model and turbulence modeling for adiabatic two-phase flow. Nuclear Engineering and Design 321, 57–68. URL: https://linkinghub.elsevier.com/retrieve/pii/S0029549317301619, doi:doi: 10.1016/j.nucengdes.2017.03.041.

Mimouni, S., Laviéville, J., Seiler, N., Ruyer, P., 2011. Combined evaluation of second order turbulence model and polydispersion model for two-phase boiling flow and application to fuel assembly analysis. Nuclear Engineering and Design 241, 4523–4536. ISBN: 0029-5493 Publisher: Elsevier.

Nakayama, A., Kuwahara, F., 1999. A Macroscopic Turbulence Model for Flow in a Porous Medium. Journal of Fluids Engineering 121, 427–433. URL: https://asmedigitalcollection.asme.org/fluidsengineering/article/121/2/427/395089/A-Macroscopic-Turbulence-Model-for-Flow-in-a, doi:doi: 10.1115/1.2822227.

NEA, 2024. Status of Simulation Capability of 3D System-scale Thermal-hydraulic (TH) Analysis Codes. OECD Publishing .

Ozaki, T., Hibiki, T., 2018. Modeling of distribution parameter, void fraction covariance and relative velocity covariance for upward steam-water boiling flow in vertical rod bundle. Journal of Nuclear Science and Technology 55, 386–399. URL: https://www.tandfonline.com/doi/full/10.1080/00223131.2017.1403382, doi:doi: 10.1080/00223131.2017.1403382.

Ozar, B., Brooks, C., Hibiki, T., Ishii, M., 2013. Interfacial area transport of vertical upward steam-water two-phase flow in an annular channel at elevated pressures. International Journal of Heat and Mass Transfer 57, 504 – 518. URL: https://www.scopus.com/inward/record.uri?eid=2-s2.0-84869881900&doi=10.1016%2fj.ijheatmasstransfer.2012.10.059&partnerID=40&md5=90df21c0bb1b7e31aec6f3cd45e448a0, doi:doi: 10.1016/j.ijheatmasstransfer.2012.10.059. type: Article.

Ozel, A., Fede, P., Simonin, O., 2013. Development of filtered Euler–Euler two-phase model for circulating fluidised bed: High resolution simulation, formulation and a priori analyses. International Journal of Multiphase Flow 55, 43–63. URL: https://linkinghub.elsevier.com/retrieve/pii/S030193221300058X, doi:doi: 10.1016/j.ijmultiphaseflow.2013.04.002.

Parent, M., Brun, B., Spindler, B., 1991. Three-dimensional two-phase flow module of the code CATHARE 2, in: Advances in Mathematics Computations and Reactor Physics, Congres ANS 1991, Pittsburgh.

Park, H.S., Lee, T.H., Hibiki, T., Baek, W.P., Ishii, M., 2007. Modeling of the condensation sink term in an interfacial area transport equation. International Journal of Heat and Mass Transfer 50, 5041 – 5053. URL: https://www.scopus.com/inward/record.uri?eid=2-s2.0-36549054122&doi=10.1016%2fj.ijheatmasstransfer.2007.09.001&partnerID=40&md5=d20d03b9aff73d175ea889e74c6390a5, doi:doi: 10.1016/j.ijheatmasstransfer.2007.09.001. type: Article.

Pedras, M.H.J., De Lemos, M.J., 2001. Macroscopic turbulence modeling for incompressible flow through undeformable porous media. International Journal of Heat and Mass Transfer , 13.

Pinson, F., 2006. Modélisation à l'échelle macroscopique d'un écoulement turbulent au sein d'un milieu poreux. Ph.D. thesis. Institut National Polytechnique de Toulouse-INPT.

Prasser, H.M., Misawa, M., Tiseanu, I., 2005. Comparison between wire-mesh sensor and ultra-fast X-ray tomograph for an air–water flow in a vertical pipe. Flow Measurement and Instrumentation 16, 73–83. URL: https://linkinghub.elsevier.com/retrieve/pii/S0955598605000142, doi:doi: 10.1016/j.flowmeasinst.2005.02.003.

Préa, R., Fillion, P., Matteo, L., Mauger, G., Mekkas, A., 2020. CATHARE-3 V2. 1: The new industrial version of the CATHARE code, in: ATH'20-Advances in Thermal Hydraulics 2020, pp. https://www. ans. org/pubs/proceedings/article–49142/.

Quintard, M., Whitaker, S., 1994. Transport in ordered and disordered porous media I: The cellular average and the use of weighting functions. Transport in Porous Media 14, 163–177. URL: http://link.springer.com/10.1007/BF00615199, doi:doi: 10.1007/BF00615199.

Ransom, V.H., 1989. Course A—Numerical modeling of two-phase flows for presentation at Ecole d'Ete d'Analyse Numerique. Technical Report. EG and G Idaho, Inc., Idaho Falls, ID (USA).

Ranz, W.E., Marshall, W.R., 1952. Evaporation from drops Part II. Chemical Engineering Science .

Rayleigh, L., 1917. VIII. On the pressure developed in a liquid during the collapse of a spherical cavity. The London, Edinburgh, and Dublin Philosophical Magazine and Journal of Science 34, 94–98. ISBN: 1941-5982 Publisher: Taylor & Francis.

Renard, P., De Marsily, G., 1997. Calculating equivalent permeability: a review. Advances in water resources 20, 253–278. ISBN: 0309-1708 Publisher: Elsevier.

Rubin, A., Schoedel, A., Avramova, M., Utsuno, H., Bajorek, S., Velazquez-Lozada, A., 2012. Oecd/nrc benchmark based on nupec pwr sub-channel and bundle test (psbt). volume i: Experimental database and final problem specifications. Technical Report. Organisation for Economic Co-Operation and Development.

Ruyer, P., Seiler, N., 2009. Advanced model for polydispersion in size in boiling flows. Houille Blanche , 65 – 71URL: https://www.scopus.com/inward/record.uri?eid=2-s2.0-72549092438&doi=10.1051%2flhb%2f2009046&partnerID=40&md5=68ee55c8702e660046ed7d6e9630f2f9, doi:doi: 10.1051/lhb/2009046. type: Article.

Ruyer, P., Seiler, N., Beyer, M., Weiss, F., 2007. A bubble size distribution model for the numerical simulation of bubbly flows, in: 6th International Conference on Multiphase Flow, ICMF. Leipzig, Germany, July, pp. 9–13.

Sabotinov, L.S., 1974. Experimental investigation of void fraction in subcooled boiling for different power distribution laws along the channel. Moskva PhD Thesis in Russian .

Sanchez-Palencia, E., 1980. Fluid flow in porous media. Non-homogeneous media and vibration theory , 129–157ISBN: 3540100008 Publisher: Springer.

Schlegel, J., Hibiki, T., 2015. A correlation for interfacial area concentration in high void fraction flows in large diameter channels. Chemical Engineering Science 131, 172 – 186. URL: https://www.scopus.com/inward/record.uri?eid=2-s2.0-84928158992&doi=10.1016%2fj.ces.2015.04.004&partnerID=40&md5=1666ef13eb7808f90b48a6246293cee5, doi:doi: 10.1016/j.ces.2015.04.004. type: Article.

Shah, M.M., 1979. A general correlation for heat transfer during film condensation inside pipes. International Journal of Heat and Mass Transfer 22, 547–556. URL: https://www.sciencedirect.com/science/article/pii/0017931079900589, doi:doi: https://doi.org/10.1016/0017-9310(79)90058-9.

Siemens, P.L.M., 2017. Simcenter STAR-CCM. Academic Research, Release 12.

Simonin, O., 2000. Statistical and continuum modelling of turbulent reactive particulate flows. Lecture series 6.

Slattery, J.C., 1967. Flow of viscoelastic fluids through porous media. AIChE Journal 13, 1066–1071. ISBN: 0001-1541 Publisher: Wiley Online Library.

Smith, T., Schlegel, J., Hibiki, T., Ishii, M., 2012. Mechanistic modeling of interfacial area transport in large diameter pipes. International Journal of Multiphase Flow 47, 1 – 16. URL: https://www.scopus.com/inward/record.uri?eid=2-s2.0-84864051185&doi=10.1016%2fj.ijmultiphaseflow.2012.06.009&partnerID=40&md5=1d0dfed5c9183073d4b48d949e86561a, doi:doi: 10.1016/j.ijmultiphaseflow.2012.06.009. type: Article.

Speziale, C.G., Sarkar, S., Gatski, T.B., 1991. Modelling the pressure–strain correlation of turbulence: an invariant dynamical systems approach. Journal of fluid mechanics 227, 245–272. ISBN: 1469-7645 Publisher: Cambridge University Press.

Sylvie Aubry, Christian Caremoli, J.O., Rascle, P., 1995. The THYC Three-Dimensional Thermal-Hydraulic Code for Rod Bundles: Recent Developments and Validation Tests. Nuclear Technology 112, 331–345. URL: https://doi.org/10.13182/NT95-A35159, doi:doi: 10.13182/NT95-A35159. publisher: Taylor & Francis _eprint: https://doi.org/10.13182/NT95-A35159.

Tartar, L., 2009. The general theory of homogenization: a personalized introduction. volume 7. Springer Science & Business Media.

Teruel, F.E., Rizwan-uddin, 2009. A new turbulence model for porous media flows. Part II: Analysis and validation using microscopic simulations. International Journal of Heat and Mass Transfer 52, 5193–5203. URL: https://linkinghub.elsevier.com/retrieve/pii/S0017931009002956, doi:doi: 10.1016/j.ijheatmasstransfer.2009.04.023.

Tomiyama, A., 1998. Struggle with computational bubble dynamics. Multiphase Science and Technology 10, 369–405. ISBN: 0276-1459.

Tomiyama, A., 2009. Progress in computational bubble dynamics, in: 7th Workshop on Multiphase Flow, May.

Tomiyama, A., Tamai, H., Zun, I., Hosokawa, S., 2002. Transverse migration of single bubbles in simple shear flows. Chemical Engineering Science , 10.

Toumi, I., Bergeron, A., Gallo, D., Royer, E., Caruge, D., 2000. FLICA-4: a three-dimensional two-phase flow computer code with advanced numerical methods for nuclear applications. Nuclear Engineering and Design 200, 139–155. URL: https://linkinghub.elsevier.com/retrieve/pii/S0029549399003325, doi:doi: 10.1016/S0029-5493(99)00332-5.

Valette, M., 2012. Analysis of Subchannel and Rod Bundle PSBT Experiments with CATHARE 3. Science and Technology of Nuclear Installations 2012, 1–10. URL: http://www.hindawi.com/journals/stni/2012/123426/, doi:doi: 10.1155/2012/123426.

Wellek, R., Agrawal, A., Skelland, A., 1966. Shape of liquid drops moving in liquid media. AIChE Journal 12, 854 – 862. URL: https://www.scopus.com/inward/record.uri?eid=2-s2.0-0000691430&doi=10.1002%2faic.690120506&partnerID=40&md5=bef6444e5654e774b71507b1fe951258, doi:doi: 10.1002/aic.690120506. type: Article.

Whitaker, S., 1967. Diffusion and dispersion in porous media. AIChE Journal 13, 420–427. ISBN: 0001-1541 Publisher: Wiley Online Library.

Whitaker, S., 1969. Advances in theory of fluid motion in porous media. Industrial & engineering chemistry 61, 14–28. ISBN: 0019-7866 Publisher: ACS Publications.

Zaepffel, D., Morel, C., Lhuillier, D., 2012. A MULTISIZE MODEL FOR BOILING BUBBLY FLOWS. Multiphase Science and Technology 24, 105–179. URL: http://www.dl.begellhouse.com/journals/5af8c23d50e0a883,419f2a377529b6f7,057b85ee23de9b27.html, doi:doi: 10.1615/MultScienTechn.v24.i2.20.

Zeitoun, O., 1994. Subcooled flow boiling and condensation. Ph.D. thesis. Alexandria University - EGYPT.

Zuber, N., 1964. On the dispersed two-phase flow in the laminar flow regime. Chemical Engineering Science 19, 897–917. URL: https://linkinghub.elsevier.com/retrieve/pii/0009250964850673, doi:doi: 10.1016/0009-2509(64)85067-3.

Zuber, N., Findlay, J., 1965. Average volumetric concentration in two-phase flow systems. Journal of Heat Transfer 87, 453 – 468. doi:doi: 10.1115/1.3689137. iSBN: 0022-1481.

Zwick, S.A., Plesset, M.S., 1955. On the dynamics of small vapor bubbles in liquids. Journal of Mathematics and Physics 33, 308–330. Publisher: Massachusetts Institute of Technology.

Appendix

I Validation of TOPFLOW numerical simulations based on local profiles

This appendix aims to complete the validation of the numerical simulations of TOPFLOW experiment done using Neptune_CFD with the new modeling developed in chapter 4. Indeed, in section 4.6, the predicted radial profiles of test cases 2, 3, and 7 are compared to the measurements. In this appendix, the four other test cases, namely 1, 4, 5, and 6 are shown in Figures I.1, I.2, I.3, and I.4. The same conclusions as the ones made in section 4.6 remain, i.e., the radial profiles are overall well predicted, but some discrepancies exist, especially on the radial position of the void fraction peak. This slight discrepancy could come from deviations on the turbulent dispersion force, and on the turbulence model.

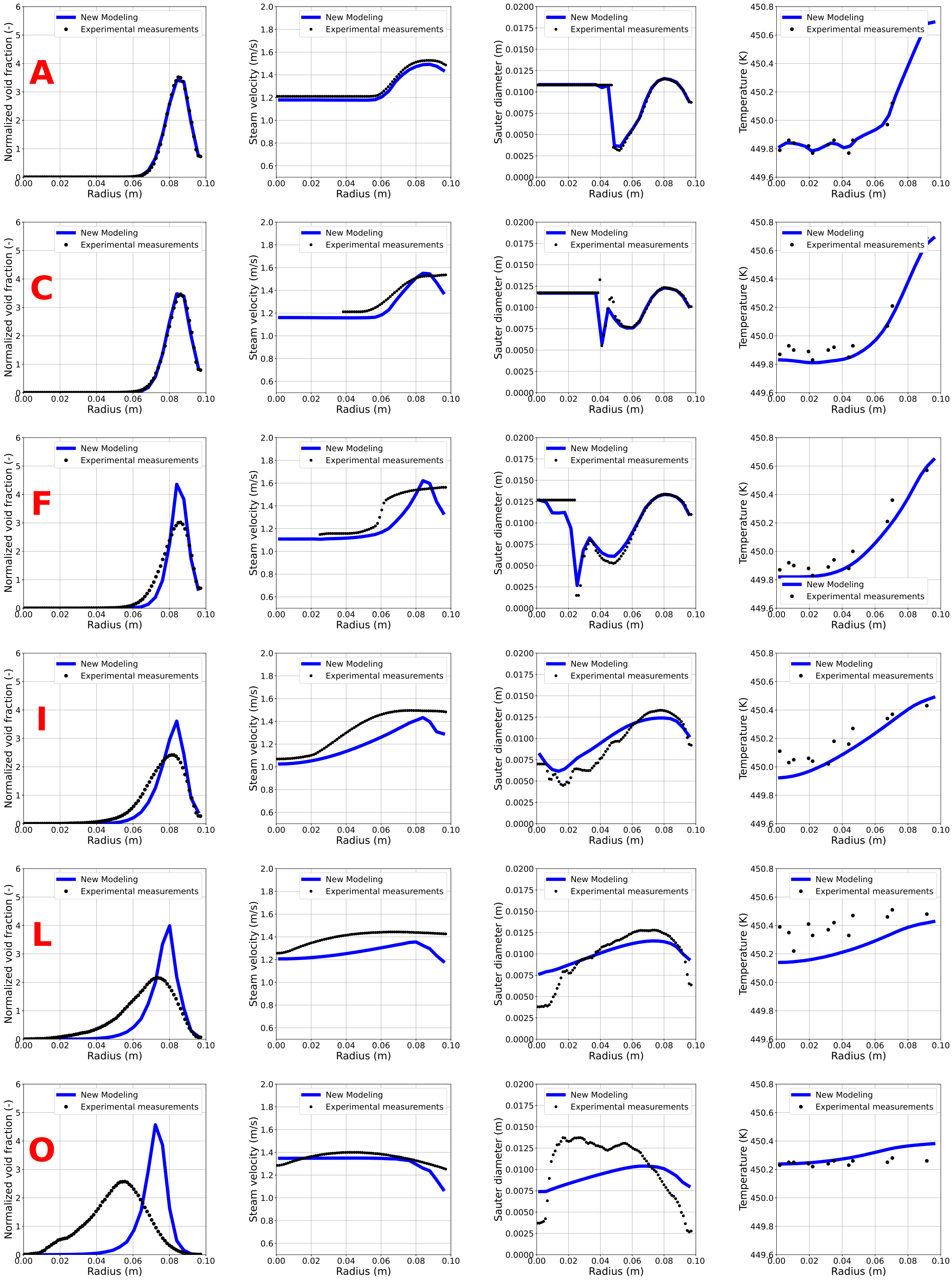

Figure I.1: Case 1

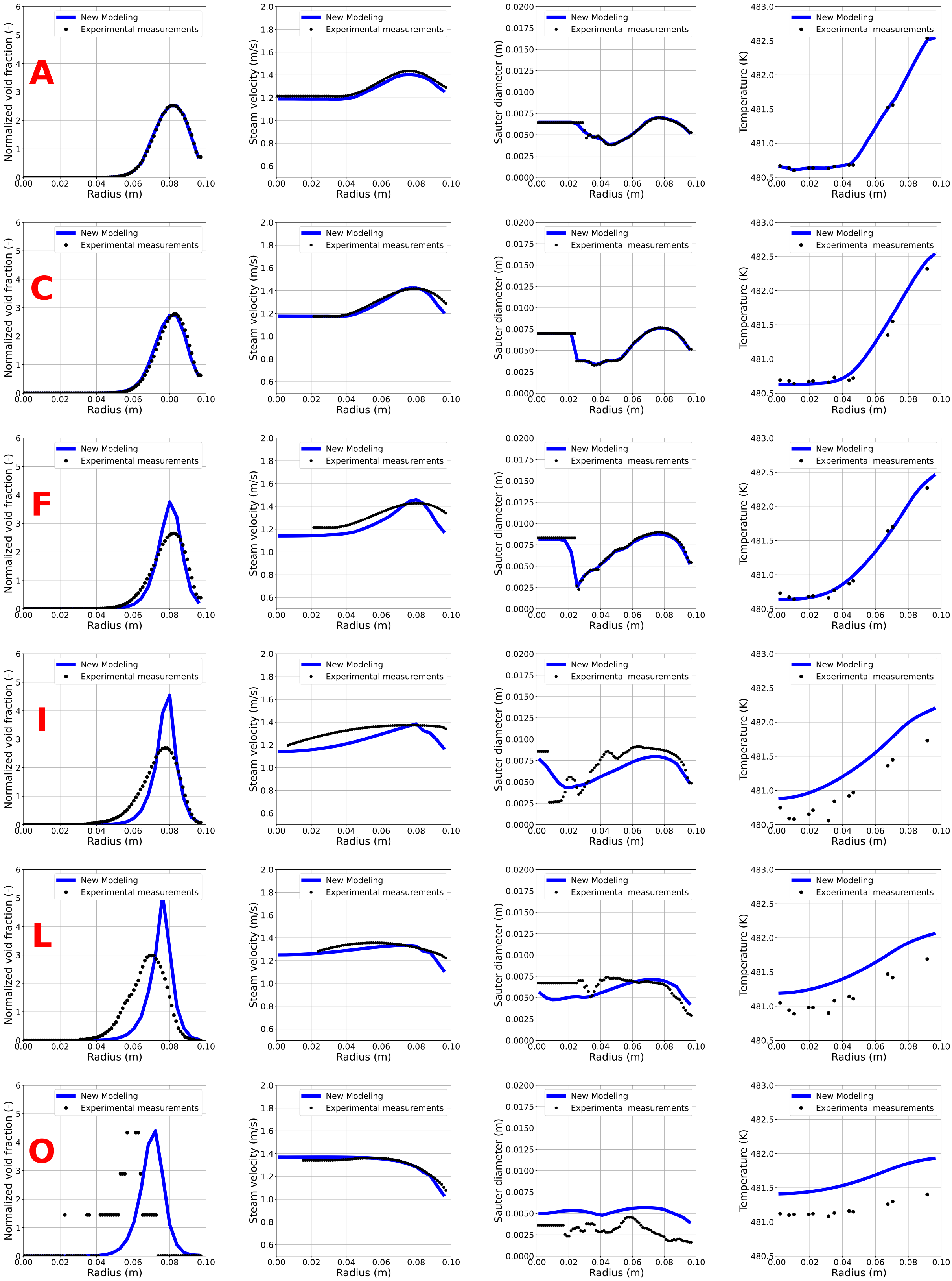

Figure I.2: Case 4

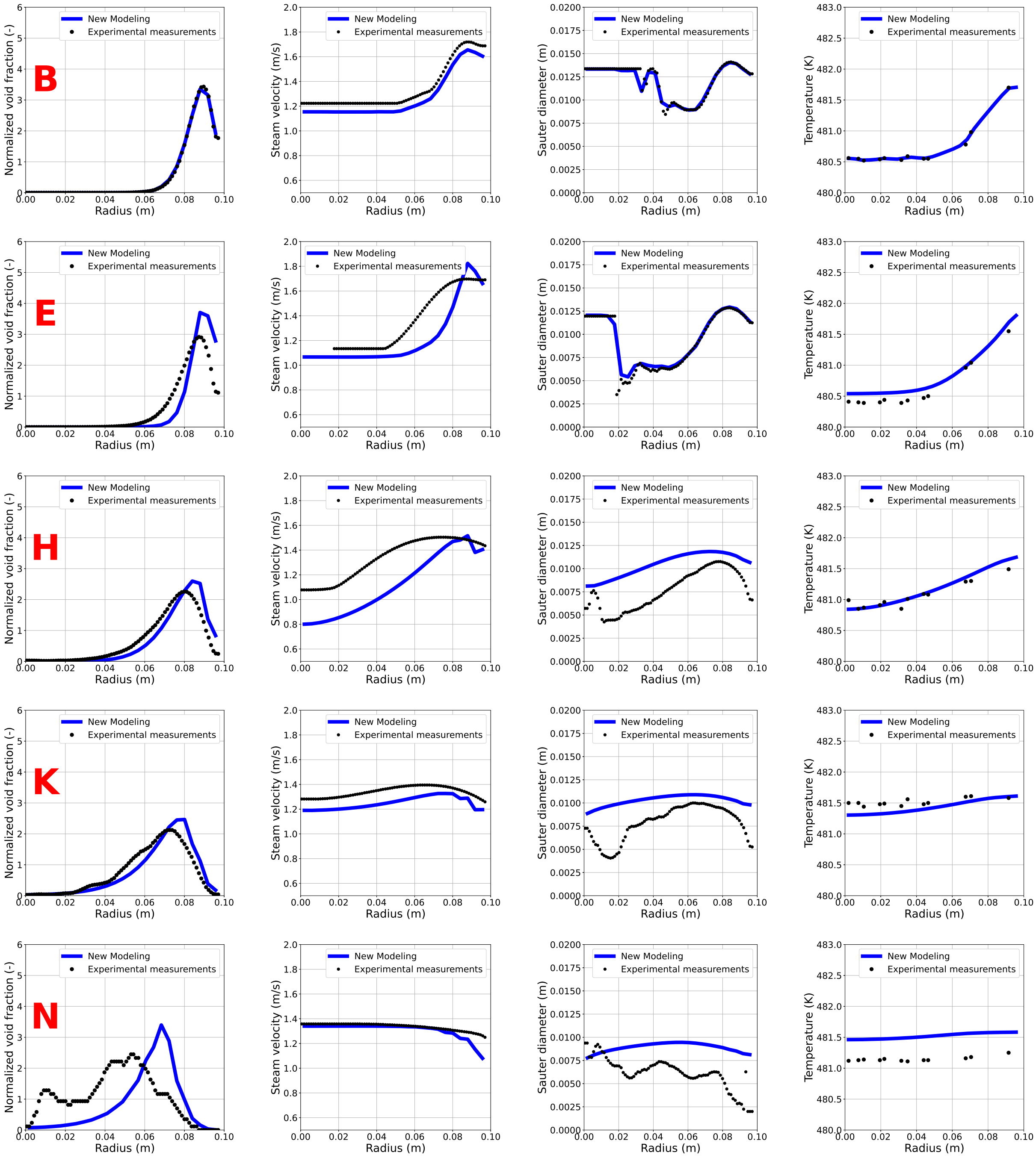

Figure I.3: Case 5

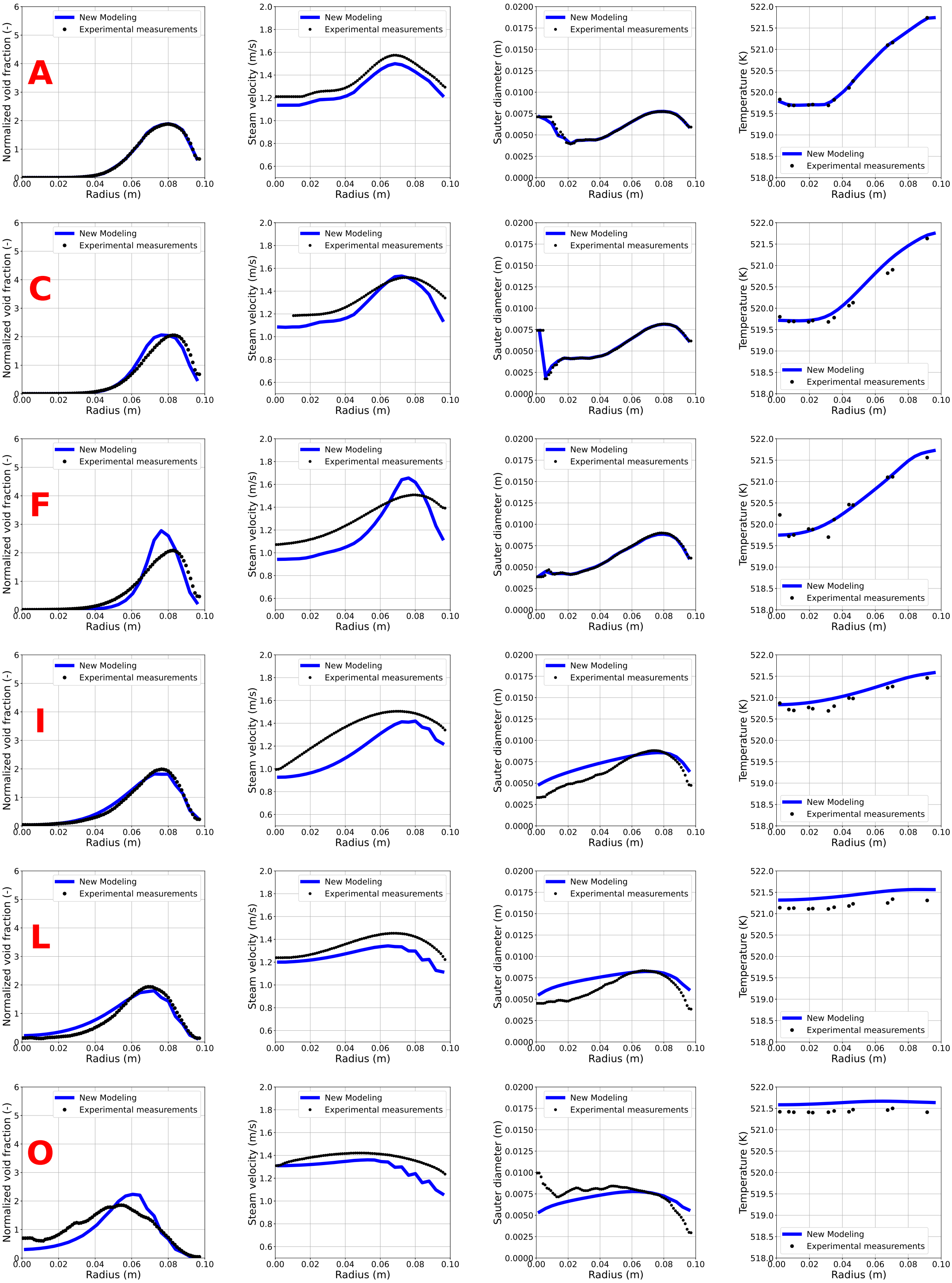

Figure I.4: Case 6

II Drag and Lift force models using quadratic distribution function

In the section 4.3.2, the drag and lift forces are expressed using the Dirac and quadratic laws. In order to be concise, the entire description of the coefficients used in the drag and lift forces are not expressed in section 4.3.2, but they are described in this appendix.

Drag

As mentioned in section 4.3.2, Ruyer et al. (2007) have expressed the drag force in the context of a quadratic law:

$$\underline{F}_D = -\rho_l \frac{3\pi}{4} 1.06 a_i |\underline{v}_r| \underline{v}_r N_D. \tag{II.1}$$

In order to describe the coefficient N_D, some variables are introduced. First, a function of the void fraction $\phi(\alpha_l)$ is defined, from Ishii and Hibiki (2011):

$$\phi(\alpha) = \left(\frac{1 + 17.67 \left[\alpha_l^m\right]^{6/7}}{18.67 \cdot \alpha_l^m} \right) \tag{II.2}$$

The coefficient m depends on the flow regime, is equal to 1.5 for bubble in water, to 2.25 for drop in liquid, and to 3 for drop in gas. In our test cases, this coefficient is equal to 1.5. Next, a new variable $Re_{\lambda,\alpha}$ is defined as:

$$Re_{\lambda_c,\alpha} = \frac{\rho_l |\underline{v}_r| \lambda_c}{\phi(\alpha) \mu_{\text{mixt}}}, \quad \text{with : } \lambda_c = \sqrt{\frac{\sigma}{(\rho_l - \rho_g) g}}. \tag{II.3}$$

with μ_{mixt} the mixture viscosity and λ_c the capillary length. Next a dimensionless diameter d^* is introduced in equation II.4 based on this $Re_{\lambda_c,\alpha}$ variable.

$$d^* = \begin{cases} 7.211 Re_{\lambda_c,\alpha}^{-0.477} & \text{if } Re_{\lambda_c,\alpha} < 5.3, \\ 5.345 Re_{\lambda_c,\alpha}^{-0.2976} & \text{if } 5.3 < Re_{\lambda_c,\alpha} < 675, \\ 2.856 Re_{\lambda_c,\alpha}^{-0.2014} & \text{if } Re_{\lambda_c,\alpha} > 675. \end{cases} \tag{II.4}$$

A new dimensionless variable is introduced as:

$$\tilde{d^*} = \min\left[1, \frac{d^*}{2 d_{10}}\right]. \tag{II.5}$$

Finally, two variables are introduced:

$$\mathrm{Eo}_{10} = \left(\frac{d_{10}}{\lambda_c}\right)^2, \tag{II.6}$$

$$\mathrm{Re}_{10} = \frac{\rho_l d_{10} |\underline{v}_r|}{\mu_{mixt}}. \tag{II.7}$$

The coefficient N_D is expressed using all these variables:

$$\begin{aligned} N_D = {} & 24 \frac{\mathrm{Re}_{10}^{-1}}{2} \left(\frac{\tilde{d^*}^3}{3} - \frac{\tilde{d^*}^4}{4} \right) + 2.4 \frac{\mathrm{Re}_{10}^{-1/4}}{2^{1/4}} \left(\frac{\tilde{d^*}^{15/4}}{15/4} - \frac{\tilde{d^*}^{19/4}}{19/4} \right) \\ & + \frac{2}{3} \sqrt{\mathrm{Eo}_{10}} \phi(\alpha) \left(\frac{1 - \tilde{d^*}^5}{5} - \frac{1 - \tilde{d^*}^6}{6} \right). \end{aligned} \tag{II.8}$$

Therefore, the drag force $\underline{F}_D$ can be calculated from the CFD variables using the method of moments with the quadratic law, using the equation (II.1).

Lift

The lift force obtained using the quadratic law is written as:

$$\underline{F}_L = 9.55\pi N_L \alpha_g \rho_l \underline{v}_r \times rot(\underline{v}_l). \tag{II.9}$$

The term N_L has been developed and is expressed by Ruyer et al. (2007). This term also requires the definition of new variables. First, the variable Re_{λ_c} is defined as:

$$\mathrm{Re}_{\lambda_c} = \frac{\rho_l||\lambda_c}{\mu_l}. \tag{II.10}$$

Next, a dimensionless diameter is introduced as:

$$d_1^* = \begin{cases} 2\lambda_c & \text{if } Re_{\lambda_c} < 3.687, \\ \lambda_c\sqrt{5.19\mathrm{Re}_{\lambda_c}^{-0.555} + 1.343\,(1.026)^{\mathrm{Re}_{\lambda_c}}} & \text{if } 3.687 < Re_{\lambda_c} < 14, \\ 1.765\lambda_c & \text{if } 14 < Re_{\lambda_c}. \end{cases} \tag{II.11}$$

Then, the variable $\tilde{d_1}$ is defined as:

$$\tilde{d_1} = \min\left[1, \frac{d_1^*}{2d_{10}}\right]. \tag{II.12}$$

Another variable $\tilde{d_2}$ is introduced as:

$$\tilde{d_2} = \min\left[1, \frac{\sqrt{10.7}\lambda_c}{2d_{10}}\right]. \tag{II.13}$$

A dimensionless capillary length is also defined as:

$$\tilde{\lambda_c} = \frac{\lambda_c}{2d_{10}}. \tag{II.14}$$

This dimensionless capillary length, and the two variables $\tilde{d_1}$ and $\tilde{d_2}$, are used to define the coefficient $\phi\left(\tilde{d_1}, \tilde{d_1}\right)$:

$$\begin{aligned} \phi\left(\tilde{d_1}, \tilde{d_2}\right) = \Bigg[&- 0.00105\tilde{\lambda_c}^{-6}\left(\frac{X^{12}}{12} - \frac{X^{11}}{11}\right) + 0.0159\tilde{\lambda_c}^{-4}\left(\frac{X^{10}}{10} - \frac{X^9}{9}\right) \\ &+ 0.0204\tilde{\lambda_c}^{-2}\left(\frac{X^8}{8} - \frac{X^7}{7}\right) - 0.474\left(\frac{X^6}{6} - \frac{X^5}{5}\right)\Bigg]_{\tilde{d_1}}^{\tilde{d_2}} \end{aligned} \tag{II.15}$$

Then, by introducing the variable $\mathrm{Re}_{2d_{10}} = \rho_l|\underline{v}_r|2d_{10}/\mu_l$, the coefficient N_L can be written as:

$$\begin{aligned} N_L = &(0.121\mathrm{Re}_{2d_{10}})^{-5}\int_0^{0.121\mathrm{Re}_{2d_{10}}d_1^*}\left(X^4 - (0.121\mathrm{Re}_{2d_{10}})^{-1}X^5\right)\tanh(X)\partial X \\ &+ \phi\left(\tilde{d_1}, \tilde{d_2}\right) + 0.278\left[\frac{X^6}{6} - \frac{X^5}{5}\right]_{\tilde{d_2}}^{1} \end{aligned} \tag{II.16}$$

The first line integral cannot be analytically expressed and is approximated using piece-wise polynomials functions as follows:

$$\int_0^x t^4\tanh(t)\partial t \approx \begin{cases} 0.148x^{5.91} & \text{if: } x < 1.39 \\ 0.199x^{5.00} & \text{if: } x > 1.39 \end{cases} \tag{II.17}$$

$$\int_0^x t^5\tanh(t)\partial t \approx \begin{cases} 0.126x^{6.91} & \text{if: } x < 0.734 \\ 0.199x^{6.00} & \text{if: } x > 0.734 \end{cases} \tag{II.18}$$

Using this approximation, the coefficient N_L can be calculated by a CFD code. Therefore, the lift force $\underline{F}_L$ defined by the method of moments using the quadratic function in equation (II.9) can be calculated.

III Wall friction correlation of CATHARE

As mentioned in the identification of the predominant terms of the momentum equations by an a priori method in section 3.2.3, the wall friction term has not been calculated directly from the CFD but has been calculated from a CATHARE correlation. This correlation is described in detail in this appendix.

The wall friction term in the case of bubbly flows is written a follows:

$$\text{Wall friction correlation} = \underline{f}_{wk} = \Phi \frac{2}{D_h} C_k \tilde{\rho}_k \underline{\tilde{v}}_k |\underline{\tilde{v}}_k|, \tag{III.1}$$

with D_h the hydraulic diameter and C_k a non-dimensional friction factor written as:

$$C_k = c_k f_k. \tag{III.2}$$

The variables f_k and c_k are respectively a single phase friction coefficient and a two-phase multiplier, which are expressed as follows:

$$f_k = \max\left\{\frac{16}{\tilde{\mathrm{Re}}_k}, \frac{0.079}{\tilde{\mathrm{Re}}_k^{0.25}}, 0.003\right\}, \quad \text{with: } \tilde{\mathrm{Re}}_k \text{ defined as:} \tag{III.3}$$

$$\tilde{\mathrm{Re}}_k = \frac{\tilde{\alpha}_k \tilde{\rho}_k \tilde{D}_h \cdot |\underline{\tilde{v}}_k|}{\mu_k} + \tilde{\mathrm{Re}}_0, \quad \text{with: } \mathrm{Re}_0 = 10, \tag{III.4}$$

$$c_l = \frac{\tilde{\alpha}_l \tilde{\rho}_l}{\tilde{\alpha}_g \tilde{\rho}_l + \tilde{\alpha}_l \tilde{\rho}_l}, \tag{III.5}$$

$$c_g = \tilde{\alpha}_g^{1.25}. \tag{III.6}$$

Then, the wall friction term can be calculated.

IV Turbulence-dispersion models in CATHARE

In section 1.3.3, the physical meaning of the turbulence and dispersion terms is described, and some models are mentioned. The model from CATHARE is expressed in detail in this appendix. This model is given as follows:

$$\underline{\underline{\tilde{\tau}_k^T}} = \left(\tilde{\nu}_{tk}^{\Phi} + \tilde{\nu}_{dk}^{\Phi}\right)\left[\underline{\nabla}(\Phi \underline{\tilde{v}}_k) + \underline{\nabla}^T(\Phi \underline{\tilde{v}}_k) - \frac{2}{3}\underline{\nabla}.(\Phi \underline{\tilde{v}}_k)\underline{\underline{\mathbb{I}}}\right], \text{with:} \tag{IV.1}$$

$$\frac{\left(\tilde{\nu}_{tk}^{\Phi} + \tilde{\nu}_{dk}^{\Phi}\right)}{D_h |\underline{\tilde{v}}_k|} = C_\mu \left[\left(\frac{120}{C_D} \frac{\sqrt{1-\Phi} + \Phi - 1}{\Phi^4} \left(\frac{\sqrt{1-\Phi}}{\mathrm{Re}} + \frac{1}{60}\right)\right)^{\frac{4}{3}} \frac{\Phi^4}{120\sqrt{1-\Phi}} \left(\frac{\sqrt{1-\Phi}}{\mathrm{Re}} + \frac{1}{60}\right)^{-1}\right], \tag{IV.2}$$

where $C_\mu = 0.09$, $C_D = 1.4$ and Re is the Reynolds number based on the hydraulic diameter D_h. It is worth to note that this model cannot be directly applied to the test cases considered in this thesis since in this thesis, the porosity is equal to 1, since the walls are at the tip of the numerical domains. In this model, a porosity of 1 would cause a division by zero, which means that this model is not suitable for the test cases considered in this thesis.

Regarding the enthalpy dispersion and turbulence terms, an option is available in CATHARE to consider both terms. Indeed, the turbulent and dispersion heat flux $\underline{\tilde{q}}_k^T$ is given by:

$$\underline{\tilde{q}}_k^T = \left(\tilde{\alpha}_{tk}\underline{\underline{\mathbb{I}}} + \underline{\underline{\tilde{D}}}_{dk}\right)\Phi.\nabla H_k, \quad \text{with } \tilde{D}_{dk}^{\text{trans}} = \frac{A\sqrt{\tilde{k}_f} D_h}{\tilde{\mathrm{Pr}}_{tk}}, \text{and: } \tilde{k}_f = 0.0367|\underline{v}_l|^2 \mathrm{Re}^{-1/6}. \tag{IV.3}$$

The macroscopic turbulent thermal conductivity $\tilde{\alpha}_{tk}$ is related to the macroscopic turbulent viscosity $\tilde{\nu}_{tk}$ via a macroscopic turbulent Prandtl number, $\tilde{\alpha}_{tk} = \tilde{\nu}_{tk}/\tilde{\mathrm{Pr}}_{tk}$. The parameter A is adjusted to 0.5 for the PWR subchannel and bundle tests PSBT benchmark, and $\tilde{k}_f$ is the spatial average turbulent kinetic energy given by a correlation from Valette (2012).

V Turbulent and dispersion models by up-scaling methods

A summary of the existing up-scaling methods that have been developed in the literature is given in section 1.1.2. The models developed by these authors are summarized in this appendix.

First, it is worth to note that all authors have used the same assumption as follows:

$$\left\langle \overline{\underline{v}'\underline{v}'} \right\rangle_f = \mu_{T\phi} \left(\underline{\nabla}\, \underline{\overline{v}} + \underline{\nabla}^T \underline{\overline{v}} \right) - \frac{2}{3} \langle \overline{k} \rangle_f \mathbb{I}, \quad \text{with: } \mu_{T\phi} = C'_\mu \frac{\langle \overline{k} \rangle_f^2}{\langle \overline{\epsilon} \rangle_f}. \tag{V.1}$$

Nakayama and Kuwahara (1999); Pedras and De Lemos (2001) and Chandesris (2006) used the same methodology and developed a $k - \epsilon$ macroscopic model. For the sake of conciseness, only the model proposed by Chandesris (2006) is shown here, in figure V.1.

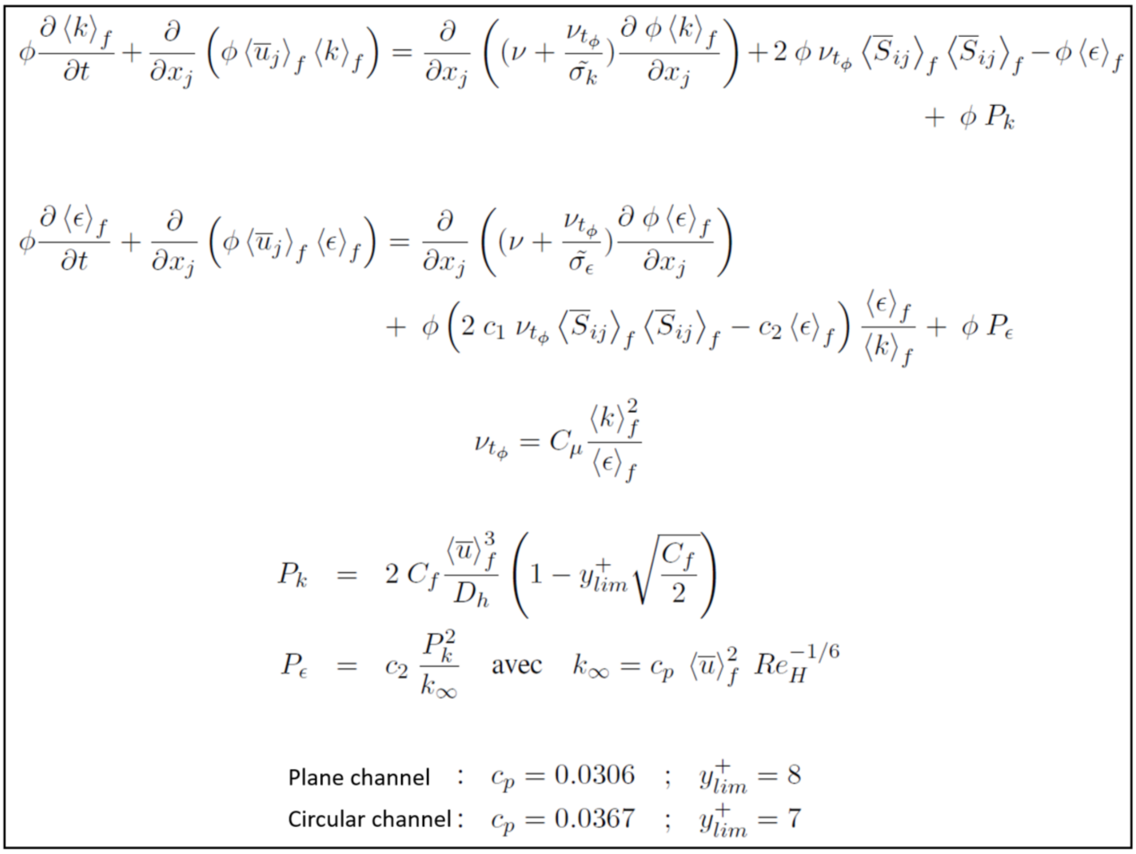

$$\phi \frac{\partial \langle k \rangle_f}{\partial t} + \frac{\partial}{\partial x_j} \left(\phi \langle \overline{u}_j \rangle_f \langle k \rangle_f \right) = \frac{\partial}{\partial x_j} \left((\nu + \frac{\nu_{t_\phi}}{\tilde{\sigma}_k}) \frac{\partial\, \phi \langle k \rangle_f}{\partial x_j} \right) + 2\, \phi\, \nu_{t_\phi} \langle \overline{S}_{ij} \rangle_f \langle \overline{S}_{ij} \rangle_f - \phi \langle \epsilon \rangle_f + \phi\, P_k$$

$$\phi \frac{\partial \langle \epsilon \rangle_f}{\partial t} + \frac{\partial}{\partial x_j} \left(\phi \langle \overline{u}_j \rangle_f \langle \epsilon \rangle_f \right) = \frac{\partial}{\partial x_j} \left((\nu + \frac{\nu_{t_\phi}}{\tilde{\sigma}_\epsilon}) \frac{\partial\, \phi \langle \epsilon \rangle_f}{\partial x_j} \right) + \phi \left(2\, c_1\, \nu_{t_\phi} \langle \overline{S}_{ij} \rangle_f \langle \overline{S}_{ij} \rangle_f - c_2 \langle \epsilon \rangle_f \right) \frac{\langle \epsilon \rangle_f}{\langle k \rangle_f} + \phi\, P_\epsilon$$

$$\nu_{t_\phi} = C_\mu \frac{\langle k \rangle_f^2}{\langle \epsilon \rangle_f}$$

$$P_k = 2\, C_f \frac{\langle \overline{u} \rangle_f^3}{D_h} \left(1 - y^+_{lim} \sqrt{\frac{C_f}{2}} \right)$$

$$P_\epsilon = c_2 \frac{P_k^2}{k_\infty} \quad \text{avec} \quad k_\infty = c_p\ \langle \overline{u} \rangle_f^2\ Re_H^{-1/6}$$

Plane channel : $c_p = 0.0306$; $y^+_{lim} = 8$

Circular channel : $c_p = 0.0367$; $y^+_{lim} = 7$

Figure V.1: Turbulence macroscopic model developed by Chandesris (2006).

In this model, the two additional transport equations for the macroscopic turbulent kinetic energy $\langle k \rangle_f$ and turbulent dissipation $\langle \epsilon \rangle_f$ are introduced and closed. Indeed, some closure laws are given as follows:

$$\langle \overline{S}_{ij} \rangle_f = 1/2 \left(\underline{\nabla} (\langle \underline{\overline{v}} \rangle_f + \langle \underline{\overline{v}} \rangle_f^T) \right) \tag{V.2}$$

$$c_k = \frac{\epsilon_\infty \sqrt{K}}{k_\infty \langle \underline{\overline{v}} \rangle_f} \quad \text{with K the porous permeability,} \tag{V.3}$$

$$\epsilon_\infty = \frac{\sqrt{k_\infty}}{\langle \underline{\overline{v}} \rangle_f}, \tag{V.4}$$

$$C_\mu = 0.09. \tag{V.5}$$

This model is very interesting since it allows to take into account the turbulence phenomena at the macroscopic scale, and also because this model is based on the existing relevant models at the RANS scale. However, the dispersion term linked to the spatial fluctuations is not taken into account in this formulation.

For this reason, Pinson (2006); Teruel and Rizwan-uddin (2009) and Drouin (2010) have introduced new models able to take into account both subgrid terms of turbulence and dispersion. Again with the aim of conciseness, only the model developed by Drouin (2010) is presented here. The same assumption done in equation (V.1) is used in this model, but in this case, the dispersion term is also taken into account in the model by introducing two new variables, the mean dispersion kinetic energy $\langle \overline{E}^m \rangle_f$ and the wake dissipation $\langle \overline{\epsilon}_w \rangle_f$, as it can be seen in equation (V.6).

$$\left\langle \overline{\underline{v}'\underline{v}'} \right\rangle_f + \langle \delta\overline{\underline{v}}\delta\overline{\underline{v}} \rangle_f = \mu_{T\phi}\left(\underline{\nabla}\,\overline{\underline{v}} + \underline{\nabla}^T\overline{\underline{v}}\right) - \frac{2}{3}\overline{\overline{\mathcal{K}}}\mathbb{I}, \quad \text{with: } \mu_{T\phi} = C'_\mu \frac{\overline{\overline{\mathcal{K}}}^2}{\overline{\overline{\mathscr{E}}}}, \quad \text{and:} \tag{V.6}$$

$$\overline{\overline{\mathcal{K}}} = \langle \overline{k} \rangle_f + \langle \overline{E}^m \rangle_f, \quad \overline{\overline{\mathscr{E}}} = \langle \overline{\epsilon} \rangle_f + \langle \overline{\epsilon}_w \rangle_f. \tag{V.7}$$

The model developed for turbulent flows is presented in Figure V.2.

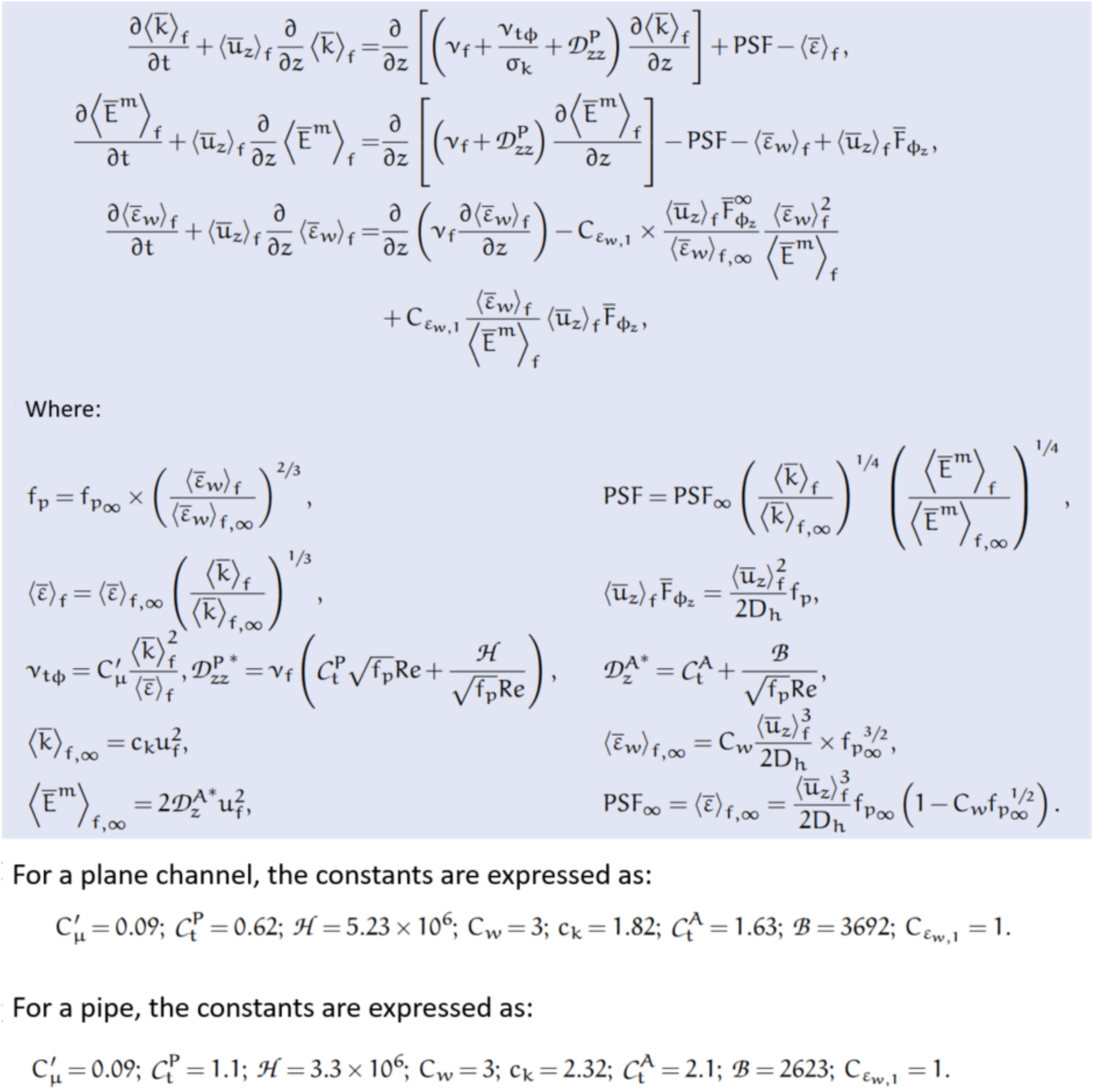

$$\frac{\partial \langle \overline{k} \rangle_f}{\partial t} + \langle \overline{u}_z \rangle_f \frac{\partial}{\partial z} \langle \overline{k} \rangle_f = \frac{\partial}{\partial z}\left[\left(\nu_f + \frac{\nu_{t\phi}}{\sigma_k} + \mathcal{D}^P_{zz}\right)\frac{\partial \langle \overline{k} \rangle_f}{\partial z}\right] + \mathrm{PSF} - \langle \overline{\varepsilon} \rangle_f,$$

$$\frac{\partial \left\langle \overline{E}^m \right\rangle_f}{\partial t} + \langle \overline{u}_z \rangle_f \frac{\partial}{\partial z} \left\langle \overline{E}^m \right\rangle_f = \frac{\partial}{\partial z}\left[\left(\nu_f + \mathcal{D}^P_{zz}\right)\frac{\partial \left\langle \overline{E}^m \right\rangle_f}{\partial z}\right] - \mathrm{PSF} - \langle \overline{\varepsilon}_w \rangle_f + \langle \overline{u}_z \rangle_f \overline{F}_{\phi_z},$$

$$\frac{\partial \langle \overline{\varepsilon}_w \rangle_f}{\partial t} + \langle \overline{u}_z \rangle_f \frac{\partial}{\partial z} \langle \overline{\varepsilon}_w \rangle_f = \frac{\partial}{\partial z}\left(\nu_f \frac{\partial \langle \overline{\varepsilon}_w \rangle_f}{\partial z}\right) - C_{\varepsilon_{w,1}} \times \frac{\langle \overline{u}_z \rangle_f \overline{F}^{\infty}_{\phi_z}}{\langle \overline{\varepsilon}_w \rangle_{f,\infty}} \frac{\langle \overline{\varepsilon}_w \rangle_f^2}{\left\langle \overline{E}^m \right\rangle_f}$$

$$+ C_{\varepsilon_{w,1}} \frac{\langle \overline{\varepsilon}_w \rangle_f}{\left\langle \overline{E}^m \right\rangle_f} \langle \overline{u}_z \rangle_f \overline{F}_{\phi_z},$$

Where:

$$f_p = f_{p_\infty} \times \left(\frac{\langle \overline{\varepsilon}_w \rangle_f}{\langle \overline{\varepsilon}_w \rangle_{f,\infty}}\right)^{2/3}, \qquad \mathrm{PSF} = \mathrm{PSF}_\infty \left(\frac{\langle \overline{k} \rangle_f}{\langle \overline{k} \rangle_{f,\infty}}\right)^{1/4} \left(\frac{\left\langle \overline{E}^m \right\rangle_f}{\left\langle \overline{E}^m \right\rangle_{f,\infty}}\right)^{1/4},$$

$$\langle \overline{\varepsilon} \rangle_f = \langle \overline{\varepsilon} \rangle_{f,\infty} \left(\frac{\langle \overline{k} \rangle_f}{\langle \overline{k} \rangle_{f,\infty}}\right)^{1/3}, \qquad \langle \overline{u}_z \rangle_f \overline{F}_{\phi_z} = \frac{\langle \overline{u}_z \rangle_f^2}{2D_h} f_p,$$

$$\nu_{t\phi} = C'_\mu \frac{\langle \overline{k} \rangle_f^2}{\langle \overline{\varepsilon} \rangle_f}, \mathcal{D}^{P*}_{zz} = \nu_f \left(\mathcal{C}^P_t \sqrt{f_p}\mathrm{Re} + \frac{\mathcal{H}}{\sqrt{f_p}\mathrm{Re}}\right), \qquad \mathcal{D}^{A*}_z = \mathcal{C}^A_t + \frac{\mathcal{B}}{\sqrt{f_p}\mathrm{Re}},$$

$$\langle \overline{k} \rangle_{f,\infty} = c_k u_f^2, \qquad \langle \overline{\varepsilon}_w \rangle_{f,\infty} = C_w \frac{\langle \overline{u}_z \rangle_f^3}{2D_h} \times f_{p_\infty}^{3/2},$$

$$\left\langle \overline{E}^m \right\rangle_{f,\infty} = 2\mathcal{D}^{A*}_z u_f^2, \qquad \mathrm{PSF}_\infty = \langle \overline{\varepsilon} \rangle_{f,\infty} = \frac{\langle \overline{u}_z \rangle_f^3}{2D_h} f_{p_\infty}\left(1 - C_w f_{p_\infty}^{1/2}\right).$$

For a plane channel, the constants are expressed as:

$C'_\mu = 0.09$; $\mathcal{C}^P_t = 0.62$; $\mathcal{H} = 5.23 \times 10^6$; $C_w = 3$; $c_k = 1.82$; $\mathcal{C}^A_t = 1.63$; $\mathcal{B} = 3692$; $C_{\varepsilon_{w,1}} = 1$.

For a pipe, the constants are expressed as:

$C'_\mu = 0.09$; $\mathcal{C}^P_t = 1.1$; $\mathcal{H} = 3.3 \times 10^6$; $C_w = 3$; $c_k = 2.32$; $\mathcal{C}^A_t = 2.1$; $\mathcal{B} = 2623$; $C_{\varepsilon_{w,1}} = 1$.

Figure V.2: Turbulence and dispersion macroscopic model developed by Drouin (2010).

This model is valuable since it allows to model not only the turbulence but also the dispersion term. This model has been established on both plane and circular channels in academic conditions, i.e., for liquid flows at atmospheric pressure, without heat sources, and for Reynolds numbers between 10^4 and 10^5.